Javier Pallarés Ranz

UNBURNED CARBON IN ASH PREDICTION IN PULVERIZED COAL UTILITY BOILERS. ANALYSIS AND ASSESSMENT OF OPERATION STRATEGIES

Doctoral Thesis

Supervisor

Dr. Inmaculada Arauzo Pelet

Zaragoza, 2007

Javier Pallarés Ranz

UNBURNED CARBON IN ASH PREDICTION IN PULVERIZED COAL UTILITY BOILERS. ANALYSIS AND ASSESSMENT OF OPERATION STRATEGIES

Doctoral Thesis

Supervisor

Dr. Inmaculada Arauzo Pelet

Zaragoza, 2007

As in any research work that demands study and dedication during a long period of time, it is impossible to reach the end without the help of many people, who collaborate unselfishly and bring their talent, time and enthusiasm. To all these people that have made the work presented in this thesis possible, the following recognition is dedicated.

First of all, I would like to express my deep thanks to my thesis supervisor, Inmaculada Arauzo, who, besides persuading me to start this work and encouraging me with her contagious optimism, has been as intensely involved as me in the work from the first day to the last. Also, within the University of Zaragoza and as the director of the thermal division of the CIRCE Foundation, I want to express my deepest gratitude to Cristóbal Cortés, for all the valuable comments and useful suggestions, and for putting his trust in me allowing me to form part of his research group.

I also wish to thank the CIRCE Foundation and its director Antonio Valero, for his involvement and commitment with research and technology, and for the opportunity that has been offered to me when supporting and financing all this work. This way, CIRCE has become my second home in the last seven years, sometimes the first one, where I have been very lucky to meet exceptional and brilliant people inside and outside the office. Thanks to all of you, especially to Luís Ignacio, Sergio, Mariano, José Miguel, José, Dani, Fernando, Jesús and Toñi, from whom I have learned very much and to whom I greatly thank their attention, collaboration and support.

I express my gratitude to the European Union for financing the research project 7220-PR-130-CARNO, and to all the partners that took park on it, whose investigations and contributions have enriched my work. Especially, I want to thank the plant personnel of Lamarmora power plant (ASM Brescia, Italia) and its generation manager Marco Treccani, which have provided us with all the technical and operational information available at the plant for the development and validation of the unburned carbon prediction system. At the same time, also within this European project, I especially want to thank Peter Stephenson for his useful suggestions and discussions about the coal combustion model development, and to Michael Whitehouse for his efforts when coordinating the project.

I also wish to thank the University of Leeds and Mohamed Pourkashanian for allowing me to work in the CFD centre that he supervises, and especially I deeply thank Alan Williams who guided me and contributed enormously in the definitive coal combustion model development. At the same time, I would like to give special thanks to Adrian, Nicu and Raymond, also from the University of Leeds, for their help in the work, especially in the revision and translation of the thesis, and above all to make me feel like home during the time I spent in Leeds and London with them.

Thanks a million to Enrique Teruel for his patience, for losing the sense of sight in front of the laptop with the weights and bias terms, and for all the work that he has done to succeed in making the neural network system come out of his Matrix and become real.

I also thank Pedro Jodrá for his commentaries and suggestions during the statistical study of the results.

Finally, the greatest acknowledgement together with a huge kiss to my parents, my sister and my aunt, for their unconditional support, for bearing with me too many times in the last years, and because I know that at this moment they are as happy as I am; to Miriam because she is everything to me, and to my friends to show me that there is Ludus Magnus life apart from the thesis.

To my parents

CONTENTS

1 INTRODUCTION

Nowadays coal is the most generous fossil resource in the world and because of this it plays a decisive role as a primary source of energy. More than 27 % of the energy consumed and more than 34 % of the electricity generated in the world originates from pulverized coal combustion (BP Statistical review of world energy, 2006). In the future, power companies and power equipment makers suggest a significant switch from gas to coal as the preferred fuel in the coming decade. This re-emergence of coal as a primary fuel for power generation is the result of technological changes that have reduced the amount of pollutants and particulate emissions to the atmosphere and recent international worries about the security of our gas supply. Consequently, in the next decades coal will continue constituting an essential energy source. Nevertheless, it is necessary to have a sensible and efficient use of this resource, pursuing two main objectives: to observe the environmental legislation and to obtain competitive generating costs in a free market.

It's some time since both these objectives have forced power plant managers to look for the most efficient combustion conditions using the cheapest fuel. The immediate consequences of this change in energy policy has led to the establishment of new technologies that minimize pollutant emissions and has encouraged the search for more flexible fuel supply alternatives such as co-combustion and blending coals.

Increasing efficiency, controlling particulate and gas emissions and minimizing unburned carbon losses are partially attained by improving the combustion process. For this reason,

predicting combustion efficiency in utility boilers, and particularly, determining unburned carbon levels are essential to reach both objectives. Unburned char particles that leave the furnace represent a heat loss in the combustion process, reducing the thermal efficiency of the unit. Moreover, they increase heat exchangers' erosion, may reduce the efficiency of dust separation/collection equipment and may impede the utilization of fly ash as a replacement for Portland cement or additives to concrete.

In this chapter the main problems associated with an unburned carbon increase in utility boilers that leads to the aforementioned situations is presented. Finally, the experimental and predictive systems that allow us to identify and avoid those boiler operating conditions that lead to excessive fuel consumption, are also described.

1.1 Coal combustion process in a utility boiler

Before studying in detail the causes and problems derived from unburned carbon losses, it is interesting to review the history of the coal as it travels around the power plant, from its reception at the coal yards to its emission from the chimney stack by means of exhausted gases and the micrometric particles suspended on them. A rigorous study of the combustion process in a utility boiler cannot be limited exclusively to the boiler.

The first step is the coal type selection. The coal that arrives at the power plant is stored in the coal yard. From this point, the incoming fuel to the different coal piles is managed and a different coal analysis is conducted to determine its composition and properties. This analysis allows the verification of the condition of the coal, since most of the plant equipment is designed to operate with a specific coal rank and coal properties. The price of coal represents the greatest cost to the plant. For this reason, a small saving in its price may imply a significant reduction in the power plant expenditure. Since generation costs are very similar for many power stations, a reduction in the coal price may determine if a power plant can offer a lower generation cost assuming a lower risk, and then to come into operation instead of another power station. Nowadays, it is a common practice to blend coals. There exist two main reasons for this: to reduce the fuel cost or to improve some property within any particular coal. Reducing the fuel cost is probably the most common reason. However, if a coal presents a known problem such as a low ash fusion point, sulphur content or low reactivity, it is possible to blend different, compatible coals to modify the properties of the original coal, thus, obtaining a better performance of the plant equipment. Another reason that has promoted power plant managers to blend coals is to obtain a higher coal supply availability (Haas et al., 2001).

The coal that meets the quality standards required by the plant is conducted via conveyor belts to storage hoppers from which the mills are fed. In the mills, coal undergoes a simultaneous drying and milling process after which the coal particles are pneumatic conveyed by the primary air to the burners. In the case of front wall fired boilers equipped with swirl burners, the primary flow (air and coal) in the burner starts mixing with the secondary air coming from the wind box. Both streams are then introduced into the boiler where a pilot gas burner starts combustion. The secondary air rotates ensuring the flame stability. Depending on the type of burners, there may exist an additional air inlet, called tertiary air, with the purpose of stepping down the combustion and decreasing the peak temperature to reduce NO_x emissions.

Strictly speaking, coal combustion, may be divided into three stages. Firstly, a rapid pyrolysis, also called devolatilization, takes place in which the volatile content of the coal is yielded; then the homogeneous combustion of the volatile products is produced; and finally, the remaining char residue oxidation takes place. Not all the char residue is completely burned and this carbon fraction is called unburned carbon loss.

The fluid flow in the region close to a burner may be divided into two zones (Unsworth et al., 1991):

- A near burner region (Figure 1.1, zone C), where two recirculation flows take place: an inner recirculation zone (Figure 1.1, zone A) where volatile products' combustion is completed and an outer recirculation zone (Figure 1.1, zone B) of the combustion products that provides the heat release to ensure the flame stability.

- A region downstream where combustion gases, the particles suspended on them, ash and unburned carbon, head for the boiler exit (Figure 1.1, zone D).

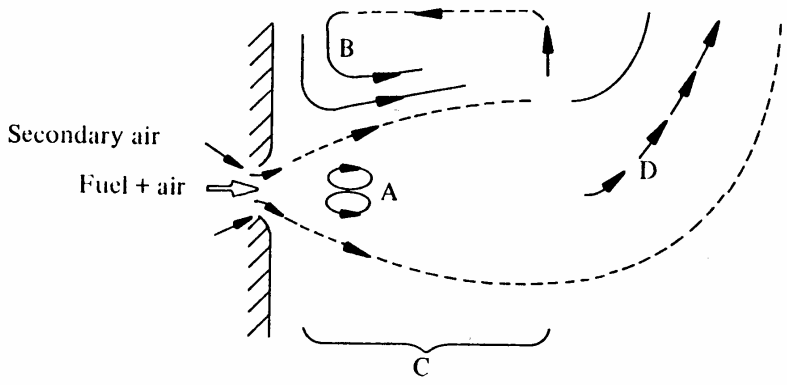

Fig. 1.1 Flow in the near burner region (Unsworth et al., 1991)

Depending on the burner's arrangement in the boiler, the possible flame to flame interactions and the reversed flow regions in the furnace, the trajectories tracked by the particles to the boiler exit may become more or less chaotic. Some of the particles, around 20 - 40 %, either remain stuck to the walls and bank tubes leading to slagging and fouling phenomena that impedes heat transfer to the water tubes, or settle in the bottom hopper (Llera, 2002). The product gases flow after passing through different heat exchangers, which vary depending on the boiler type (superheaters, reheaters, economizers, air preheaters). Here, particles can also settle before they reach the dust separation/recollection equipments. Electrostatic precipitators are the most widespread separation/recollection equipment used, with efficiencies over 95 %. Finally, depending on coal rank and properties, other gas cleaning systems, such as NO_x reduction reactors and desulphuration plants are introduced before expelling the exhausted gas flow to the atmosphere.

1.2 Problems derived from unburned carbon losses

Unburned char particles that leave the furnace represent a heat loss in the combustion process, reducing the thermal efficiency of the unit. Furthermore, various related publications agree that other effects are derived from an increase in unburned carbon in ash levels as it will be presented subsequently (Walsh and Xie, 1992).

First, unburned carbon levels may increase bank tubes erosion and the deposition over them thus decreasing heat transfer to the water tubes. The formation of ash deposits on the furnace walls is a well studied phenomena since it has a great impact in the boiler operation. The variation in type, shape and location of these deposits, depend very much on the coal type and the boiler design and operation. For this reason, special attention is taken during the plant design, increasing the thermal exchange effective area using high resistant steel in the more exposed tubes and installing cleaning systems such as soot blowers that remove these ash deposits from the walls (Llera, 2002).

Another disadvantageous effect of unburned carbon in ash reported by many authors is a decrease in the electrostatic precipitator efficiency. However, within the literature empirical models do not exist that directly relate an increase in carbon in ash levels with a decrease in the electrostatic precipitator efficiency. This is because that while many parameters such as ash particles size, composition, morphology, cohesion index and resistivity, all have an impact on collection efficiency, there is not one parameter in particular that stands out over the others.

Instead, the collection efficiency depends on the coal composition and combustion conditions. In general, it can be stated that (Wu, 2000):

- Greater particle size increases the electrostatic precipitator efficiency.

- Irregular, highly porous and complex morphology particles register higher drag forces, decreasing the migration velocity to the electrodes and thus the collection equipment efficiency.

Low rank coals tend to swell during combustion while they are burned from different fronts, increasing their porosity. If a particle is fragmented due to a high pressure inside the pores, a number of small sized, highly porous particles with complex morphology are obtained. Therefore, the collection efficiency depends on the fragmentation level attained during combustion. A higher fragmentation level will result in a greater number of small sized particles (negative effect), with less complex morphologies (positive effect). The contrary effects are encountered when a lower fragmentation level is produced. High rank coals have a low tendency to swell and facilitate cohesion with mineral matter inclusions. Consequently, less porous morphologies (positive effect) and variable particle sizes are encountered depending on the cohesion level attained. In spite of these general behaviours, particles from the same coal may exhibit different combustion behaviour as a function of coal macerals (rich vitrinite particles tend to swell during combustion, whilst exinite rich particles tend to fragment during pyrolysis), or as a function of the char residue matrix composition, especially the sulphur content which reduces ash resistivity expediting its capture.

A last relevant effect of unburned carbon in ash is that it may impede the utilization of fly ash as a replacement for Portland cement or an additive to concrete. If carbon in ash content exceeds a reference level established in the concrete quality regulations (BS8500 in the UK, BS EN206 in the rest of Europe), this ash cannot be used in concrete manufacture (Sear, 2001). By substituting up to 30 % of the cement content in building applications with fly ash is advantageous for several reasons: it increases concrete strength, decreases its permeability, reduces its manufacturing costs and reduces the heat released in the hydration reactions leading to a net reduction in CO_2 emissions of 30 % (Suuberg et al., 1999). Nevertheless, fly ash used in concrete production should comply with different specifications related to its size, density, SO_3 and NH_3 content, colour and carbon content. Aggregates typically take up three quarters of the total volume in structural concretes. The rest of the volume is made up of hard cement paste, and air bubbles. Commonly, a controlled quantity of air in uniformly dispersed microscopic bubbles (air-entraining admixtures, AEA) is introduced to impart desirable properties to the

concrete, including increased durability. The adverse effect of unburned carbon in the concrete matrix is that this carbon adsorbs these air additives (AEA) decreasing the number of bubbles, and then, degrading its strength (Külaots et al., 1999; Maroto-Valer et al., 2001).

To determine the carbon in ash content, the loss of ignition test (LOI) is commonly carried out, the description of which is presented in Section 1.3. LOI values of 5 % (BS EN206) or 7 % (BS8500) represent the unburned carbon limit in building applications (Sear 2001, 2002). However, since these kinds of tests are based on the determination of the carbon fraction in ash, recent studies have shown that it is probably more interesting and precise to determine the unburned carbon porosity and surface area as these parameters finally determine the capability of carbon to adsorb AEAs. The ability of a particular fly ash to adsorb AEAs depends upon three main factors: the total surface area presented by the carbon in the ash, the accessibility of the surface area in the carbon and the nature of the carbon surface which is influenced by the degree of carbon surface oxidation (Külaots et al., 1999). Most fly ash carbon samples have surface areas much larger than would be expected from the external geometric area, since carbon particles have a large amount of porosity including micropores (< 20Å), mesopores (20 Å - 500 Å) and macropores (> 500 Å). Standard LOI tests do not give information about the intrinsic morphology of the particle. For example, low rank coals give typically low LOI values indicting a conducive property for conforming with concrete while in reality they tend to be the more problematic coals for this application. The reason for this is that low rank coals typically have larger porosity and surface areas than high rank coals. The test used to determine the adsorption of AEAs is known as Foam index test (Suuberg et al., 1999).

1.3 Factors influencing unburned carbon losses

In order to predict and control unburned carbon levels in power plants, it is necessary to determine which factors influence their reduction and quantify their relevance. As it was presented in Section 1.1, unburned carbon formation is not restricted to the combustion process in the furnace.

The main factors affecting unburned carbon losses may be classified into three categories (Walsh and Xie, 1992):

1. Coal and char related properties.

2. Coal preparation and grinding pre-treatments.

3. Burner and boiler designs and operation conditions.

Hereinafter, each source's characteristics are summarized.

1. Coal and char related properties

This first category comprises coal and char properties such as: elemental and maceral composition, high temperature pyrolysis yield, char intrinsic structure and reactivity and ash properties and composition. Their influence on unburned carbon formation is explained through the combustion process itself.

Coal composition and properties partly determine unburned carbon losses. Coal ultimate analysis is used to determine the stoichiometric air and therefore the total air mass flow for a given firing rate and excess oxygen level consign. As it was presented in Section 1.1, the combustion process may be divided into three stages: devolatilization, volatiles products' homogeneous combustion and char oxidation. During devolatilization, volatile matter, which is formed by hydrogen, nitrogen, sulphur, oxygen and part of the carbon not fixed to the char residue, is yielded. This stage has a great influence on combustion since it controls the particle ignition. It takes place during the first 100 ms at the near burner inner recirculation region and is also responsible for stabilizing the flame. Moreover, coal pyrolysis has a great effect on the structural and reactive properties of char. Standard proximate analysis of coal allows us to determine the coal volatile content. However, under high temperature combustion processes, such as those found in real utility boilers, part of the carbon in the coal matrix is also volatilized yielding a higher volatile content than the one obtained from the proximate analysis. The high temperature volatile released is determined as a function of temperature, heating rate and coal type, by means of thermogravimetric (TGA) and drop tube furnace (DTF) analysis. In order to give an idea of the importance in the determination of this high temperature released, the volatile yield may increase 20 – 75 % (dry ash free, d.a.f.) with respect to the proximate analysis. This can lead to a factor of two reduction in the weight of the char residue, whose oxidation rate is the determining step in coal combustion (Kobayashi et al., 1976). Volatile products' combustion controls flame temperature and oxygen concentration in the near burner region, directly influencing the char oxidation rate.

Char morphology and porosity are determined by coal related properties and the devolatilization process history. Char oxidation is the slowest stage in coal combustion and therefore has a great influence on the combustion behaviour as well as many other aspects such as: the coal structure and reactivity variations with burnout, diffusion effects through the porous structure or char fragmentation (Chan et al., 1999). In Section 1.2, it was described how coal structure and

maceral content did not only have an effect on the combustion process, but also over the dust collection equipments' efficiency and in the quality of fly ash used in the manufacturing of Portland cement and concrete.

Coal ash content has a double effect on coal combustion kinetics. Mineral matter content may produce a catalytic effect increasing char reactivity at low temperatures. However, it also obstructs the combustion process since ash forms a film layer covering the particle surface as combustion proceeds, impeding oxygen diffusion to the active sites and therefore decreasing combustion efficiency.

Finally, increasing coal moisture content results in a decrease of the flame temperature reducing the combustion efficiency followed by an increase in unburned carbon loss (Kurose et al., 2001). This behaviour is more relevant with bituminous and sub-bituminous coal blends since the latter has greater moisture content (Ikeda et al., 2002). However, in general, coal moisture content is not a relevant cause of unburned carbon formation since the primary air (previously heated), that conveys the particles from the mills to the burners, removes most of it.

2. Coal preparation and grinding pre-treatments

Another relevant factor affecting unburned carbon losses is the fineness of the particles entering the furnace. Higher particle sizes result in greater carbon losses. For this reason, the milling process has an outstanding importance in unburned carbon reduction and it is necessary to control the pulverized coal particle size distribution. Again, many factors determine the final size distribution: primary air mass flow, coal mass flow, coal properties (composition and grindability index HGI) and also the mill's classifier position and grinding pieces ageing since their last replacement. Furthermore, since the primary air, that pneumatically conveys the pulverized coal particles to the burners, is pre-heated, it removes part of the moisture content improving combustion efficiency. Finally, the design of the ducts and pipes that connect the mills to the burners may lead to mass flow imbalances in the load fed from each burner and this can produce flow asymmetries in the boiler that may produce an increase in the unburned carbon loss.

3. Burners and boiler designs and operation conditions

This category comprises the characteristics and adjustments of burners, primary and secondary air inlets designs (and tertiary air inlets if available), swirling secondary air vanes, the number of burners in operation, primary and secondary air temperatures and boiler design and operation conditions. The combination of these factors determine the air/coal mixing, combustion peak temperatures, residence times for particles and finally the operation conditions in which

combustion takes place. Previously, the relevance was mentioned of the near burner region in burnout determination where the secondary air rotation helps to stabilize the flame mixing the hot combustion gases with the primary air and coal mixture that enters the furnace from the mills. Moreover, the char structure is not only determined by coal properties but also by the temperature and oxygen partial pressure history of the particles on their way through the boiler. Consequently, these variables, together with the coal properties, determine the nature and yield of volatile products, its yielding rate and the morphology and microscopic porous structure of char.

Porosity is particularly important since it controls species' diffusion in and out of the char. Finally, to understand the great relevance of char intrinsic characteristics on the combustion process, it is necessary to highlight the efforts realized in recent years to describe how they vary and affect species' diffusion and the chemical reaction processes. Historically, pulverized coal combustion has been modelled as a process controlled by both oxygen diffusion and oxidation reaction rates at the particles' surface (Zone II[1]). However, experimental studies have shown a variation in the particle intrinsic structure as char oxidation proceeds, promoting a decrease in char reactivity in the late stages of combustion leading to a transition from Zone II to the Zone I[1], controlled by reaction rate. This phenomena known as thermal annealing of char, has given rise to new char oxidation kinetic models that are gradually replacing traditional models (Chapter 2).

[1] Three-zone theory (Unsworth et al., 1991; Hong, 2000) (Chapter 2, Section 2.3.1):

Zone I: Combustion controlled by reaction rate. Oxygen diffuses to particle's surface faster than it is consumed. Oxygen partial pressure at the particle surface is almost identical to that of the bulk gas stream. The oxygen partial pressure penetrates the particle, which burns both on the outer surface and inside the pores.

Zone II: Combustion controlled by both oxygen diffusion and reaction rate. Oxygen diffuses to the particle surface and partially penetrates the particle since the oxygen is consumed by the oxidising carbon before it can completely penetrate the pores. Consequently, its concentration is less inside than outside the particle.

Zone III: Combustion controlled by oxygen diffusion. Oxygen diffuses to the particle surface where, due to very high char reactivity, it immediately combines with carbon. The oxygen partial pressure at the particle surface is close to zero and combustion takes place only on the particle outer surface.

1.4 Unburned carbon in ash measurements

To follow-up unburned carbon levels in a power plant, ash samples from the different hoppers located in the chimney exhaust are regularly taken. Generally, ash samples are compiled from the hopper of the first dust separation/recollection equipment because of its easy accessibility. Before this, combustion gases flow through the economizer and air pre-heaters, where part of the fly ash deposits in both their respective hoppers and stagnation zones. Three standardized methods are used to determine unburned carbon in ash:

1. Carbon-in-ash (CIA). This is the carbon percentage in ash after combustion. It should be taken into account that fly ash generally represents 60-80 % of the total ash making it difficult to quantify this percentage in a power plant.

2. Loss of ignition (LOI). Expresses the heat released from the ash at specified test conditions, including effects of the char sulphur content. The LOI test value is generally one or two percentage points higher than the CIA value.

3. Combustion loss (CL). This test involves measuring the heat remaining in the unburned carbon and expressing it as a percentage of the calorific value of the original coal.

The unburned carbon in ash fraction also depends on the ash content of the parent coal. Even if combustion efficiency is high, unburned carbon in ash values are greater for a low ash content coal than for a high ash content coal. Therefore, it is difficult to compare the combustibility of different coals from this parameter. To achieve this, the overall unburned carbon fraction may be calculated according to Eq. 1.1 (Kurose et al., 2001).

$$U_c = 1 - \eta = \frac{U_{c\_ash}}{1 - U_{c\_ash}} \cdot \frac{C_{ash}}{1 - C_{ash}} \qquad \text{(Ec. 1.1)}$$

Where U_c is the unburned carbon fraction per coal kg, η is the combustion efficiency, U_{cash} is the unburned carbon in ash fraction and C_{ash} is the ash content of the parent coal.

1.5 Unburned carbon prediction systems

Just as important as the empirical determination of the unburned carbon level is its prediction under any given operating conditions. The combustion behaviour of pulverized coal can be investigated by means of pilot-scale experiments, advanced combustion kinetics models and CFD codes. Pilot-scale testing suffers from two basic shortcomings. Firstly, the physical processes involved in utility boilers are not completely scalable and as a consequence, small-scale experiments can be only considered as approximations. Also, an experimental rig involves very high investment and maintenance costs. A complementary method to pilot-scale testing is using a detailed combustion kinetics model. The basis of the method is to separate the influence of fuel properties and combustion conditions on coal burn-out behaviour. The fuel-related empirical parameters in the model have to be fitted from laboratory experiments. These data are then used to predict burn-out behaviour under full-scale furnace conditions (Unsworth et al., 1991). Coal combustion models are made up of a devolatilization submodel and a char oxidation submodel. Traditional devolatilization submodels such as the single reaction model or the two competing reactions model are being progressively substituted by commercial codes that predict concentration and yield from major species, for example FG-DVC or FLASHCHAIN. Single film char oxidation models have led to other advanced kinetics models, which account for variations in reactivity during combustion and internal pore structure. In general, the benefit of using detailed combustion kinetics models is that their results can be obtained quickly and at low cost for boilers of different designs and operating conditions. However, these models cannot completely capture the complexity of the physical and chemical phenomena that occur in an industrial furnace such as burner to burner interactions or turbulent mixing and they generally under-predict carbon in ash levels for utility boilers. Dealing with these aspects, the use of computational fluid dynamics (CFD) codes constitutes a powerful tool to study and characterize some complex processes that take place in the boiler providing a great amount of precise numerical values such as velocity, temperature and concentration fields, irradiation profiles, heat transfer distribution and pollutants formation. In spite of this fact, most of the commercial CFD codes, due to the great variety of phenomena to be modelled, still use simple models to describe turbulence, thermal radiation or combustion kinetics. Consequently, none of the advanced combustion kinetics models mentioned above has been fully coupled to a commercial CFD code (Pallarés et al., 2005).

1.6 Aims and objectives of thesis

In the last decades, pulverized coal-fired steam generators have been progressively affected by more restrictive requirements for particulate and gas emissions, in order to reduce atmospheric pollution, acid rain and the greenhouse effect. Thus, low NO_x techniques and efficient gas cleaning systems have been implemented to satisfy the environmental legislations. However, some drawbacks may arise when emission reduction techniques are applied. Unburned carbon levels increase when excess air decreases, limiting the reduction in NO_x formation which can be achieved by primary techniques through combustion modification. As a consequence, power plant managers look for the most efficient combustion conditions, in order to maximize coal conversion while meeting the environmental legislations.

To achieve this, the main goal of this thesis work is to develop an unburned carbon prediction system that provides an on-line estimation of carbon in ash losses for a given operating condition in a utility boiler. At the same time, a system with such characteristics may allow the plant personnel to identify the source of an increase in the carbon in ash level or to look for the most suitable conditions to minimize this loss.

Developing a system with these characteristics implies modelling all the processes that take part in pulverized coal combustion in a utility boiler. It is necessary to model in detail the transport phenomena of the problem and the micrometric coal particles' combustion. Moreover, in order to use it in an on-line monitoring system of a power station, the computational time should be reasonably short. Within the different predictive systems of combustion, CFD codes give a detailed treatment of the transport phenomena involved in the boiler. However, commercial CFD codes use simplified combustion models that prove to be inadequate for quantitative unburned coal determination. To balance this deficiency, we have developed a methodology that makes use of an advanced combustion model, which is used as a post-processor on the temperature and oxygen partial pressure profiles obtained from a CFD simulation. Another disadvantage of CFD codes is their typically high computational cost, as creating and solving new simulations may take several days, which makes the use of this kind of tool in taking in situ real plant decisions impossible. A system that includes a CFD code in its structure can be seriously restrictive. In the beginning we proposed to use a zonal approach to characterize the fluid and thermal behaviour of the problem. However, these zonal models also present serious limitations such as the impossibility to correctly characterize many relevant factors that affect the combustion process so finally we discarded this avenue of research. To overcome the computational cost limitation, without leaving aside the detailed fluid and thermal description of the CFD codes, we have developed a neural network system. The neural network is trained with

data generated from the CFD simulations, namely, the temperature and oxygen profiles found by the particles in their trajectories through the boiler and their residence times. The advantage of this system is that it allows us to obtain profiles under any other condition not specifically used during the training stage of the networks. Moreover, the computational cost is negligible (less than a minute) when compared with CFD simulations.

For the development and validation of this work, a unit from Lamarmora power plant (ASM Brescia, Italy) has been chosen as the case-study boiler. This selection was taken as a result of the close partnership established between ASM and CIRCE Foundation during the European research project 7220-PR-130-130-CARNO. The preliminary revision work and the development of the unburned carbon prediction system are presented in this thesis work and have been divided into the following chapters:

- Chapter 2. Combustion models' revision: In this chapter a revision of pulverized coal combustion, explaining the different stages and mechanisms of the process (devolatilization, homogeneous combustion of volatile products and char oxidation), and the most representative combustion models in the literature are presented.

- Chapter 3. CFD codes: In this chapter the general characteristics of CFD codes are described. Since in this work we have made use of the commercial code CFX-4 (AEA Technology), the numerical resolution method and the physical and chemical models involved in the problem are particularized for this code. Finally, the validation process followed in this work is presented.

- Chapter 4. Sensitivity study of main factors affecting unburned carbon loss: In this chapter, a sensitivity analysis is performed of the main factors affecting unburned carbon losses that the technical personnel in the plant can either actuate directly or indirectly. To achieve this, we have carried out a double study of theses parameters. Firstly, we have evaluated the contribution of each factor to the final unburned carbon level in the regular range of variation keeping the rest of parameters constant. Subsequently, we have evaluated cross-related effects and interactions among factors. This study, in which we have made use of multi-parameter factorial analysis techniques, gives a more realistic view of the problem since the contribution of one factor may vary depending on the conditions of the rest of factors.

- Chapter 5. Local combustion conditions model: Throughout the chapter, the general characteristics of neural networks and their applications are introduced and the development

of the local combustion conditions' model is described: design of the neural network system structure, training of the system from a number of CFD simulations of the plant and finally, its validation. The aim of this model is to obtain an autonomous, fast and accurate model that may substitute the CFD code, generating for every simulated particle, the residence time and temperature and oxygen partial pressure history, for a given boiler operating condition.

- Chapter 6. Combustion model: This chapter analyzes the definition of the combustion model. The description and development of the model is focused on the reactions that take place on the particle surface, i.e. devolatilization and char oxidation. Devolatilization was modelled using a macromolecular network pyrolysis model (FG-DVC), whilst the char oxidation was modelled and programmed in Fortran using a developed intrinsic formulae based on the carbon burnout kinetic model (CBK8) (Sun and Hurt, 2000). This model allows the transition to Zone I and includes the variation in the porous structure and reactivity of the char as combustion proceeds, mineral matter effects and the influence of the coal's maceral content. Finally, the validation of the combustion model was carried out considering nine operation scenarios of the case-study plant and comparing predictions from the burnout model against the plant values.

- Chapter 7. Unburned carbon prediction system: Throughout this chapter, the coupling of the local combustion conditions model and the advanced combustion model is described. Finally, the system is validated using standard plant instrumentation measurements gathered during three months at the Lamarmora plant (ASM Brescia) under different operation conditions. From these results, an evaluation of the system is assessed hinting at the most significant conclusions and comparing its features and accuracy with other unburned carbon predictive systems.

Nomenclature

C_{ash}	ash content in the parent coal (%, wt)
U_c	unburned carbon fraction
U_{cash}	unburned carbon in ash fraction
η	combustion efficiency

Acronyms

AEA	air entrainment admixtures
CBK	carbon burnout kinetic
CFD	computational fluid dynamics
CIA	carbon in ash
CL	combustion loss
DTF	drop tube furnace
HGI	hardgrove grindability index
HTVM	high temperature volatile matter
LOI	loss of ignition
TGA	thermo-gravimetric analysis

2 COMBUSTION MODELS' REVISION

One of the main goals in coal combustion research is the development of mathematical models to describe, in a realistic way, the combustion process undergone by a pulverized coal particle. To carry out a complete description of the coal combustion process, a particle reaction model must be included. In general, coal combustion may be divided into the three following stages: coal devolatilization (R 2.1), homogeneous combustion of volatile products (R 2.2) and heterogeneous char oxidation (R 2.3) (Badzioch and Hawksley, 1970; Backreedy et al., 1999, 2002)

1. Coal → Volatiles + Char (R 2.1)
2. Volatile (HC) + O_2 → CO + CO_2 + H_2O (R 2.2)
3. φC(Char) + O_2 → 2(φ-1)CO + (2-φ)CO_2 (R 2.3)

Nevertheless, the complexity of the physical and chemical phenomena, together with the conditions and duration variability of each stage, make the use of a global particle combustion models impossible (Figure 2.1). Consequently, each stage must be modelled independently:

- Coal devolatilization: This stage of the process takes place while the coal particle is rapidly heated in an oxidizing atmosphere. During the process, the particle bears an inner transformation, in which tar and a mixture of reacting and non reacting gases are expelled from the particle, leaving a residual carbon rich core (Badzioch and Hawskley, 1970). Volatile release may exceed 50 % of the total weight of the particle and takes place in a few

milliseconds. Furthermore, it has a great influence on the ignition of the particle and in the global combustion process, since it determines the reactive and structural nature of the resulting char (Smith, 1982).

- Homogeneous combustion of volatile products: At this stage, the species released during devolatilization, including tar, hydrocarbons, CO_2, CO, H_2, H_2O and HCN, react with the bulk oxygen increasing the particle temperature. This reactive process has a great relevance on nitrogen oxides and soot formation, flame stability, and char ignition (Bartok and Sarofim, 1991).

- Char oxidation: At this stage, the char residue, at elevated temperature, reacts with the oxygen in the vicinities of the particle. The gas-solid reactions take place when oxygen diffuses to the interior of the particle and reacts at its surface. This heterogeneous process is much slower than devolatilization, requiring time scales of the order of seconds to be completed (Field, 1967). The reaction rate depends on the reactive and structural characteristics of char and also on combustion conditions such as pressure, temperature and oxidant concentration (Unsworth et al., 1991).

The aim of this chapter is to carry out a revision of each stage in the combustion process, describing the mechanisms and the more characteristic models available in the specialized literature. Of course, it is not possible to perform a complete compilation of all the published models used for modelling coal combustion. However, we have attempted to present the most classical models together with advanced models that go deeply into more particular aspects of pulverized coal combustion. The selection criteria for the models described in this work responds to three premises:

- The general applicability under typical pulverized coal combustion conditions.
- The acceptance level in the scientific community.
- That serves as reference and starting point for the coal combustion model development carried out in this work in Chapter 6.

Finally, it should be mentioned that by analogy with most of the combustion related publications, and since the research work in this study is focused on the gas-solid reactions that take place at the particle's surface, the stage corresponding to the homogeneous combustion of volatile products is only tackled in a descriptive way as a connection link between the other stages.

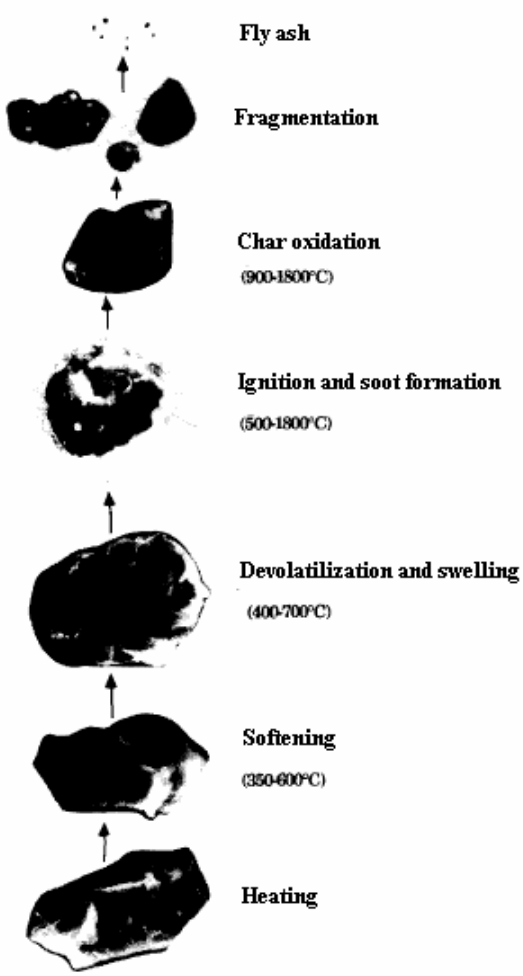

Fig. 2.1 Stages in the combustion process of a coal particle (Solomon et al., 1993)

2.1 Devolatilization

The study of coal devolatization kinetics and its influence on the global coal combustion process has aroused a special interest within the scientific community. The reason for this motivation is not strange since more than 50 % of the coal mass (d.a.f.) fed into the boiler is volatilized and burned in the gas phase. The volatile matter content of a coal indicates its reactivity and ignition capabilities. In this way, the volatile matter content determines the boiler and burner design of a combustion facility. Furthermore, devolatilization also determines the char mass fraction and its reactivity and porous structure. This fact has great relevance, since char oxidation determines the burnout degree achieved. That is, devolatilization indirectly determines the adequate particle residence time to minimize unburned carbon losses (Bartok and Sarofim, 1991).

2.1.1 Description of the process and more significant results

Devolatilization is the first stage in coal combustion consisting of a process in which coal, at elevated temperature, is thermally decomposed producing gas, tar and char products. In spite of the fact that it is extremely fast (takes place in about 10 to 200 ms) it has an outstanding importance in the global coal combustion process (Smoot and Smith, 1985).

A hypothetical coal molecule is assumed to be a network formed by low molecular weight units –aromatic ring clusters– mainly made up of carbon, with a lower proportion of oxygen, sulphur and nitrogen atoms, and connected to each other by means of covalent –aliphatic and oxygen and sulphur atoms– and non covalent bonds –van der Waals and hydrogen bonds– (Figure 2.2) (Solomon et al., 1988).

The devolatilization process starts with a progressive heating of the particle by convection and radiation, until its temperature reaches 150 – 200 º C. During this heating stage, the moisture content on the coal matrix is released. Then, as long as the temperature increases between 200 and 400 º C, some hydrogen bonds start to break. At the same time, in the 300 to 400 º C range, new bridges are created as a result of the cross-linking of some aromatic ring clusters. This phenomena is known as recombination and is especially marked in low rank coals with a high oxygen content (> 10 %) (Glarborg, 1991).

Once this initial low temperature stage is completed, a primary devolatilization starts. This primary devolatilization takes place at temperatures over 600 º C and is characterized by the bridge breaking of the weaker covalent bonds in the coal molecule, producing isolated molecular fragments called metaplast. These fragments, which account for free radicals in their structure, capture hydrogen atoms in order to be stable. If the molecule formed is light enough to vaporize out of the particle, it is released in the form of tar. On the contrary, if it is too heavy to vaporize, it stays in the particle and participates in other recombination processes. Aside from the tar yield, there also exist other releases of volatile matter due to the decomposition of functional groups at elevated temperatures in form of carbon dioxide, methane, ethane, propane and water vapour. The characteristics of the volatile matter yielded in the form of tar or gases, depends on the coal type. For example, low rank coals (lignite and sub-bituminous) release a greater amount of gas than tar, mainly in form of carbon dioxide and carbon monoxide. Whilst high rank coals (bituminous) release a greater amount of tar than light gases, mainly in form of methane (Genetti, 1999). Primary devolatilization finishes once the donatable hydrogen atoms are depleted (Solomon et al., 1988).

Finally, a secondary devolatilization takes place in which the metaplast that have not vaporized can either participate in recombination processes, repolymerize into char, or give raise to secondary reactions yielding less abundant compounds such as CH_4 from methyl groups, HCN from ring nitrogen compounds, CO from ether links, and H_2 from ring condensation (Solomon et al., 1988).

The volatile matter content of a coal is determined from its proximate analysis. However, from the very first experimental studies in combustion facilities, it was found that the amount of volatile yield obtained in the tests was considerably larger than the one obtained from the proximate analysis (Badzioch and Hawskley, 1970). This increase in the volatile yield under high heating rates and elevated temperatures put in order of relevance, the important dependence of coal pyrolysis on combustion conditions.

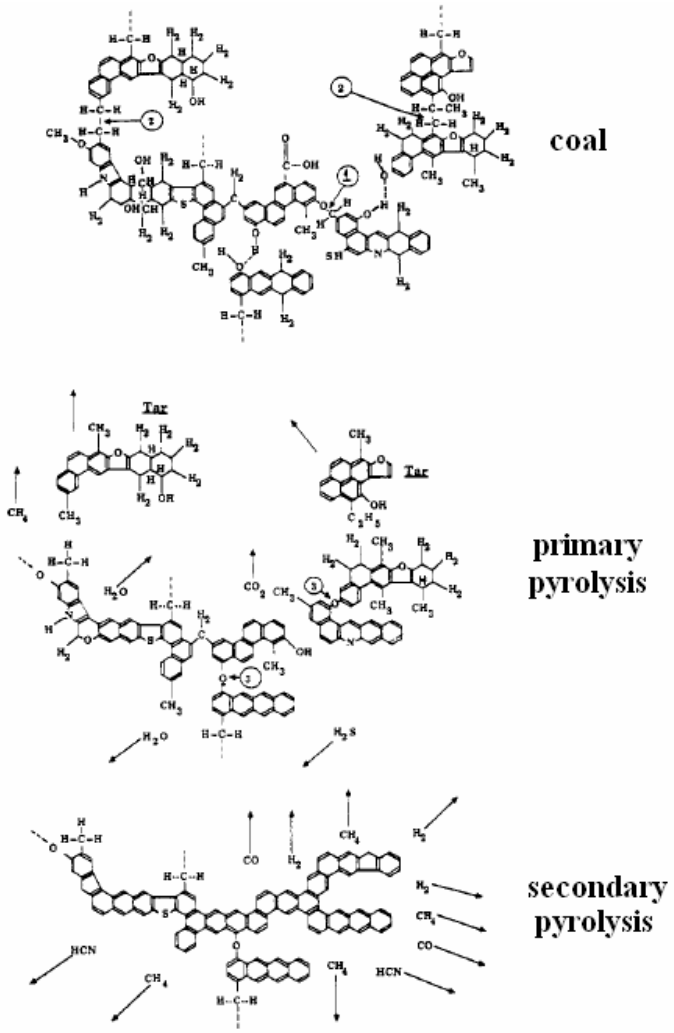

Fig. 2.2 Hypothetical coal molecule during the stages of pyrolysis (Solomon et al., 1988)

Hereinafter, the influence of the main parameters affecting the amount of volatile yield is summarized:

- Temperature: It is the most influential factor in terms of final volatile yield. Under typical pulverized coal combustion temperatures (1750 – 2250 K), the weight loss increases from 5 to above 60 % with respect to the loss estimated with the proximate analysis (Smoot and Smith, 1985).

- Heating rate: It does not significantly affect the final weight loss in practical combustion processes. However, the heating rate strongly influences the rate of the volatile yield, especially at high heating rates (Glarborg, 2001).

- Pressure: In general, the weight loss increases when pressure is decreased and vice versa (Anthony et al., 1976). As it was previously described, the metaplast may either vaporize and leave the particle as tar that crack into simpler gases and char by secondary reactions, or repolymerize into char. Higher pressures confer a longer residence time for metaplast species in the particle and a better chance to crack into char rather than being released as tar (Glarborg, 2001).

- Particle size: The influence of particle size is similar to the influence of pressure. An increased particle size gives an increased residence time of reactive species in the particle with an increased chance for secondary reactions and repolymerization (Glarborg, 2001; Smoot and Smith, 1985).

- Coal type: In general, lower rank coals give higher volatile yield and rate than higher rank coals. This behaviour is explained in terms of the cross-linking and bridge-breaking balance competition on the depolymerization of the macromolecular network. Consequently, for lower rank coals, cross-linking rates occur in advance of the bridge breaking, increasing the coordination number of the macromolecular network, and thus, reducing the yield (Solomon et al., 1993).

Moreover, the influence of coal devolatilization in the global combustion process is not only limited to the amount of volatile yield, but also determines the reactive and structural properties of char. There exists a consensus among the specialized researchers (i.e. Ubhayakar et al., 1976; Kobayashi et al., 1976) denoting the heating rate as the most relevant factor. Increasing the heating rate barely affects the final weight loss. However, it produces abrupt changes in the coal structure, leading to swelling, softening, cracking and sometimes fragmentation due to

thermal and mechanical stresses. These abrupt changes are a result of the high temperature gradients and the pressure forces of the impeding gases in and out of the particle through the pores (Stubington et al., 1989). Furthermore, a rapid devolatilization minimizes the chance for secondary reactions and repolymerization, expediting the yield of mineral matter and other impurities (S, N, H) from the char matrix. This way, the char H/C ratio is reduced decreasing its intrinsic reactivity (Gale et al., 1996). In the same way, an increase in temperature also produces a decrease in char reactivity (Gale et al., 1996).

Finally, another outstanding aspect of the devolatilization process is its influence on the ignition of char and flame stability. The combustion of the volatile products in the vicinity of the particle's surface, reverts part of the heat released in the reactions to the particle, enhancing the heating for ignition. In spite of this fact, the main source of heat does not come from the volatiles' combustion, but from the hot combustion gases re-circulated towards the ignition region. Another ignition source comes from the environment radiation, in which the volatiles' combustion also indirectly participates (Bartok and Sarofim, 1991).

2.1.2 Devolatilization models

The first kinetic study of the devolatilization process was published in 1950. According to Bazdzioch and Hawskley (1970), the soviet authors, Shapatania, Kalyuzhnyi and Chukhanov, studied the possibility of controlling the composition of the volatile released by varying the heating conditions. In spite of the fact that temperatures, reaction rates and particle sizes did not correspond to the typical conditions in combustion reactors, they found one of the most relevant and wide spread results in devolatilization studies. They showed that the weight loss obtained by means of the proximate analysis, undervalued the real volatiles released obtained in their experiments. From this result, according to Badzioch and Hawskley (1970), other research groups (Chukhanov et al., 1962; Loison and Chauvin, 1964; Yellow, 1965), obtained similar conclusions. At the same time, the influence of combustion conditions (temperature, pressure, heating rate, particle diameter, coal rank and properties) on the rate and yield of volatiles was investigated.

However, in spite of all these experimental studies, there still existed little information about the mechanisms and kinetics of the process, especially under typical pulverized coal combustion conditions (heating rates of 10^5 K/s and peak temperatures around 1750 ºC). In 1970, Badzioch and Hawskley were the first ones in publishing a kinetic study that correlated the change in the volatile matter yield as a function of time and temperature, giving birth to the first devolatilization model. This model was the precursor of other classical weight loss models, i.e. two competing reaction models or distributed activation energy models, based also on empirical

approaches. Even nowadays, these models are still in use in most of the CFD codes and other combustion applications that do not require an exigent detailed level. However, in the 80's, the development of novel techniques for coal characterization led to a higher understanding of the coal molecular structure and the reactions that take place within it. This fact resulted in the development of mechanistic approaches based on the chemical structure of the parent coal. Theses models, known as network pyrolysis models, describe the decomposition and recombination of the macromolecular network from coal properties and combustion conditions. Examples of this kind of models are the FG-DVC model (Solomon et al., 1988, 1990, 1993), the CPD model (Fletcher et al., 1989, 1990, 1992), and the FLASHCHAIN model (Niksa et al., 1991, 1994).

Single first order reaction models (SFOR)

The first kinetic model of the coal devolatilization process, commonly known as single first order reaction model (SFOR), was proposed by Badzioch and Hawskley in 1970. From experimental tests with different coals in a laminar flow reactor at temperatures ranging from 400 to 1000 º C and residence times ranging from 30 to 110 ms, they obtained a set of isothermal curves of coal pyrolysis that suggested an exponential behaviour described by Eq. 2.1.

$$\frac{V}{V_f} = 1 - \exp\left(-\int_0^t k_v \cdot dt \right) \qquad \text{(Eq. 2.1)}$$

Expressing Eq. 2.1 in a linear form, Eq. 2.2, the isothermal decomposition curves from different temperatures turn into straight lines starting from approximately 20 ms (Figure 2.3), corresponding to the transit time required for heating the particle before the primary devolatilization starts.

$$\ln\left(1 - \frac{V}{V_f}\right) = -k_v \cdot t \qquad \text{(Eq. 2.2)}$$

Then, they investigated how the slope varied with temperature. From different tests with heating rates ranging from 25000 to 50000 K/s, they proposed an Arrhenius form expression for this variation (Eq. 2.3).

$$k_v = A_v \cdot \exp(-E_{vT} / T) \qquad \text{(Eq. 2.3)}$$

Finally, adjusting the values for the pre-exponential factor A_v and the activation energy E_{vT}, for the conditions and coals used in the tests, the model was completely defined.

The main advantage of a model with these characteristics is its simplicity, since it is defined with only three parameters (V_f, A_v and E_{vT}) it permits us to give a quick estimate of the degree of devolatilization. A major problem of using this model is that the kinetic parameters determined from experiments depend on the heating rate. This means that in order to use it, the rate constants should be determined from data obtained at conditions which closely resemble the conditions at which the model is to be used. Moreover, the final volatile yield V_f depends on the peak temperature, and again the practice conditions in the test should resemble the conditions at which the model is to be used. In spite of these drawbacks, which make the model rigid in its general application, it is one of the most wide spread models in combustion codes.

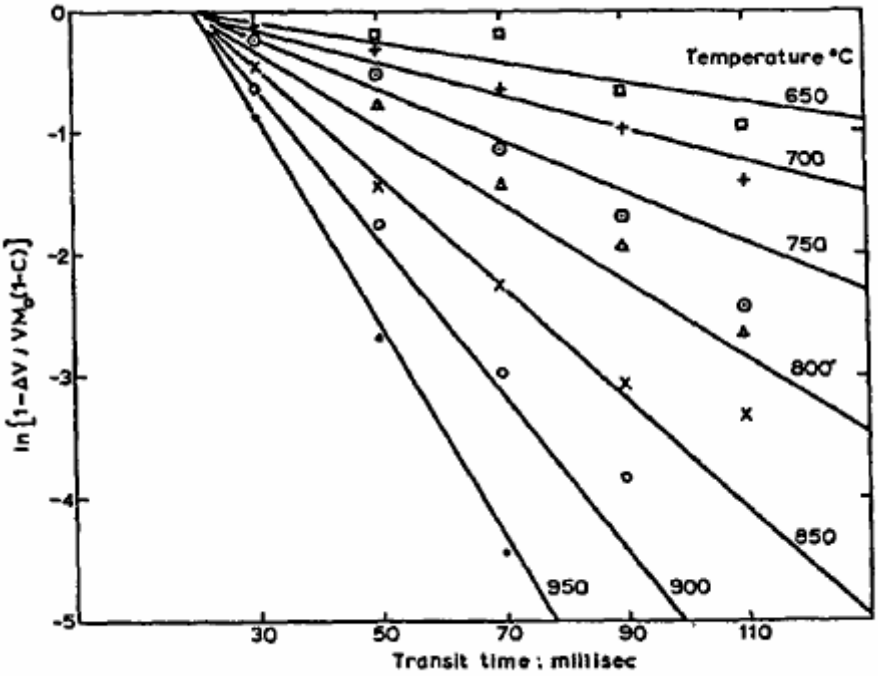

Fig. 2.3 Isothermal decomposition curves for different temperatures (Badz. and Hawsk., 1970)

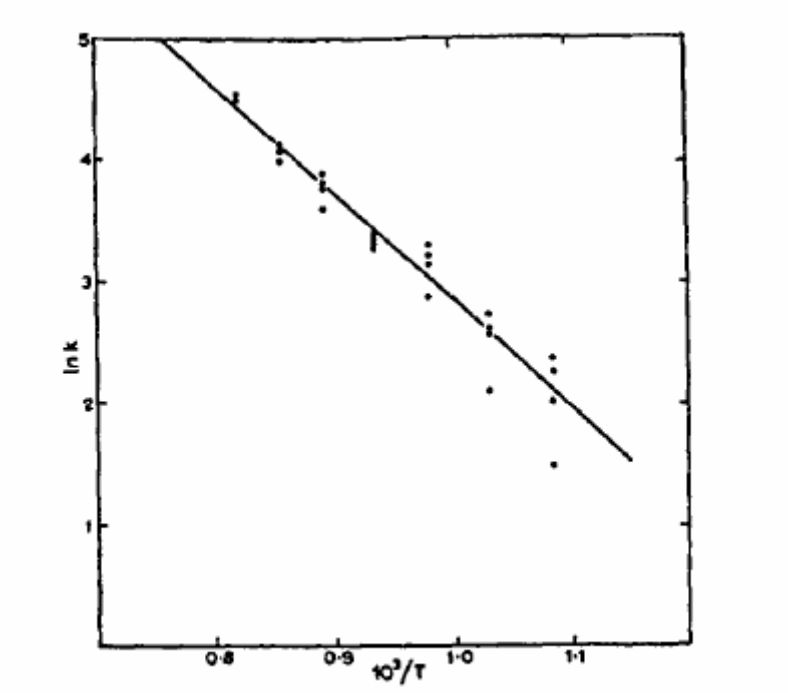

Fig. 2.4 Devolatilization curve fitting for a tested coal (Badz. and Hawsk., 1970)

Distributed activation energy models (DAEM)

SFOR models assume that all the chemical bonds are identical. However, coal decomposition is the result of a large number of chemical reactions that produce the rupture of various bonds within the coal molecule (Glarborg, 2001). A better approach would be to consider the evolution of volatiles from the breaking of each type of chemical bond. In this way, we would have a single first order reaction for each type of chemical bond *i*, where the values of the kinetic parameters A_{vi}, E_{vTi} and V_{fi} should be determined for every *i* reaction that participate in the decomposition. In order to simplify the problem, Anthony et al. (1976) assumed that the rate constants only differ in activation energy, and that the number of reactions is so large that this activation energy can be described by a continuous distribution function f(E_{vT}). By analogy with the SFOR model, the evolution of volatiles is obtained by integrating over the time the distributed activation energy E_{vT} (Eq. 2.4).

$$\frac{V}{V_f} = 1 - \int_o^{\infty} \exp\cdot\left(-\int_0^t k_v \cdot dt\right)\cdot f(E_{vT})\cdot dE_{vT} \qquad \text{(Eq. 2.4)}$$

In most literature, the distribution function is approximated by a Gaussian distribution with a mean activation energy E_{vTo} and a standard deviation σ (Eq. 2.5).

$$f(E_{vT}) = \frac{1}{\sigma \cdot \sqrt{2 \cdot \pi}} \cdot \exp\left[-\frac{(E_{vT} - E_{vTo})^2}{2 \cdot \sigma^2} \right] \qquad \text{(Eq. 2.5)}$$

In practice, the integration over activation energy in Eq. 2.4 is performed between limits which cover most of the volatiles ($E_{vTo} \pm 4\sigma$). The main advantage of this model is that the heating rate dependency of the kinetic parameters (V_f, A_v, E_{vTo}, σ) has been eliminated. Moreover, the temperature dependency of the final weight loss is partly eliminated, since volatiles related to high activation energies evolve slowly at low temperatures.

Two competing step models (2CSM)

Two competing step models assume that two reactions with different rate parameters and volatile yields compete to pyrolyse the raw coal. One reaction dominates at lower temperatures, whilst the other dominates at higher temperatures (Eq. 2.6). Therefore, coal is decomposed by two parallel reactions that depend on the temperature-time history of the particle (Ubhayakar et al., 1976; Kobayashi et al., 1976).

$$\left.\begin{array}{l} C \xrightarrow{k_{v1}} (\omega_1) \cdot V_1 + (1-\omega_1) \cdot R_1 \\ \\ C \xrightarrow{k_{v2}} (\omega_2) \cdot V_2 + (1-\omega_2) \cdot R_2 \end{array}\right\} \quad \frac{dV}{dt} = V_1 \cdot k_{v1} + V_2 \cdot k_{v2} = (\omega_1 \cdot k_{v1} + \omega_2 \cdot k_{v2}) \cdot (V_f - V)$$

(Eq. 2.6)

Where,

$$k_{v1} = A_{v1} \cdot \exp(-\frac{E_{vT1}}{T}) \quad \text{and} \quad k_{v2} = A_{v2} \cdot \exp(-\frac{E_{vT2}}{T}) \qquad \text{(Eqs. 2.7)}$$

The kinetic rate constant are of the Arrhenius form with the feature that $E_{vT1} < E_{vT2}$ and $V_{f1} < V_{f2}$ (Eqs. 2.7). This means that if the decomposition occurs at low temperature, reaction 1 is dominating and the asymptotic volatile yield is V_{f1}; and if the decomposition occurs at high temperature, reaction 2 is dominating and the volatile yield is V_{f2}. The global evolution of volatiles as a function of time is obtained in the same way as in the previous models expressions (Eq. 2.8).

$$\frac{V_1 + V_2}{V_f} = 1 - \exp\left(-\int_0^t (k_{v1} + k_{v2}) \cdot dt \right) \qquad \text{(Eq. 2.8)}$$

The main advantage of this model is that it can predict variations in the volatile yield with temperature. However, again the rate constants should be determined from data obtained at conditions which very closely resemble the conditions at which the model is to be used, and this time, six parameters are required (V_{f1}, V_{f2}, A_{v1}, A_{v2}, E_{vT1}, E_{vT2}).

Network pyrolysis models

Weight loss models use rate constants fitted from experiments to predict the evolution of volatiles for a given coal type and reactor conditions. However, these empirical values cannot be generalized for all conditions. Moreover, the devolatilization of the coal particle is mainly associated with two processes: tar and light gases release. Gases yield is related to the thermal decomposition of specific functional groups, and may be predicted using first order reaction kinetics, together with the coal proximate analysis. However, tar and char evolutions are difficult to model and weight loss models fail in their prediction. Network pyrolysis models are free of this problem. Predicting tar formation is important for several reasons. Firstly, tar is the major volatile product. Moreover, it is often the volatile product of highest initial yield, and thus, controls ignition and flame stability. And finally, tar formation is linked to the physical and chemical structure of the char, and so it is important to char swelling and reactivity (Solomon et al., 1988). Network pyrolysis models are based on a detailed treatment of coal structure that permits us to precisely predict the thermal coal decomposition. To achieve this, coal structure is modelled as a network of aromatic rings linked by bridges of different reactivity. The devolatilization process is modelled using first order expressions with statistical distributions for the activation energy and statistical distributions that describe the bridge breaking rate, bridge formation by recombination processes and bridges cracking into char (Solomon et al., 1988; Genetti, 1999).

Examples of these models are the FG-DVC model (Solomon et al., 1988, 1990, 1993), the CPD model (Fletcher et al., 1989, 1990, 1992), and the FLASHCHAIN model (Niksa, 1991, 1994).

FG-DVC (Solomon et al., 1988, 1990, 1993)

The structure of the FG-DVC model (Functional-Group Depolymerisation Vaporisation Cross-Linking) is divided in two sub-models. The Functional Groups sub-model describes the evolution of light gases as a result of the decomposition of certain functional groups. Depolymerisation Vaporisation and Cross-Linking sub-model describes the bridge-breaking and recombination competition to produce metaplast, the condensation to produce char and the tar vaporization out of the particle. Figure 2.5 shows a representation of the evolution of the char structure in a DVC simulation.

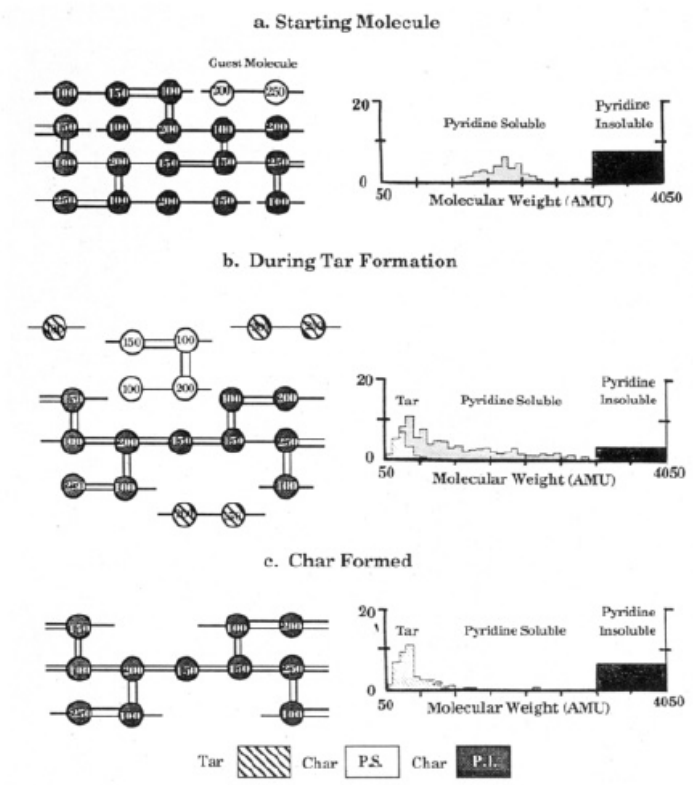

Fig. 2.5 Formation process of tar and char in the DVC sub-model (Solomon et al., 1988)

The mathematical description of the model transforms the coal structure on a bi-dimensional Bethe lattice of aromatic rings linked by aliphatic bridges. Metaplast formation and the subsequent tar evolution are described using statistical techniques of the percolation theory. The kinetics of the functional groups' decomposition process is modelled assuming first order reactions with distributed activation energy.

Coal characterization and the parameters of the model are determined using thermo-analytic techniques such as TG-FTIR, NMR and FIMS. The model provides the gas yield, the elemental and functional group composition of tar and char, and the weight distribution for tar, gas and char.

CPD (Fletcher et al., 1989, 1990, 1992)

The CPD model applies the percolation theory on a Bethe lattice to describe the formation of metaplasts, and a vapour-liquid equilibrium model to predict tar evolution. Finally, it uses the same reaction scheme proposed by Solomon et al. (1988) to predict light gases evolution. The main contribution of the model was the introduction of a new methodology based on the percolation theory that reduces notably the computing time with respect to the FG-DVC model, based on the Monte Carlo method (Solomon et al., 1988). The model provides the evolution and weight distributions for gas, tar and char.

FLASHCHAIN (Niksa, 1991, 1994)

The FLASHCHAIN model, unlike the previous models, describes the coal structure as a mixture of chain fragments ranging in size from a monomer to very long chains with peripherical groups in some of the fragment ends and linked to each other by stable and non stable bonds. The model is formed by four reaction mechanisms: statistical functions to determine the bridge-breaking and cross-linking probability; statistical functions to determine the chemical composition of fragments; and finally, a vapour-liquid equilibrium model to predict tar evolution from the lower molecular weight fragments.

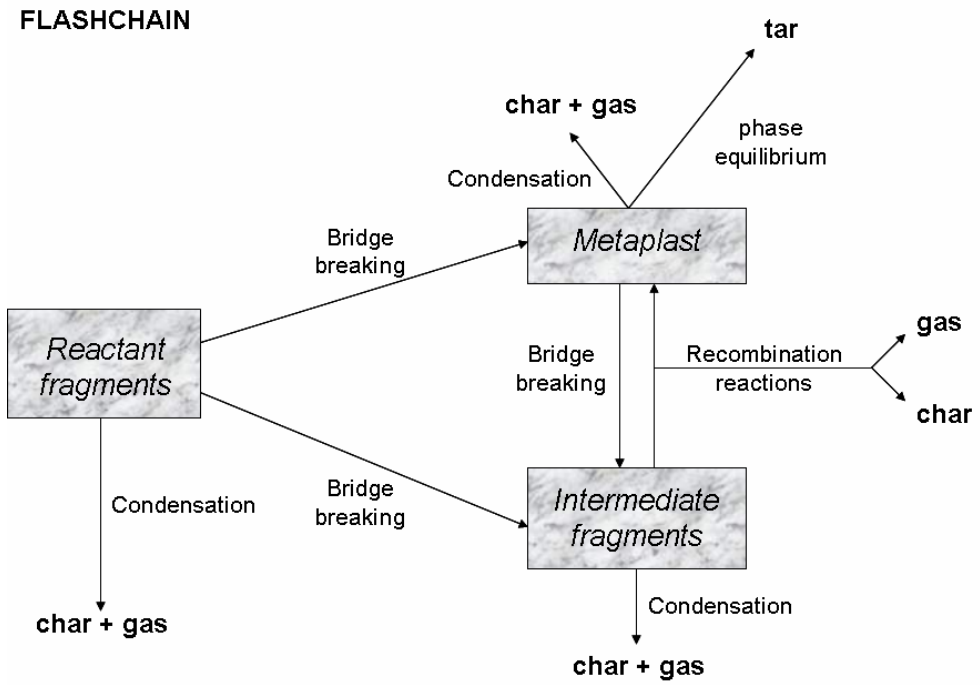

Fig. 2.6 Reaction mechanism in FLASHCHAIN (Niksa, 1991)

Chain fragments are divided into three groups: reactant fragments which correspond to the intact chains in the beginning of the devolatization process; intermediate fragments which correspond to the chains once some bridges have excised; and finally, metaplast fragments when there are no bridges to link the chain to the macromolecular structure. Figure 2.6 shows a representation of the reaction mechanisms in FLASHCHAIN: bridge breaking, condensation of bridges into char links, recombination processes and reactions of the pheripheric groups that lead to light gas yield. Tar evolution is described by means of the metaplast vapour-liquid equilibrium. This model provides the evolution and weight distributions for gas, tar and char.

2.2 Homogeneous combustion of volatile products

During devolatilization a great variety of volatile products in the form of tar and other hydrocarbon gases, CO_2, CO, H_2, H_2O and HCN are produced. At the same time, tar is formed by hundreds of compounds, mostly aromatic hydrocarbons. These products are expelled from the porous coal particle, forming a cloud of volatiles that reacts with oxygen in the vicinity of the char particles, increasing temperature and depleting the oxidizer. Four different phases may be distinguished in the process (Bartok and Sarofim, 1991):

- Macro-mixing of the devolatilizing coal particles with the oxidizer
- Micro-mixing of the volatiles cloud and the oxygen
- Oxidation of the gaseous species to combustion products
- Heat transfer from the reacting fluids to the char particles

At the same time, oxidation reactions of the gaseous species to combustion products undergo three steps. In the beginning, tar is cracked into smaller hydrocarbon fragments, with local production of soot, H_2 and CO. Then, hydrocarbon gases are oxidized to CO, H_2 and H_2O. Finally, H_2 and CO are completely burned to produce CO_2 and H_2O, and NO_x and SO_x are formed.

However, in practical combustion simulation, it is not possible to model all these phenomena. The reason for this is that hydrocarbon chains represent only a few of the thousands of complex compounds released during devolatization. Moreover, there is no simple reaction mechanism that allows us to describe a turbulent flow involving such a huge number of species and reactions. In general, two main approaches are usually considered to describe the combustion of the volatile products: local equilibrium and global reactions. The local equilibrium approach considers that volatile products and the oxidizer are in local thermodynamic equilibrium. This hypothesis allows us to determine the gas temperature and its composition from the elemental composition of volatiles and the heat released during devolatilization. The global reactions approach allows us to determine the global reaction rate from correlations of a priori known reaction rates for several reactants (CH_4, C_2H_6, $C_xH_yO_z$). In general, this approach overpredicts the reaction rate, resulting in errors in the calculated time required to complete the reaction. In spite of this fact, since homogeneous volatile combustion is completed in a few milliseconds, the election of one or another reaction scheme does not affect the global burnout of the particle, which is determined by the oxidation of char. However, the choice of the reaction scheme may become important if stoichiometry, ignition, flame temperature, or NO_x and SO_x predictions are desirable (Sami et al., 2001; Backreedy, 2002).

2.3 Char oxidation

Char oxidation is the last step in the combustion process. An understanding of this stage is important for most combustion problems, since it is slower than devolatilization and gas phase reactions, and maintains a close relation with combustion efficiency. Many factors have an influence on the char oxidation process. The most important factors are set out below (Unsworth et al., 1991):

- Coal structure variation
- Reactant diffusion
- Particle size effects
- Pore diffusion
- Thermal annealing of char
- Mineral matter catalytic effects
- Particle surface area changes
- Char fragmentation
- Pressure and temperature variations
- Oxygen partial pressure variation

Nevertheless, it is difficult to include all these effects in the combustion model, and thus, there does not exist any model that includes all these factors in a general form, for a great variety of coal types and combustion conditions.

2.3.1 Description of the process and more significant results

The char is the carbon rich particle formed during the devolatilization process. Therefore, it is mainly made of carbon although it also contains some nitrogen, sulphur and most of the mineral matter of the parent coal (Essenhigh and Howard, 1967). Its surface is full of cracks and holes, forming a highly porous structure from which the oxidant can penetrate. Char intrinsic properties are determined by the parent coal properties and also by the conditions in which devolatilization has taken place (Smith, 1982). Char oxidation starts at elevated temperatures in an oxidizing atmosphere. The most relevant reactions of the process are (Field, 1967):

$C + CO_2 \rightarrow 2CO$ (R 2.4)

$C + H_2O \rightarrow CO + H_2$ (R 2.5)

$C + 2\,H_2 \rightarrow CH_4$ (R 2.6)

$C + \frac{1}{2}\,O_2 \rightarrow CO$ (R 2.7)

$$C + O_2 \rightarrow CO_2 \qquad \text{(R 2.8)}$$

The reactions with carbon dioxide (R 2.4) and water vapour (R 2.5) are only relevant for gasification processes, and are much slower (10^0 s^{-1} at 1100 K) than reactions with oxygen (10^5 s^{-1} at 1100 K) (R 2.7 and R 2.8) which are thermodynamically favoured at combustion temperatures. The reaction with hydrogen (R 2.6) is too slow (10^{-3} s^{-1} at 1100 K) to be important for most practical applications. Therefore, generally, only the reactions with oxygen are considered for the study of combustion systems that do not involve gasification processes (Field, 1967; Glarborg, 2001).

Reactions C-O_2

Reaction rates depend on the structural and reactive characteristics of char. They also depend on the pressure, temperature and oxidant partial pressure combustion conditions. The rate-limiting step in the char oxidation can be chemical (adsorption of the oxidant, reaction, and desorption of products) or gaseous diffusion (bulk phase or pore diffusion of oxidant and products). As a function of the rate-limiting factor, three zones or regimes are commonly defined (Unsworth et al., 1991; Hong, 2000; Backreedy, 2002):

- Zone I (< 900 K): Oxygen diffuses to the surface of the particle at a rate faster than it is consumed. The oxygen concentration inside the pores is the same as the one in the bulk gas. Oxygen penetrates the particle and combustion takes place in the interior of the pores. Particle diameter remains constant, but decreases in density. Combustion is controlled by reaction rate.

- Zone II (1200 – 1700 K): Oxygen diffuses to the surface of the particle, and partly penetrates inside the pores. Oxygen concentration decreases in the interior of the pores, since it is consumed before reaching the end of the pores. Combustion, is then controlled by oxygen diffusion and reaction rate. Therefore, oxidation also depends on char porous structure through a diffusion resistance. Particle decreases both in diameter and density.

- Zone III (> 1700 K): Oxygen diffuses to the surface of the particle, and immediately reacts with carbon due to the high reactivity of the char. Oxygen concentration at the surface of the particle is close to zero. Combustion is controlled by oxygen diffusion. Particle decreases in diameter.

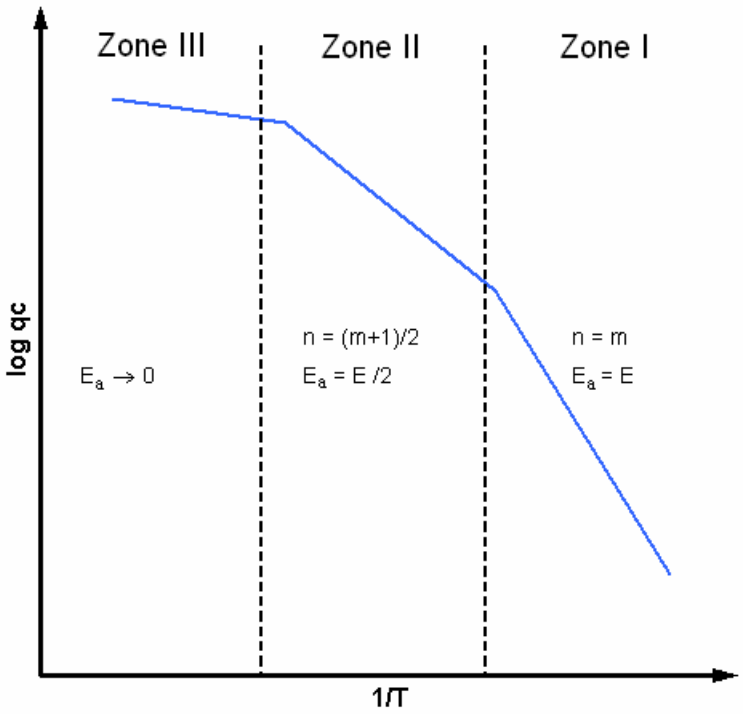

Fig. 2.7 Three-zone theory combustion regimes

During the combustion process, the burning particle usually undergoes all the processes involved in these three regimes. In the beginning, reaction rate is still slow and diffusion rate is fast enough to make the oxygen concentration equal inside the pores and at the surface of the particle. Thus, the global combustion rate is controlled by the chemical reaction rate (Zone I). As particle temperature increases, reaction rates increases too and the oxidant is consumed before it can completely penetrate the particle. Therefore, the global combustion rate is controlled by oxygen diffusion and reaction rate (Zone II). As long as temperature keeps increasing, a point may be reached in which reaction rate is so high that all the oxygen is consumed at the surface of the particle. Then, the global combustion rate is controlled by oxygen diffusion (Zone III). During combustion, typically the temperature evolution of the particle is characterized by a sharp increase during the first instants until a peak temperature is reached followed by a decrease until a relative constant value is reached. Consequently, if the particle has reached the Zone III regime, a decrease in temperature results in a transition from Zone III to Zone II. Finally, in the later stages of combustion, due to extinction phenomena, a transition from Zone II to Zone I is produced (Abd El-Samed et al., 1990; Hurt et al., 1993, 1999; Shim et al., 2000). These extinction phenomena are discussed throughout the chapter and have a great importance in the burnout determination in utility boilers.

To determine the combustion time of a particle, it is necessary to describe the kinetics of the gas-solid reactions within the particle. There exist several mechanisms that model these reactions. The most popular ones in the heterogeneous char oxidation are:

1. Global power-law kinetics
2. Langmuir-Hinshelwood semi-global kinetics

However, in spite of their great acceptance, they is still debate around the theoretical base that support these mechanisms and it is generally accepted that there is room for further research. For example, the global power law mechanisms when using the appropriate activation energies can correctly describe the real process with some success. With the use of the Langmuir-Hinshelwood expressions sometimes the values of the activation energies, for the adsorption and desorption process, is inverted in order to correctly reproduce the global reaction order obtained from experiments. To overcome this, other authors (Haynes, 2001; Hurt and Calo, 2001) have developed more complex mechanisms that explain theoretically the results obtained from experiments. An example of this kind of mechanisms is:

3. Three-step semi-global kinetics (Hurt and Calo, 2001)

1. Global power-law kinetics (Bews, 2001; Hurt et al., 2001, 2004)

Global power-law kinetics is the mechanism most often used in combustion codes. It assumes one step for the carbon oxidation, producing CO and CO_2 (R 2.9).

$$C + O_2 \rightarrow CO / CO_2 \qquad \text{(R 2.9)}$$

The reaction rate by surface area unit q_c, is expressed as the product of a kinetic rate constant k_c and a power of the oxidant concentration at the surface of the particle (Eq. 2.9).

$$q_c = k_c \cdot P_s^{\,n} \qquad \text{(Eq. 2.9)}$$

Where, n represents the apparent reaction order and the kinetic rate constant k_c varies exponentially with temperature according to an Arrhenius form expression (Eq. 2.10).

$$k_c = k_0 \cdot \exp(-E / R \cdot T) \qquad \text{(Eq. 2.10)}$$

To obtain the kinetic parameters (k_o, E, n) it is assumed that reactions take place at the particle's surface. However, the char is a porous structure in which oxygen penetrates and reacts in the interior. Kinetic parameters based on the external surface of the particle are only valid in a narrow range of conditions. These parameters are called extrinsic parameters. On the contrary, when the kinetic parameters are defined considering the internal surface area of the particle, they are called intrinsic parameters. In this way, in Zone III, where the combustion reactions take place at the particle surface, the activation energy and reaction order experimentally observed agree with the extrinsic values. In Zone I, since the reactions take place in the whole particle, including the interior area of the pores, the observable parameters correspond to that of the intrinsic values. In Zone II, where most of the combustion process is produced, and the reactions take place at the particle surface and partly in the interior of the pores, the relationship between the observed parameters and the intrinsic values can be approached by the expressions given in Eqs. 2.11 and 2.12 (Smith, 1978, 1982).

$$n = \frac{(m+1)}{2} \qquad \text{(Eq. 2.11)}$$

$$E_a = E/2 \qquad \text{(Eq. 2.12)}$$

The suitability of the model is obtained by adequately reproducing the temperature dependence of the reaction through the activation energy E_a, and the oxygen concentration dependence through the reaction order n, throughout the whole combustion process. However, in the literature there is not a consensus on the values of these parameters (Bews et al., 2001). These discrepancies may be due to errors associated with the experimental tests, since often the kinetic parameters have been obtained from samples statistically non representative of the parent coal heterogeneity (Hurt et al., 2004).

Figure 2.8 shows some of the reaction order values obtained from experiments by several authors. In Zone I, at low temperatures, high order values are obtained (0.6 – 1). However, in Zone II, the first discrepancies appear. Some authors obtained reaction orders close to zero (Tyler et al., 1976), whilst others obtained reactions orders close to unity (Field, 1967; Smith et al., 1971, 1972; Charpenay et al., 1992; Backreedy et al., 2006). In addition to this, some authors opt for using in the combustion calculations reaction orders of 0.5 (Hurt et al., 1982, 1998; Mitchell and McLean, 1982; Young and Smith, 1989; Sun et al., 2000). With regard to the activation energy there exists a greater agreement and typically values between 105 to 200 kJ/mol are used (Backreedy, 2002). From these studies, it has been deduced that in spite of the

extended use of power-law kinetics, a general form expression can not be formulated and must be particularized for each application.

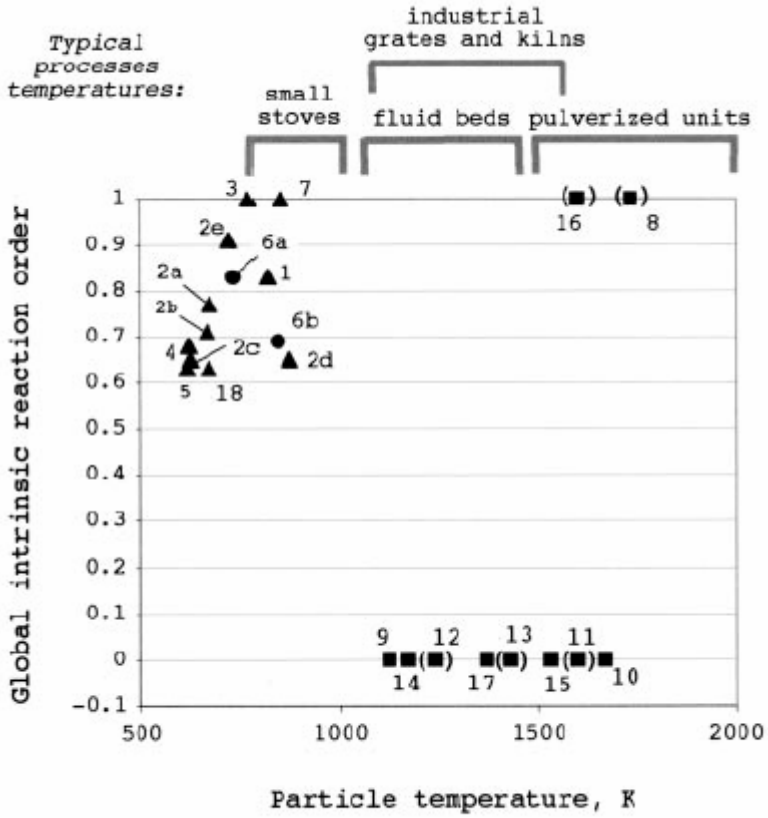

Fig. 2.8 Reaction order for various regimes obtained by several authors (Hurt and Calo, 2001)

2. Langmuir-Hinshelwood semi-global kinetics (Hong, 2000; Hurt and Calo, 2001)

The simplest form of the Langmuir-Hinshelwood kinetics is also widely used in combustion studies. These kinetics considers a two reaction mechanism corresponding to the oxygen adsorption (R 2.10) and the carbon monoxide desorption (R 2.11) (Langmuir, 1921).

$$C + O_2 \rightarrow C(O) \qquad \text{(R 2.10)}$$

$$C(O) \rightarrow CO \qquad \text{(R 2.11)}$$

The reaction rate per surface area unit q_c, is expressed as a function of the kinetic rate constants k_{c1}, k_{c2}, and the oxygen concentration at the surface of the particle P_s (Eq. 2.13).

$$q_c = \frac{k_{c1} \cdot k_{c2} \cdot P_s}{k_{c1} \cdot P_s + k_{c2}} \qquad \text{(Eq. 2.13)}$$

Where, k_{c1} and k_{c2} are the adsorption (R 2.10) and desorption (R 2.11) kinetic rate constants respectively (Eqs. 2.14 and 2.15).

$$k_{c1} = k_{01} \cdot \exp(-E_{ads} / R \cdot T) \quad \text{(Eq. 2.14)}$$

$$k_{c2} = k_{02} \cdot \exp(-E_{des} / R \cdot T) \quad \text{(Eq. 2.15)}$$

The activation energy of the adsorption process, E_{ads}, is in the range of 10 – 125 kJ/mol, while that corresponding to the desorption process, E_{des}, is in the range of 160 – 400 kJ/mol. The effective reaction order varies with temperature and oxygen concentration according to Eq. 2.13, suggesting two limiting cases. At low temperature, the oxygen partial pressure is very high, and the adsorption process dominates ($E_{des} >> E_{ads}$). Therefore, from Eq. 2.13, a zero order reaction rate expression is obtained (Eq. 2.16).

$$q_c = \frac{k_{c1} \cdot k_{c2} \cdot P_s}{k_{c1} \cdot P_s + k_{c2}} \xrightarrow[k_{c1} >> k_{c2}]{} q_c \cong k_{c2} \quad \text{(Eq. 2.16)}$$

At high temperature the contrary behaviour occurs, the oxidant partial pressure is very low, and the desorption process dominates, obtaining a first order reaction rate expression (Eq. 2.17).

$$q_c = \frac{k_{c1} \cdot k_{c2} \cdot P_s}{k_{c1} \cdot P_s + k_{c2}} \Rightarrow \xrightarrow[k_{c2} >> k_{c1}]{} q_c \cong k_{c1} \cdot P_s \quad \text{(Eq. 2.17)}$$

In between these two limiting cases, intermediate values are found that suggest a regime transition. However, returning to Figure 2.8, the opposite behaviour is represented. This result indicates the presence of other intermediates competing with the adsorption and desorption processes. As a result, many authors have decided to adjust the values of the activation energies for the adsorption, E_{ads}, and desorption processes, E_{des}, in order to describe a decrease in the reaction order with temperature that fits the experimental results. Therefore, the mechanistic significance of the model is lost.

3. Three-step semi-global kinetics (Hurt and Calo, 2001)

The experimental results from the previous model suggested the existence of complex O_2-C reactions. These secondary reactions produce carbon dioxide complex compounds that finally react with oxygen to produce most of the CO_2 formation. Therefore, an intermediate step (R 2.13) that competes with the CO desorption process (R 2.14) is introduced into the reaction mechanism.

$C + O_2 \rightarrow 2C(O)$ (R 2.12)

$C(O) + O_2 \rightarrow CO_2 + C(O)$ (R 2.13)

$C(O) \rightarrow CO$ (R 2.14)

The strength of the desorption process explains why the Langmuir-Hinshelwood kinetics correctly fits the experimental data when inverting the activation energies, significantly decreasing one of the desorption process ($E_{des} \approx 170$ kJ/mol) and increasing one of the adsorption process ($E_{ads} \approx 200$ kJ/mol).

The reaction rate per surface area unit q_c, is expressed as a function of the kinetic rate constants k_{c1}, k_{c2}, k_{c3} and the oxygen concentration at the surface of the particle P_s (Eq. 2.18).

$$q_c = \frac{k_{c1} \cdot k_{c2} \cdot P_s^2 + k_{c1} \cdot k_{c3} \cdot P_s}{k_{c1} \cdot P_s + k_{c3} / 2} \quad \text{(Eq. 2.18)}$$

Where, k_{c1}, k_{c2} and k_{c3} are the adsorption (R 2.12), oxygen complex secondary reactions (R 2.13), and desorption (R 2.14) kinetic rate constants respectively (Eqs. 2.19 to 2.21).

$$k_{c1} = k_{01} \cdot \exp(-E_{ads} / R \cdot T) \quad \text{(Eq. 2.19)}$$

$$k_{c2} = k_{02} \cdot \exp(-E_{O2} / R \cdot T) \quad \text{(Eq. 2.20)}$$

$$k_{c3} = k_{03} \cdot \exp(-E_{des} / R \cdot T) \quad \text{(Eq. 2.21)}$$

The activation energies of the reaction mechanisms were adjusted to E_{ads}=35 kJ/mol, E_{O2}=130 kJ/kmol and E_{des}=180 kJ/kmol. The effective reaction rate varies with temperature and oxygen concentration according to Eq. 2.18 suggesting two limiting cases and the transition between them. At low temperatures, the adsorption process dominates, with the desorption process being the rate-limiting step ($k_{c3} << k_{c2}, k_{c1}$). Therefore, from Eq. 1.18 a first order reaction rate is obtained (Eq. 2.22).

$$q_c = \frac{k_{c1} \cdot k_{c2} \cdot P_s^2 + k_{c1} \cdot k_{c3} \cdot P_s}{k_{c1} \cdot P_s + k_{c3} / 2} \xrightarrow[k_{c3} << k_{c2}, k_{c1}]{} q_c \cong k_{c2} \cdot P_s \quad \text{(Eq. 2.22)}$$

At high temperatures, the desorption process dominates ($k_{c3} >> k_{c2}, k_{c1}$), with the adsorption process being the rate-limiting step. Therefore, from Eq. 2.18, again a first order reaction rate is obtained (Eq. 2.23).

$$q_c = \frac{k_{c1} \cdot k_{c2} \cdot P_s^2 + k_{c1} \cdot k_{c3} \cdot P_s}{k_{c1} \cdot P_s + k_{c3} / 2} \xrightarrow[k_{c3} >> k_{c2}, k_{c1}]{} q_c \cong 2 \cdot k_{c1} \cdot P_s \qquad \text{(Eq. 2.23)}$$

Finally, a transition regime takes place at moderate temperatures, where there is competition between the complex secondary reactions (R 2.13) and the desorption process (R 2.14) ($k_{c1} P_s >> k_{c3} >> k_{c2} P_s$). From Eq. 2.18, a zero order reaction rate is obtained (Eq. 2.24).

$$q_c = \frac{k_{c1} \cdot k_{c2} \cdot P_s^2 + k_{c1} \cdot k_{c3} \cdot P_s}{k_{c1} \cdot P_s + k_{c3} / 2} \xrightarrow[k_{c1} >> k_{c3} >> k_{c2}]{} q_c \cong k_{c3} \qquad \text{(Eq. 2.24)}$$

Returning to Figure 2.8, with the introduction of an intermediate step, the reaction mechanism correctly reproduces the experimental data and so conserving the mechanistic significance of the model.

In general, C-O_2 reactions are very complex and are highly influenced by the heterogeneous reactivity of the particle. Every particle has local variations in its composition, reactivity and microstructure. This intrinsic heterogeneity is put into context with the variation in the activation energies of the steps in the reaction mechanism (Hurt et al., 2004). Another relevant factor that affects the reaction kinetics is the mineral matter content of the char (Essenhigh, 1981). Mineral matter, besides consuming thermal energy, has a double effect on combustion kinetics. On one hand, it produces a catalytic effect that enhances char reactivity at low temperature. On the other hand, the ash film layer that covers the particle as combustion proceed and impedes the diffusion of the oxidant agent to the reactive surface of the particle (Hampartsoumian et al., 1989; Charpeney et al., 1992). Definitively, the global effect on the combustion of mineral matter is uncertain and difficult to predict and it depends on the ash content and properties, char properties, and combustion conditions (Backreedy, 2002).

2.3.2 Char oxidation models

Before describing some of the most popular char oxidation sub-models in the literature, a general classification of the existing models is presented:

1. Global models: These models assume that the char particle is impervious to pore diffusion effects, and thus, reactions take place in the outer surface of the particle. All the intrinsic phenomena (porosity of the char, diffusion and reaction in the interior of the particle), are included through the kinetic rate parameters of the model. For this reason, global models

are very empirical, and thus, the practice conditions and coal properties in the test should resemble the conditions and coal type at which the model is to be used.

2. Intrinsic models: Intrinsic models provide general kinetic correlations that directly relate the char structural characteristics with coal properties and combustion conditions, assuming an oxygen concentration profile in the interior of the particle. Therefore, they can be used with less restriction for different coals and combustion conditions.

1. Global models

The most wide spread combustion model used in combustion codes is the classical film model (Field et al., 1967). Field's model assumes a spherical char particle surrounded by a gas boundary layer, through which oxygen diffuses from the bulk gas stream. Then, oxygen reacts at the surface of the particle, releasing combustion products that diffuse again through the boundary layer to the bulk gas. Combustion products are formed by a mixture of CO and CO_2 (Longwell et al., 1993), but it is usually assumed that the carbon monoxide oxidation takes place near the surface of the particle, and thus, only carbon dioxide is obtained at the boundary layer.

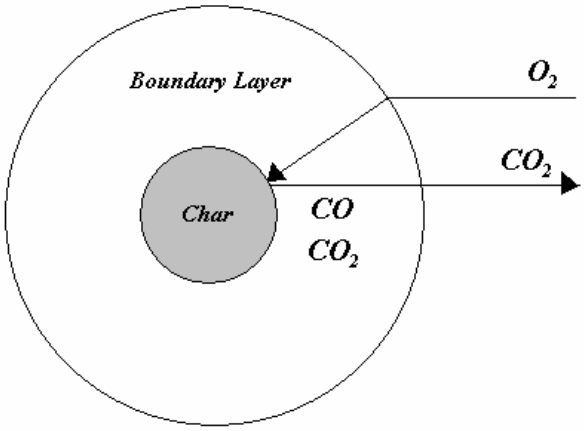

Fig. 2.9 Representation of the film model (Field, 1967).

The combustion rate of the particle is determined in terms of the chemical reaction rate k_c (according to a C-O_2 global power-law kinetics) and the diffusion rate k_d in the boundary layer.

$$q_c = k_c \cdot P_s^{\,n} \qquad \text{(Eq. 2.25)}$$

$$q_c = k_d \cdot (P_g - P_s) \qquad \text{(Eq. 2.26)}$$

Combining the expressions obtained for the species diffusion (Eq. 2.26), and assuming a first order reaction (n = 1) at the particle surface (Eq. 2.25), an alternative expression for the global combustion rate as a function of the oxygen partial pressure in the bulk gas phase P_g, is obtained (Eq. 2.27).

$$q_c = \frac{P_g}{\left(1/k_d + 1/k_c \right)} \qquad \text{(Eq. 2.27)}$$

Since the internal structure of the char particle is unknown, it is assumed that reactions take place at the surface of the particle, and thus, only the oxygen diffusion through the boundary layer is considered (Eq. 2.28).

$$k_d = \frac{24 \cdot \varphi \cdot D_{O2}}{d_p \cdot R \cdot T_m} \qquad \text{(Eq. 2.28)}$$

Where, φ is the stoichiometric coefficient of the oxidation reaction (φ = 1 for CO_2 combustion products, or φ = 2 for CO combustion products). The molecular diffusion coefficient for O_2 into N_2, D_{O2}, may be estimated by means of binary-diffusion coefficients (Turns, 1993) (Eqs. 2.29 – 2.33).

$$D_{O2} = \frac{0.0266 \cdot T_m^{3/2}}{P_{boiler} \cdot PM_{O2N2}^{1/2} \cdot \sigma_{O2N2}^2 \cdot \Omega_D} \qquad \text{(Eq. 2.29)}$$

$$PM_{O2N2} = 2 \cdot \left[(1/PM_{O2}) + (1/PM_{N2}) \right]^{-1} \qquad \text{(Eq. 2.30)}$$

$$\sigma_{O2N2} = (\sigma_{O2} + \sigma_{N2})/2 \qquad \text{(Eq. 2.31)}$$

$$\Omega_D = \frac{1.06036}{\left(T^*\right)^{0.15610}} + \frac{0.193}{\exp\left(0.47635 \cdot T^*\right)} + \frac{1.03587}{\exp\left(1.52996 \cdot T^*\right)} + \frac{1.76474}{\exp\left(3.89411 \cdot T^*\right)}$$

(Eq. 2.32)

$$T^* = k_{N2} \cdot T_m / \left(\varepsilon_{O2} \cdot \varepsilon_{N2} \right)^{1/2} \qquad \text{(Eq. 2.33)}$$

Where, σ_{O2} (≈3.467 Å) and σ_{N2} (≈3.798 Å) are the hard-sphere collision diameters of the respective species, and Ω_D is a dimensionless collision coefficient calculated as a function of a dimensionless temperature T^*. This dimensionless temperature is expressed as a function of the bulk gas temperature and the characteristic Lennard-Jones energy coefficients ε_{O2}/k_{N2} ≈106.7 K and ε_{N2}/k_{N2} ≈71.4 K. Alternatively, the molecular diffusion coefficient D_{O2} may be also calculated through Eq. 2.34 (Jensen, 2001), where D_0 is the molecular diffusion coefficient calculated at reference conditions (P_0 and T_0), and T_m is the averaged of bulk gas and particle surface temperatures.

$$D_{O2} = D_0 \cdot \frac{T_m^{1.75}}{P_{boiler}} \qquad \text{(Eq. 2.34)}$$

On the other hand, the chemical reaction rate k_c is described by an Arrhenius form expression (Eq. 2.35). Intrinsic characteristics are included in the model through the activation energy E_a and the pre-exponential factor A_a, calculated for a given set of coal and combustion conditions (Eq. 2.35).

$$k_c = A_a \cdot \exp(-E_a / R \cdot T_p) \qquad \text{(Eq. 2.35)}$$

Another popular single film model is the one of Baum and Street (1971), which slightly differs from Field's model in the expressions used for describing the kinetic and diffusion rate parameters.

For the moment, both Field's and Baum and Street's models assume a first order C-O_2 reaction mechanism. However, as explained previously, the reaction order varies ranging from zero to one, depending on char properties and combustion conditions (Bews et al., 2001; Hurt and Calo, 2001). Therefore, in such cases, it is necessary to solve iteratively the general expression of the combustion rate with an arbitrary *n*-order reaction (Eq. 2.36).

$$q_c = k_d \cdot \left[P_g - \left(\frac{q_c}{k_c} \right)^{1/n} \right] \qquad \text{(Eq. 2.36)}$$

With the intention of improving and generalizing the use of combustion models, several authors have developed different correlations that allow us to link the kinetic rate constants with coal properties, leading to an extent of the model to different coal types. One of the most widespread

correlations was proposed by Hurt and Mitchell (1992). This correlation relates E_a and A_a with the coal elemental analysis for a wide range of coals from different ranks (Eqs. 2.37 – 2.39).

$$E_a = (-5{,}94 + 35{,}5 \cdot \%C) \quad \text{(Eq. 2.37)}$$

$$A_a = \exp(\ln(k_{c,1750K}) + \frac{E_a}{1750R}) \quad \text{(Eq. 2.38)}$$

Where,

$$\ln(k_{c,1750K}) = (2{,}80 - 0{,}0758 \cdot wt\%C(d.a.f.)) \quad \text{(Eq. 2.39)}$$

All the models described above assume that the char reactive characteristics remain invariable during the whole combustion process. However, experimental studies suggested that different phenomena during char combustion such as: variation in the internal porous structure of char, fracturing of the char, mineral matter effects, thermal annealing, etc., produce an increase in the time required to complete char conversion (Hurt et al., 1998). One of the most important contributions to this effect is the extinction phenomena. The extinction phenomena is mainly due to two contributions: the reactivity loss in the late stages of combustion (thermal annealing of char) (Suuberg, 1991), and the existence of an ash film layer covering the surface of the particle that impedes the oxygen diffusion to the actives sites. Moreover, the extinction phenomena involve a regime transition from Zone II to Zone I (Abd El-Samed et al., 1990; Hurt et al., 1993, 1999; Shim and Hurt, 2000). Therefore, not including this effect in the combustion calculations explains why many models adequately predict the combustion degree attained in a laboratory reactor, where typically below 70 % of the coal conversion is studied, but fail with the prediction in practical utility boilers, where the coal conversion attained is over 90 %. The first model that accounts for these extinction phenomena (thermal annealing of char, and ash inhibition effects), was developed by Hurt et al. (1998), and it is known as the carbon burnout kinetic model (CBK). Consequently, this model notably improves burnout prediction in utility boilers (Figure 2.10).

The first version of the CBK model consists of a single film model and different sub-models that account for morphological changes in the char structure and extinction phenomena. The CBK model comprises the following four main components:

- Single film model (Field, 1967) with rank-dependent kinetic correlations (Hurt and Mitchell, 1992)

- Thermal annealing sub-model
- Ash inhibition sub-model
- A physical property sub-model describing swelling, and diameter/density/porosity changes during oxidation

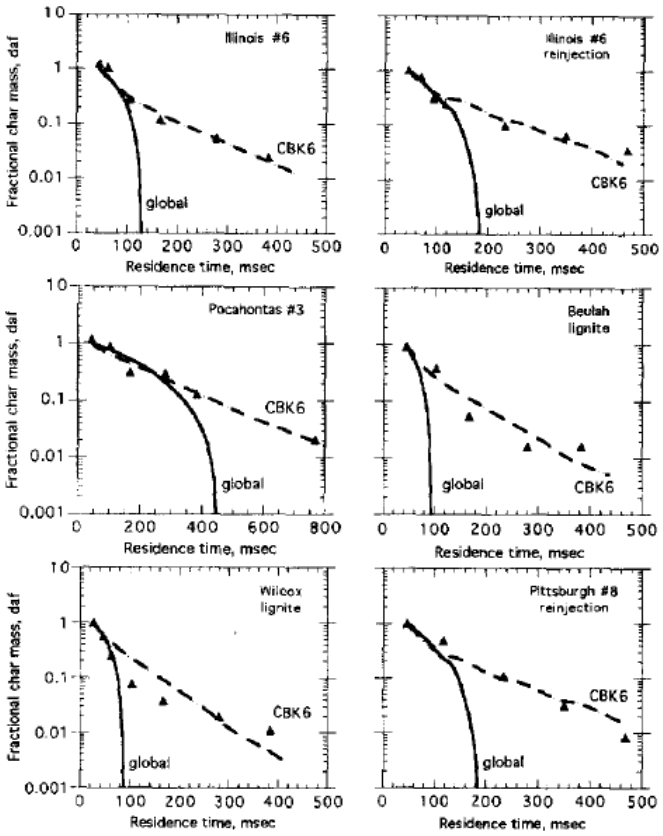

Fig. 2.10 Comparison of measured conversion profiles from laboratory reactors (triangles) with predictions of the simple global model (solid line) and the CBK model (dashed line) (Hurt et al., 1998)

Originally, the CBK model also accounted for a sub-model describing statistical variations in single-particle reactivity and density. However, this sub-model was discarded in later versions of the code.

These sub-models are included in the single film model through the diffusion and reaction rate constants. The reaction rate constant k_c is determined according to Eq. 2.35; where, the activation energy E_a, is calculated from the Hurt and Mitchell (1992) rank-dependent correlations (Eq. 2.37). The thermal annealing process is taken into account through the pre-exponential factor A_a. This pre-exponential factor depends on the history of the particle, and accounts for the char reactivity loss. The reactivity change between two consecutive instants,

$A_i/A_{i-1,}$ for the Zone II, if the effects of annealing are limited to changes in surface area and changes in intrinsic surface reactivity, is described by Eq. 2.40.

$$A_i = A_{i-1} \cdot \sqrt{\frac{N}{N_o}} \qquad \text{i = 1,2,3,...} \qquad \text{(Eq. 2.40)}$$

Where, N/N_o represents the decreasing of active sites (local emplacements in which oxidation reactions may take place) in the char matrix. Therefore, the model assumes that the global reactivity is the result of independent parallel oxidation reactions on different actives sites within the particle. These sites are destroyed by a first order thermal process (Eq. 2.41).

$$\frac{dN_j}{dt} = -N_j \cdot A_d \cdot e^{\left(-E_d/R \cdot T_p\right)} \qquad \text{(Eq. 2.41)}$$

Where, A_d and E_d are the kinetic rate parameters of the deactivation process. The model assumes that all the active sites share the same pre-exponential factor A_d, but they are to be distributed with respect to the activation energy E_d, which governs the thermal deactivation process (Eq. 2.42).

$$\sqrt{\frac{N}{N_o}} = \int_0^{\infty} f_E(E_d, t) \cdot dE_d \qquad \text{(Eq. 2.42)}$$

Where, f_E is assumed to be a log-normal distribution with parameters E_d =16.44 kcal/mol, σ_d=0.46, A_d =8.863E+7 s^{-1} (Eq. 2.43).

$$f_E(E_d) = \frac{1}{\sigma_d \cdot \sqrt{2 \cdot \pi}} \exp\left[\frac{-\left(E_d - E_{do}\right)^2}{2 \cdot \sigma_d{}^2}\right] \qquad \text{(Eq. 2.43)}$$

Returning to Eq. 2.40, the initial reactivity of the char, A_o, is calculated for vitrinite-rich coals with carbon contents from 60 % to 90 % according to Eq. 2.44.

$$\ln(A_0) = (10{,}82 - 7{,}15 \cdot wt\%C(d.a.f.)) \qquad \text{(Eq. 2.44)}$$

This initial value does not correspond to the reactivity of any real test sample but that of a hypothetical initial state calculated by regression techniques from measured experiments knowing the temperature history of the particle.

The diffusion rate constant adds, to the single film model, an additional resistance to account for the effect of the ash film layer covering the surface of the particle and impeding the diffusion of oxygen (Eq. 2.45).

$$k_d = \frac{Sh \cdot D_{O2} \cdot d_p \cdot \theta_{af}^{2,5}}{R \cdot T_m \cdot (Sh \cdot \delta \cdot d_c + \theta_{af}^{2,5} \cdot d_c^{2,5})} \qquad \text{(Eq. 2.45)}$$

Where, Sh is the dimensionless Sherwood number (for typical pulverized fuel particle sizes, Sh = 2), D_{O2} is the molecular diffusion coefficient, d_p is the particle diameter, θ_{af} is the ash film porosity (according to Hurt et al., (1998), θ_{af} = 0,16 ÷ 0,25), R is the ideal gas constant, δ is the ash film layer and d_c is the char particle core diameter ($d_c = d_p - (2\delta)$).

In the beginning, when char conversion is still very low, the ash film is dispersed in grains over the surface of the particle, forming a minimum ash film of thickness δ_m (with unknown coals δ_m = 1 μm) (Figure 2.11).

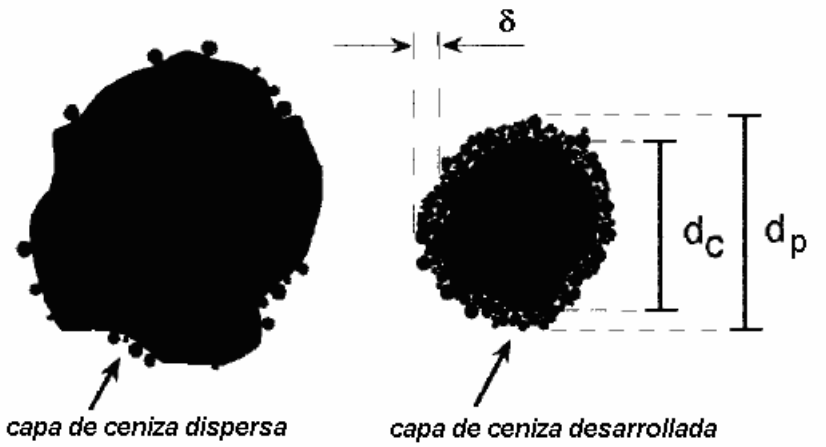

Fig. 2.11 Ash inhibition sub-model (Hurt et al., 1998)

As combustion process proceeds, more grains are added to the film, decreasing its porosity. After a certain time, the grains start to agglomerate, increasing the ash film thickness, while maintaining a constant porosity called critical ash film porosity (θ_{af}).

$$\theta_{af} = 1 - \left(\frac{X_a \cdot \rho - X_{a0} \cdot \rho_0 \cdot (1 - \frac{2 \cdot \delta_m}{d_p})^3}{\rho_{at} - \rho_{at} \cdot (1 - \frac{2 \cdot \delta_m}{d_p})^3} \right) \qquad \text{(Eq. 2.46)}$$

Eq. 2.46 allows us to calculate, at any time considered, the ash film porosity from the current particle properties before the critical ash film porosity, $\theta_{af,}$ is reached. After this moment, the ash film porosity remains constant. In the same way, since char oxidation is a dynamic process, it is necessary to determine the density and particle size histories along the combustion process. The variation of the particle core density, excluding the ash film layer, is calculated according to Eq. 2.47, as a function of carbon conversion raised to the power of an empirical combustion factor α (with unknown coals α = 0.2).

$$\frac{\rho_c}{\rho_{c0}} = \left(\frac{m_c}{m_{c0}} \right)^{\alpha} \qquad \text{(Eq. 2.47)}$$

Then, it is possible to determine the overall density of the particle (Eq. 2.48).

$$\frac{1}{\rho} = \frac{(1 - X_a)}{\rho_c} + \frac{X_a}{\rho_a} \qquad \text{(Eq. 2.48)}$$

Finally, from geometric considerations the particle diameter is obtained (Eq. 2.49).

$$\frac{d_p}{d_{p0}} = \left(\frac{m_p}{m_{p0}} \cdot \frac{\rho_0}{\rho} \right)^{1/3} \qquad \text{(Eq. 2.49)}$$

To conclude with the description of the CBK model, it should be remarked upon that the CBK model is widely accepted in the scientific community and has been a precursor of many other advanced combustion models (Domino and Smith, 1999; Cloke et al., 2003; Pallarés et al., 2005).

2. Intrinsic models

The origin of the intrinsic models arose from the results of experimental investigations on coal combustion that suggested that the internal surface area of the char and the diffusion effects within the interior of the pores had a great influence on the overall burnout of the particle. Therefore, it was important to determine, not only the intrinsic kinetics of the oxidation reactions, but also the intrinsic porous structure of the particle and its evolution along the combustion process.

In general, within intrinsic models, the reaction rate is expressed as the product of a reaction rate coefficient (R_c) and the oxygen partial pressure at the surface of the particle P_{O2} (Eq. 2.50).

$$q_c = R_c \cdot P_{O_2}^n \qquad \text{(Eq. 2.50)}$$

The reaction rate coefficient R_c, depends on both the intrinsic char structure properties and combustion conditions (Eq. 2.51). This rate parameter is usually modelled as a function of: an effectiveness factor (η) that represents the ratio of the instantaneous reaction rate and the maximum reaction rate attainable when no diffusion resistance in the pores exists; a characteristic particle size (γ); the apparent density (ρ); the active surface area (A_g); an intrinsic reaction rate coefficient (R_i); the temperature of the particle (T_p); the coal ultimate analysis (C) and sometimes the maceral composition of coal (M_{ac}).

$$R_c = f\left(\eta, \gamma, \rho, A_g, R_i, T_p, C, M_{ac}, ...\right) \qquad \text{(Eq. 2.51)}$$

For the development of this kind of model it is essential to know how combustion affects the char porous structure. Firstly, the size of the pores controls oxygen diffusion when Knudsen diffusion dominates over molecular diffusion with pores sizes below 1 μm (Jensen, 2001). Moreover, the pore size evolution determines the instantaneous active surface area in which oxidation reactions may take place. As long as combustion proceeds, the size of the pores increase, resulting in a larger surface area. However, this increase of the surface area reaches a limit when the pores become so large that their walls collapse into each other, and thus, the surface area decreases (Figure 2.12).

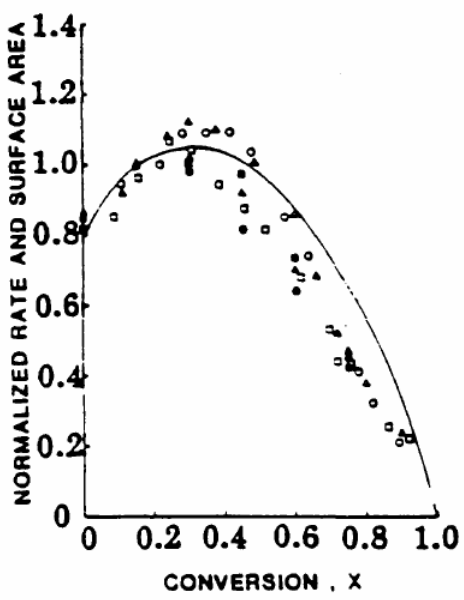

Fig. 2.12 Evolution of the surface area during char combustion (Jensen, 2001)

For this reason, one of the more relevant characteristics of intrinsic models consists of describing the char porous morphology and the oxidant diffusion through the pores along the whole combustion process. To achieve this, several approaches, known as pore models, have been proposed by many authors. Depending on the macroscopic or microscopic treatment of the problem, respectively two different groups of models are found.

Macroscopic approaches, used in most combustion codes, introduce the porous nature of char and its influence on the combustion process, through an effective diffusion coefficient. This effective diffusion coefficient combines the effects of both the effective molecular diffusion and the effective diffusion due to pore walls' collisions (Eq. 2.52).

$$D_{eff} = \left(\frac{1}{D_{eO2}} + \frac{1}{D_{ekn}} \right)^{-1} \qquad \text{(Eq. 2.52)}$$

The effective molecular diffusivity D_{eO2}, is defined analogously with the description of D_{O2} (Eqs. 2.29 - 2.34), but this time it also includes the effect of the porous structure of the char (Eq. 2.53). The presence of the pores slows down the diffusion process since only a fraction of the char, its porosity θ, provides the paths for diffusion. Furthermore, the pores are not straight and may be irregular and intricate, slowing down the diffusion process too. This effect is introduced in the model with a factor known as tortuosity τ.

$$D_{eO2} = D_{O2} \cdot \frac{\theta}{\tau} \qquad \text{(Eq. 2.53)}$$

In the same way as the char porosity θ changes during combustion (Eq. 2.54), there also exist expressions to estimate the tortuosity variation as a function of burnout (Backreedy, 2002) (Eq. 2.55). The initial char totuosity τ_0 may be approximated as $\sqrt{2}$ for unknown coals.

$$\theta = 1 - \frac{\rho}{\rho_c} \qquad \text{(Eq. 2.54)}$$

$$\tau = 1 + \left\{ (\tau_0 - 1) \cdot \left(\frac{m_c}{m_{c0}} \right) \right\} \qquad \text{(Eq. 2.55)}$$

The diffusion mechanism due to the collisions of the oxygen molecules with the pore walls is known as Knudsen diffusion. Knudsen diffusion dominates in very small pores, where collisions with pore walls are more frequent than collisions with other molecules. Knudsen diffusivity depends on the molecules' velocity and the pore radius (Eq. 2.56).

$$D_{kn} = 97 \cdot r_{por} \cdot \sqrt{\frac{T_p}{PM_{O2}}} \qquad \text{(Eq. 2.56)}$$

The mean pore radius r_p may be obtained by means of geometric considerations (Eq. 2.57), from the active surface area of the char A_g, which may be obtained experimentally with CO_2 or N_2 adsorption techniques.

$$r_{por} = 2 \cdot \theta \cdot \tau^{0.5} / A_g \cdot \rho \qquad \text{(Eq. 2.57)}$$

By analogy with the effective molecular diffusivity, the effective Knudsen diffusivity is obtained by introducing the porosity and tortuosity of the char (Eq. 2.58)

$$D_{ekn} = D_{kn} \cdot \frac{\theta}{\tau} \qquad \text{(Eq. 2.58)}$$

With regard to microscopic pore models, a brief discussion and some relevant references are presented. While macroscopic models use a global expression for the diffusion process through the porous structure of the particle, microscopic approaches try to explain the diffusion process through a single pore. Subsequently, by means of statistical models that describe the pore size distribution in the particle, they extend the behaviour of a single pore to the whole particle, obtaining a global description of the diffusion process. In this way, instead of assuming an isotropic diffusivity within the particle, this is assumed to vary with position, pore size distribution and burnout (Smoot and Smith, 1985). Some microscopic models even consider blocked hole effects, pore coalescence and fracturing of the char. Definitively, microscopic models provide a more detailed and realistic treatment of the diffusion process in the particle at the expense of a higher complexity and computational cost. Some examples of popular references of microscopic pore models are: Gavalas et al. (1981), Bhatia and Perlmutter (1981), and Simons et al. (1982).

Returning to the general description of intrinsic models, one of the more widespread and accepted models is the Smith model (1982). In this model, the reaction rate coefficient, $R_{c,}$ is given by Eq. 2.59.

$$R_c = \eta \cdot \gamma \cdot \rho \cdot A_g \cdot R_i \qquad \text{(Eq. 2.59)}$$

The effectiveness factor, η, represents the ratio between the real reaction rate and the maximum reaction rate attainable when the whole particle is exposed to the oxygen concentration at the surface (Levenspiel, 2001; Santamaría et al., 1999). Assuming a first order reaction, the effectiveness factor can be determined by solving the mass balance across the particle. The equation is solved for the reactant oxygen diffusion for a porous spherical particle under catalytic reaction (Eq. 2.60). The integration of Eq. 2.60, describes the oxygen partial pressure variation within the particle as a function of the particle radius r_p (Eq. 2.61).

$$D_{eff} \cdot \nabla^2 P_{O2} = -q_c \cdot \rho \qquad \text{(Eq. 2.60)}$$

$$P_{O2} = P_s \cdot \frac{r_p}{r} \cdot \frac{senh(\phi \cdot \frac{r}{r_p})}{senh(\phi)} \qquad \text{(Eq. 2.61)}$$

Where, ϕ is the Thiele modulus that combines the reaction and diffusion phenomena as shown in Eq. 2.62. A high value of the Thiele modulus indicates that the reaction rate is higher than the diffusion rate. On the contrary, a low value of the Thiele modulus indicates that the reaction rate is low as compared with the oxygen diffusion rate (Levenspiel, 2001; Santamaria et al., 1999).

$$\phi = r_p \cdot \sqrt{\frac{k_c \cdot \rho}{D_{eff}}} \qquad \text{(Eq. 2.62)}$$

Combining the definition of the effectiveness factor with Eqs. 2.61 and 2.62, an expression that relates the effectiveness factor and the Thiele modulus is obtained (Eq. 2.63).

$$\eta = \frac{3}{\phi}\left[\frac{1}{\tanh(\phi)} - \frac{1}{(\phi)}\right] \qquad \text{(Eq. 2.63)}$$

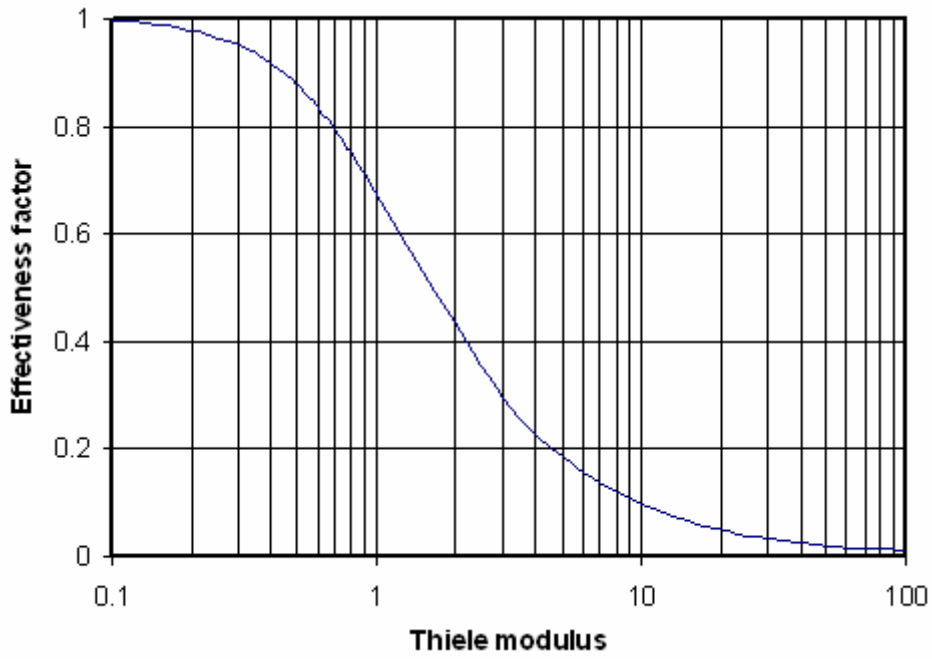

Fig. 2.13 Relationship between the Thiele modulus and the effectiveness factor for spherical particles

Figure 2.13 shows that values of the Thiele modulus below 0.2 correspond to effectiveness factors close to unity which indicates that combustion is controlled by the reaction rate (Zone I); while values of the Thiele modulus over 30, corresponds to effectiveness factors close to zero which indicates that combustion is controlled by oxygen diffusion (Zone III).

The mass balance across the particle in Eq. 2.60 corresponds to the simplest case, assuming a first order reaction. For reaction mechanism involving an arbitrary *n*-order reaction, it is necessary to fall back on numerical methods for its resolution. For the particular case of the Smith intrinsic model (1978, 1982), assuming a *n*-order reaction (Eqs. 2.50 and 2.59), the relation between the effectiveness factor and the Thiele modulus is given by Eq. 2.64.

$$\eta \cdot \phi^2 \cdot (n+1)/2 = \gamma \cdot q_c \cdot (n+1)/(8 \cdot D_{eff} \cdot P_s) \qquad \text{(Eq. 2.64)}$$

In order to solve Eq. 2.64, it is necessary to determine all the terms on the right hand side of the equation from experiments, and subsequently, use the Mehta and Aris (1971) graphs that relate η and $\eta\phi^2$ (Figure 2.14).

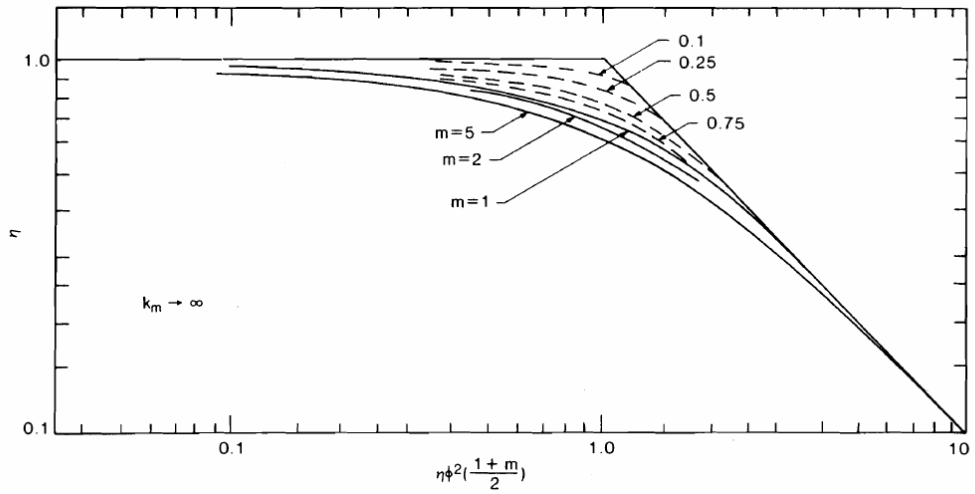

Fig. 2.14 Thiele modulus and effectiveness factor relationship for spherical particles and various reaction orders (Mehta and Aris, 1971)

The effective diffusivity D_{eff} is defined as the effective molecular diffusivity D_{eO2} in pores larger than 1 μm (Eq. 2.53) and as the effective Knudsen diffusivity D_{kn} in pores smaller than 1 μm (Eq. 2.58).

Finally, the intrinsic reaction coefficient is modelled in an Arrhenius form expression (Eq. 2.65).

$$R_i = A_{ai} \cdot \exp(-E_{ai}/R \cdot T) \qquad \text{(Eq. 2.65)}$$

Parallel to the evolution of global models, Sun et al. (2000) developed an intrinsic version of the CBK model, called CBK8. This model accounts for the same sub-models as in the global version, but adapted to an intrinsic description:

- Intrinsic model, with a macroscopic pore model to describe the diffusion process within the particle
- Thermal annealing sub-model
- Ash inhibition sub-model
- A physical property sub-model describing swelling and diameter/density/porosity changes during oxidation

This way, the CBK8 model accounts for the extinction phenomena in the late stage of combustion (> 95 % burnout), as a result of the decrease in the char reactivity (Thermal annealing sub-model) and the appearance of an ash film layer covering the surface of the

particle (Ash inhibition sub-model). Since most of the sub-models were defined in the CBK model description, the next pages are exclusively focused on the intrinsic characteristics of the model.

In CBK8, the combustion rate is determined by the general expression given in Eq. 2.50, in which the reaction rate coefficient R_c is calculated according to Eq. 2.66.

$$R_c = \eta \cdot k_o \cdot S \cdot e^{\left(-E/R \cdot T_p\right)} \cdot m_c \qquad \text{(Eq. 2.66)}$$

The effectiveness factor dependency on reaction conditions is established through the Thiele modulus according to Eqs. 2.62 and 2.63. A value of η close to unity indicates that the reaction is in the Zone I regime, in which the combustion rate is approximately equal to the intrinsic reaction rate. A value of η lower than unity indicates that the reaction is in the Zone II or III regime, where the combustion rate is much lower than the reaction rate.

The effective diffusion coefficient D_{eff} is calculated assuming a negligible contribution from the smaller pores (micropores and mesopores) to the transport of the oxidant (Gale et al., 1996). Consequently, only the contribution of the effective molecular diffusivity is considered (Eq. 2.53).

The product k_oS, known as specific intrinsic reactivity, introduces the thermal deactivation of char (Eq. 2.67).

$$k_0 \cdot S = k_0 \cdot S_0 \cdot \int_0^{\infty} f_E(E_d, t) dE_d \qquad \text{(Eq. 2.67)}$$

The initial specific intrinsic reactivity k_oS_o is calculated from rank-dependent correlations (Eq. 2.68) and the log-normal distribution $f_{E,}$ is obtained, as it was explained in the global model description, according to Eq. 2.43.

$$Log_{10}(k_0 \cdot S_0) = 14{,}97 - 0.0764 \cdot \%C \qquad \text{(Eq. 2.68)}$$

Another model of great interest was developed by Hampartsoumian et al. (1989), studying the influence of coal maceral types on the global combustion process. The reaction rate coefficient expression, was obtained by multiple regression techniques including an additional term which accounts for the influence of coal macerals on char reactivity, f_{mac} (Eq. 2.69).

$$R_c = \exp^{(-89)} \cdot \rho^{(-7.5)} \cdot A_g{}^{(-0.5)} \cdot \%C^{(3.5)} \cdot T_p{}^{(9.5)} + f_{mac} \quad \text{(Eq. 2.69)}$$

Where, the maceral correction factor f_{mac} is described as a function of the vitrinite and inertinite content of the parent coal according to Eq. 2.70.

$$f_{mac} = \left[1.4 \cdot \left(Vit_M + 0.83 \cdot Vit_{PS}\right)\right] - \left[0.6 \cdot \left(In_R + 1.6 \cdot In_{LR}\right)\right] \quad \text{(Eq. 2.70)}$$

To conclude this revision, another relevant model, developed by Backreedy et al. (2006), proposed an alternative intrinsic description to CBK8, introducing coal maceral expressions to the model. The reaction rate coefficient R_c is expressed according to Eq. 2.71.

$$R_c = (\alpha_D \cdot A_g) \cdot f_{ann} \cdot R_i \cdot m_c \cdot \eta \cdot f_{mac} \quad \text{(Eq. 2.71)}$$

In this expression, the product $(\alpha_D A_g)$ determines the variation of the specific surface area with burnout, through a parameter α_D (Eq. 2.72), which is previously determined from experimental studies.

$$\alpha_D = 0.3 \cdot (-28.44 \cdot \left(\frac{m_c}{m_{c0}}\right)^4 + 85.33 \cdot \left(\frac{m_c}{m_{c0}}\right)^3 - 85.33 \cdot \left(\frac{m_c}{m_{c0}}\right)^2 + 28.44 \cdot \left(\frac{m_c}{m_{c0}}\right) + 1)$$

(Eq. 2.72)

Thermal annealing is introduced in a simplified form through the factor f_{ann}, in order to reduce the computational time. It is set to 0.9 only in certain cases: (70 % < *%wt C (daf)* < 90 %), (20 μm < d_p < 100 μm) and (T_p > 1400 K).

The effectiveness factor, assuming a first order reaction, is calculated according to Eqs. 2.62 and 2.63.

And finally, for rich-inertinite coals, the maceral correction factor given in Eq. 2.70 or an abbreviated form of it given in Eq. 2.73, is introduced.

$$f_{mac} = 1.68 \cdot Vit - 0.6 \cdot In \quad \text{(Eq. 2.73)}$$

As it was mentioned in the introduction of this chapter, there exist several global and intrinsic models in the literature which have not been included in this brief revision (Charpenay et al., 1992; Cloke et al., 2003; Pallarés et al., 2007; etc.). However, the interested reader is referred to the bibliography.

2.4 Summary

Coal combustion research requires dealing with the study of the physical and chemical phenomena taking place during the combustion process and with the development of mathematical models to describe them. Coal combustion is divided into three distinct stages, although generally they overlap during the process. These stages are: devolatilization, homogeneous combustion of volatile products and char oxidation. Although particle heating and ignition are initial phase of combustion stages, they have a great importance in the overall burnout process. Throughout the chapter, a revision of each stage in the combustion process, describing the mechanisms and the more characteristic models available in the specialized literature was undertaken.

Although the devolatilization process takes place in the very first milliseconds, it has a great relevance on the overall particle burnout. The conditions in which devolatilization takes place notably influence the volatile yield and rate, and thus, the resultant structural and reactive properties of the char. To describe the thermal decomposition process, weight loss models based on empirical approaches (SFOR, DAEM, 2CSM) are generally used. However, weight loss models use rate constants fitted from experiments to predict the evolution of volatiles for a given coal type and set of reactor conditions. Therefore, these empirical values cannot be used in a general form. Moreover, the devolatilization of the coal particle is mainly associated with two processes, tar and light gases release, and weight loss models fail in their prediction. Therefore, in combustion applications that require an exigent detailed level of the devolatization process, we should fall back on network pyrolysis models that are based on mechanistic approaches of the coal structure (FG-DVC, CPD, FLASH-CHAIN) and which are free of the aforementioned problems.

The homogeneous combustion of volatile products has a great influence on stoichiometry, ignition, flame temperature and pollutant formation, and thus, in the overall combustion process. To model this stage, two main approaches are usually considered: local equilibrium and global reactions.

Finally, char oxidation is the slowest step in the coal combustion process, and thus, it determines the burnout degree achieved. Whether we consider an implicit or explicit view of the structural and reactive properties of the particle, char oxidation models may be also divided into global or intrinsic models, respectively. Global models are based on the classical single film model, in which the combustion rate is determined in terms of the chemical reaction rate at the surface of the particle and the diffusion rate of the oxidizer through the boundary layer. The intrinsic phenomena are included through the kinetic rate parameters of the model. On the contrary, intrinsic models provide general kinetic correlations that directly relate the char structural and reactive characteristics with coal properties and combustion conditions. Both approaches are extensively used in combustion codes and their precursor models (Field's global model, and Smith's intrinsic model) have given raise to more advanced models, that include for example: complex reaction mechanisms (Hurt et al., 2001), detailed pore models (Gavalas et al., 1981), thermal annealing of char effects (Hurt et al., 1998, 2000), ash inhibition effects (Hampartsoumian et al., 1989; Hurt et al., 1998), coal macerals effects (Cloke et al., 2003; Backreedy et al., 2003, 2006), etc. Summarizing, in the literature there exist a great variety of models to choose from, depending on the needs of the study.

Nomenclature

A_a pre-exponential factor (g C/cm^2 s)

A_{ai} intrinsic pre-exponential factor (g C/cm^2 s atm^n)

A_d pre-exponential factor of the thermal annealing process

A_i pre-exponential factor (g C/cm^2 s atm^n)

A_g intrinsic surface area (cm^2)

A_v pre-exponential factor of the devolatilization process (s^{-1})

A_0 initial pre-exponential factor (g C/cm^2 s atm^n)

d_c char particle core diameter (cm)

d_p char particle diameter (cm)

D_{eff} effective diffusion coefficient (cm^2 /s)

D_{ekn} effective Knudsen diffusion coefficient (cm^2 /s)

D_{kn} Knudsen diffusion coefficient (cm^2 /s)

D_{eO2} effective molecular diffusion coefficient for O_2 into N_2 (cm^2 /s)

D_{O2} molecular diffusion coefficient for O_2 into N_2 (cm^2 /s)

D_0 reference molecular diffusion coefficient for O_2 into N_2 (cm^2 /s)

E activation energy (J/mol)

E_a activation energy (J/mol)

E_{ai} intrinsic activation energy (J/mol)

E_{ads} activation energy of the adsorption process (J/mol)

E_{ap} apparent activation energy (J/mol)

E_d activation energy of the thermal annealing process (kJ/mol)

E_{des} activation energy of the desorption process (J/mol)

E_{O2} activation energy of the oxygen complex reactions (J/mol)

E_{vT} activation temperature of the devolatilization process (K)

f_{ann} thermal annealing factor

$f_E(E_d)$ statistical distribution function in E_d of the thermal annealing process

$f_E(E_v)$ statistical distribution function in E_v of the devolatilization process

f_{mac} maceral correction factor

In inertinite

In_{LR} fusinite

In_R semi-fusinite

k_c reaction rate constant (g C/cm^2 s atm^n)

k_d diffusion rate constant (g C/cm^2 s atm)

k_o pre-exponential factor (g C/cm^2 s atm^n)

k_v reaction rate constant (s^{-1})

k_0S specific intrinsic reactivity (1/s atm^n)

m true reaction order

m_c carbon mass of the char (g C)

m_{c0} initial carbon mass of the char (g C)

m_p mass of the char particle (g)

m_{p0} initial mass of the char particle (g)

n apparent reaction order

N active sites

N_0 initial active sites

P_{boiler} furnace pressure (Pa)

P_g bulk gas oxygen partial pressure (atm)

P_{O2} oxygen partial pressure (atm)

P_s oxidant partial pressure at the particle surface (atm)

PM_{O2} molecular weight of O_2 (32 g/mol)

PM_{N2} molecular weight of N_2 (28 g/mol)

q_c combustion rate (g C/cm^2 s)

r_p radius of the char particle (cm)

r_{por} mean pore radius (cm)

R universal ideal gas constant (8.3145 J/mol K)

R_c reaction rate coefficient (g C/cm^2 s atm^n)

R_i intrinsic reaction rate coefficient (g C/cm^2 s atm^n)

Sh Sherwood dimensionless number $\left(Sh = k_m \ L_c / D\right)$

t time (s)

T temperature (K)

T_g bulk gas temperature (K)

T_m averaged temperature (K)

T_p particle temperature (K)

T* dimensionless temperature

V instantaneous volatile yield

V_f final volatile yield

Vit vitrinite and pseudo-vitrinite

Vit_M vitrinite

Vit_{PS} pseudo-vitrinite

X_a ash mass fraction

X_{a0} initial ash mass fraction

%C % wt. carbon content (d.a.f.)

α	combustion factor (0.2)
α_D	deactivation factor
γ	characteristic size of the char particle (cm)
δ	ash film thickness (cm)
δ_m	minimum ash film thickness (cm)
Ω_d	dimensionless coefficient of the collision between molecules
φ	stoichiometric coefficient
ϕ	Thiele modulus
η	effectiveness factor
θ_{af}	ash film porosity
θ	porosity of the char particle
ρ	density of the char particle (g/cm^3)
ρ_{at}	ash true density (g/cm^3)
ρ_c	carbon density (g/cm^3)
ρ_{c0}	initial carbon density (g/cm^3)
ρ_0	initial density of the char particle (g/cm^3)
τ	tortuosity
τ_0	initial tortuosity ($\sqrt{2}$)
σ	standard deviation
σ_d	standard deviation of the thermal annealing process (kJ/mol)
σ_{O2}	mean diameter of the O_2 molecule (Å)
σ_{N2}	mean diameter of the N_2 molecule (Å)
ω	distribution coefficient

Acronyms

CFD	computational fluid dynamics
DAEM	distributed activation energy models
FIMS	field-ionization mass spectroscopy
NMR	nuclear magnetic resonance
2CSM	two-competing step model
SFOR	single first order reaction
TG-FTIR	thermo-gravimetric Fourier transform infrared spectroscopy

3 CFD CODES

Traditionally, experiments have constituted the more widespread and efficient methodology to determine the global parameters that allow us to describe a flow field. However, the continuous technological demand for more specialized designs has increased the need for more precise descriptions of the fluid dynamic behaviour of the problem. Carrying out this work by means of experimental techniques is highly expensive and both time and work consuming. To this effect, computational fluid dynamics (CFD) offers an attractive alternative to experimental methods, procuring an important saving of time and money without compromising the accuracy of the solution.

The basics of differential equations' numerical resolution methods was established more than one century ago. Nevertheless, their applications were insignificant until the appearance of the first computers in the 50's decade. From that moment onwards, the calculation capabilities provided by these machines led the resurgence of numerical methods for the resolution of all kinds of problems. In this way, so long as the storage and computation capability of computers was increased, the number of problems manageable from a numerical point of view also rose. By the time this innovating tendency reached the study of fluid dynamics, it had such a great acceptance and development that it did not take long to give rise to a new independent study field called computational fluid dynamics (CFD).

In spite of the fact that in the beginning, computational fluid dynamics was limited to research investigations, again thanks to the rapid evolution of computers, it did not take long to jump into the world of industry, where today it constitutes a common tool in prediction or design

problems. To absorb this technological demand, different commercial code vendors compete in the CFD market. Among these commercial codes, FLUENT, CFX and StarCD, stand out since they are the most widely used within industries and research centres.

In this chapter, the general characteristics of CFD codes are described. Since in this work we have made use of the commercial code CFX-4 (AEA Technology), the numerical resolution method and the physical and chemical models involved in the problem are particularized for this code. Finally, the validation process followed in this work is presented. To achieve this, the chapter is divided in the following sections:

- Finite volume method: discretization of the domain and the transport equations governing the problem.
- Description of the mathematical models involved in the problem.
- Description of the boundary conditions for the problem.
- Validation of the numerical resolution method.

3.1 Numerical resolution method

The description of fluid flow is performed by means of differential equations that, in general, cannot be analytically solved. Consequently, to obtain a numerical solution, we should use a discretization method to approximate the differential equations by a system of linear algebraic equations (Ferziger and Peric, 2002).

The fluid field is discretized in a number of non overlapped cells that fill the whole domain (Dick, 2002). Conservation equations are applied to determine the fluid variables at discrete points of the cells, called nodes. Nodes may be defined either at the cell vertex or at the cell centre. CFX-4 defines the nodes at the cell centres (Figure 3.1, node P). Therefore, the nodes in which the flow variables are calculated are defined by a mesh of cells that is essentially a representation of the geometric domain in which the problem is solved.

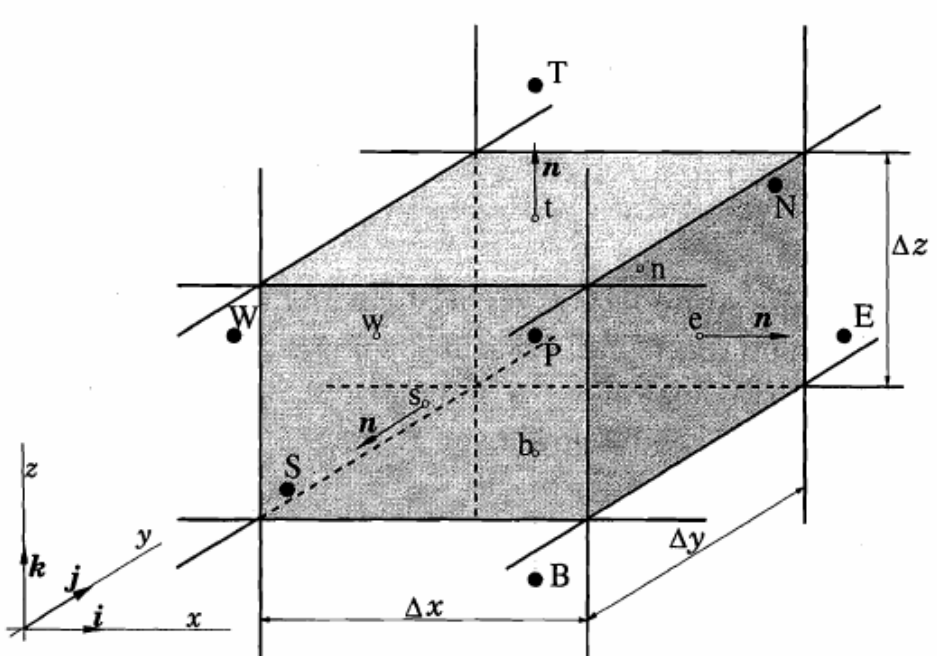

Fig. 3.1 Fluid cell typically used in the FVM (Ferziger and Peric, 2002)

Mesh generation is a long and difficult task. The resolution of the mesh usually consumes most of the time during the problem setup, since the solution accuracy depends on the mesh quality and on the approaches used for the discretization of the equations. There exist different types of meshes classified as a function of the disposition of the cells in it: structured, non structured and hybrid. A structured mesh consists of a family of curves with the property that the curves from the same family do not cross each other and only cross with the curves from other families once. This is the simplest mesh type, equivalent to a cartesian mesh, in which each node (Figure 3.1, node P) has six neighbouring nodes corresponding to the adjacent cells (Figure 3.1, nodes B,T,E,W,S,N). This type of connectivity simplifies the programming work, and the matrix of the algebraic equations system is regular, so that there exist plenty of efficient resolution techniques. One disadvantage of structured meshes is that they may be exclusively used when the geometric domain is relatively simple. Another disadvantage is that it is difficult to control the distribution of the nodes in the domain. Thus in order to obtain a better solution in one region of the domain a local refinement is required which will often force refinements in other regions of the domain, wasting computational resources and affecting the convergence of the problem (Ferziger and Peric, 2002). Non structured meshes are more flexible than structured meshes, since they have no restriction in the number of adjacent nodes. The advantage of the flexibility of this type of mesh is counteracted by the disadvantage of using an irregular mesh. The matrix of the algebraic equations system is not diagonal, and therefore, the resolution is much slower (Ferziger and Peric, 2002).

As it will be seen in the next chapter, the mesh type used in this work is structured. However, CFX-4 implements a special type of structured mesh called body-fitted mesh, which permits the introduction of complex geometries. To this effect, the mesh is deformed following the domain contours. At the same time, for the resolution of the transport equations, the cartesian physical coordinate system is transformed into a non orthogonal curvilinear coordinate system. With this transformation, the complexity in the resolution of the transport equations is increased, but the setting of boundary conditions is simplified.

The finite volume method (FVM) uses the integral form of the conservation equations. These conservation equations are then applied to each domain cell to determine the flow variables in the numerical mesh nodes. The general form of the conservation equations, with the exception of the continuity equation, has the structure of Eq. 3.1. This equation expresses that the variation with time of a generic property ϕ in the control volume is due to the contribution of the diffusive and convective fluxes through the volume surfaces, plus the generation or destruction of this property in the interior of the cell represented by the source term S_ϕ.

$$\int_V \frac{\partial \rho \phi}{\partial t} \cdot dV + \int_A \rho \phi \vec{v} \cdot \vec{n}\, dA = \int_A \Gamma \nabla \phi \cdot \vec{n}\, dA + \int_V \vec{S}_\phi \cdot dV \qquad \text{(Eq. 3.1)}$$

Surface and volume integrals are approximated by using adequate quadrature functions. This way, an algebraic equation for each control volume as a function of the values of the neighbouring nodes is obtained. Hereinafter, the numerical approach for each term in Eq. 3.1 is presented:

- Discretization of surface integrals: The net flux through the border of the control volume is the addition of the integrals through the six faces of the cell.

$$\int_{A_i} f \cdot \vec{n}_i\, dA_i = \sum_{i=1}^{n_c} \int_{A_i} f \cdot \vec{n}_i\, dA_i \qquad \text{(Eq. 3.2)}$$

Where, f is the convective ($f_c = \rho\phi v \cdot n$) or diffusive ($f_d = \Gamma \nabla\phi \cdot n$) component of the flux vector in the normal direction to the control volume face.

To determine the integral in Eq. 3.2 it is necessary to know the integrand f at every point of each surface A_e (face e of the cell). This information is not available, since variables are only

calculated in the cell centres. As a result, the integrand is approximated as an averaged value in centre of the face according to Eq. 3.3.

$$F_e = \int_{A_e} f \cdot \vec{n}_e dA_e = \bar{f}_e \cdot A_e \approx f_e \cdot A_e \qquad \text{(Eq. 3.3)}$$

Since the value of f in the centre of the face e is not known, it is obtained by interpolating between the values from the neighbouring cells. To carry out this approach, there exist many algorithms with different precision orders. In general, first order approximations are more robust, but introduce relevant numerical errors. Therefore, they are used to obtain a first approximation to the solution of the problem. Afterwards, higher order approximations are used to obtain the definitive solution. CFX-4 allows us to use different algorithms: upwind (UDS), central difference scheme (CDS), second order upwind (HUW), third order upwind (QUICK).

- Discretization of volume integrals: Some of the terms in Eq. 3.1 require an integration over the cell volume. The simplest second order approximation consists of replacing the integral volume by the product of the averaged value of the integrand and the cell volume, and approximating the averaged value of the integrand by the value of the variable in the cell centre (Eq. 3.4).

$$Q_p = \int_V \phi_p \cdot dV = \bar{\phi}_p \cdot V \qquad \text{(Eq. 3.4)}$$

Where, the average of ϕ_p is the variable value at the cell centre, which is easily calculable since all the variables are defined at the node P and no interpolation is needed.

Therefore, to obtain the discretization of Eq. 3.1, surface integrals are approximated as the sum of the integrals for each face of the volume, and the volume integrals as the product of the averaged variable value in the cell and the cell volume (Eq. 3.5).

$$\frac{\partial}{\partial t}(\rho\bar{\phi}V) + \sum_{i=1}^{n_c}\int_{A_i} \rho\phi\vec{v} \cdot \vec{n}_i \, dA_i = \sum_{i=1}^{n_c}\int_{A_i} \Gamma \nabla\phi \cdot \vec{n}_i \, dA_i + \bar{S}_\phi \cdot V \qquad \text{(Eq. 3.5)}$$

Eqs. 3.1 and 3.5 express the general form of a conservation equation. Nevertheless, in the momentum conservation equations there exists a contribution due to the pressure that requires special treatment as will be explained later.

The convection term is not linear and can be resolved as explained before (Eq. 3.6). The diffusion term introduces the stress tensor τ_{ij} (Eq. 3.7) which is decomposed into the pressure related forces and viscous stresses (Eq. 3.8).

$$\int_A \rho\phi\vec{v}\cdot\vec{n}\,dA = \int_A \rho\vec{v}\vec{v}\cdot\vec{n}\,dA \qquad \text{(Eq. 3.6)}$$

$$\int_A \Gamma\nabla\phi\cdot\vec{n}\,dA = \int_A \vec{\vec{\tau}}_{ij}\cdot\vec{n}\,dA \qquad \text{(Eq. 3.7)}$$

$$\vec{\vec{\tau}}_{ij} = -p\cdot\delta_{ij} + \vec{\vec{\tau}}'_{ij} \qquad \text{(Eq. 3.8)}$$

The Navier-Poisson's law establishes that viscous stresses are proportional to the components of the deformation tensor (Eq. 3.9).

$$\vec{\vec{\tau}}'_{ij} = \mu\cdot\nabla v_i + \lambda\cdot\nabla\vec{v}\cdot\delta_{ij} \qquad \text{(Eq. 3.9)}$$

In this way, the diffusion term can be expressed according to Eq. 3.10.

$$\int_A \Gamma\vec{\nabla}\phi\cdot\vec{n}\,dA = \int_A (\mu\cdot\nabla v_i + \lambda\cdot\nabla\vec{v}\cdot\delta_{ij})\cdot\vec{n}\,dA + \int_A (-p\cdot\delta_{ij})\cdot\vec{n}\,dA \qquad \text{(Eq. 3.10)}$$

And then, it can be discretized as was previously explained, according to Eq. 3.11.

$$\sum_{l=1}^{n_c}\int_A \Gamma\vec{\nabla}\phi\cdot\vec{n}\,dA = \sum_{l=1}^{n_c}\int_A (\mu\cdot\nabla v_i + \lambda\cdot\nabla\vec{v}\cdot\delta_{ij})\cdot\vec{n}\,dA + \sum_{l=1}^{n_c}\int_A (-p\cdot\delta_{ij})\cdot\vec{n}\,dA_i \qquad \text{(Eq. 3.11)}$$

The resolution of the Navier-Stokes equations is complicated since there does not exist an independent equation for the pressure, and furthermore, its gradient contributes in each momentum equation component. Consequently, the pressure-velocity coupling must be resolved. To achieve this, we start from the continuity equation (Eq. 3.12) and the momentum equations corresponding to the three velocity components (Eq. 3.13).

$$\frac{\partial}{\partial t}\left(\int_V \rho\cdot dV\right) + \int_A \rho\vec{v}\cdot\vec{n}\,dA = 0 \qquad \text{(Eq. 3.12)}$$

$$\frac{\partial}{\partial t}\int_V \rho\vec{v}\cdot dV + \int_A \rho\vec{v}\vec{v}\cdot\vec{n}\,dA = \int_A (-p\cdot\delta_{ij} + \vec{\vec{\tau}}'_{ij})\cdot\vec{n}\,dA + \int_V \rho\cdot\vec{f}_v\cdot dV \qquad \text{(Eq. 3.13)}$$

Expressing in differential form Eqs. 3.12 and 3.13, they turn into Eqs 3.14 and 3.15.

$$\frac{\partial\rho}{\partial t} + div(\rho\cdot\vec{v}) = 0 \qquad \text{(Eq. 3.14)}$$

$$\frac{\partial(\rho\vec{v})}{\partial t} + div(\rho\cdot\vec{v}\cdot\vec{v}) = div(-p\cdot\delta_{ij} + \vec{\vec{\tau}}'_{ij}) + \rho\cdot\vec{f}_v \qquad \text{(Eq. 3.15)}$$

Applying the divergence to each momentum equation, and simplifying from the continuity equation, a Poisson expression for the pressure, that relates the velocity and pressure fields, is obtained (Eq. 3.16).

$$div(grad\ p) = -div\left[\, div\left(\rho\cdot\vec{v}\cdot\vec{v} - \vec{\vec{\tau}}'_{ij}\right) - \rho\cdot\vec{f}_v + \frac{\partial(\rho\vec{v})}{\partial t}\right] \qquad \text{(Eq. 3.16)}$$

To solve this equation numerically we should fall back on implicit or explicit numerical methods. These methods use a pressure correction equation to force the mass balance at each iteration. Implicit methods are often used in stationary flow problems (SIMPLE, SIMPLEC, and PISO).

To solve the velocity-pressure coupling, CFX-4 solves sequentially the momentum equations, where only the velocity components u_i^m* are unknowns, by using the pressure calculated in the previous iteration p^{m-1} and the velocities in the adjacent nodes as a first estimate. However, the velocities obtained do not satisfy the continuity equation so to balance this continuity equation, the velocities must be corrected (Eq. 3.17). Finally as a result, the pressure field now also has to be modified (Eq. 3.18). Then, these calculated values are introduced into the continuity equation giving rise to a Poisson discrete equation for the pressure. Following this, the pressure correction term *p'* is calculated; and consequently, it is possible to determine the velocities u_i^m and pressure p^m that satisfy the continuity equation, but not the momentum equations. In this way, an iterative process is carried out until the calculated velocities satisfy both equations.

$$u_i^m = u_i^{m*} + u' \qquad \text{(Eq. 3.17)}$$

$$p^m = p^{m-1} + p' \qquad \text{(Eq. 3.18)}$$

Where, u_i^m is the i velocity component at the m iteration, u_i^m* the i velocity component at the m iteration, obtained from solving the momentum equations, and u' is the velocity correction term. And p^m is the pressure at the iteration m, p^{m-1} is the pressure is the previous iteration, and p' the pressure correction term.

Depending on the treatment given to the pressure correction equation, different resolution methods are obtained: SIMPLE, SIMPLEC, PISO.

Once the discretization of the transport equations and the pressure-velocity correction were established, Figure 3.2 describes the general resolution method performed by the CFX code.

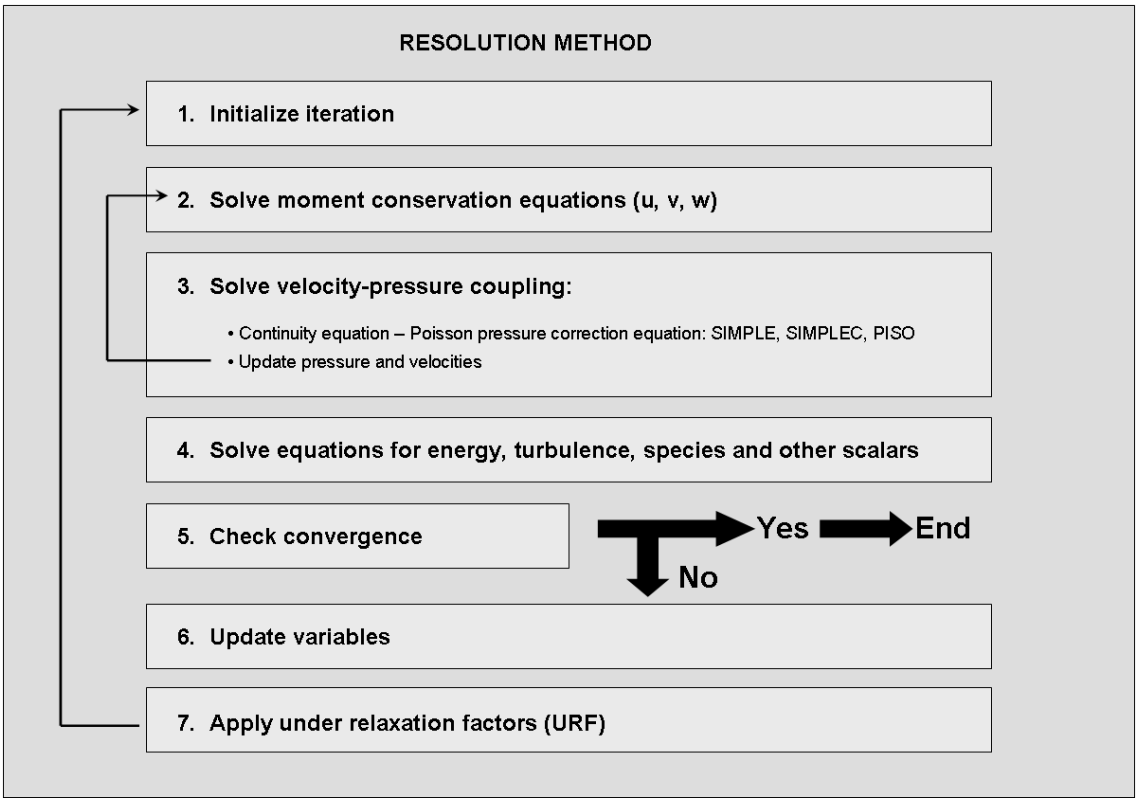

Fig. 3.2 Finite volume resolution method in CFX

3.2 Mathematical models

The numerical solution of the governing equations implies the modelling of all processes that take place in the furnace:

1. Turbulence
2. Particle transport
3. Coal combustion
4. Homogeneous combustion of volatile products
5. Radiation

Hereinafter, these models are described, particularizing for the case-study of this work.

1. Turbulence model (Launder and Spalding, 1974)
The gas flow is modelled, under the Eulerian assumption, solving the steady-state Reynolds average Naviers Stokes equations (RANS) along the computational domain.

These can be summarized as follows:

- Continuity equation

$$\frac{\partial \rho}{\partial t} + \frac{\partial \rho u_i}{\partial x_j} = 0 \qquad \text{(Eq. 3.19)}$$

- Momentum conservation equation

$$\rho \frac{\partial u_i}{\partial x_j} + \rho u_j \frac{\partial u_i}{\partial x_j} = -\frac{\partial p'}{\partial x_j} + \frac{\partial}{\partial x_j}\left(\left(\mu + \mu_T\right)\left(\frac{\partial u_i}{\partial x_j} + \frac{\partial u_j}{\partial x_i} \right)\right) + S_M \qquad \text{(Eq. 3.20)}$$

- Energy conservation equation

$$\rho \frac{\partial h_T}{\partial t} + \rho u_j \frac{\partial h_T}{\partial x_j} = \frac{\partial p}{\partial t} + \frac{\partial}{\partial x_j}\left(\left(\frac{\lambda}{C_P} + \frac{\mu_T}{\sigma_H} \right) \frac{\partial h_T}{\partial x_j} \right) + S_R \qquad \text{(Eq. 3.21)}$$

- Species conservation equation

$$\rho\frac{\partial Y_i}{\partial t}+\rho u_j\frac{\partial Y_i}{\partial x_j}=\frac{\partial}{\partial x_j}\left(\left(\rho D_i+\frac{\mu_T}{\sigma_i}\right)\frac{\partial Y_i}{\partial x_j}\right)+S_i \qquad \text{(Eq. 3.22)}$$

A detailed explanation of the RANS equations is omitted since it is widely described in general fluid mechanics publications (i.e. Pope, 2000).

The widely used standard k - ε model (Launder and Spalding, 1974) is coupled to close the turbulence. It solves two additional transport equations, for the turbulent kinetic energy k (Eq. 3.23) and for the viscous dissipation ε (Eq. 3.24):

- Transport equation for the turbulent kinetic energy

$$\rho\frac{\partial k}{\partial t}+\rho u_j\frac{\partial k}{\partial x_j}=\frac{\partial}{\partial x_j}\left(\left(\mu+\frac{\mu_T}{\sigma_k}\right)\frac{\partial k}{\partial x_j}\right)+\tau_{ij}\frac{\partial u_i}{\partial x_j}-\varepsilon+G \qquad \text{(Eq. 3.23)}$$

- Transport equation for the viscous dissipation

$$\rho\frac{\partial \varepsilon}{\partial x_j}+\rho u_j\frac{\partial \varepsilon}{\partial x_j}=\frac{\partial}{\partial x_j}\left(\left(\mu+\frac{\mu_T}{\sigma_\varepsilon}\right)\frac{\partial \varepsilon}{\partial x_j}\right)+C_1\frac{\varepsilon}{k}\tau_{ij}\frac{\partial u_i}{\partial x_j}-C_2\frac{\varepsilon^2}{k} \qquad \text{(Eq. 3.24)}$$

The definition of the turbulent viscosity and the closure coefficients to complete the problem are:

$\mu_T = C_\mu k^2 / \varepsilon$ $\quad C_\mu = 0{,}09$ $\quad C_1 = 1{,}44$

$C_2 = 1{,}92$ $\quad \sigma_k = 1$ $\quad \sigma_\varepsilon = 1{,}3$

In the previous equations, density has been extracted from the partial derivatives assuming a constant value. The flow is assumed to behave similarly to incompressible flow, making the density only dependent on temperature through a reference pressure, a reasonable assumption for problems with Mach number under 0.3. CFX-4's compressibility model assumptions are:

- Pressure fluctuations are ignored

$$p' = p + \frac{2}{3}\rho \cdot k + \left(\frac{2}{3}\mu_{eff} - \mu_v\right)\frac{\partial u_i}{\partial x_j} \cong p \qquad \text{(Eq. 3.25)}$$

- The kinetic terms of the total enthalpy are neglected

$$h_T = h + \frac{1}{2}u_i^2 + k \cong h \qquad \text{(Eq. 3.26)}$$

Therefore $\rho = \rho(T)$, which is calculated from the equation of state $\rho = \frac{P_0 \cdot PM}{R \cdot T}$.

To complete the turbulence model, it is necessary to define the fluid behaviour in the near wall regions, where most of the variables change abruptly. Therefore, an extraordinarily refined mesh is required to solve these variations. Instead of this, it is possible to use wall functions, which are semi-empirical expressions that entail the solution of the variables in the near wall region. These wall functions are used for the mean velocity, temperature and other scalars (Wilcox, 1998).

- Law of the wall for mean velocity:

Different experiments have shown that the viscous stress variation is very small near the walls, and therefore it may be approximated by the wall shear stress τ_w. Establishing a velocity scale, known as friction velocity $u_\tau = \sqrt{\frac{\tau_w}{\rho}}$ (Wilcox, 1998); two dimensionless variables are defined:

$$u^+ = \frac{u}{u_\tau} \quad \text{and} \quad y^+ = \frac{(\rho \cdot \tau_w)^{1/2}}{\mu} y \qquad \text{(Eqs. 3.27 and 3.28)}$$

From these dimensionless variables, the profiles obtained near the walls are given according to Eqs. 3.29 and 3.30 (Figure 3.3).

$$u^+ = y^+ \qquad \text{for } y^+ < y_0^+ \qquad \text{(Eq. 3.29)}$$

$$u^+ = \frac{1}{\kappa}\ln(E^+ \cdot y^+) \qquad \text{for } y^+ > y_0^+ \qquad \text{(Eq. 3.30)}$$

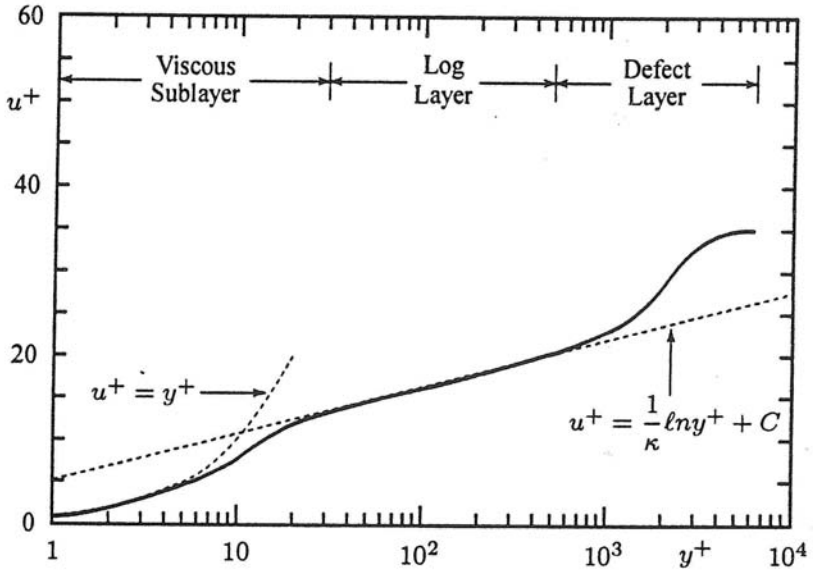

Fig. 3.3 Typical velocity profile for a turbulent boundary layer (Wilcox, 1998)

- Law of the wall for temperature and other scalars:

In the same way it is possible to define boundary wall conditions for temperature and other scalars (f, G):

$$\phi^+ = \mathrm{Pr}_\phi \cdot y^+ \qquad \text{for } y^+ < y_\phi^+ \qquad \text{(Eq. 3.31)}$$

$$\phi^+ = \frac{\sigma_\phi}{\kappa} \ln(E_\phi^+ \cdot y^+) \qquad \text{for } y^+ > y_\phi^+ \qquad \text{(Eq. 3.32)}$$

Where, ϕ^+ is a dimensionless property $\phi^+ = \dfrac{(\rho \cdot \tau_w)^{1/2}}{J_\phi}(\phi_w - \phi)$; where J_ϕ is the wall flux of ϕ, Pr_ϕ is the Prandtl number, σ_ϕ is the turbulent Prandtl number and $E^+{}_\phi$ is calculated from the Jayatilleke expression (1969) (Eq. 3.33).

$$E_\phi^+ = E^+ \cdot \exp\left[9 \cdot \kappa \cdot \left(\left(\frac{\mathrm{Pr}}{\sigma_\phi}\right)^{0.75} - 1\right)\left(1 + 0.28 \exp\left(-0.007 \frac{\mathrm{Pr}}{\sigma_\phi}\right)\right)\right] \qquad \text{(Eq. 3.33)}$$

For the species concentration, the same wall relations are used, but substituting the Prandtl number by the Schmidt number.

$$Y^+ = Sc_\phi \cdot y^+ \qquad \text{for } y^+ < y_\phi^+ \qquad \text{(Eq. 3.34)}$$

$$Y^+ = \frac{Sc_\phi}{\kappa} \ln(E_\phi^+ \cdot y^+) \qquad \text{for } y^+ > y_\phi^+ \qquad \text{(Eq. 3.35)}$$

Therefore, using the k-ε model, the transport equation for the turbulent kinetic energy k (Eq. 3.23) is solved at the wall adjacent cells. Solving this equation, the production term τ_{ij} is approached for the wall shear stress τ_w, and it is kept constant in the cell. The transport equation for the viscous dissipation ε is not solved, and ε is computed from the expression $\varepsilon = \frac{C_\mu^{3/4} \cdot k^{3/2}}{\kappa \cdot y}$, which is also kept constant in the cell.

2. Particle transport model (Sommerfeld, 2000)

A Lagrangian approach was chosen, considering the influence of a diluted particle phase on the fluid flow (dispersed flow), two-way coupling (Sommerfeld, 2000), since the volumetric particles' fraction was approximately $\Phi_v \approx 10^{-4}$ at the boiler inlets (Figure 3.4). On the contrary, the contribution due to particle - particle interactions (four-way coupling) was neglected. The total flow is modelled describing the spatial and time evolution of the trajectories of a representative number of spherical particles through the continuous phase.

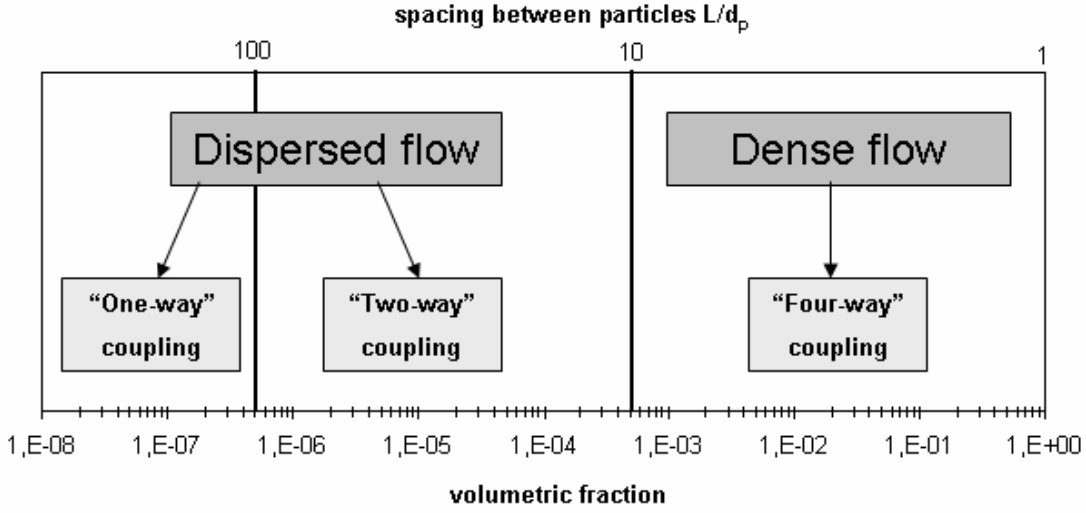

Fig. 3.4 Two-phase flow regimes as a function of particles' volumetric fraction (Sommerfeld, 2000)

The movement of the particles in the flow is described by solving the differential equations along the particle trajectories, calculating variations in the particle position and velocity (Eqs. 3.36 and 3.37).

$$m_p \cdot \frac{d\overrightarrow{u_i}}{dt} = \sum \overrightarrow{F_i} \qquad \text{(Eq. 3.36)}$$

$$\frac{d\overrightarrow{x_p}}{dt} = \overrightarrow{u_p} \qquad \text{(Eq. 3.37)}$$

Within the forces acting over the particle, the most relevant contribution is due to the drag force (Eq. 3.38).

$$F_D = \frac{1}{8} \cdot \pi \cdot d_p^2 \cdot \rho \cdot C_D \cdot |v_R| \cdot v_R \qquad \text{(Eq. 3.38)}$$

Where, v_R is the relative velocity of the particle with respect to the flow, and C_D is a drag coefficient, defined for different flow regimes as follows:

$$C_D = \frac{24}{\mathrm{Re}} \qquad \text{for} \quad \mathrm{Re} < 0.5 \qquad \text{(Eq. 3.39)}$$

$$C_D = 24(1 + 0.15 \cdot \mathrm{Re}^{0.687}) / \mathrm{Re} \qquad \text{for} \quad 0.5 < \mathrm{Re} < 1000 \qquad \text{(Eq. 3.40)}$$

$$C_D = 0.44 \qquad \text{for} \quad \mathrm{Re} > 1000 \qquad \text{(Eq. 3.41)}$$

Although their contribution is negligible, other forces considered in the resolution of the problem are:

- Pressure gradient force: $F_P = -\frac{1}{4} \cdot \pi \cdot d_p^3 \cdot (\nabla P)$ (Eq. 3.42)
- Mass added force: $F_A = -\frac{1}{12} \cdot \pi \cdot d_p^3 \cdot \rho \cdot \frac{du}{dt}$ (Eq. 3.43)

At the same time, another relevant consideration in problems involving turbulent flows is that the motion of the particles is affected by turbulent fluctuations in eddies (Cortés and Gil, 2007).

These fluctuations are modelled by adding a diffusion velocity to the particle convective velocity. This phenomenon is known as turbulent diffusion. While some authors (Coimbra et al., 1994; Fan et al., 2001; Belosevic et al., 2006) account for this phenomenon in pulverized coal boiler simulations, most of them prefer to neglect it since the number of particles to be modelled is at least one order of magnitude higher, increasing considerably the computing time. Furthermore, some authors suggest that including this effect, it is more difficult to achieve the convergence of the problem (Chen and Shuen, 1993). In this work, following the typical methodology in utility boiler simulations, turbulent diffusion effects have been omitted. The reason for this lies in the previous discussion, and in the final use of the CFD results within the unburned carbon predictive system. As will be explained in the following chapters, for us it is more interesting to approach the temperature and oxygen partial pressure found by the particles in their way through the boiler than the motion of the particles itself. Consequently, it is reasonable to assume that turbulent diffusion will slightly modify the particles' velocities and tracks, but not enough to alter markedly the local temperature and oxygen partial pressure in cells. Finally, since the Lagrangian approach is modelled by tracking a number of trajectories, preferably not very large, assuming that each simulated particle represents a sample of the real number of particles, and considering that these trajectories are especially chaotic in such a big fluid domain, the omission of turbulent diffusion effects do not affect the general results of our model.

Moreover, since this problem involves combustion, the particle temperature change should be considered. This process is governed by three mechanisms: convection, reaction and radiation.

- Convection heat transfer

$$Q_C = 4 \cdot \pi \cdot d_p \cdot \lambda \cdot Nu \cdot (T_g - T_p) \qquad \text{(Eq. 3.44)}$$

Where,

$$Nu = 2 + 0.6 \cdot \mathrm{Re}^{0.5} \left(\mu \cdot \frac{C_p}{\lambda}\right)^{1/3} \qquad \text{(Eq. 3.45)}$$

- Heat of reaction

As it will be explained later, reaction heat transfer at the particle surface is due to two mechanisms, devolatilization and char oxidation. Heat transfer during the devolatilization stage is described according to Eq. 3.46.

$$Q_M = \frac{dm_p}{dt} \cdot \Delta H_{dev} \quad \text{(Eq. 3.46)}$$

Where, the particle mass variation corresponds to the high temperature volatile yield, and ΔH_{dev} is the heat consumed during coal pyrolysis.

Heat transfer during the char oxidation stage is described according to Eq. 3.47.

$$Q_M = f_h \cdot \frac{dm_p}{dt} \cdot \Delta H_{react} \quad \text{(Eq. 3.47)}$$

Where, ΔH_{react} is the reaction heat during char oxidation, and f_h represent the fraction of heat absorbed by the particle.

- Radiation heat transfer

Finally, the radiative heat transfer between the particles and the environment is considered according to Eq. 3.48.

$$Q_R = \varepsilon_p \cdot \pi \cdot d_p^2 \cdot \left(I - \sigma_B \cdot T_p^4\right) \quad \text{(Eq. 3.48)}$$

Particle emissivity ε_p is assumed to vary linearly between two defined values, corresponding to char emissivity ($\varepsilon_{char} = 0.6$) and coal emissivity ($\varepsilon_{coal} = 1$), according to Eq. 3.49.

$$\varepsilon_p = (1 - V_f) \cdot \varepsilon_{coal} + V_f \cdot \varepsilon_{char} \quad \text{(Eq. 3.49)}$$

Adding up the three heat transfer contributions (Eqs. 3.44, 3.46, 3.47 and 3.48), a differential equation that solves the temperature change in the particle is obtained (Eq. 3.50).

$$\sum \left(m_p \cdot C_p\right) \frac{dT}{dt} = Q_C + Q_M + Q_R \quad \text{(Eq. 3.50)}$$

All momentum, mass and heat transfer from the particles, produces a source of momentum, mass and heat in the continuous phase (two-way coupling), through the source terms in the conservation equations according to a PSI-cell model (Crowe et al., 1977).

3. Coal combustion model

Coal combustion calculations are combined with the particle transport, which has been analyzed in the previous subsection. Homogeneous combustion of volatile products will be described in point 4, while at this point we will focus on the mechanisms and models for devolatilization and char oxidation.

- Devolatilization (Badzioch and Hawskey, 1970)

Devolatilization rate is modelled using the single step model of Badzioch and Hawskey (1970), which states that the rate of production of volatile gases is given by a first-order reaction (Eq. 3.51).

$$\frac{dV}{dt} = k_v (V_f - V_{fi}) \qquad \text{(Eq. 3.51)}$$

Where, V_{fi} is the parent coal volatile content obtained from the standard proximate analysis, and k_v is the reaction rate expressed in an Arrhenius form (Eq. 3.52).

$$k_v = A_v \cdot e^{\left(-\frac{E_{vT}}{T_p}\right)} \qquad \text{(Eq. 3.52)}$$

- Char oxidation

Char oxidation is modelled using the popular single film char oxidation model (Field et al., 1967; Baum and Street, 1971). However, as explained in Chapter 2, to improve the prediction capability of the model, both rank-dependent empirical correlations and a specific submodel describing ash inhibition in the late stages of combustion were coupled (Pallarés et al., 2005). Since the elements of the combustion model were explained in detail in Chapter 2, below only the more characteristic equations are summarized.

Global reaction rate is calculated according to Eq. 3.53.

$$q_c = \frac{P_g^{\,0.5}}{\frac{1}{k_d} + \frac{1}{k_c}} \qquad \text{(Eq. 3.53)}$$

Diffusion rate is calculated according to Eq. 3.54 (Hurt et al., 1998).

$$k_d = \frac{Sh \cdot D_{O2} \cdot d_p \cdot \theta_{af}^{2.5}}{R \cdot T_m (Sh \cdot \delta \cdot d_c + \theta_{af}^{2.5} \cdot d_c^{2.5})} \quad \text{(Eq. 3.54)}$$

Chemical reaction rate is calculated according to Eq. 3.55.

$$k_c = A_a \cdot e^{(\frac{-E_a}{R \cdot T_p})} \quad \text{(Eq. 3.55)}$$

The activation energy E_a, and pre-exponential factor A_a, are obtained from the proximate and ultimate coal analysis according to Eqs. 3.56 and 3.57 (Hurt and Mitchell, 1992).

$$E_a = (-5.94 + 35.5 \cdot \%C) \cdot 4.1869.10^3 \quad \text{(Eq. 3.56)}$$

$$A_a = \exp(\ln(k_{c,1750K}) + \frac{E_a}{1750 \cdot R}) \cdot \frac{10}{101325^{1/2}} \quad \text{(Eq. 3.57)}$$

4. Volatile products combustion model

The homogeneous combustion of volatiles released from the particle is modelled using the mixed-is-burnt model (Warnatz et al., 1996), which assumes infinitely fast chemistry. This assumption is adequate for reacting flows with high Damköhler numbers ($D_a >> 1$). The mean and mass fraction of fuel, oxidant and products are obtained by solving the mean f (Eq. 3.58) and variance G of the mixture fraction (Eq. 3.59) transport equations.

$$\rho \frac{\partial f}{\partial t} + \rho u_j \frac{\partial f}{\partial x_j} = \frac{\partial}{\partial x_j}\left(\left(\frac{\mu_T}{\sigma_T} + \frac{\mu}{\sigma_L}\right)\frac{\partial f}{\partial x_j}\right) \quad \text{(Eq. 3.58)}$$

$$\rho \frac{\partial G}{\partial t} + \rho u_j \frac{\partial G}{\partial x_j} = \frac{\partial}{\partial x_j}\left(\left(\frac{\mu_T}{\sigma_T} + \frac{\mu}{\sigma_L}\right)\frac{\partial G}{\partial x_j}\right) + C_{g1}\mu_T \frac{\partial}{\partial x_j}\left(\frac{\partial G}{\partial x_j}\right) - C_{g2}\rho \frac{\varepsilon}{k} G \quad \text{(Eq. 3.59)}$$

Mixture fraction f is defined from Eqs. 3.60 and 3.61.

$$f = \frac{\chi - \chi_O}{\chi_F - \chi_O} \quad \text{(Eq. 3.60)}$$

$$\chi = m_F - \frac{m_O}{\varphi} \quad \text{(Eq. 3.61)}$$

Furthermore, a stoichiometric mixture fraction F_{st} is defined according to Eq. 3.62.

$$F_{st} = \frac{1}{1+\varphi} \quad \text{(Eq. 3.62)}$$

The fuel and oxidant cannot co-exist, since the reaction is instantaneous and the respective mass fractions are determined as a function of the mean f and variance G of the mixture fraction. A beta probability density function (β-PDF) p(f) is assumed to model the mixture fraction fluctuations (Eqs. 3.63 and 3.64).

$$m_F = \int_0^1 \max\left[\frac{f - F_{st}\cdot(1-m_{PC})}{1-F_{st}}, 0\right]\cdot p(f)\cdot df \quad \text{(Eq. 3.63)}$$

$$m_O = \int_0^1 \max\left[1 - m_{PC} - \frac{f}{F_{st}}, 0\right]\cdot p(f)\cdot df \quad \text{(Eq. 3.64)}$$

Finally, the products' mass fraction m_{PR} is calculated by the difference of the fuel, oxidant and char products mass fractions (Eq. 3.65).

$$m_{PR} = 1 - m_F - m_O - m_{PC} \quad \text{(Eq. 3.65)}$$

5. Radiation model

The thermal radiation in the furnace is the dominant heat transfer mechanism due to the presence of a mixture of participative gases and particles at high temperature. Gases absorb and emit thermal radiation as a function of temperature and wave length. Particles also participate in the radiative interchange. The radiative heat transfer has been modelled using the Discrete Transfer method (Lockwood and Shah, 1981), which solves a transport equation for the radiation intensity along paths between two boundary walls. Every ray (path) considered is discretized at each volume cell, assuming constant properties within the cell. Defining the radiative heat balance along one direction s, the variation with s of the radiation intensity is determined by adding up the contributions due to emission, absorption, incoming dispersion in

the *s* direction and outgoing dispersion from the *s* direction. Consequently, a transport equation for the radiation intensity is obtained (Eq. 3.66) (Hottel and Sarofim, 1967; Modest, 1993).

$$\frac{dI_\lambda}{ds} = \varepsilon \cdot I_{b\lambda} - (k_a + k_s) \cdot I_\lambda + \frac{k_s}{4\pi} \int_{4\pi} I_\lambda(\hat{s}_i) \cdot \Phi_\lambda(\hat{s}_i, \hat{s}) \cdot d\Omega_i \qquad \text{(Eq. 3.66)}$$

According to Planck's law, the black body intensity I_b, is obtained integrating the intensity corresponding to each wave length λ for the whole wavelength spectrum (Eqs. 3.67 and 3.68).

$$I_b(T) = \int_0^\infty I_{b\lambda}(T) \cdot d\lambda = \sigma_B \cdot T^4 \qquad \text{and} \qquad I_{b\lambda}(T) = \frac{C_1}{\lambda^5 (e^{C_2/\lambda \cdot T} - 1)} \qquad \text{(Eqs. 3.67 and 3.68)}$$

From Kirchhoff's radiation law, the spectral emissivity $\varepsilon(\lambda)$ and the spectral absorption coefficient $k_a(\lambda)$ will adopt the same value. This value, may be estimated by applying a multi-grey gas model, decomposing the real gas into one non participating gas and several grey gases. In this way, the emissivity and absorptivity of a real gas can be characterized as the sum of the emissivities for the real gas decomposition considered, and the product of the participating gases partial pressure p and a characteristic length L_c (Eq. 3.69) (Taylor and Foster, 1974).

$$\varepsilon = \sum_{i=1}^{N_g} a_{ni}(T) \cdot \left[1 - e^{-k_i \cdot p \cdot L_c}\right] \qquad \text{(Eq. 3.69)}$$

Where,

$$\sum_{i=1}^{N_g} a_{ni}(T) = 1 \qquad \text{(Eq. 3.70)}$$

There exist many emissivity graphs in the literature for different H_2O-CO_2 mixture proportions (Hadvig, 1970; Leckner, 1972; Beer, Foster and Siddall, 1971). The last ones (Beer et al., 1971) also account for the CO and other unburned hydrocarbons contribution to calculate the real gas emisivity (Eq. 3.71).

$$\varepsilon = \sum_{i=1}^{N_g} a_{ni}(T) \cdot \left[1 - e^{-(k_i \cdot (p_w + p_c) + k_{HCi} \cdot p_{HC}) \cdot L_c}\right] \qquad \text{(Eq. 3.71)}$$

Where,

$$a_{ni} = b_{1i} + 10^{-5} \cdot b_{2i} \cdot T \qquad \text{(Eq. 3.72)}$$

Table 3.1 shows the empirical constant values b_{1i}, b_{2i} (K^{-1}), k_i ($m^{-1}atm^{-1}$) and k_{HCi} ($m^{-1}atm^{-1}$) (Beer et al., 1971).

	$p_w/p_c=2$				$p_w/p_c=1$			
Nº Gas	b_{1i}	b_{2i}	k_i	k_{HCi}	b_{1i}	b_{2i}	k_i	k_{HCi}
1	0.437	7.13	0	3.85	0.486	8.97	0	3.41
2	0.39	-0.52	1.88	0	0.381	-3.96	2.5	0
3	1.173	-6.61	68.83	0	0.133	-5.01	109	0

Table 3.1 Experimental constants for a multi-grey gas model (Modest, 1993)

For simplicity, a grey gas model is considered to evaluate the properties of the gas phase, considering a constant value for the absorption coefficient over the whole wavelength spectrum.

With regard to the dispersion of particles; this is assumed to be isotropic, simplifying the last term in the radiative intensity transport equation (Eq. 3.66), $\Phi_\lambda(\hat{s}_i,\hat{s})=1$.

Defining q_R as the radiative power per area unit, obtained from the integration of the radiation intensity I_λ over the solid angle in the whole wavelength spectrum (Eq. 3.73), and integrating the radiative intensity transport equation (Eq. 3.66) over the solid angle, the general conservation equation for the radiative energy is obtained (Eq. 3.74).

$$q_R = \int_0^\infty q_{R\lambda}\cdot d\lambda = \int_0^\infty \int_{4\pi} I_\lambda(\hat{s})\cdot d\Omega\cdot d\lambda \qquad \text{(Eq. 3.73)}$$

$$\nabla q_R = \nabla\int_0^\infty q_{R\lambda}\cdot d\lambda = -4\cdot\pi\cdot(k_a+k_s)\cdot J + \int_{4\pi} Q\cdot d\Omega_s \qquad \text{(Eq. 3.74)}$$

Where,

$$J=\frac{1}{4\pi}\int I\cdot d\Omega_s \quad \text{and} \quad \int Q\cdot d\Omega_s = 4\cdot k_a\cdot I_b + 4\cdot\pi\cdot k_s\cdot J \qquad \text{(Eqs. 3.75 and 3.76)}$$

This transport equation allows us to determine at each cell the radiation source term q_R (or sink term), which is then introduced in the mean flow energy transport equation (Eq. 3.21, S_R term).

Table 3.2 summarizes the models used in the CFD simulation of the case-study boiler in this work.

Problem	Model	Reference
Main Flow (Eulerian)	RANS	
Turbulence	k-ε standard	Launder and Spalding, 1971
Devolatilization	Single first order reaction (SFOR)	Badzioch and Hawskley, 1970
Volatile combustion	Mixed is burnt	Wartnatz et al., 1996
Char oxidation	Conventional single film + Rank dependant correlations + Ash inhibition (CBK)	Field et al., 1967 Hurt and Mitchell, 1992 Hurt et al., 1998
Radiation	Discrete Transfer	Lockwood and Shah, 1981
Particles transport	Lagrangian approach (two-way coupling)	

Table 3.2 Summary of the models used in the CFD simulation of the case-study boiler

3.3 Boundary conditions

Once the models have been introduced, the required boundary conditions to solve the problem are set below (Versteeg and Malasekera, 1995):

1. Fluid boundaries:

- Inlets:

Generally, all the variables are specified at the inlets. Moreover, it is useful to locate the inlets as far as possible from the region of interest. In this work, the continuous phase (gas stream) was defined by the normal and angular components of velocity. The normal component was calculated from the mass flow, inlet section and primary air temperature, under an ideal gas assumption. The angular component was calculated from the burner geometry (Basu et al., 2000). Furthermore, inlet flow temperature, turbulence intensity and dissipation length scale were also defined. Radiation related properties were defined in terms of emissivity, specular roughness and radiation temperature.

The particles' phase was defined by the coal mass flow, a Rosin Rammler size distribution (Eq. 3.77) and the inlet velocity, which coincides with the one defined for the flow, since the particles' phase is diluted in the gas stream.

$$FV(d_p > d) = 100 \cdot \exp\left(-\left(\frac{d}{d_{pm}}\right)^{n_{rr}}\right) \quad \text{(Eq. 3.77)}$$

- Outlets:

Generally, there is little information about the flow at the outlets. For this reason, again it is advisable to locate the outlets as far as possible of the interest study region. In this work, open boundary conditions were assumed in the outlet: $\frac{\partial u_n}{\partial n} = 0$ and $\frac{\partial T}{\partial n} = 0$. Radiation related properties were defined again in terms of emissivity, specular roughness and radiation temperature.

2. Walls:

At the walls, no slip conditions and logarithmic profiles (wall functions) for velocity to adequately represent turbulence in the near wall region were defined. Radiation boundary conditions were defined again in terms of emissivity, specular roughness and radiation temperature.

3.4 Verification and validation

The last step in the resolution process is to determine the accuracy of the solution and if the results obtained with the numerical simulation adequately reproduce and describe the real processes. These aspects are known as verification and validation of the numerical simulation.

In the same way that there exist uncertainties in the solution when experimental techniques are used, there also exist uncertainties associated with numerical resolution methods. As a result of the rapid spreading of the use of computational tools, many standard error quantification and simulations validation procedures have arisen (Velilla, 2004). However, as stated by Velilla (2004), there is still not a unique methodology accepted globally.

Generally, in CFD related publications, the most widespread validation method used is to compare results from the simulations with experimental data. However, being rigorous, the fact that the results from a simulation correctly reproduce the experimental results does not ensure that the numerical model adequately reproduces the real process. The numerical errors of the method should be also determined. To achieve this, it is necessary to distinguish two stages in the approval of the simulation: verification, that accounts for the numerical errors, and

validation, that accounts for uncertainties in the mathematical models used in the characterization of the real processes.

- Verification

The verification stage consists of determining the numerical errors of the computational method. That is, errors related to the correct numerical resolution of the differential equations. The errors obtained may be considered the numerical uncertainty of the simulation. The numerical errors that may be taken into account are:

- Error due to the iterative method in the resolution of the equations: This error is associated with the global convergence of the method. The better the convergence of the solution in obtaining the lowest values for the variables' residules (< 1E-4) and in minimising the mass balance error over the whole domain, the lower is the contribution of this error. In general, when using the robust commercial CFD codes, this error is usually negligible and may be estimated from graphical methods or theoretical approaches.

- Error due to the spatial discretization: This error is associated with the size of the computational grid. Of all the numerical errors it is the most relevant. The method used to determine this error consists of performing a progressive refinement of the mesh, studying the convergence until a mesh-independent solution under a specified tolerance is achieved.

- Error due to the time discretization: This error is associated with the time step in transitory problems. In the same way as with the previous error, the method to determine this error consists of performing a progressive decreasing of the time step, studying the convergence until a mesh-independent solution under a specified tolerance is achieved.

- Validation

The validation stage consists of determining the modelling errors of the computational method. These are errors derived from the assumptions, hypothesis and simplifications used for the mathematical description of the real process. The modelling errors that may be taken into account are:

- Error due to numerical errors: This error was previously determined in the verification stage.

- Error due to experimental data uncertainties: This error is determined from the precision of the plant instrumentation and the accuracy of the data gathering process.

- Error due to the hypothesis and assumptions of the mathematical models: This error is estimated by comparing experimental data against simulated results taking into account the previous calculated errors.

3.5 Summary

Computational fluid dynamics together with the continued evolution of computers has succeeded in establishing an essential calculation tool. Its growth has gone beyond the research field being introduced in the industry through many commercial codes. The main advantage of these computational techniques is that they represent an economic and accurate alternative to experimental methods. Moreover, CFD codes allow us to resolve a great variety of problems involving turbulence, multi-phase flows, reactive flows, etc.

CFD codes are based on the numerical resolution of the differential equations that describe the flow dynamics. To achieve this, it is necessary to discretize the study domain and choose an approach to discretize the equations that govern the process. The domain is divided into a number of control volumes called cells. Subsequently, to determine the flow variables, the conservation equations are calculated at discrete points in the cells called nodes. Three discretization methods are commonly used: finite elements, finite volumes and finite differences. In this work, the commercial code CFX-4 based on the finite volume method was used. This method numerically solves the integral form of the conservation equations, using different order algorithms as described in the chapter. Another important feature of these codes is the mathematical models that describe the physical and chemical processes that the fluid undergoes. A complete section in the chapter has been dedicated to describe how these models are implemented in the code, with emphasis on the pulverized coal combustion problem (turbulence, multi-phase flow, homogeneous combustion, coal pyrolysis, char oxidation, radiation). Finally, the last section presents a methodology to validate the CFD simulation. To this end, all the uncertainties associated with the numerical discretization of the equations and the uncertainties associated with the modelling of the real processes are described and it is suggested how to estimate their contribution.

Nomenclature

a_{ni} participation coefficient for the gas i

A area (m^2)

A_a pre-exponential factor (g C/cm^2 s)

A_v pre-exponential factor of the devolatilization process (s^{-1})

b_{1i} experimental constant of a multi-grey gas model

b_{2i} experimental constant of a multi-grey gas model

C_D drag coefficient

C_{g1} mixture fraction transport coefficient

C_{g2} mixture fraction transport coefficient

C_p specific heat (kJ / kg K)

C_1 turbulence closure coefficient (k-ε model)

C_2 turbulence closure coefficient (k-ε model)

C_{I1} radiation constant (3.7415 W/m^2)

C_{I2} radiation constant (1.4388 m^2K)

C_μ turbulence closure coefficient (k-ε model)

d mesh sieve diameter (m)

d_c char particle core diameter (cm)

d_p particle diameter (m)

d_{pm} mean diameter Rosin Rammler distribution (m)

D diffusion coefficient (m^2 /s)

D_a Damköhler dimensionless number $\left(D_a = \tau_t / \tau_c\right)$

D_{O2} molecular diffusion coefficient for O_2 into N_2 (cm^2 /s)

E^+ law of the wall dimensionless constant (11.225)

E_a activation energy (J/mol)

E_{vT} activation temperature of the devolatilization process (K)

f mixture fraction

f_c integrand of the convective term in a generic conservation equation

f_d integrand of the diffusive term in a generic conservation equation

f_h heat fraction absorbed by the particle

f_v integrand of the volume forces term in a generic conservation equation

F_A mass added force (N)

F_i i component of the force F (N)

F_D drag force (N)

F_P pressure gradient force (N)

F_{st} stoichiometric mixture fraction

FV volume fraction of particles passing through a mesh sieve *d* in a Rosin Rammler distribution

G variance of the mixture fraction

h enthalpy (kJ/kg)

h_c convective coefficient (W/m K)

h_T total enthalpy (kJ/kg)

I radiation intensity per solid angle unit (W/m^2 sr)

I_b blackbody radiation intensity per solid angle unit (W/m^2 sr)

I_λ radiation intensity in the λ wave length per solid angle unit (W/m^2 μm sr)

$I_{b\lambda}$ blackbody radiation intensity in the λ wave length per solid angle unit (W/m^2 μm sr)

J radiosity (W/m^2)

J_ϕ flow of the generic variable ϕ (W/m^2)

k turbulent kinetic energy (m^2 s^2)

k_a absorption coefficient

k_c chemical reaction rate (g C/cm^2 s atm^n)

k_d diffusion rate (g C/cm^2 s atm)

k_i experimental constant of a multi-grey gas model

k_{HCi} experimental constant of a multi-grey gas model

k_s dispersion coefficient

k_m mass transfer coefficient (m/s)

k_v kinetic rate constant of the devolatilization process (s^{-1})

L_c characteristic length (m)

Ma Mach dimensionless number $\left(Ma = v/v_s\right)$

m_F fuel mass fraction

m_O oxidant mass fraction

m_{PC} char products mass fraction

m_{PR} products mass fraction

m_p particle mass (g)

n unitary normal vector

n_c number of faces in a cell

n_{rr} dispersion factor Rosin Rammler distribution

N_g number of participating gases

N_R number of reactions

Nu Nusselt dimensionless number $\left(Nu = h_c\ L_c / \lambda\right)$

p pressure (N / m^2)

p_c carbon dioxide partial pressure (atm)

p_{HC} carbon monoxide and other hydrocarbon partial pressure (atm)

p_w water vapour partial pressure (atm)

p^m pressure iteration m (N / m^2)

p' pressure correction term (N / m^2)

P_g bulk oxidant partial pressure ((atm)

PM molecular weight (kg/kmol)

Pr Prandtl dimensionless number $\left(\mathrm{Pr} = \mu\, C_p / \lambda\right)$

P_0 pressure (N/m^2)

q_c combustion rate (g C/cm^2 s)

q_R radiative heat transfer (W/m^2)

$q_{R\lambda}$ radiative heat transfer in the wave length λ (W/m^2 μm)

Q_c particle-environment convective heat transfer (W)

Q_M heat transfer associated with the particle mass transfer (W)

Q_R particle-enviroment radiative heat transfer (W)

R universal ideal gas constant (8.3145 J/mol K)

Re Reynolds dimensionless number $\left(\mathrm{Re} = \rho\, v\, L_c / \mu\right)$

s radiation direction

Sh Sherwood dimensionless number $\left(Sh = k_m\ L_c / D\right)$

Sc Schimdt dimensionless number $\left(Sc = \mu / \rho\, D\right)$

S_i source term species conservation equation

S_M source term momentum conservation equation

S_R source term energy conservation equation

S_ϕ source term generic variable ϕ conservation equation

t time (s)

T temperature (K)

T_g bulk gas temperature (K)

T_m average temperature (K)

T_p particle temperature (K)

u friction velocity (m/s)

u_i component i of velocity (m/s)

u_i^m component i of velocity at iteration m (m/s)

u_p component u of particle velocity (m/s)

u^+ law of the wall dimensionless velocity

u' velocity correction term (m/s)

v	velocity (m/s)
v_R	fluid-particle relative velocity (m/s)
v_s	speed of sound (m/s)
V	cell volume (m^3)
V_{fi}	instantaneous volatiles fraction
V_f	yield volatiles fraction
x_i	spatial coordinate i (m)
x_p	spatial coordinate x of the particle (m)
y^+	law of the wall dimensionless distance
Y_i	specie I mass fraction
%C	% weight of carbon in the parent coal (d.a.f.)
ΔH_{dev}	combustion enthalpy of the devolatilization process (kJ)
ΔH_{react}	combustion enthalpy of the char oxidation process (kJ)
δ_{ij}	Dirac delta
δ	ash film thickness (cm)
ε	eddy dissipation ($m^2\ s^{-3}$)
ε_p	particle emissivity
ε_{coal}	coal emissivity
ε_{char}	char emissivity
κ	Von Karman constant (0.419)
φ	stoichiometric coefficient
λ	Reynolds stress tensor coefficient
	thermal conductivity (W/m K)
	wave length (m)
ϕ	generic variable
Φ	dispersion of radiation
Φ_v	volumetric fraction of particles in the gas phase
θ_{af}	ash film porosity
ρ	density (g/cm^3)
τ_w	wall shear stress
τ_{ij}	stress tensor
τ_{ij}'	viscous stress tensor
Ω	solid angle (rad)
Γ	effective diffusivity (m^2/s)

σ_B Stephan Boltzman constant (5.67 E-12 W/cm^2 K^4)

σ_H Prandtl turbulent dimensionless number $\left(\sigma_H = \mu_T \ C_p / \lambda\right)$

σ_i Prandtl turbulent dimensionless number $\left(\sigma_i = \mu_T \ C_p / \lambda\right)$

σ_k turbulence closure coefficient (k-ε model)

σ_L Prandtl dimensionless number $\left(\sigma_L = \mu \ \ C_p / \lambda\right)$

σ_T Prandtl turbulent dimensionless number $\left(\sigma_T = \mu_T \ C_p / \lambda\right)$

σ_ε turbulence closure coefficient (k-ε model)

σ_ϕ Prandtl turbulent dimensionless number $\left(\sigma_\phi = \mu_T \ C_p / \lambda\right)$

τ_c characteristic time for chemical reaction

τ_t characteristic time for fluid dynamics

μ viscosity (kg/m s)

μ_{eff} effective viscosity (kg/m s)

μ_v kinematic viscosity (kg/m s)

μ_T turbulent viscosity (kg/m s)

χ molar fraction

χ_F fuel molar fraction

χ_O oxidant molar fraction

Acronyms

CDS	central differences scheme
CFD	computational fluid dynamics
FVM	finite volume method
PDF	probability density function
PSI-cell	particle-source-in cell
RANS	Reynold's averaged Navier Stokes equations
SFOR	Single first order reaction
UDS	upwind differential scheme

4 SENSITIVITY STUDY OF MAIN FACTORS AFFECTING UNBURNED CARBON LOSS

In Chapter 1, the main factors affecting unburned carbon losses were described and classified into three categories: coal and char related properties, coal preparation and grinding pre-treatments and burner and boiler design and operation conditions.

Nevertheless, not all these factors are relevant during the daily operation of the plant. For example, coal type, composition and intrinsic characteristics, have a great influence on the combustion process. However, the selection of the coal type has been previously done based on coal rank, composition, HHV, stock availability, price, etc. In other words, coal properties are not a decision parameter that may be modified during the daily operation of the plant. On the other hand, other factors such as the milling process or the combustion conditions are liable to be modified, thus impacting the unburned carbon loss.

In this chapter, a sensitivity analysis of the main factors affecting unburned carbon losses is performed which can be actuated by the technical personnel in the plant either directly or indirectly. To achieve this, we have carried out a double study of theses parameters. Firstly, in the regular range of variation we have evaluated the contribution of each factor to the final unburned carbon level, keeping constant the rest of the parameters. Subsequently, we have evaluated cross-related effects and interactions amongst these various factors. This study, in which we have made used of multi-parameter factorial analysis techniques, gives a more

realistic view of the problem since the contribution of one factor may vary depending on the conditions of the other factors.

For this purpose, a set of CFD simulations of the study plant (Lamarmora ASM Brescia) under different scenarios were carried out using a commercial CFD code, CFX 4.4. This chapter is divided into three main sections. Firstly, information about the ASM power plant, including geometrical and operational characteristics to carry out the CFD simulations, is presented. Secondly, the CFD furnace model of the study plant is described: domain description, mathematical models, boundary conditions and validation process. Finally, a description of case-study factors and scenarios and the sensitivity study itself, are presented.

4.1 ASM Brescia power plant description

Lamarmora ASM Brescia power plant generates a total output of 139 MWe and consists of three front-fired units with natural circulation and single reheat. The case-study unit is 63 MWe gross load, equipped with four burners arranged in two rows of two burners each. A vertical rod mill feeds the two burners of the same row. In the study, two coals from Central America commonly used in the plant over the last five years (Guasare from Venezuela and Carboandes from Colombia) and a coal from Russia, recently used to evaluate its influence on combustion efficiency, were burned separately. Proximate and ultimate analysis and gross calorific values for the coals involved are shown in Table 4.1, as provided by the plant laboratory. The three coals fall within the category of high volatile bituminous coals according to the ASTM classification standards.

Proximate analysis (as received)	**Guasare**	**Carboandes**	**Russian**
Moisture (%)	6.91	9.6	9.56
Ash (%)	5.75	6.44	7.14
Volatile (%)	35	34.17	36.09
Fixed carbon (%)	52.34	49.79	47.21
Ultimate analysis (as received)			
Carbon (%)	72.75	69.21	65.62
Hidrogen (%)	4.93	4.38	4.66
Oxigen (%)	7.75	8.38	10.74
Nitrogen (%)	1.27	1.36	1.9
Sulfur (%)	0.64	0.64	0.38
Heating value			
HHV (kcal/kg)	7220	6715	6725

Table 4.1 Proximate and ultimate analysis for the three study coals
(fixed carbon calculated by difference)

Figures 4.1 and 4.2, show the boiler geometry and the primary and secondary air flow arrangement respectively.

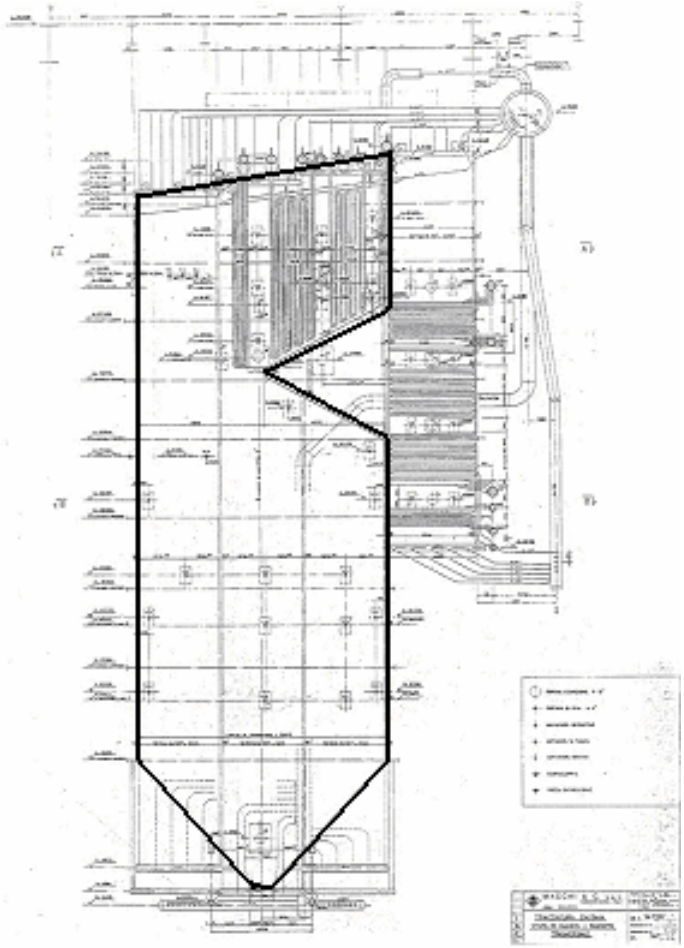

Fig. 4.1 Case-study unit geometry (ASM Brescia)

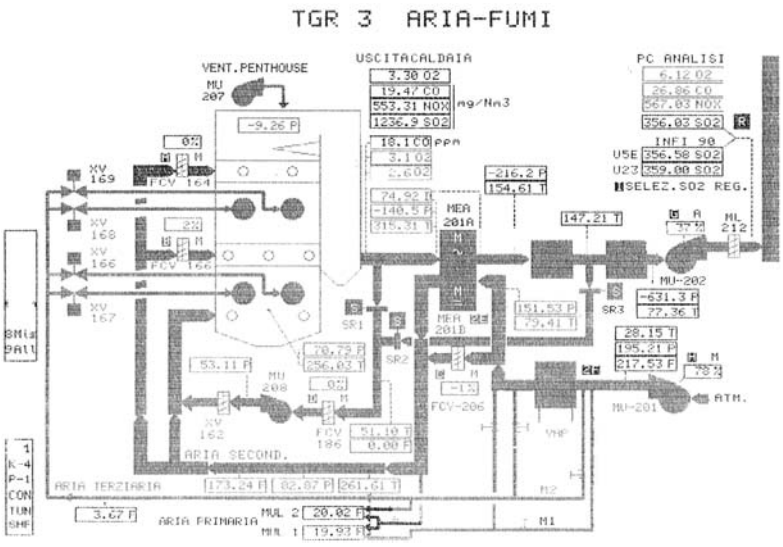

Fig. 4.2 Primary and secondary air flow arrangement (ASM Brescia)

4.2 CFD model of the ASM Brescia case-study unit

A commercial CFD application, CFX 4.4 (AEA Technology plc.) running on a Windows machine, Pentium IV X-dual processor 2.8 GHz, 2 GB RAM each, has been chosen to perform the simulations. Further information about CFX-4 code and the resolution methods used within it were presented in Chapter 3.

4.2.1 Geometry description

The Full boiler geometry has been modelled up to the plenum to facilitate the definition of an appropriate boundary condition at the outlet section and allowing the inclusion of the radiant superheater geometry in a further development (bold contour in Figure 4.1). The selected mesh is structured and made up of 130 000 square elements (Figure 4.3). Its size is refined in the vicinity of the burners' belt to better characterize the major gradients and is progressively made more coarse up to the top of the furnace. A detailed description of the burners' grid structure is displayed in Figure 4.4, where the square elements in the middle are considered as solid walls, simulating the zone where the ignitors and flame detectors are located. The three internal circular rings simulate the inlet section for coal and primary air and the other three external circular rings simulate the inlet section for secondary and tertiary air.

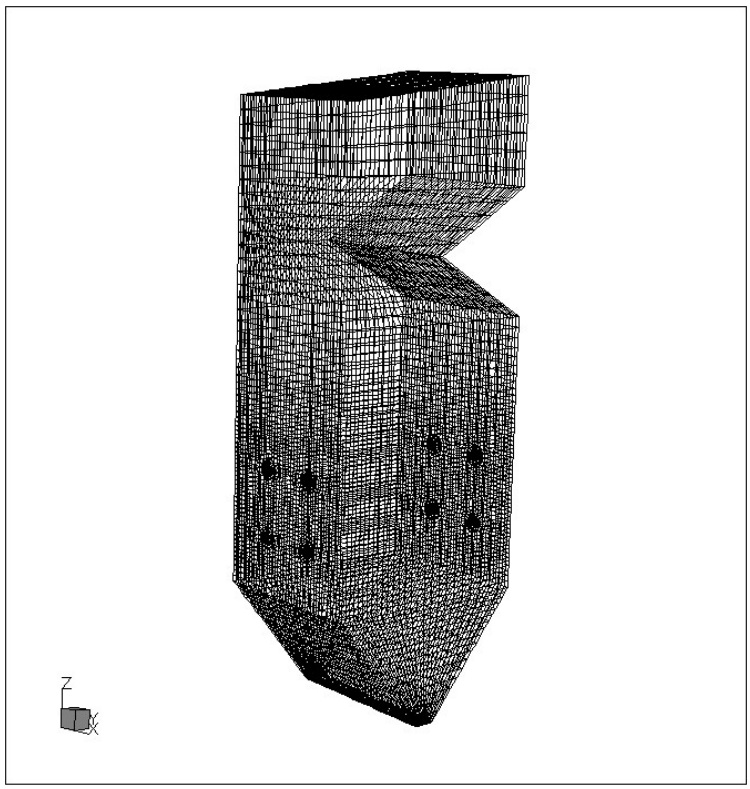

Fig. 4.3 Meshed boiler geometry

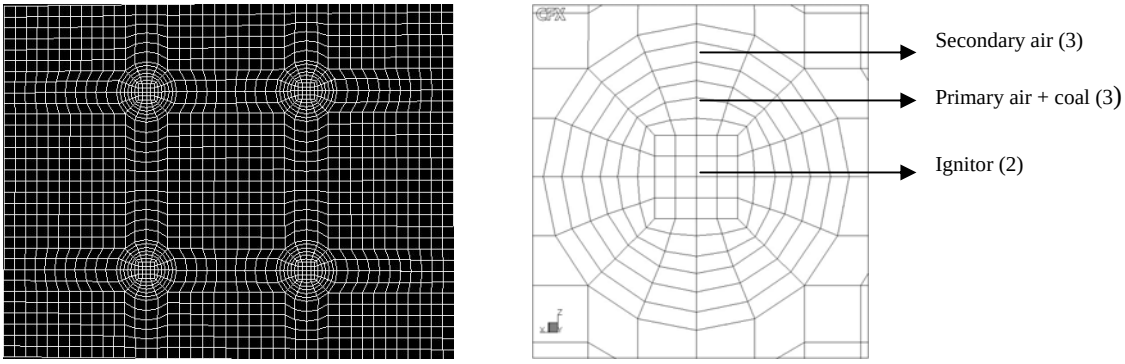

Fig. 4.4 Detail of mesh structure at the burner belt region

4.2.2 Mathematical models

The numerical resolution of the governing equations implies the modelling of all processes that take place in the furnace:

- Turbulent flow
- Coal combustion and mass transfer
- Particle transport
- Radiative heat transfer.

The gas flow is modelled by solving the steady-state Reynolds average Navier Stokes equations (RANS) along the computational domain using the Eulerian assumption. Since the flow is turbulent, the widely used standard k-ε model (Launder and Spalding, 1974) is coupled to close the turbulence problem. The flow is assumed to behave similar to incompressible flow, making the density only dependent on temperature through a reference pressure $\rho = \rho(T, P_{ref})$, a reasonable assumption for problems with a Mach number under 0.3. In the near wall region logarithmic variations for velocity and other scalar fields (temperature, species concentration) are assumed (Versteeg and Malasekera, 1995).

Coal combustion modelling comprises volatiles' yield and homogeneous combustion, and char heterogeneous oxidation. The devolatilization rate is modelled using the single step model of Badzioch and Hawskley (1970), which states that the rate of production of volatile gases is given by a first order reaction and the rate constant is expressed in an Arrhenius form. The homogeneous combustion of volatiles released from the particle are modelled using the mixed-is-burnt model, see for instance Warnatz et al. (1996), which assumes infinitely fast chemistry. The instantaneous mass fractions are given in terms of the instantaneous mixture fraction. The mean mass fraction of fuel, oxidant and products are obtained from the mean and variance of the mixture fraction assuming the beta probability density function, β-PDF.

Char oxidation is modelled using the popular single film char oxidation model (Baum and Street, 1971), but coupling both rank dependent empirical correlations and a specific sub-model describing ash inhibition at the late stages of combustion. As a matter of fact, the inclusion of rank dependant correlations within this enlarged combustion model for the global pre-exponential factor, A_a, and for the global activation energy, E_a, establishes a direct dependence between char reactivity and coal properties (Hurt and Mitchell, 1992). These empirical correlations are suitable for the prediction of coal burning under pulverized coal conditions in utility boilers: gas temperatures over 1500 K, particle diameters in the range from 75 to 200 μm and oxygen partial pressures over 0.03 bar. Furthermore, the ash inhibition sub-model introduces an additional diffusion resistance to account for the inhibitory effect of ash on char oxidation, introducing two new parameters: the critical ash porosity and the minimum ash film thickness (Hurt and Sun, 1998). All the expressions used in the combustion model are summarized in Chapters 2 and 3.

It is necessary that the coal combustion model be combined with a particle transport calculation. A Lagrangian approach has been chosen, considering the influence of a diluted particle phase on the fluid flow, two-way coupling (Sommerfeld, 2000). Interactions between particles have been neglected. The total mass flow of particles has been modelled by tracking 1920 trajectories, assuming that each simulated particle represents a sample of the real number of particles.

The thermal radiation in the furnace is the dominant heat transfer mechanism due to the presence of a mixture of participative gases and particles at high temperature. The radiative heat transfer has been modelled using the Discrete Transfer method (Lockwood and Shah, 1981) which solves a transport equation for the radiation intensity along paths between two boundary walls. For simplicity, a grey gas model is considered to evaluate the properties of the gas phase, considering a constant value for the absorption coefficient over the whole wavelength spectrum. The influence of the particles, also participating in the radiative heat transfer, is accounted for by including a specific heat source in the energy conservation equation.

A summary of the combination of models used for performing the CFD simulation of the case-study boiler was shown in Table 3.2 (Chapter 3).

4.2.3 Boundary conditions

Once the models have been presented, the required boundary conditions to solve the problem are set below (Versteeg and Malasekera, 1995):

1. Fluid boundaries:

- Inlets:

The continuous phase (gas stream) was defined by the normal and angular components of velocity. The normal component was calculated from the mass flow, inlet section and primary air temperature, under an ideal gas assumption. The angular component was calculated from the burner geometry (Basu et al., 2000). Furthermore, inlet flow temperature, turbulence intensity and the dissipation length scale were also defined. Radiation related properties were defined in terms of emissivity, specular roughness and radiation temperature. The particles' phase was defined by the coal mass flow, a Rosin Rammler size distribution and the inlet velocity which coincides with the one defined for the flow, since the particles phase is diluted in the gas stream.

- Outlets:

Open boundary conditions were assumed at the outlet: $\frac{\partial u_n}{\partial n} = 0$ and $\frac{\partial T}{\partial n} = 0$. Radiation related properties were defined again in terms of emissivity, specular roughness and radiation temperature.

2. Walls:

At the walls, a no slip condition and logarithmic profiles (wall functions) for velocity were defined in order to adequately represent turbulence in the near wall region. Radiation boundary conditions were set considering a wall temperature 50 K higher than the saturation temperature of the steam flowing inside the boiler tubes and assuming diffuse reflection with an emissivity value of 0.8.

4.2.4 Verification and validation

Verifying and validating the numerical simulation was carried out according to the methodology described in Chapter 3. Firstly, the verifying process was performed by determining the numerical error of the CFD simulation. The numerical error, δ_{SN} may be separated into three contributions (Eq. 4.1): an error due to the iterative method δ_I, an error due to the spatial domain discretization δ_M, and an error due to the time discretization δ_T.

$$\delta_{SN} = \delta_I + \delta_M + \delta_T \qquad \text{(Eq. 4.1)}$$

- Error due to the iterative method δ_I: The minimum convergence criteria were established through the numerical resolution method itself as follows:

- Transport equations residues < 1 E-4
- Continuity equation error < 1 E-2
- Variation of a control variable < 1 E-2

This way, the error is bounded and may be considered negligible ($\delta_I \approx 0$).

- Spatial discretization error δ_M: To define a proper mesh size in the domain we carried out a progressive refinement of the mesh studying the convergence in the solution. To achieve this, three grid sizes (fine, medium and coarse) were considered, with a size relation, $r_k = \sqrt{2}$ defined by Eq. 4.2.

$$r_k = \Delta x_{ki} / \Delta x_{kj} \qquad \text{(Eq. 4.2)}$$

Mesh size	x	y	z
Fine	56	38	46
Medium	40	26	32
Coarse	28	19	24

Table 4.2 Number of elements in the burner's belt region in every direction for the three mesh structures considered

Generally, a key variable (velocity, temperature, etc.) determined at a point or within a domain region is used as a control variable for convergence. In this work, since the goal of the study is to develop an unburned carbon predictive system, we have selected burnout (% coal basis) as control variable, establishing the convergence criteria for its variation of 0.1 %. In this way, a medium mesh size structure proves to be adequate for our problem, and consequently, this was used in the simulations.

- Time discretization error, δ_T: Since this problem was assumed stationary, this error term was neglected.

Once the numerical error of the simulation was bounded the validation process was carried out to determine the modelling error. The modelling error, δ_S may also be separated into three contributions (Eq. 4.3): an error due to the numerical resolution method δ_{SN}, an error due to experimental data uncertainties δ_{SDP}, and an error due to the hypothesis and assumptions of the mathematical models δ_{SMA}.

$$\delta_S = \delta_{SMA} + \delta_{SDP} + \delta_{SN} \quad \text{(Ec. 4.3)}$$

The numerical error δ_{SN} has been already defined at the verifying stage. With regard to the other contributions, the error corresponding to the experimental data may be determined from the precision of the plant instrumentation and the accuracy of the data gathering process. Whilst the models assumptions' error may be determined by comparing experimental data against simulated results, taking into account the previous calculated errors.

Since, the sensitivity study in this work analyzes unburned carbon formation trends with the variation of boiler conditions, a comparison of experimental data against simulated results is enough to validate the simulations. Aside from the main validation of the target prediction of this work (unburned carbon in ash level), additional verifications of the furnace simulation accuracy are highly desirable. Unfortunately, the available instrumentation in the case-study boiler does not allow a detailed validation, just limiting it to the prediction of the oxygen content in flue gases. In fact, this is a common situation in large-scale utility boilers which are conventionally instrumented for control and safe operation purposes but not for undertaking accurate thermal calculations. Moreover, the aggressive environment of high temperatures and ash particles in the furnace makes the insertion of long-term durable measurement probes unfeasible in most cases, thus, restricting the available on-line information to very few gas temperature and oxygen samples at the cold exit of the boiler convective section.

4.3 Sensitivity study

The aim of the sensitivity study is to determine the real influence of different parameters on unburned carbon formation. This way, it will be possible to lay down the guidelines to correct and minimize this loss. Additionally, in order to develop an unburned carbon predictive system, this study allows us to identify which parameters should be included in the final model from their relevance.

The main parameters analyzed in this work are set out below:

1. Primary air to coal mass flow ratio (keeping constant the total air mass flow): This relationship is set by adjusting the milling system operation. Firstly, the primary air is responsible in starting combustion, creating a recirculation area in the near burner region which provides the heat release needed to ensure a constant ignition source.

2. Excess air (stoichiometry): Excess oxygen at the exit of the boiler is a common control signal in power plants which is modified by varying the air mass flow driven by the forced-draft fans. Since coal combustion depends directly on oxidant partial pressure, its influence on carbon burnout usually represents the most important contribution.

3. Particle size: Particle size distribution is also determined by the milling system operation, through the milling pressure, the classifier position and the ageing of the grinding pieces. In general, larger particles result in longer combustion times, increasing unburned carbon levels.

4. Secondary air swirl intensity (rotation index): Swirl intensity is modified by varying the position of the burner vanes that guide the entrance of the secondary air from the wind box. High swirl numbers intensify the secondary air rotation which results in an enhancement to the primary and secondary air mixing and consequently combustion. Furthermore, it stabilizes the flame. Swirl intensity, n_{sw}, usually called swirl number, is defined as the quotient of the fluid angular moment M, and the fluid axial moment K multiplied by a characteristic length L_c (i.e. hydraulic diameter) (Basu et al., 2000) (Eq. 4.4).

$$n_{sw} = \frac{M}{K \cdot L_c} = \frac{U_t \cdot r}{U_k \cdot L_c} \qquad \text{(Eq. 4.4)}$$

5. Fuel/air mass flow imbalances through the burners: This situation may respond either to an operational order, or to a deficient design of the ducts that connect the mills with the burners. As a result of this, there may exist different flow patterns in the boiler that may lead to interactions amongst the burner flames or to an alteration of the particles' trajectories each of which has a large effect on the combustion process (Lockwood and Parodi, 1998).

To study the influence of these parameters we have carried out 64 CFD simulations with operating data provided by ASM Brescia power plant. Some of the simulations do not correspond with the regular operational conditions of the plant. The reason being is that this way we will be able to analyze these parameters under conditions outside the optimal design conditions. The first 32 simulations studied the contribution of each factor to the final unburned carbon level while keeping the rest of the parameters constant. Next, with the most relevant factors, the other 32 CFD simulations are carried out to evaluate cross-related effects and the interactions amongst them.

Once the simulations have been performed, unburned carbon in ash is calculated by computing the trajectories of the particles obtained from the CFD code. The code generates an output file which contains the local position, velocity, time, temperature, diameter, mass, etc., for every particle at any cell it passes through. At the same time, after a complete iteration (flow and particles), the code gives the total amount of volatiles and char product yield to the gas phase. Since volatiles are completely transferred to the gas phase, the total amount of carbon losses can be calculated from the final mass of the particles that leave the flow domain, assuming that they are exclusively formed by carbon and ash.

4.3.1 Individual parameters sensitivity study

To carry out the sensitivity study of individual parameters, we have established a master case simulation (Case 1), which corresponds to nominal-load conditions from the study boiler. The reference coal used in the whole study has been Guasare (Table 4.1). Table 4.3 summarizes boiler conditions used in the base case simulation (Case 1).

Operating conditions		
Natural gas	0	m^3/s
Coal load *Total*	7.08	kg/s
Per mill / per burner	3.61/1.805	"
Total air mass flow in the boiler	93.119	kg/s
Primary air mass flow	14.319	kg/s
Secondary air	78.8	kg/s
Mass flow percentage of coal through each burner	25	%
Primary air/coal mass flow ratio	1.98	kg air/kg coal
Excess air at the exit of the boiler	37	%
Excess oxygen at the exit of the boiler	5.5	% (w.b.)
Primary air temperature	80	ºC
Secondary air temperature	260	ºC

Table 4.3 Nominal-load operating scenario from the case-study power plant (Base Case)

To characterize the particle size sieve fractions provided by the plant, we have made use of a Rosin Rammler distribution with parameters d_{pm}= 50 μm and n_{rr} = 1.02. This distribution has been split up into ten intervals which contain the same coal mass flow. Table 4.4 shows the mean diameters that represent each size interval considered.

Cases 2 to 32 simulate variations in the conditions of a single parameter with respect to the base case (Case 1) (Table 4.5).

Interval	Accumulative %	Mean diameter (μm)
0 – 10 %	5 %	2.5
10 – 20 %	15 %	7.7
20 – 30 %	25 %	13.6
30 – 40 %	35 %	20.1
40 – 50 %	45 %	27.9
50 – 60 %	55 %	36.9
60 – 70 %	65 %	48.3
70 – 80 %	75 %	63.4
80 – 90 %	85 %	86.2
90 – 100 %	95 %	134.9

Table 4.4 Particle size distribution (Case 1)

Case nº	Description	Incidence	Base Case (Case 1)
2	Primary air/coal mass flow ratio	Qpa/Qcoal = 3	Qpa/Qcoal = 2
3		Qpa/Qcoal = 2.5	
4		Qpa/Qcoal = 2.25	
5		Qpa/Qcoal = 1.75	
6		Qpa/Qcoal = 1.5	
7	Excess oxygen	$\%O_2 = 7$	$\%O_2 = 5.5$
8		$\%O_2 = 5$	
9		$\%O_2 = 4.5$	
10		$\%O_2 = 4$	
11		$\%O_2 = 3$	
12	Mean particle diameter (Rosin Rammler distribution)	Mean diameter[2] = 60μm	Mean diameter = 50μm
13		Mean diameter[2] = 80μm	
14		Mean diameter[2] = 100μm	
15	Swirl Intensity (swirl number)	Swirl = 2	Swirl = 1
16		Swirl = 3	
17	Primary air mass flow imbalances through burners of the same row; that is, through burners feed from the same mill	Burner 1, 4 = 47.5%, Burner 2,3 = 52.5%	Burner 1, 2, 3, 4 = 25%
18		Burner 1, 4 = 45%, Burner 2,3 = 55%	
19		Burner 1, 4 = 42.5%, Burner 2,3 = 57.5%	
20		Burner 1, 4 = 40%, Burner 2,3 = 60%	
21		Burner 1, 3 = 47.5%, Burner 2,4 = 52.5%	
22		Burner 1, 3 = 45%, Burner 2,4 = 55%	
23		Burner 1, 3 = 42.5%, Burner 2,4 = 57.5%	
24		Burner 1, 3 = 40%, Burner 2,4 = 60%	
25	Primary air mass flow imbalances through mills; but identical, through burners feed from the same mill	Mill 1 = 60%, Mill 2 = 40%	Mill 1, 2 = 50%
26		Mill 1 = 40%, Mill 2 = 60%	
27		Mill 1 = 57.5%, Mill 2 = 42.5%	
28		Mill 1 = 42.5%, Mill 2 = 57.5%	
29		Mill 1 = 55%, Mill 2 = 45%	
30		Mill 1 = 45%, Mill 2 = 55%	
31		Mill 1 = 52.5%, Mill 2 = 47.5%	
32		Mill 1 = 47.5%, Mill 2 = 52.5%	

Table 4.5 Sensitivity analysis simulations plan

[2] Rosin Rammler distribution

d_{pm}	n_{rr}	< 75 μm (%)	75 – 150 μm (%)	150 – 300 μm (%)	> 300 μm (%)
60	1.02	71.51	20.65	7.27	0.57
80	1.02	60.79	24.23	12.86	2.13
100	1.02	52.56	25.40	17.38	4.66

Figure 4.5 shows a scheme of mills and burners' disposition with the numbering followed in this work. Mill 1 feeds the upper row of burners, with burner 1 on the left hand side and burner 2 on the right hand side (looking head on to the boiler from the outside). In the same way, Mill 2 feeds the lower row burners, with burner 3 on the left and burner 4 on the right.

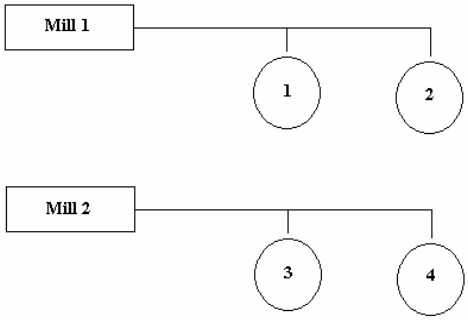

Fig. 4.5 Mills and burners disposition scheme (ASM, Brescia)

Validation of the simulations has been performed according to the methodology explained in Section 4.2.4. Thus, once the accuracy of the numerical resolution has been verified, we have proceeded with the validation. For that purpose, the oxygen values at the exit of the boiler obtained in the simulations are compared against the predetermined values for each case. Figure 4.6 shows the results obtained that allow us to accept the accuracy of the simulation.

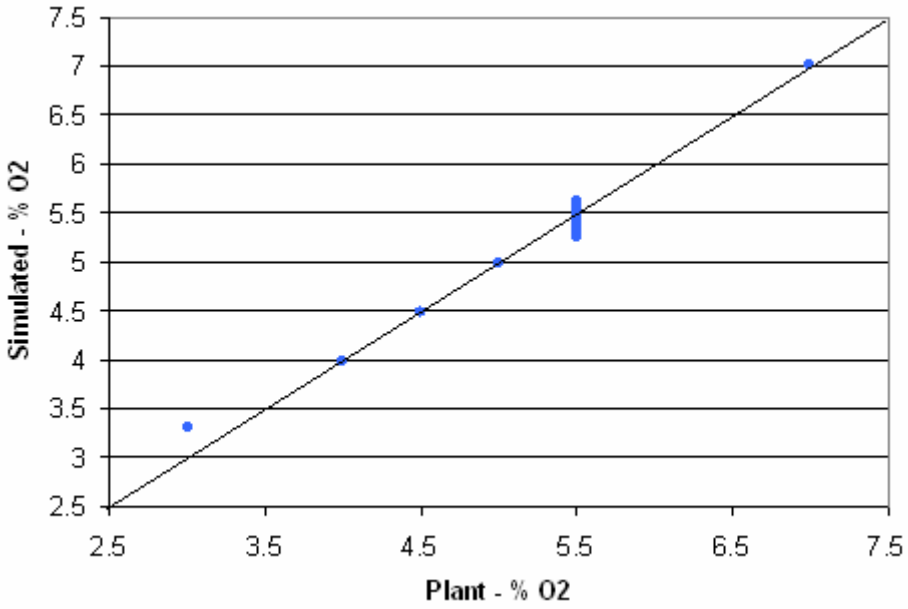

Fig. 4.6 Simulated % O_2 vs. Plant % O_2

After solving Case 1, an unburned carbon in ash value of 7.08 % was obtained. This result itself, does not give any relevant information. Moreover, it cannot be compared with a punctual

estimation of the carbon-in-ash value at the plant since averaged values have been used in the simulated scenarios. It should be remembered that at this point the aim of the study is to determine the sensitivity of different factors to unburned carbon formation and not the precise calculation for the existing conditions. This task will be carried out in Chapters 6 and 7, during the combustion model and the unburned carbon predictive system validations respectively. However, analyzing the results for all the simulations as a whole, their influence on unburned carbon losses can be investigated. Next, the results of the individual analysis for these factors are presented (Base case is represented with a circle in figures):

1. Primary air/coal mass flow ratio (keeping constant the total air mass flow):

Cases 2 to 6 analyze the variation in the primary air to coal mass flow relation, when the total air supply (primary and secondary air) remains constant. Figure 4.6 shows that Case 1, in which the primary air to coal mass flow ratio was set to 2, is the most advantageous scenario with respect to unburned carbon losses. This result was expected since under nominal-load conditions it corresponds to the design ratio. Lower ratios result in an increase of the unburned carbon losses since decreasing the primary air mass flow results in a poor stoichiometry in the near burner area where combustion starts.

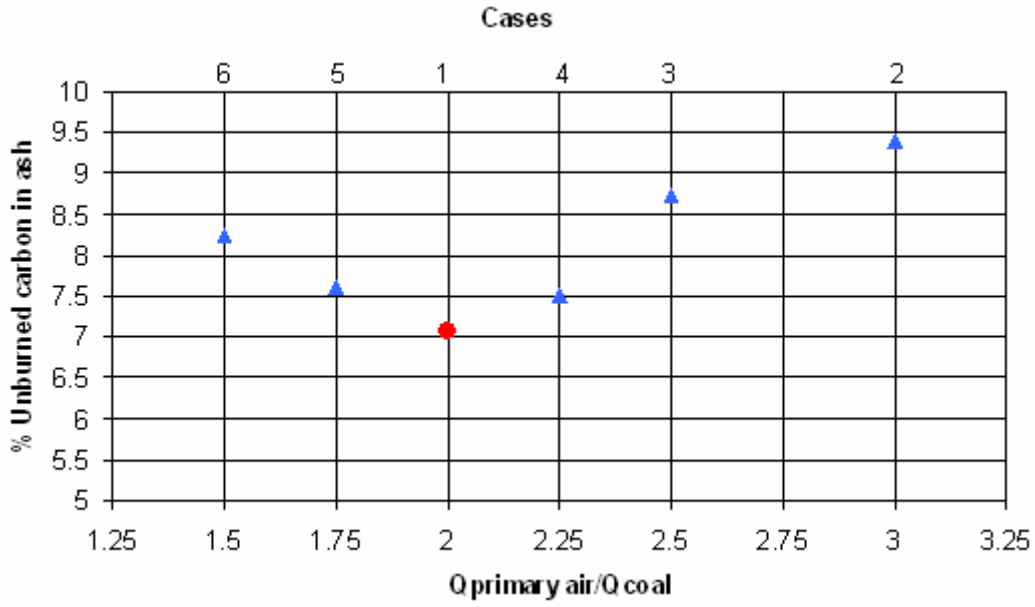

Fig. 4.7 % Unburned carbon in ash vs. Primary air to coal mass flow ratio

Higher ratios also result in an increase of the unburned carbon losses since reducing the secondary air mass flow, the outer recirculation loop intensity is reduced which causes a decrease in the primary and secondary air mixing effectiveness and as a consequence a lower peak combustion temperature. This parameter, as it will be seen later from the multi-parameter

analysis, is highly correlated with the excess oxygen level and its relevance under some particular operating conditions may be greater than other apparently more influential factors.

2. Excess air level (stoichiometry):

Cases 7 to 11 analyze the variations in the excess air level. In general, in power plants the oxygen excess level is used as a control signal to adjust the air flow for a given coal load, operating over the primary and/or secondary air forced-draft fans. In the simulation, in order to keep constant the primary air to coal mass flow ratio, the variation in the air supply to the boiler is obtained through the variation in the secondary air. Figure 4.8 suggests a great influence of this factor, mainly for excess oxygen levels below 4 %.

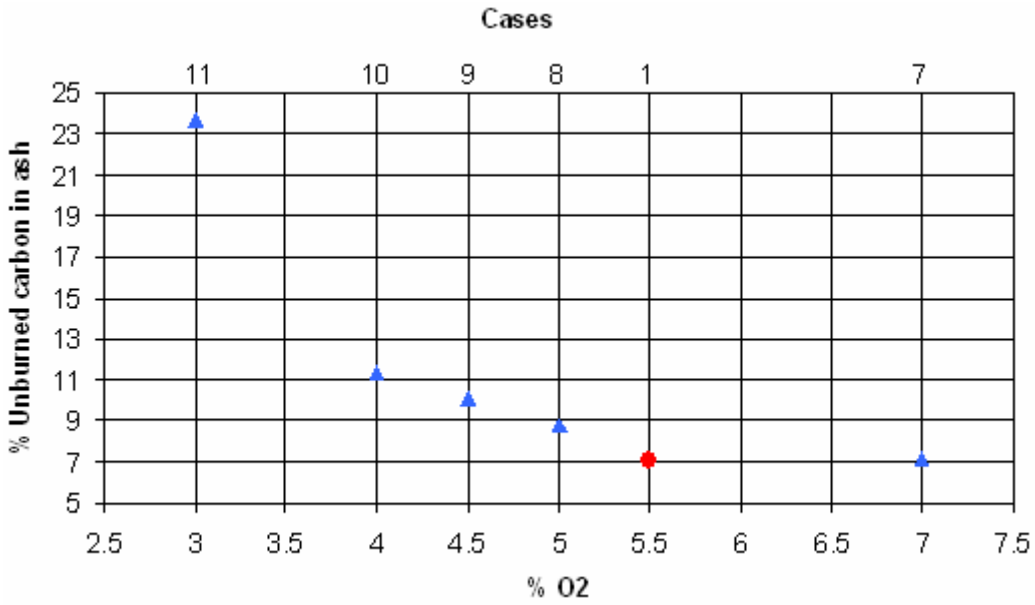

Fig. 4.8 % Unburned carbon in ash vs. Excess O_2

3. Particle size:

Cases 12 to 14 analyze the variations in particle size. In general, for a given coal mass flow, by increasing the mean size of the particle distribution the total surface area exposed to the oxidant is reduced resulting in an increase of the combustion time and of the unburned carbon level. In power plants, particle size is adjusted modifying the mechanical action of the grinding pieces and adjusting the mills' classifiers. Figure 4.9 shows a linear increase of unburned carbon in ash with particle size. It is also noticeable that the influence of this factor is greater than the primary air to coal mass flow ratio, while much less relevant than the excess oxygen level. In spite of this fact, as it will be seen in the multi-parameter study, particle size is generally not as significant as other study factors in unburned carbon formation under regular pulverized fuel conditions (d_{pm} < 100 μm).

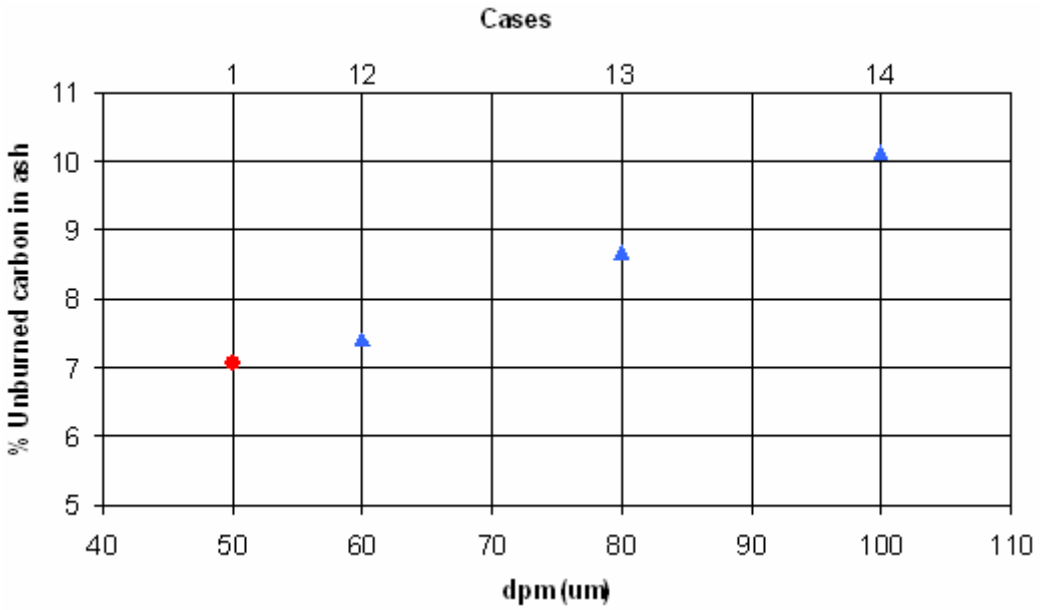

Fig. 4.9 % Unburned carbon in ash vs. Mean particle size Rosin Rammler distribution (μm)

4. Secondary air swirl intensity (rotation index):

Cases 15 to 16 analyze the variation in the secondary air swirl intensity. Increasing the swirl intensity enhances turbulence and mixing in the outer recirculation that surrounds the primary air flow stream thereby improving combustion and flame stability. However, there exists a limit. If rotation intensity is very strong, the secondary air may distort the internal recirculation in front of the burner, affecting flame stability and primary and secondary air mixing.

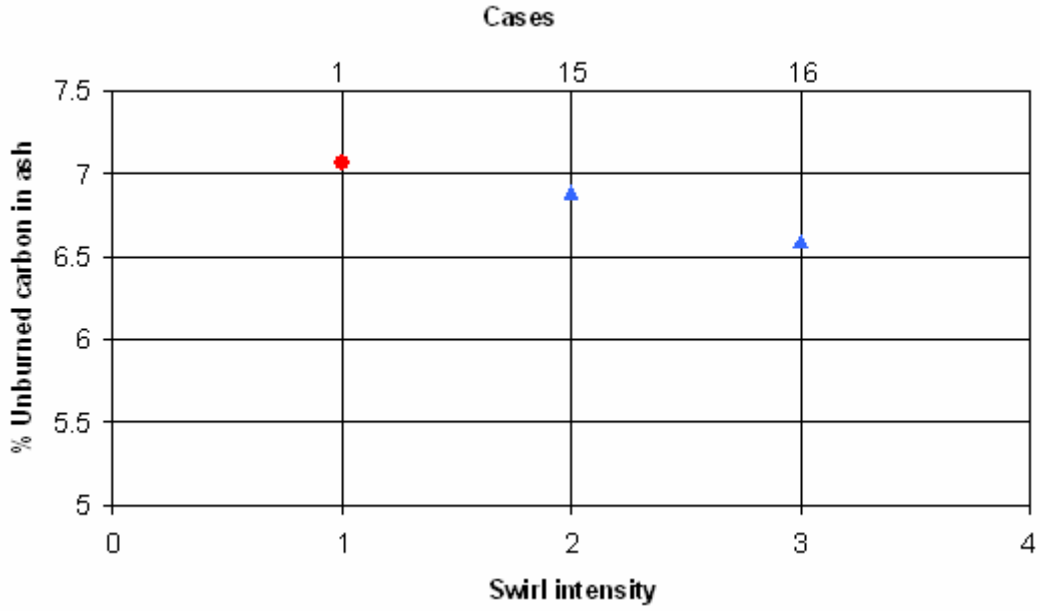

Fig. 4.10 % Unburned carbon in ash vs. Swirl intensity (swirl number)

Figure 4.10 suggests a slight decrease in the unburned carbon in ash level with decreasing swirl intensity. Finally, it is noteworthy that, since earlier burners were designed to obtain high

mixing rates while maintaining flame stability, nowadays new burner solutions look for a gradual mixing which may reduce NO_x formation even at the expense of increasing unburned carbon.

5. Fuel/air mass flow imbalances through burners:

Cases 17 to 32 analyze the influence of the fuel/air mass flow imbalances through the burners on unburned carbon losses:

- Mass flow imbalances through burners fed from different mills (configurations 1 and 2, Cases 25-32). This situation may take place as a result of:

  - A full load operating strategy (configuration 1), to reduce NO_x emissions, creating a reduced atmosphere in the lower level of burners and an oxidizing atmosphere in the upper level.

  - A partial load operating strategy (configuration 2), to reach high enough temperatures in the upper section of the boiler that permits an adequate steam production.

  This situation may be also caused by an operation problem within the mills.

- Mass flow imbalances through burners fed from the same mill (configurations 3 and 4, Cases 17-24). This situation may take place as a result of:

  - A fault design (initially or as a consequence of a modification or damage in the plant, etc.) of the ducts that transport the primary air and coal from the mills to the burners.

Two different configurations for each imbalance situation have been considered simulating uneven mass flow distribution variations in the range 0 to 10 %. Figure 4.11 shows the four simulated configurations, where the symbol "+" indicates that the higher mass flow is fed from this burner and the lower mass flow is fed from the burners marked with the symbol "-". For example, assuming a coal load of 10 kg/s and a mass flow imbalance of 10 % for a configuration type 1, the coal mass flow distribution through the burners would be as follows: since in a configuration type 1 the mass flow imbalance takes places through the mills (the burners fed from the same mill have identical mass flow distribution), instead of giving 50 % of the total mass flow to each mill, the mill that feeds the upper row of burners (see burners with symbol "-") gives only 40 % of the total, while the mill that feeds the lower row of burners (see burners with symbol "+") gives 60 % of the total. Therefore, the upper row of burners (burners

1 and 2 in Figure 4.5) feed 2 kg/s each, and the lower row burners (burners 3 and 4 in Figure 4.5) feed 3 kg/s each. In the same way, the coal mass flow distribution for the other configurations are obtained (Table 4.5).

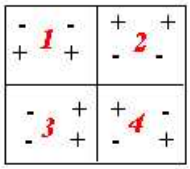

Fig. 4.11 Diagram depicting the four different simulation configurations

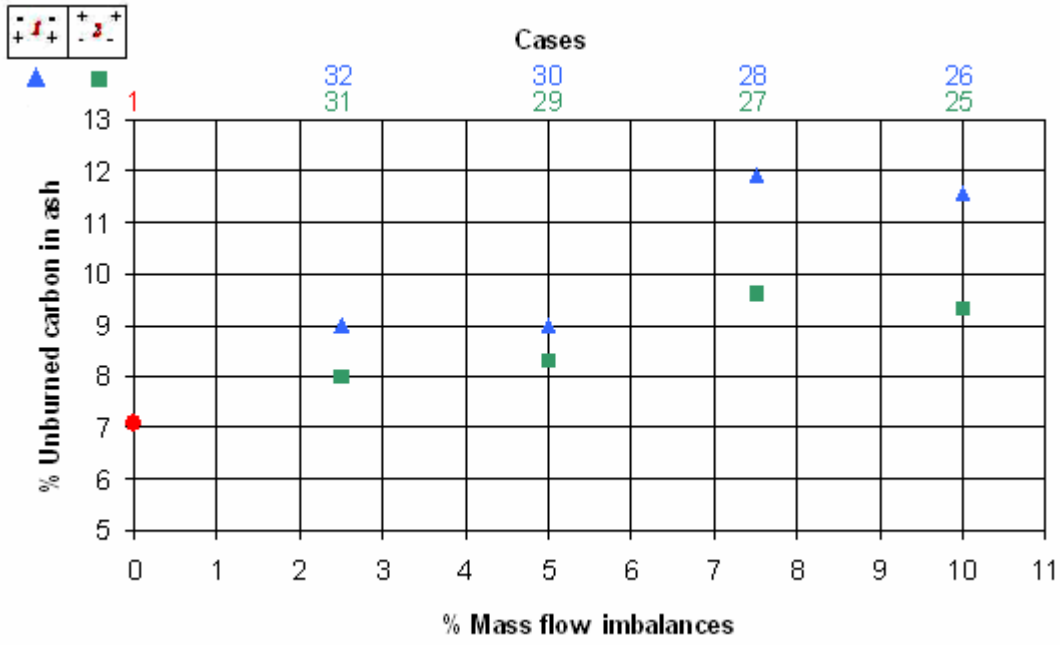

Fig. 4.12 % Unburned carbon in ash vs. % Mass flow imbalances (Config. 1 and 2)

Figure 4.12 shows the results for configurations 1 and 2. The first noticeable result is that increasing the imbalance level, the unburned carbon losses increment is comparable to that obtained when increasing the mean particle size over 100 μm. This result suggests the importance of these flow asymmetries in the operation of the boiler. Another remarkable and surprising result is that the unburned carbon level is higher with configuration type 1 than with configuration type 2. Since in configuration 2 most of the coal is fed through the upper row of burners in which the particles' residence times are lower, we would expect the opposite result. To explain this, we should fall back on the special behaviour of the lower row of burners, from which the particles' trajectories are largely affected by a recirculation loop in the bottom hopper region (Figure 4.13). In addition to this reversed-flow region, the interactions between the inlet flows from neighbouring burners and interactions with the confining walls are significant

enough to noticeably distort the coal particles' trajectories, modifying the oxygen-temperature history of the particles and thus coal burnout behaviour. To conclude, as it will be confirmed from the factorial analysis in the next section, this surprising result only takes place when the boiler is operated under high excess oxygen conditions. In the case of operating under low excess oxygen conditions, in spite of the fact that there is a distortion in the particles trajectories since the oxygen level is lower and the particles fed from the upper row of burners have shorter residences times, the higher unburned carbon losses are encountered in configuration 2.

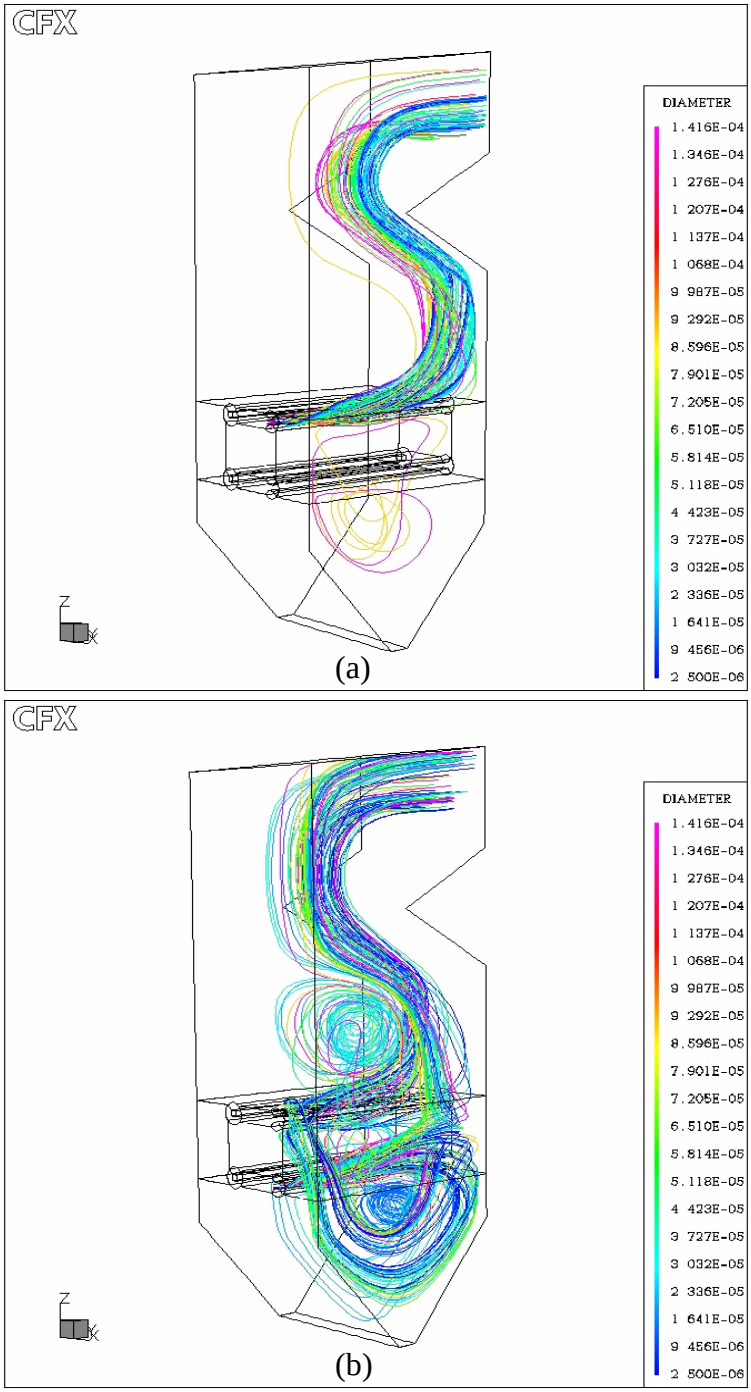

Fig. 4.13 Predicted particles' trajectories tracked from different inlets: upper row (a) and lower row (b)

Figure 4.14 shows the results for configurations 3 and 4. These results suggest a remarkable increment of the unburned carbon loss as the mass flow imbalances increase. This situation is specially marked for configuration 3, where the flow asymmetry is complete in the full boiler.

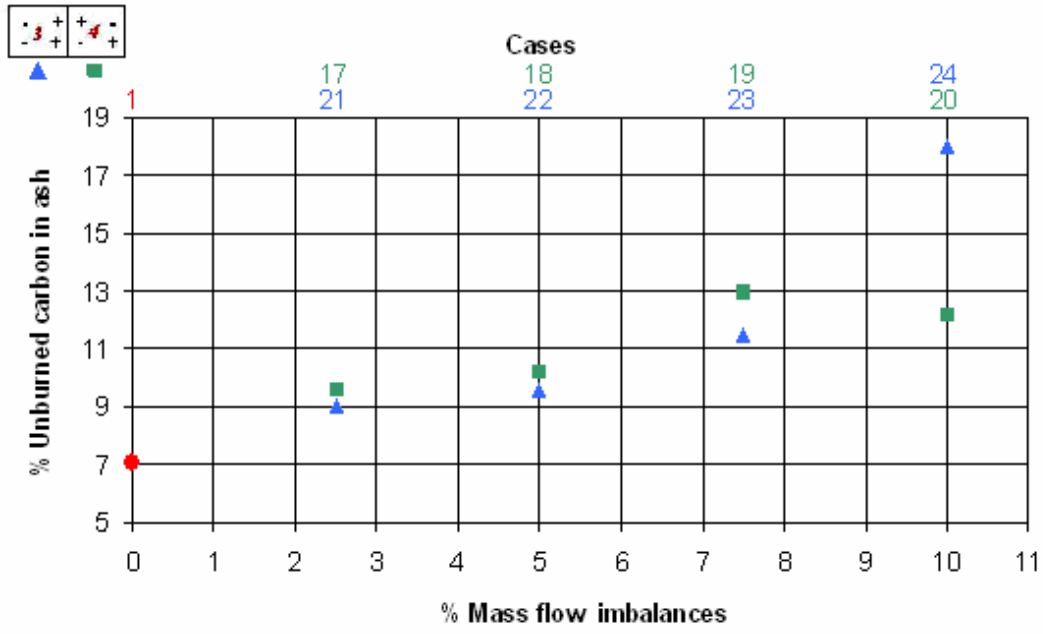

Fig. 4.14 % Unburned carbon in ash vs. % Mass flow imbalances (Config. 3 and 4)

For the moment, we have analyzed individual contributions of the study-factors. Now it is possible to establish a preliminary comparison of the relative influence of the study factors as shown in Figure 4.15. The dashed line in the figure represents the reference unburned carbon level of the base case (Case 1).

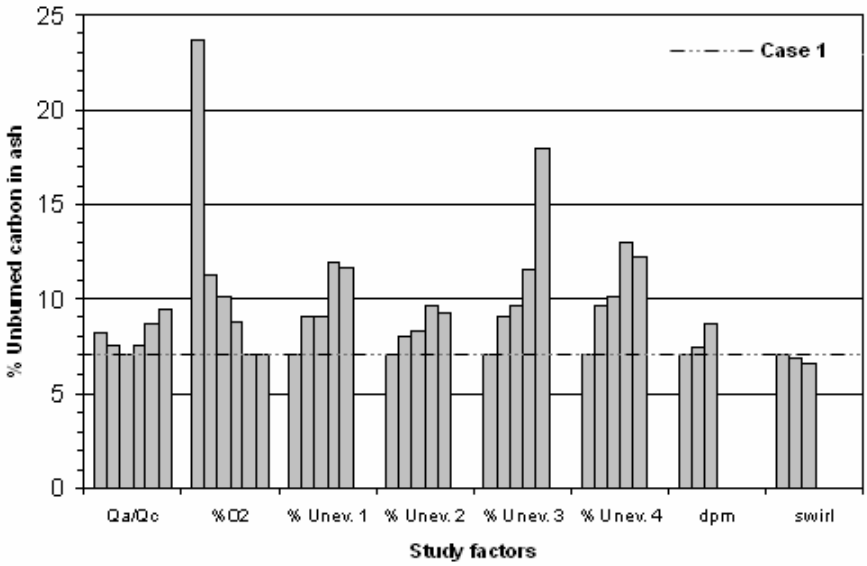

Fig. 4.15. Unburned carbon level for all the study-factors and scenarios

Figure 4.15 suggests that the oxygen level is the most relevant factor in unburned carbon formation, especially for excess oxygen values under 4 %. However, the rest of the factors, such as: mass flow imbalances, particles' size and primary air to coal mass flow ratio, may turnout to be relevant for excess oxygen values over 4 %. In spite of these general results, in a real power plant all these factors take place simultaneously. The next part of the study is focused on the analysis of cross-related effects and interactions amongst these factors.

4.3.2 Multi-parameter sensitivity study

The individual parameter sensitivity study has shown that many factors affect carbon burnout. In real utility boilers these factors do not take place individually and their interaction may have an important influence on the total unburned carbon. Since it is not easy to differentiate individual contributions and interactions of these factors, an efficient experimental design may reduce the number of scenarios required to complete the study. A factorial experiment is an experiment which extracts information on several design factors more efficiently than can be done by a traditional test. The main objective is to determine the effect of various factors of interest. Analysis of variance is a powerful technique for analysing experimental data involving quantitative measurements. It is particularly useful in factorial experiments where several independent sources of variations may be present. When several sources of variation are acting simultaneously on a set of observations, the variance of the observations is the sum of the variances of the sources. This property makes the application of the analysis of variance particularly useful in factorial experiments. By this method, the total variation within an experiment can be broken down into variations due to each main factor, interacting factors and residual error. The significance of each variation is then tested and variables other than those investigated should be properly controlled. The choice of a factorial analysis has several important features. First, it minimizes the number of experiments needed to be carried out and it has a great flexibility. Second, factorial designs are efficient so instead of conducting a series of independent studies we are effectively able to combine these studies into one. Finally, factorial designs are the only effective way to examine interaction effects (Lipson and Sheth, 1977; Montgomery, 1991).

Two levels of the most influential factors have been selected for the factorial analysis (see Figure 4.16). From the individual parameter sensitivity study in Section 4.3.1, swirl intensity has been excluded from the analysis. The remaining factors are classified in five groups as follows:

- A – Primary air mass flow to coal mass flow ratio

- B – Excess O_2 (%)
- C – Particle size distribution
- D – Mass flow imbalances (%)
- E,F – Four different imbalance mass flow configurations

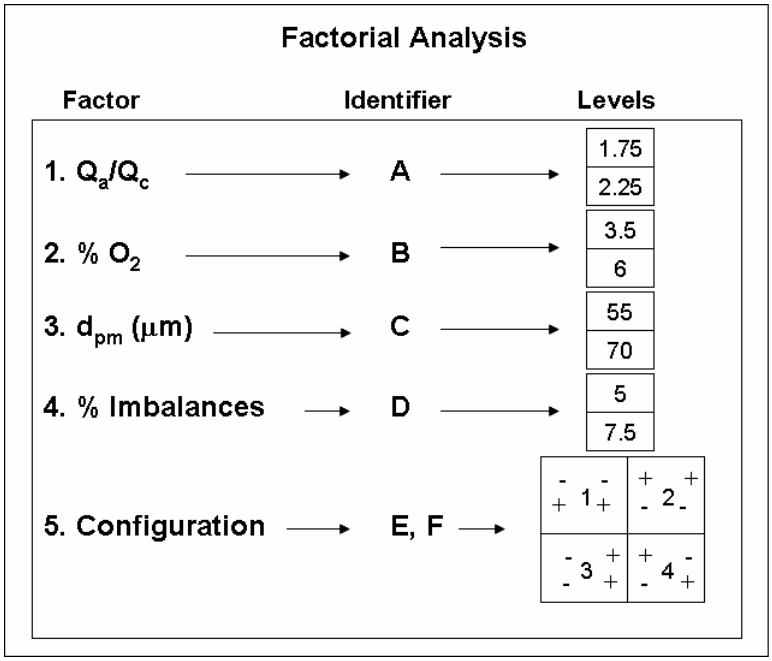

Fig. 4.16 Multi-parameter factorial analysis design

The total number of tests required for a full experiment is 64 simulations (2 x 2 x 2 x 2 x 4 → 64). However, in order to reduce the number of simulations, and thus, the computational cost for this task, a fractional factional analysis has been applied. This requires testing only a fraction of the total number of possible test combinations. This fraction is the representative test combination carefully selected from the total test combinations. Fractional factorial experiments cannot produce as much information as the full factorial experiment. However, economy is achieved at the expense of assuming that some of the interactions between factors are negligible. Later, if any of the rejected interactions turns out to be relevant, it is possible to include additional scenarios until reaching, if it is necessary, the full factorial experiment. The fractional analysis design in this work is formed by simulating 32 scenarios (2^{4-1} x 4 → 32) and selecting two levels of the most influential factors. To achieve a maximum resolution design we have chosen a generation function I = ABCD (Montgomery, 1991). Then, we have built the basic design corresponding to a configuration 2^3 for the factors A, B and C, where the labels "-1" and "+1" indicate the lower and the higher level of the factor considered, respectively. The fourth factor D, is found from the generation function I = ABCD, resulting in D = ABC. Therefore, the level of the D factor is the product of the positive and negative signs in the

columns A, B and C. Finally, two additional E and F factors are included whose combinations "-1 -1", "+1 -1", "-1 +1" and "+1 +1" correspond to the imbalances in configurations 1, 2, 3 and 4, respectively (X factor). Table 4.6 summarizes the fractional design of experiments.

Scenario	Treatment	A	B	C	D	E	F	X = E x F
1	(1)	-1	-1	-1	-1	-1	-1	1
2	e	-1	-1	-1	-1	1	-1	-1
3	f	-1	-1	-1	-1	-1	1	-1
4	ef	-1	-1	-1	-1	1	1	1
5	ab	1	1	-1	-1	-1	-1	1
6	abe	1	1	-1	-1	1	-1	-1
7	abf	1	1	-1	-1	-1	1	-1
8	abef	1	1	-1	-1	1	1	1
9	ac	1	-1	1	-1	-1	-1	1
10	ace	1	-1	1	-1	1	-1	-1
11	acf	1	-1	1	-1	-1	1	-1
12	acef	1	-1	1	-1	1	1	1
13	ad	1	-1	-1	1	-1	-1	1
14	ade	1	-1	-1	1	1	-1	-1
15	adf	1	-1	-1	1	-1	1	-1
16	adef	1	-1	-1	1	1	1	1
17	bc	-1	1	1	-1	-1	-1	1
18	bce	-1	1	1	-1	1	-1	-1
19	bcf	-1	1	1	-1	-1	1	-1
20	bcef	-1	1	1	-1	1	1	1
21	bd	-1	1	-1	1	-1	-1	1
22	bde	-1	1	-1	1	1	-1	-1
23	bdf	-1	1	-1	1	-1	1	-1
24	bdef	-1	1	-1	1	1	1	1
25	cd	-1	-1	1	1	-1	-1	1
26	cde	-1	-1	1	1	1	-1	-1
27	cdf	-1	-1	1	1	-1	1	-1
28	cdef	-1	-1	1	1	1	1	1
29	abcd	1	1	1	1	-1	-1	1
30	abcde	1	1	1	1	1	-1	-1
31	abcdf	1	1	1	1	-1	1	-1
32	abcdef	1	1	1	1	1	1	1

Table 4.6 Fractional factorial analysis design 2^{4-1} x 4

From the interpretation of the identifiers and the level assigned to each factor in Table 4.6, Table 4.7 summarizes the conditions for the simulations and carbon in ash value results for each scenario (shaded cells).

	Qa/Qc		%O2		dp (μm)		% Imbalances		Configuration				% CIA
	1.75	2.25	3.5	6	55	70	5	7.5	1	2	3	4	
1													13.02
2													28.29
3													27.57
4													16.69
5													8.01
6													7.13
7													10.19
8													6.78
9													22.51
10													32.02
11													27.03
12													23.56
13													23.81
14													40.73
15													34.78
16													27.38
17													14.89
18													8.72
19													8.67
20													13.01
21													11.43
22													6.57
23													10.73
24													8.95
25													15.06
26													25.01
27													29.93
28													16.19
29													6.99
30													6.46
31													11.26
32													6.16
MC	Qa/Qc = 2		% O2 = 5.5		dp = 50 um		% Imbalance = 0						7.08

Table 4.7 Conditions for the simulations of the factorial analysis design (MC → Master Case)

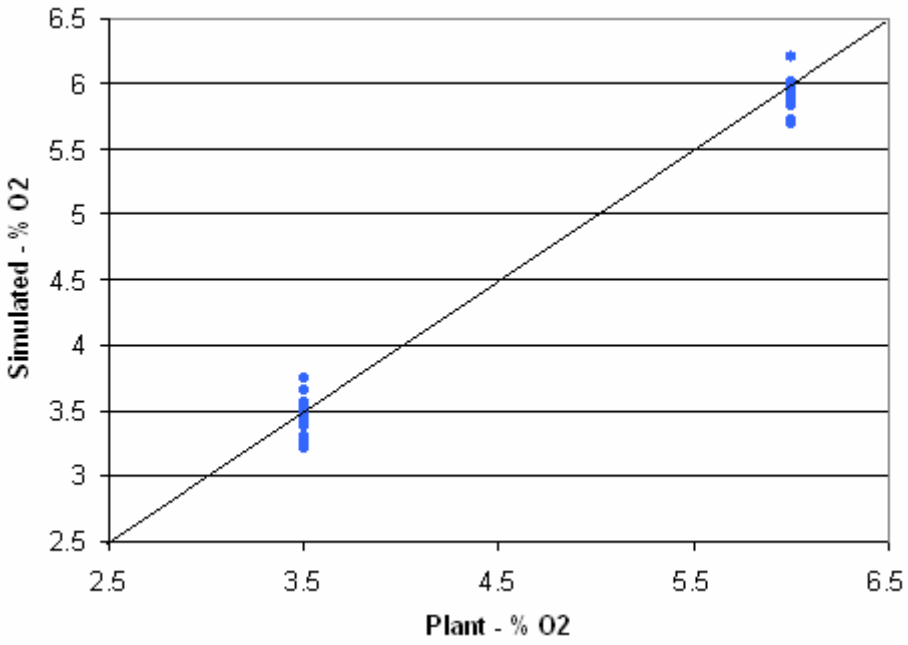

Fig. 4.17 Simulated % O_2 vs. Plant % O_2

Validation of the simulations has been performed according to the methodology explained in Section 4.2.4. Once the accuracy of the numerical resolution has been verified we have proceeded with its validation. For that purpose, the oxygen values at the exit of the boiler

obtained in the simulations are compared against the predetermined values for each case. Figure 4.17 shows the results obtained and allow us to accept the suitability of the simulation.

To analyze the influence of the study-factors, we have carried out a variance analysis of the results. An unbiased estimator for the total variance in the data set is the sum of squares (SSi). Since we have performed a fractional analysis, the resulting effects obtained from the study are the main effect plus a linear combination of the observed interactions related to this effect, which is assumed negligible (Table 4.8).

Effect	Real Effect
A	A + BCD ≈ A
B	B + ACD ≈ B
C	C + ABD ≈ C
D	D + ABC ≈ D
AB	AB + CD
AC	AC + BD
BC	BC + AD

Table 4.8 Estimated effects (Real) in a fractional analysis 2^{4-1}

One of the main conclusions of the individual parameter sensitivity study was that an excess oxygen level was the most influential factor, independent of the other factors. Carrying out the variance analysis for the whole simulated scenarios, this result is confirmed in Table 4.9.

Treatments	A (Qa/Qc)	B (%O2)	C (dpm)	D (% Imbal.)	AB + CD	AC + BD	BC + AD
SSi	200.7	8296.7	26.6	22.3	801.0	120.5	93.4

Table 4.9 Variance analysis for the whole simulated scenarios

The individual parameter sensitivity study showed that the primary air to coal mass flow ratio had less influence on unburned carbon losses than other factors such as particle size or mass flow imbalances. However, Table 4.9 shows a noticeable influence of this factor, nine times greater than other factors, which were hidden in the individual analysis. Moreover, the analysis of the interaction effects of this factor, mainly with the oxygen excess level (AB), also suggests a greater contribution to unburned carbon formation than other interaction effects.

To analyze the influence of the four mass flow imbalance configurations proposed in the study, we have divided the problem into four groups (one for each configuration) performing a variance analysis for each one. Configurations 1 and 2 study a range of conditions that usually take place in the regular operation of the plant. The former is a typical configuration under

nominal load conditions whilst the latter is more typical under partial-load conditions. Configurations 3 and 4 study a range of conditions that may take place as a result of fault designs or malfunctions of plant equipment. Below, the four configurations are analyzed:

- Configuration 1: In this configuration, most of the primary mass flow is fed into the boiler through the burners in the lower row of the boiler. Table 4.10 shows the variance analysis for this configuration. The first important conclusion is that the interaction effect of the primary air to coal mass flow ratio is almost as relevant as the excess oxygen contribution.

Treatments	A (Qa/Qc)	B (%O2)	C (dpm)	D (% Imbal.)	AB + CD	AC + BD	BC + AD
SSi	6.0	136.8	1.3	0.2	109.2	7.6	0.4

Table 4.10 Variance analysis, Configuration 1

Another remarkable result, is that this variance analysis, as compared with the ones from other configurations (Tables 4.10 to 4.13), shows a smaller dependence of the unburned carbon losses on the oxygen excess level. The reason for this is that since most of the primary mass flow is introduced in the boiler through the lower row burners, the global residence time for particles is increased and even at low oxygen excess conditions, particles have a longer time to complete combustion.

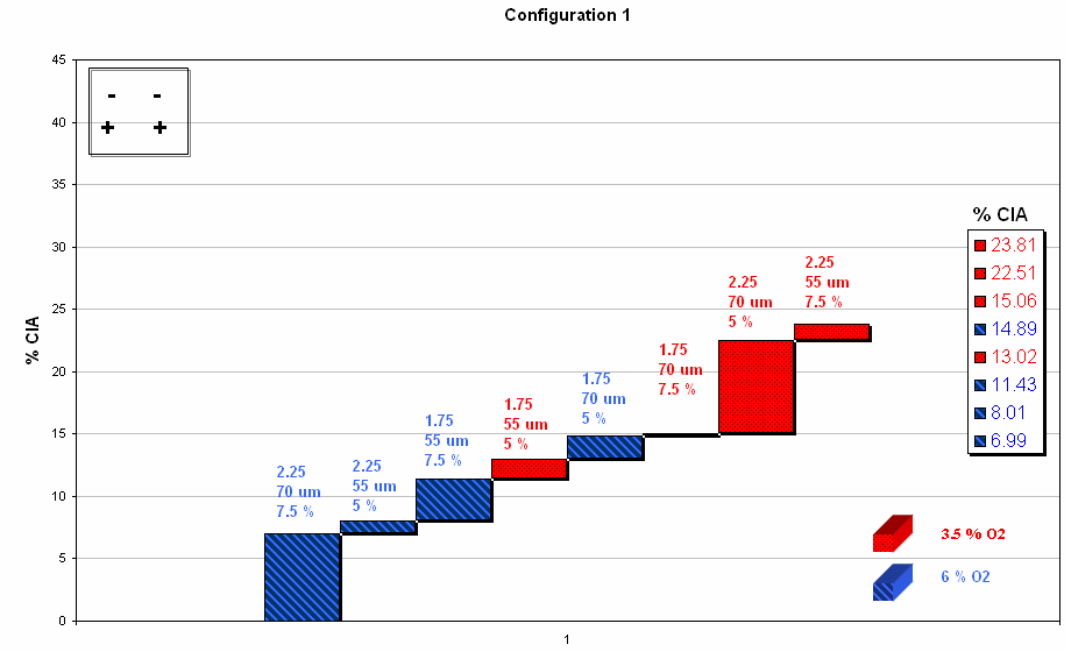

Fig. 4.18 Factorial analysis results, Configuration 1

Figure 4.18 summarizes the results obtained in the simulations where it can be seen two noticeable points stand out. Firstly, in this type of configuration, in spite of the fact that the excess oxygen level is the most influential factor, varying the other factors it is possible to obtain relatively low unburned carbon levels even at low excess oxygen conditions. This behaviour only takes place under this configuration type. Finally, looking at each oxygen level individually, the unburned carbon loss variations respond to variations in the primary air to coal mass flow ratio, confirming what was obtained in the variance analysis. The remaining factors hardly have an effect on burnout in the selected study range.

- Configuration 2: In this configuration, most of the primary mass flow is fed into the boiler through the burners in the upper row of the boiler. Table 4.11 shows the variance analysis for this configuration. This time, the oxygen excess level has an outstanding influence on burnout over the rest of the study factors. Interaction effects hardly had an impact and only primary air to coal mass flow ratio is slightly higher than the others.

Treatments	A (Qa/Qc)	B (%O2)	C (dpm)	D (% Imbal.)	AB + CD	AC + BD	BC + AD
SSi	39.4	1180.3	13.8	0.9	55.9	8.5	22.7

Table 4.11 Variance analysis, Configuration 2

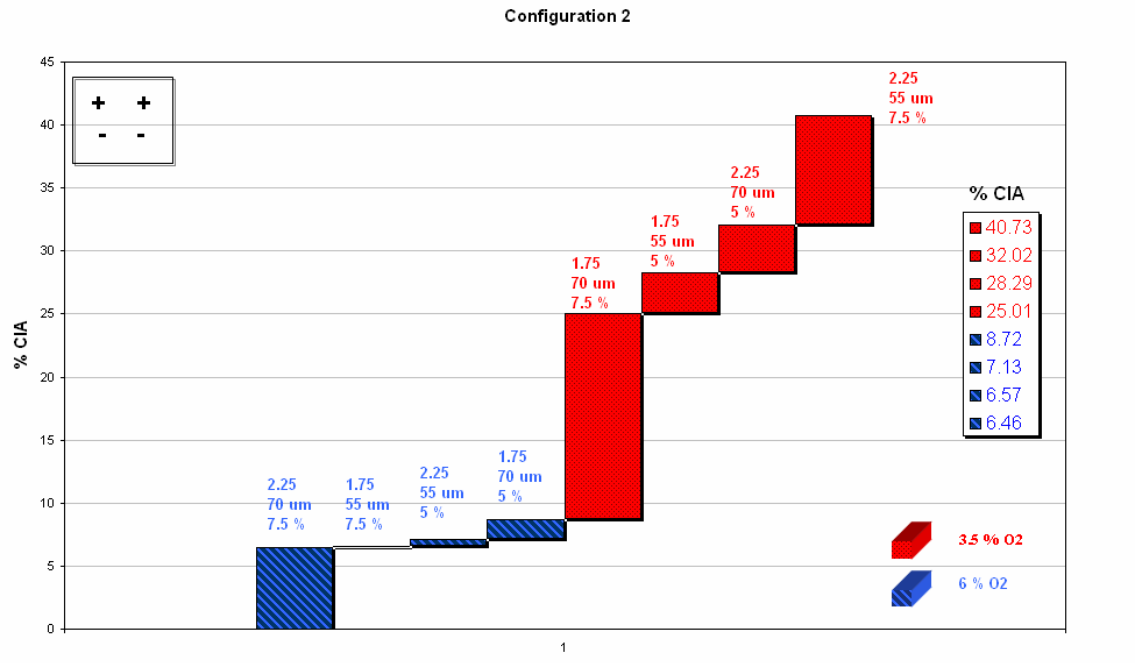

Fig. 4.19 Factorial analysis results, Configuration 2

This configuration type is the most disadvantageous under low excess oxygen conditions. Figure 4.19 shows an abrupt change in the carbon in ash values when switching from one oxygen level to another. It is also noticeable that under low excess oxygen conditions, unburned carbon losses vary as a function of the primary air to coal mass flow ratio, confirming what was shown in the variance analysis. However, under high excess oxygen conditions this relationship disappears and there is not a significant variation in burnout with the other factors.

Finally, returning to the discussion about the results of the individual parameter study, in which surprisingly we found lower unburned carbon in ash values within configuration 2 compared to configuration 1. The factorial study results confirm this under high excess oxygen conditions, since particles' trajectories from the upper row of burners are not distorted by the presence of the reversed-flow in the bottom hopper region, they mostly move along the flame where the most suitable combustion conditions are to be found. Consequently, even though the residence time is shorter in the upper row, most of the particles are under favourable combustion conditions and have enough time to complete combustion. Comparing Figures 4.18 and 4.19 this behaviour under high excess oxygen levels is shown. However, under low excess oxygen conditions, we obtain as expected, higher carbon in ash values for configuration 2 since lower residence times in the upper row of burners together with low oxygen conditions leads to a lower carbon conversion as shown in Figures 4.18 and 4.19.

- Configuration 3: This configuration type produces an uneven mass flow distribution between the burners of the same row, and at the same time, a global asymmetry in the flow within the boiler. Results from the variance analysis (Table 4.12), shows an outstanding influence of excess oxygen over the other factors, comparable to the results obtained for configuration 2.

Treatments	A (Qa/Qc)	B (%O2)	C (dpm)	D (% Imbal.)	AB + CD	AC + BD	BC + AD
SSi	5.1	769.5	5.1	21.9	0.6	6.1	2.4

Table 4.12 Variance analysis, Configuration 3

The main difference between this configuration as compared with configuration 2, is that instead of the primary air to coal mass flow ratio, mass flow imbalances turn into the second relevant factor since it noticeably influences the particles' trajectories. Figure 4.20 shows this behaviour since the carbon in ash variation, in the same excess oxygen level, corresponds to variations in the mass flow imbalances.

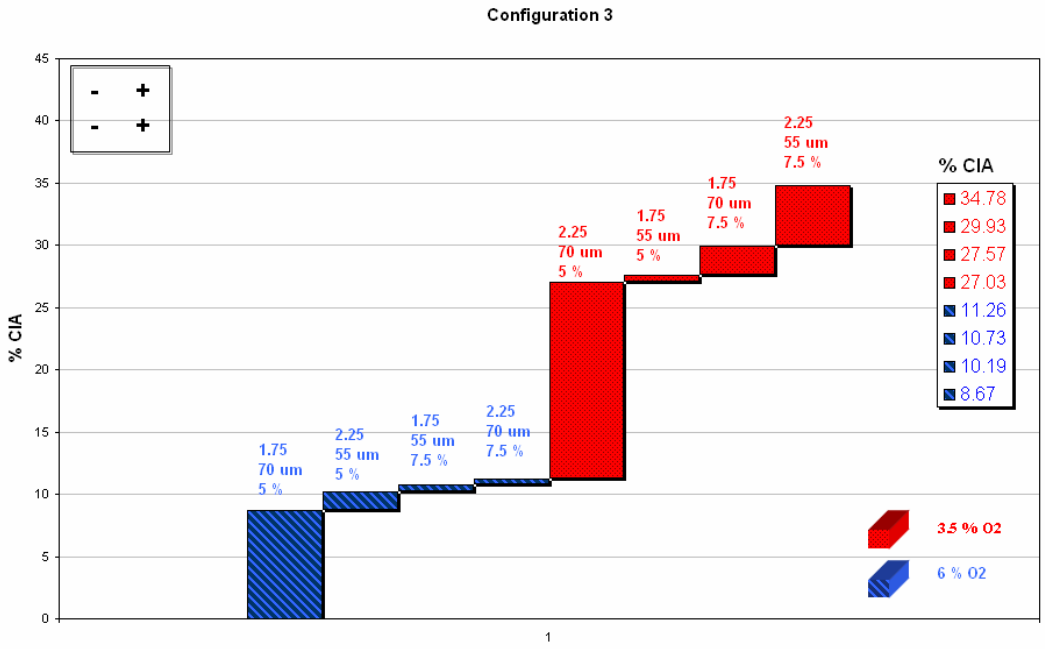

Fig. 4.20 Factorial analysis results, Configuration 3

- Configuration 4: This configuration type produces an uneven mass flow distribution between the burners of the same row, but provides for a global symmetry of the flow in the boiler. Results from the variance study show, as compared with configuration 3, lower carbon in ash values are obtained from the most symmetric flow in the furnace (Table 4.13). Moreover, this configuration type suggests a lower dependence of burnout on excess oxygen level.

Treatments	A (Qa/Qc)	B (%O2)	C (dpm)	D (% Imbal.)	AB + CD	AC + BD	BC + AD
SSi	10.2	299.1	0.1	0.2	91.7	8.0	7.5

Table 4.13 Variance analysis, Configuration 4

Finally, Figure 4.21 shows that, for the same excess oxygen level, carbon in ash values depend on the primary air to coal mass flow ratio, confirming what we obtained in the variance analysis.

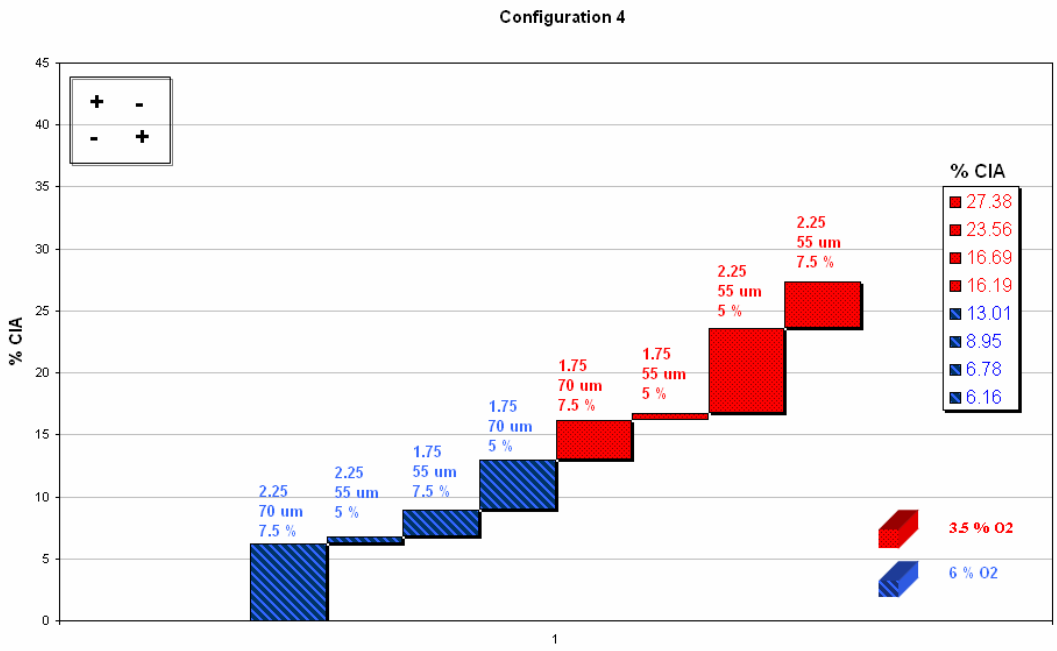

Fig. 4.21 Factorial analysis results Configuration 4

4.4 Conclusions

The starting point for the construction of an unburned carbon prediction system is to determine which factors are relevant in carbon burnout and to quantify their influence. We first performed a review of combustion related publications, in which reaction stoichiometry and coal grain-size distributions were reported as the most influential factors on combustion efficiency. In spite of this, most of these studies were carried out in scale burner-test facilities, in which some determining factors such as primary and secondary air mixing, swirling intensity, burner to burner flow interactions, reversed-flow regions or mass flow imbalances, were not possible to study. For this reason, in this work, since CFD tools are not limited with respect to these aspects, we included all the factors that may have an effect on combustion and studied their influence on unburned carbon losses. To achieve this, we performed a sensitivity study of the main factors affecting carbon burnout: excess oxygen, primary air to coal mass flow ratio, particle size distribution, secondary air swirl intensity and mass flow imbalances through the burners. The study was divided in two phases. First, we performed a preliminary sensitivity study to analyze individual contributions of each factor keeping the rest constant. Results suggested that the oxygen level is the most relevant factor in unburned carbon formation, especially for excess oxygen values under 4 %. However, the rest of the factors, such as mass flow imbalances, particles' size and primary air to coal mass flow ratio, may become relevant for excess oxygen values over 4 %. Next, a second sensitivity study was performed analyzing

the effects of interactions, since in real utility boilers these factors do not take place individually and their interaction may have an important influence on the total unburned carbon. When several sources of variation are acting simultaneously on a set of observations, it is particularly useful to fall back on variance analysis techniques. In order to reduce the number of simulations needed to complete the full experiment, a fractional factional analysis was applied, performing a variance analysis of the simulated values. Results from this multi-parameter sensitivity study confirmed the results from the preliminary study, showing that other factors such as primary air to coal mass flow ratio or mass flow imbalances through the burners, or their interactions may have a remarkable relevance in coal burnout depending on the boiler conditions.

From the results obtained in the sensitivity study, it is possible to establish action lines that allow the plant personnel to identify the source of an increase in the carbon in ash level or to look for the most suitable conditions to minimize this loss. Some possible actions and their associated costs are summarized in Table 4.14.

Factor	Practicability	Cost
Qa/Qc	Immediate	Primary air forced-draft fans power consumption. Erosion of the ducts due to a higher air-coal flow velocity.
$\%O_2$	Immediate	Forced-draft fans and induced-draft fans power consumption. Electrostatic precipitator efficiency reduction due to shorter ash residence times. Higher sensible heat loss, since the mass flow increases more than the increase on the product gases exit temperature
d_{pm}	Using an adjustable classifier: Immediate Not using an adjustable classifier: Complicated (through Qa/Qc (AD))	Milling power consumption (It is lower than fans power consumption)
%Imbal. 1 and 2	Immediate (coal feeders) if there are not milling system maintenance problems.	Variations in the heat absorbed and NO_x production
%Imbal. 3 and 4	Complicated (ducts redesign)	Engineering remodelling and uncertainties on results

Table 4.14 Actions and associated costs for CIA reduction strategies

Nomenclature

d_{pm}	mean diameter Rosin Rammler distribution (m)
K	flow axial moment (kg m/s^2)
L_c	characteristic length (m)
M	flow angular moment (kg m^2/s^2)
n	normal unitary vector
n_{rr}	dispersion factor Rosin Rammler distribution
n_{sw}	swirl intensity number
r	radius (m)
r_k	grid mean size relation
SSi	sum of squares
T	temperature (K)
u_i	velocity i component (m/s)
U_k	axial velocity (m/s)
U_t	tangential velocity (m/s)

Δx_{ki}	length in the direction x_k of the mesh i (cm)
δ_I	error due to the iterative method
δ_M	error due to the spatial discretization
δ_T	error due to the time discretization
δ_S	modelling error
δ_{SDP}	error associated with the experimental data
δ_{SN}	numerical resolution error
δ_{SMA}	error due to the assumptions and hypothesis in the mathematical models

Acronyms

CIA	carbon in ash
CFD	computational fluid dynamics
HHV	high heating value
PDF	probability density function
RANS	Reynolds averaged Navier Stokes equations

5 LOCAL COMBUSTION CONDITIONS MODEL

There exist many approaches, experimental and computational, to develop an unburned carbon predictive system. Experimental approaches are very useful in design studies. However, for the daily monitoring of a real plant, the computational methods offer a flexibility as well as a saving of time and money, over current experimental facilities. Within the computational methods regularly used, CFD codes can precisely characterize the processes that take place inside the furnace. Despite this, for the study of unburned coal in utility boilers, these codes have two important drawbacks. Firstly, as it is referred in Chapter 3, for the heterogeneous char particle combustion modelling, these codes rely on simple models, that prove to be inadequate for obtaining quantitative values of the combustion process. To solve this difficulty we present a methodology in Chapter 6 based on obtaining temperature and oxygen partial pressure profiles for a representative number of particles, that are entered in an advanced combustion model using a CFD code. The second disadvantage of CFD codes is their typically high computational cost as creating and solving new simulations may take several days, which makes the use of this kind of tool in taking in situ real plant decisions impossible. Thus, in the development of predictive systems for combustion, many authors prefer to sacrifice part of the problem information using zonal approaches to solve the fluid-dynamics (Fiveland et al., 1992; Severin et al., 2005). However, these zonal models also present serious limitations such as the impossibility to correctly characterize many relevant factors that affect the combustion process, as it was presented in Chapter 4. For that reason, in this research work, we decided to keep the

use of the CFD code as a thermal and fluid-dynamic characterization tool. To solve the problem of the high computational cost, we propose the utilization of a neural network system that generates the oxygen partial pressure, and temperature profiles, and the residence time of particles for any operating condition. In this way, a number of CFD simulations, that are representative of the factors influencing unburned carbon losses within the plant operating condition ranges, are carried out. These simulations are then used to train the neural network system, so that this system is able to reproduce the solutions given by the CFD code. As in the case of the CFD code, the solutions from the neural network system are given in the form of oxygen partial pressure and temperature profiles, and particles residence times, to run immediately after the advanced combustion model. The advantage of introducing the neural network system in this way, is that it is possible to perform the calculations in a short period of time (less than a minute), and therefore, it can be used in the construction of an on-line predictive system. Another advantage is that, if the neural network system is appropriately trained, considering the variations and interactions of all parameters affecting unburned carbon formation, this system permits to interpolate in the range of variation used during the training stage. Thus, a predictive system covering the whole operational range of the plant can be obtained. From now on, the neural network system will be referred to as the local combustion conditions model.

For the development of the model, the commercial code Matlab Neural Network Toolbox 4.0 has been used. Throughout the chapter, the general characteristics of neural networks and their applications are introduced and the development of the local combustion conditions model is described: design of the neural network system structure, training of the system from a number of CFD simulations of the plant, and finally, its validation.

5.1 Neural networks

Neural networks form a set of programming and controlling techniques within the subject of Artificial Intelligence, which allows a system to learn; that is, recognize patterns and predict the behaviour from a number of training data (Bishop, 1995). The development of neural networks started in the early 40's, when McCullogh and Pitts devised the "artificial neuron" concept, from an electric device with multiple inputs which, after being weighted and processed by a non-linear function, returned a true or false response. In 1958, Rosenblatt was the pioneer in defining the concept of neural network by combining the use of several artificial neurons. This primitive network was able to generalize results. At the same time, other researchers such as Widrow and Hoff developed the first training algorithms. However, the use of neurons with a

binary response led to limitations in developing complex neural systems and in the 70's the progress of this technique stalled. Only a decade later, thanks to the contribution of Hopfield and the development of computers, was the interest for these algorithms recovered. The incorporation of more structures and the use of algorithms that were permitted to control systems with increasing complexity involving multiple inputs and outputs led the resurgence in Neural Network techniques. Nowadays, neural networks are used in many scientific and technological fields. Within the energy and combustion field, these kinds of models are becoming more and more popular. For example, Zhu et al. (1999) make predictions on char combustion, Carsky and Kuwornoo (2000) study the pyrolisys of coal, Hao et al. (2001) combine neural networks and genetic algorithms to optimize coal combustion reducing NO_X emissions, or Romeo and Gareta (2006) and Teruel et al. (2006) evaluate the influence of boiler conditions in slaging.

The use of neural networks present many advantages over more traditional techniques. Firstly, they use simple mathematical calculations, reducing the computational cost, which allows them to be used in an on-line application. Moreover, these systems are very robust and fault-tolerant; that is, if a punctual error occurs in an input, the system does not produce an error in the output.

Neural networks work like "black box" models. They are not governed by physical principles, and the relationship between inputs and outputs is established from the variations observed during the training stage. Thus, it is necessary to have a wide input data set available which provides, through the training of the network, the knowledge map relating the inputs to the corresponding outputs. In this way, the training of the network lies in continually modifying "weight" parameters until the simulated and the real outputs resemble each other.

The structure of the neural network is made up of several layers of neurons: an input layer where the inputs are introduced into the system, a set of intermediate or hidden layers where the weights and bias (constant parameters) are adjusted, and finally, an output layer where the solutions from the network are obtained (Figure 5.1). Each neuron receives information from a number of inputs (p_i). These inputs are then combined using a transfer function ($f(w_p+b)$), which returns an input value (n) to the core of the neuron. This transfer function, which depends on the type of neuron, combines the inputs (p_i) and the weights (w_i) adding an error span (b). Finally, an activation function is applied to the input value of the core (n), returning an output from the neuron (a), which is transferred to the next layer or to the output of the system depending on the location of the neuron in the network. There exist several types of activation functions (Demuth and Beale, 2002):

- Hard-limit transfer function: Limits the output to either 0, if the net input argument *n* is less than 0; or 1, if *n* is greater than or equal to 0. Neurons of this type are used in decision making systems.

- Linear transfer function: Returns a corrected value for the input.

- Sigmoid transfer function: Transforms values from negative to positive infinity into values in the range -1 to 1 (tangential sigmoid), or in the range 0 to 1 (logarithmical sigmoid). This transfer function is commonly used in Feedforward networks.

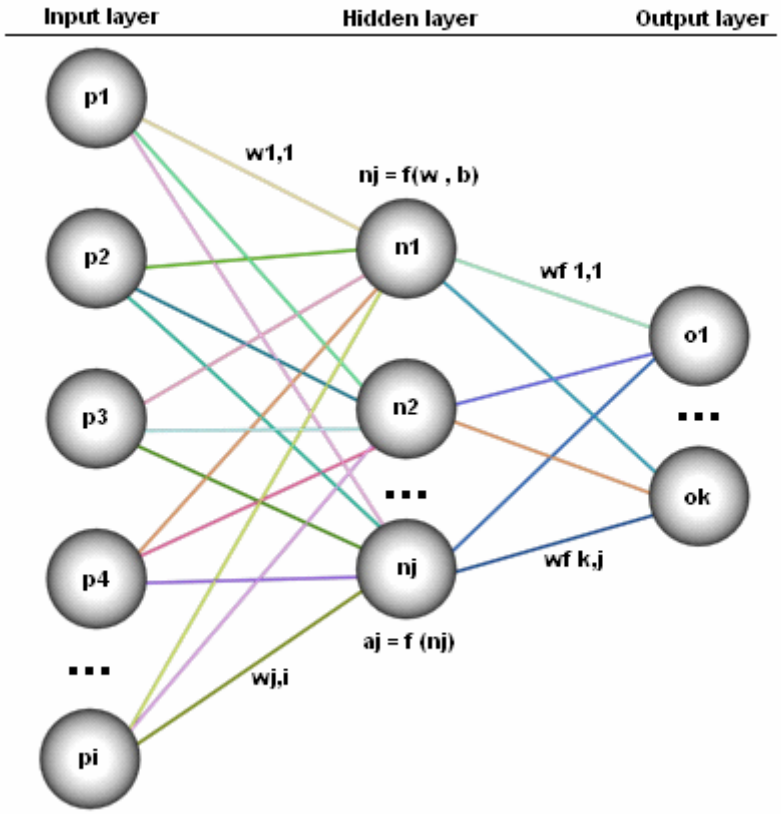

Fig. 5.1 General sketch of a neural network with one hidden layer

The network architecture depends on the type of neurons selected and the connections among them. The choice of the type of neuron to be used will depend on the purpose of the network design.

In spite of the countless advantages that this kind of system presents, it also has some limitations which must be taken into account to correctly interpret the results (Russell and Dobbiens, 1990; Gareta, 2004):

- Neural networks do not obey physical principles. They constitute an alternative to other mathematical techniques, such as correlations or statistical methods.

- Neural networks work as “black box” models. The whole information of the network is stored within the network parameters. Therefore, it is not possible to infer logical conclusions based on physical principals just from its structure.

- Achieving a good generalization takes too much time in appropriately selecting the input data set, and developing the final design of the network structure.

- Results cannot be extrapolated outside the range of the input variables that were used during the training stage.

- Neural networks cannot identify errors when the input information is wrong.

Before starting the set up of the model, it is important to know about the physic fundamentals behind the problem, and recover all the information available about it (operation data, design data, precedent experiences). Knowing the physics of the problem helps in identifying what parameters take part in it, how they are related each other, and in which proportion they contribute to the final result. These kinds of models, where a background knowledge of the problem is understood, are called “grey box” models. Sometimes, it is also useful to filter the input data set and so avoid erroneous or unnecessary data which may disturb and slow down the training stage.

Once these considerations are taken into account, the constitution of the neural network model is divided into three stages:

- Design of the structure: The suitable type of neural network and the resolution algorithm for the problem are selected.

- Training of the neural network: At this stage, a portion of the available data is used to force the network to learn how the inputs and outputs are related.

- Validation: At this stage, it is verified that the neural network properly carried out the goal intended for it.

Among these three stages, an iterative revision process that concludes once the neural network obeys the design criteria is established.

5.2 Neural networks system structure

The choice of the neural network architecture is one of the most important stages in designing the system. The first step consists of selecting the most suitable type of neural network for the problem. At this point, we chose a Feedforward network type, since, as opposed to other designs, it has a great generalization capability and generates reasonable outputs even when the inputs have not been explicitly defined during the training stage. In this type of design, the basic structure is made up of an input layer, a hidden layer, which may include several layers formed by sigmoid type neurons, and an output layer with linear type neurons. Furthermore, in this type of network the connections among layers are always established in the forward direction; that is, there exist no connections among neurons of the same layer or in the backward direction.

Figure 5.2 shows a sketch of a Feedforward neuron. The hidden layer is made up of sigmoid type neurons since they allow the simulation of both linear and non linear systems (Eqs. 5.1 and 5.2). The output layer is formed by linear type neurons to allow the network to simulate any function without discontinuities (Eqs. 5.1 and 5.3).

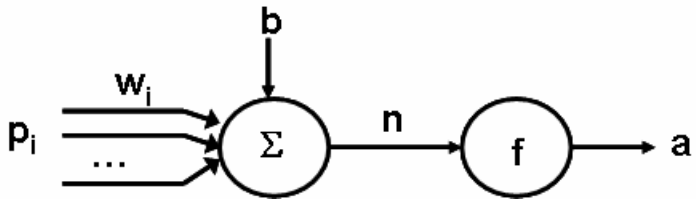

Fig. 5.2 Feedforward neuron sketch

$$n_j = \left(\sum_i p_i \cdot w_{j,i} \right) + b_j \qquad \text{(Eq. 5.1)}$$

$$a_j = 1/\left(1 + e^{-n_j}\right) \qquad \text{(Eq. 5.2)}$$

$$a_j = n_j \qquad \text{(Eq. 5.3)}$$

Once the network type has been defined, the next step in the design process lies in defining the outputs and inputs of the network with the number of hidden layers and neurons for each layer depending on the linearity between inputs and outputs.

The outputs of our system are the oxygen partial pressure, the temperature and the residence time of each particle. The system can be constituted with different architectures using multi input-multi output networks (MIMO) or multi input-single output networks (MISO). The former architecture may save efforts in the design process, since a single network that produces several outputs is used. However, since the weights of the network are the same, the convergence of one output will determine the convergence of the others therefore complicating the process. In this way, it is advisable to use MIMO networks when the simulated outputs bear a similar relation to the inputs and depend on similar parameters. In this work, we chose two independent neural network systems: a MISO network to generate the particles' residence time, and two-outputs MIMO networks to obtain the oxygen partial pressure and temperature profiles.

The choice of the inputs must contribute to achieve the simplest model possible. For this reason, all the irrelevant inputs that do not influence the outputs must be excluded from the analysis therefore improving the convergence of the problem. From the factorial analysis developed in Chapter 4, which established the most relevant parameters affecting carbon losses, the inputs for both neural networks were selected:

1. Residence time neural network (1 MISO network)

- Load (full or partial load): 1 input
- Excess O_2: 1 input
- Air to coal mass flow ratio: 1 input
- Particle diameter: 1 input
- Uneven mass flow distributions among burners: 4 inputs
- Burner position (upper or lower row): 1 input

2. Oxygen partial pressure and temperature neural network (4 MIMO networks: Full load/Upper row of burners, Full load/Lower row of burners, Partial load/Upper row of burners, Partial load/ Lower row of burners):

- Excess O_2: 1 input
- Air to coal mass flow ratio: 1 input
- Particle diameter: 1 input

- Uneven mass flow distributions among burners: 4 inputs
- Starting feeding position of the particle in the burner: 1 inputs
- Time: 1 input

As it was previously mentioned, the construction of the network system is carried out through an iterative process through the design, training and validation stages. In this way, the initial design of the oxygen partial pressure and temperature neural network could be built using a single MIMO network for the whole operational range of the plant. However, we found large differences in the behaviour of the simulated profiles between full and partial load conditions. Therefore, we decided to use separate networks for both load conditions. Similarly, in order to improve the convergence and accuracy of the results, separate networks for the upper and lower row of burners were considered. As a consequence of these modifications, the final design of the oxygen and temperature profiles network was formed by four MIMO networks. As far as the residence time network was concerned, a high fitness allowed only one MISO network to be adopted for the whole operational range.

In the same way, following an iterative designing process, we included an additional parameter for the starting feeding position of the particle in the burner, in order to improve the quality of the results. The trajectories and the temperature and oxygen profiles of the particles can vary considerably depending on their injection location in the boiler. For example, the particles fed close to the axis of the burner are influenced by an internal recirculation, while the particles fed at the periphery are strongly influenced by the secondary air flow and an external recirculation of the products of combustion (Chapter 1, Figure 1.1). Since there are 48 particle inlet nodes for each burner, it is difficult to achieve a correct generalization of the network for all the parameters and conditions used in the study. To delimit the problem, it was decided to divide each burner into six regions, as a function of the radius and the relative position with respect to the axis of the burner (Figure 5.3). In this way, every particle is assigned to one region depending on its starting feeding position. Once this region factor was introduced in the neural network system, the improvement in the accuracy of the results was remarkable. The final structure of the neural network system (local combustion conditions model) is summarized in Figure 5.4.

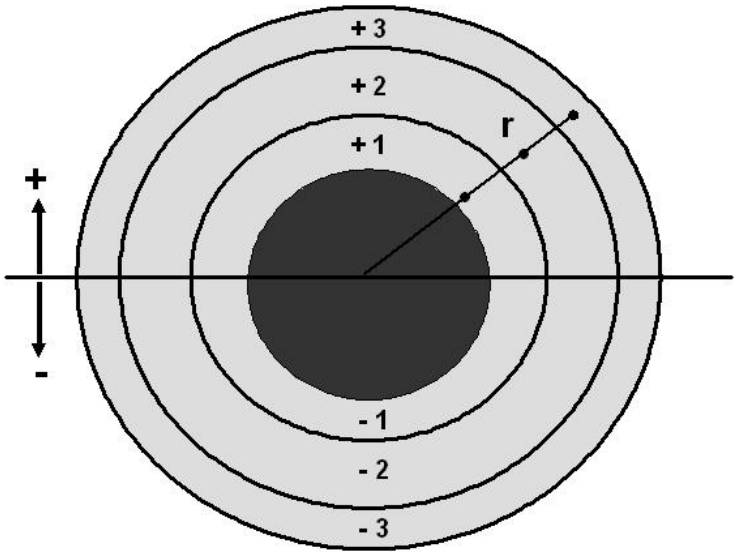

Fig. 5.3 Details of the six region division of the coal inlet in a burner

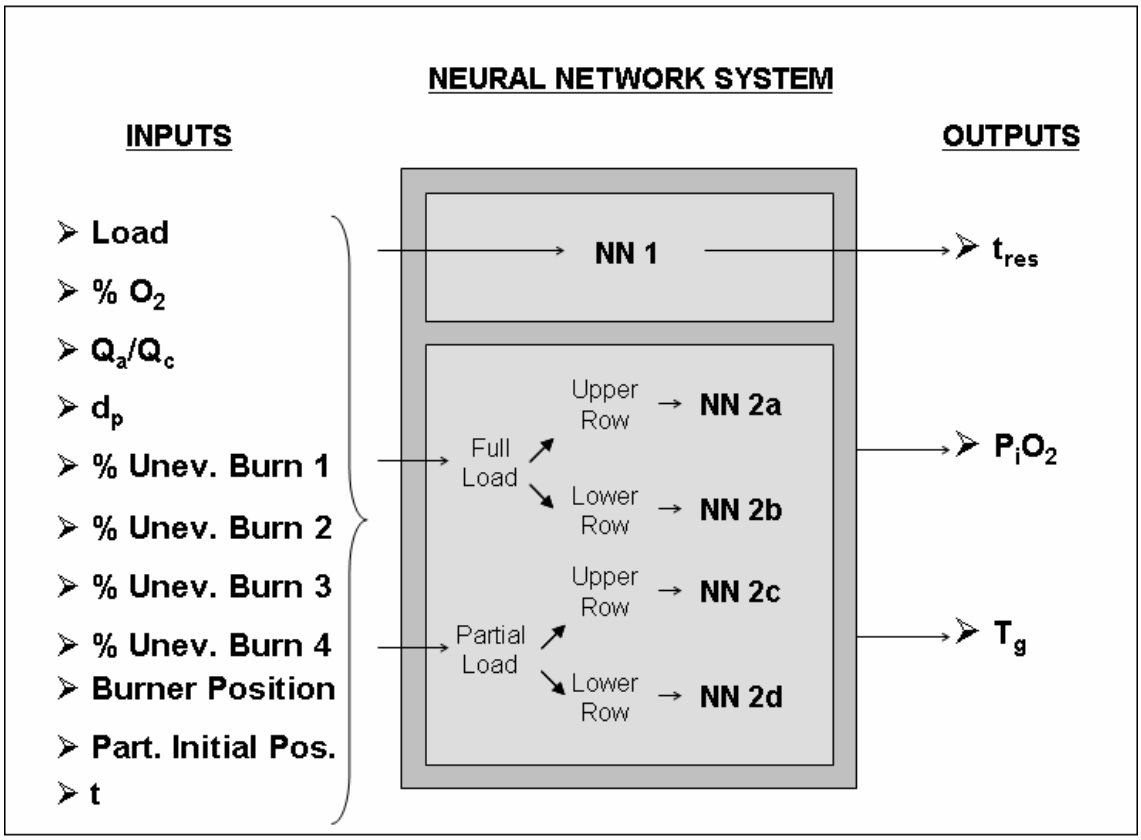

Fig. 5.4 Local combustion conditions model diagram

Once the output and input layers have been defined, only the hidden layer structure remains. It is this hidden layer which gives the network the capability of reproducing non linear effects. Since, in Feedforward neurons the hidden layer is made up of sigmoid functions which by themselves have the capability of simulating these non linear effects, it is enough to include one single hidden layer and thus reduce the complexity of the network (Gareta, 2004).

Next, the number of neurons that will constitute the hidden layer is determined. Increasing the number of neurons is equivalent to increasing the degrees of freedom of the system, which means that the network will be able to reproduce more accurately the training data. However, an excessive number of neurons should be avoided, since it will result in an overtraining situation. Overtraining takes place when the network memorizes the examples used for the training, and generates false predictions when other inputs are used. On the contrary, reducing the number of neurons, increases the network capability to generalize, at the expense of a decrease in the accuracy. It is necessary to balance both situations. Usually, the number of neurons is determined according to previous experiences, and then, from the results, an iterative process for the proper selection of the number of neurons is carried out. In general, it is preferable to start with a reduced number of neurons, and then increase this number by one unit at a time until the addition of a new neuron does not improve anymore the convergence of the problem.

The hidden layer of the local combustion conditions model was constructed as follows:

1. Residence time neural network (NN 1): 20 neurons.

2. Oxygen partial pressure and temperature neural network (NN 2a, NN 2b, NN 2c, NN 2d): 15 neurons.

5.3 Training of the neural networks system

Before starting the training of the neural network, it is interesting to carry out a pre-treatment of the input data in order to expedite the learning process. Usually, any error in the inputs is removed from the training set. Besides, it is necessary to normalize the input and output data, for example, in the range -1 to 1. In this way, the range of values for all the inputs is the same, and as a consequence, the training is faster, and accuracy problems in the variables with lower values are avoided.

In order to obtain the data used to train the neural network, a new design of experiments based on factorial analysis was carried out, in such a way that three levels of the most relevant factors affecting carbon losses were included, differentiating between full and partial load conditions (Figure 5.5). With regard to the factorial analysis executed in Chapter 4, the number of levels of each parameter has been increased up to three, with the exception of the particle size distribution. In this case, it is enough to use only one particle size distribution, because it

already includes different particle sizes, so that the neural network can learn variations with regard to this factor. Specifically, ten particle sizes, as in the CFD simulations, were considered.

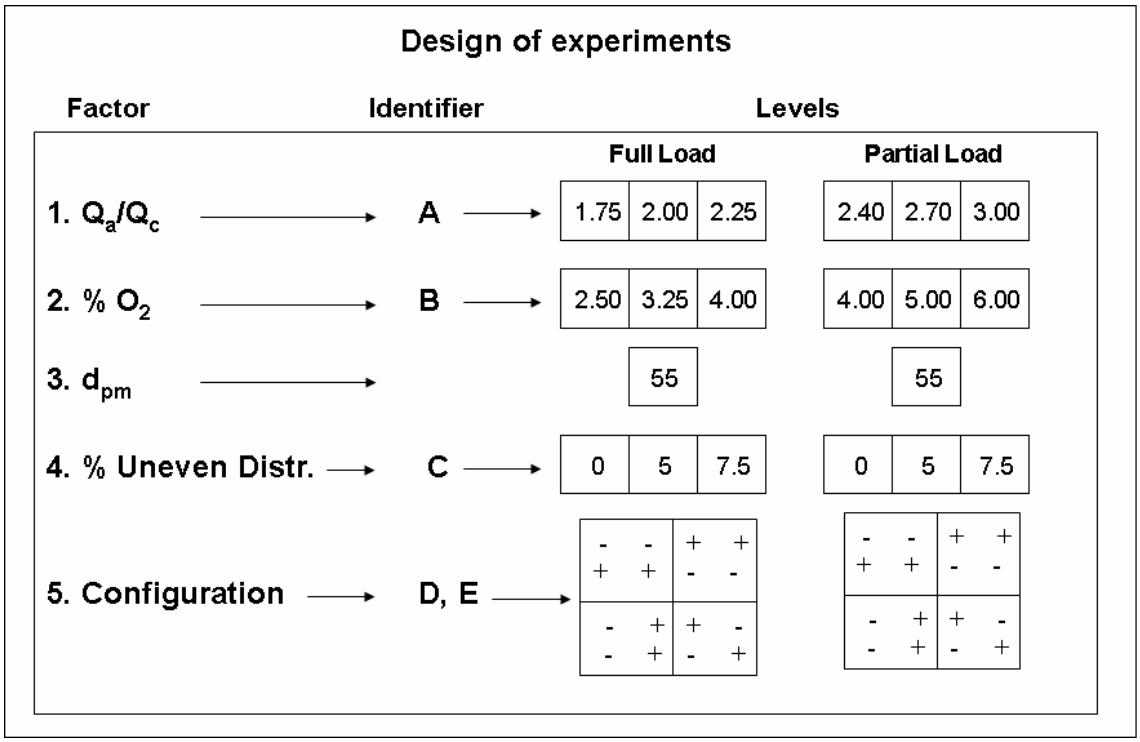

Fig. 5.5 Design of experiments

In order to completely characterize this design, 256 CFD simulations are needed (3 x 3 x 1 x 3 x 4 x 2 → 256). However, as it was done in Chapter 4, to reduce the total number of simulations, a fractional factorial analysis has been implemented. In this way, only a fraction of the total number of possible combinations of simulations is performed. This fraction is chosen in order to obtain a representative sample of the results, covering the whole range of the operating conditions at the plant. From that, a three levels fractional factorial analysis 3^{3-1} x 4 has been performed, so that 36 simulations for each, partial and full, load conditions must be solved, giving a total number of 72 CFD simulations. In order to construct this design, one component of the interaction ABC (I=ABC, AB^2C o AB^2C^2) with two degrees of freedom is selected. Then, the complete design 3^3 is divided into three groups, each one corresponding to a fractional design 3^{3-1}. There exist twelve different fractions one third of the design 3^3 defined by the Eq. 5.4 (Montgomery, 1991).

$$x_1 + \alpha_2 \cdot x_2 + \alpha_3 \cdot x_3 = u(\mathrm{mod}\,3) \qquad \text{with } u = 0, 1, 2. \qquad \text{(Eq. 5.4)}$$

Where, α_i = 1 ó 2 are the exponents of the factors in the definition relation I.

Selecting a definition relation of highest resolution I = AB^2C^2, that is α_2 = 2 and α_3 = 2, the resulting fraction of the design 3^{3-1} is exactly formed by 3^2 treatment combinations that satisfy Eq. 5.5 (Table 5.1, when u = 0).

$$x_1 + 2 \cdot x_2 + 2 \cdot x_3 = u(\mathrm{mod}\,3) \qquad \text{with } u = 0, 1, 2. \qquad \text{(Eq. 5.5)}$$

A	B	C
0	0	0
0	1	2
1	0	1
2	0	2
0	2	1
1	1	0
1	2	2
2	1	1
2	2	0

Table 5.1 One third fraction u = 0 of the design 3^3 with a definition relation I = AB^2C^2

Assigning the values 0, 1 and 2 to the low, medium and high levels respectively, the design of experiments is generated. From the interpretation of the identifiers and the levels assigned to each factor, Table 5.2 summarizes the conditions for the simulations (shaded cells). The rest of conditions, models and hypothesis, required to complete the simulations, are the same conditions as the ones described in Chapter 4.

	Qa/Qc			%O2			dp (μm)	% Uneven flow distribution			Configuration			
Full Load	1.75	2	2.25	2.5	3.25	4	55	0	5	7.5	1	2	3	4
1														
2														
3														
4														
5														
6														
7														
8														
9														
10														
11														
12														
13														
14														
15														
16														
17														
18														
19														
20														
21														
22														
23														
24														
25														
26														
27														
28														
29														
30														
31														
32														
33														
34														
35														
36														
Partial Load	2.4	2.7	3	4	5	6	55	0	5	7.5	1	2	3	4
37														
38														
39														
40														
41														
42														
43														
44														
45														
46														
47														
48														
49														
50														
51														
52														
53														
54														
55														
56														
57														
58														
59														
60														
61														
62														
63														
64														
65														
66														
67														
68														
69														
70														
71														
72														

Table 5.2 Design of experiments simulations' conditions

Just like in previous chapters, once the simulations have been run and the correctness of the numerical resolution has been verified, we have proceeded with their validation. For that purpose, the oxygen values at the exit of the boiler obtained in the simulations are compared against the predetermined values for each case. Figures 5.6 and 5.7 show the results obtained, and allows us to accept the correctness of the simulation.

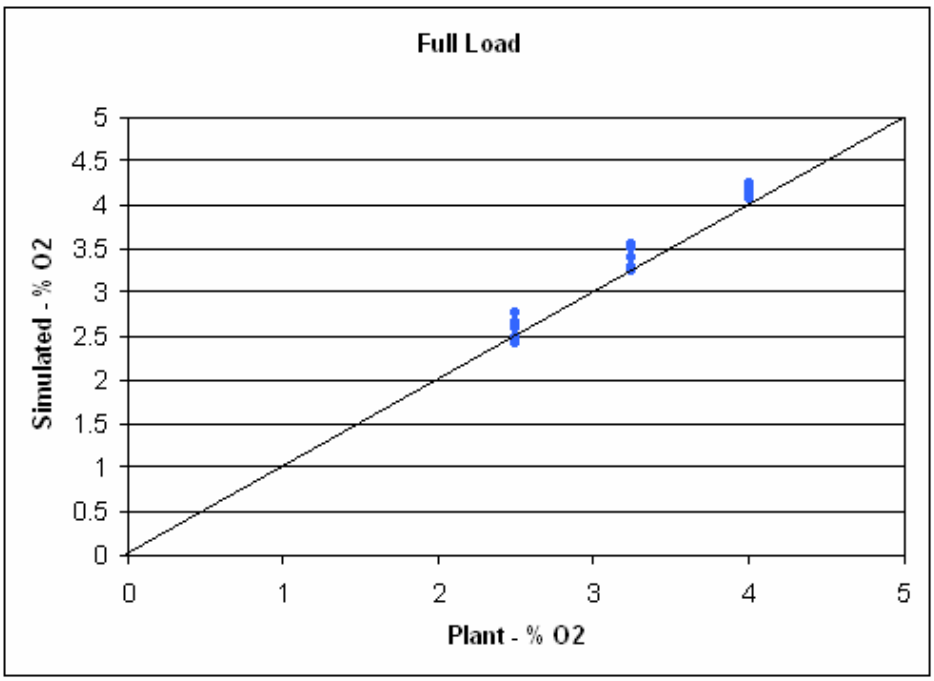

Fig. 5.6 Simulated % O_2 vs. Plant % O_2. Full load conditions

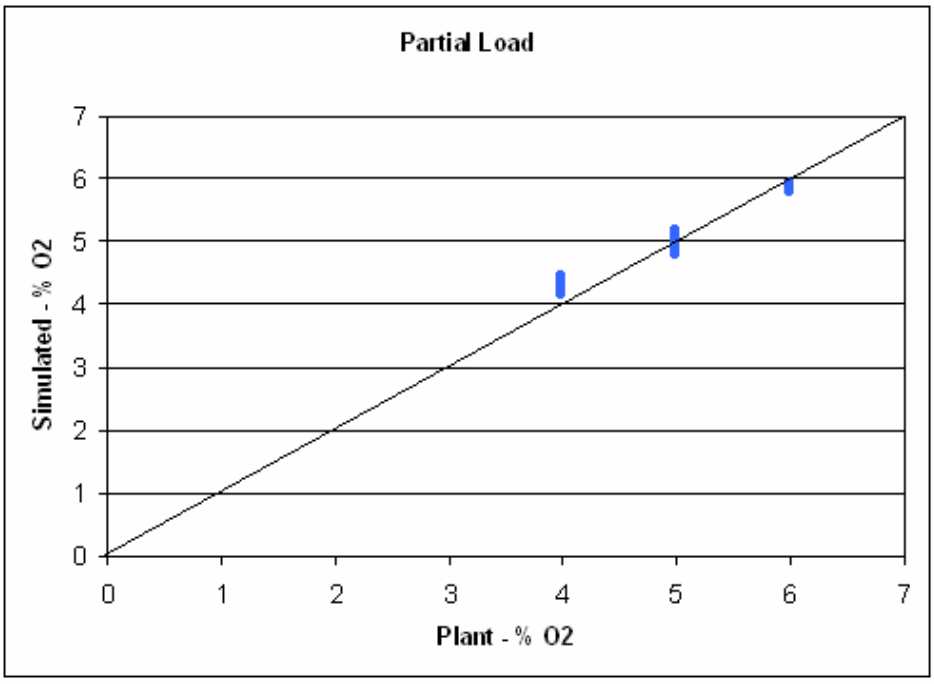

Fig. 5.7 Simulated % O_2 vs. Plant % O_2. Partial load conditions

For training the networks, the Levenberg-Marquardt algorithm with Bayesian regularization implemented in MatLab (trinbr), has been used. This algorithm uses an approximation technique based in Newton's method (Eq. 5.6). In this way, the network learns by modifying the weights vector of the neurons.

$$w_{k+1} = w_k - \left[J^T \cdot J + \mu \cdot I_d\right]^{-1} \cdot J^T \cdot e \qquad \text{(Eq. 5.6)}$$

Where, w_{k+1} is the weights and bias vector in the next iteration, w_k is the weights and bias vector in the current iteration, J is the Jacobian matrix that contains the first derivative of the network errors related to the weights and bias terms, I_d is the identity matrix, e is the errors vector, and μ is a convergence coefficient.

The Levenberg-Marquardt algorithm as compared with other training methods, gives the fastest response with a minimum convergence error. In addition, the Bayesian regularization provides the training algorithm with a superior generalization capability. This technique modifies the optimization function, including the quadratic sum of the network parameters (weights and bias) into the sum of the quadratic errors. This way, at the same time as the error is reduced, the network parameters are reduced too, so that the network generates softer responses that contribute to avoid overtraining situations (Demuth and Beale, 2002). The stop criterion for the training is reached when the quadratic errors and the weights remain relatively constant.

In general, not all the available data are used during the training stage. The fraction of data used for training the network may vary depending on the size of the data set. Commonly, when there exists a huge set of data, as in the case of the temperature and oxygen profiles networks; this set is divided in two groups: training and test data. In addition to this, depending on the validation procedure, there can be a third group of data, used in the validation stage. The training data are used to train the network. At the same time, test data are used to check the fitness of the simulated outputs to the real values. This way, the evolution of the error calculated for the test data should be similar to the error obtained for the training data. In the case where a decrease in the training errors does not involve a decrease in the test errors, this is an indication that overtraining is taking place.

5.4 Validation of the neural networks system

Once the training stage is completed and the weights of the network have been calculated, the accuracy of the model should be determined. The validation process lies in verifying the correlation and generalization capabilities of the network. There exist many validation tests, most of them based on graphical comparisons of real and simulated data. It is also interesting to confirm that the outputs generated by the network for a particular input condition make physical sense. Therefore, during the validation process, not only is the correct performance of the

network evaluated, but also the quality of the proposed structure and the data are assessed. In this way, depending on the results obtained in the validation, it may be necessary to revise previous stages of the model development, modifying the structure of the network or selecting more carefully the training data. This iterative process among the different stages finishes once the modelled network carries out properly and accurately the performance expected of it.

Comparing the simulated and real outputs, the error obtained can be classified into three categories:

- Overtraining error: This error takes place when the error obtained using the training data is much smaller than the one obtained with the validating or test data. This error is due to an excessive number of neurons in the hidden layer, which enhances the memorizing capability of the network.

- Generalization error: This error takes place when the function reproduced by the network is smoothed, thus resulting in a high error with the training and validating data. This error is due to a reduced number of neurons in the hidden layer.

- Data errors: There is also an error or noise associated with the raw data used in the model.

The validating methods widely used in the research community are based on graphical techniques. These kinds of methods vary also depending on the type of output that needs to be validated. As a result, in this work, we have applied two different graphical techniques to validate the residence time network and the oxygen and temperature profiles network. For the former, we have used a correlation graph that shows the comparison of the simulated and real data (Figure 5.8). In this way, it is possible to verify the fitness and the range of values where the best fit is attained.

Figure 5.8 shows a good fitness for the residence times generated by the neural network over a wide range of values (4 s – 25 s), which covers the most probable variation of this parameter. Since most of the particles have residence times under 15 seconds, the fitness of the diagram in this range is better. Nevertheless, the generalization over the whole range is adequately correct, above all, considering the dispersion on the data due to the particles coming from the lower row of burners which may be trapped in a recirculation loop.

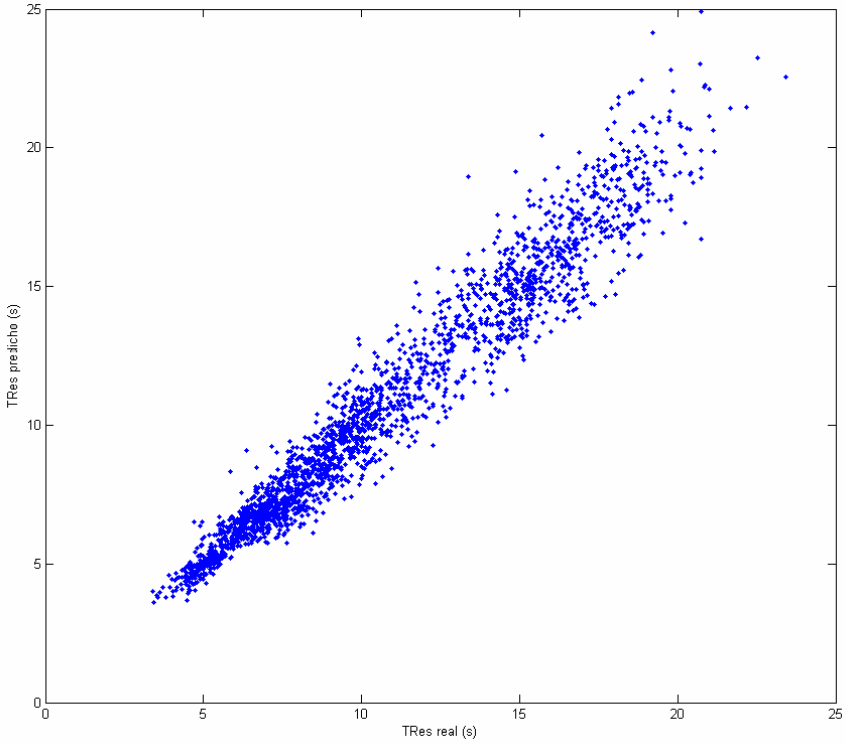

Fig. 5.8 Correlation graph of simulated and real residence time

With regard to the oxygen and temperature profiles networks validation, the most suitable graphical method to validate these is to represent together the real and simulated values as a function of time. Since the neural networks produce individual data for any time considered and the final use of the network lie in generating oxygen partial pressure and temperature profiles as a function of time for a particular operating condition; it is appropriate to verify if the simulated data adequately reproduces the oxygen and temperature profiles obtained by the CFD code for a wide range of conditions. Since there is a large number of profiles for each output (72 simulations x 1920 particles = 138240 profiles), the validation is a tedious and difficult task. So in order to interpret and compare the results, average temperature and oxygen profiles in five sieve fractions (< 30 μm, 30 – 60 μm, 60 – 90 μm, 90 -120 μm, > 120μm) were represented for each burner and simulation case considered. In addition to the seventy two CFD simulations used for the model development, twenty additional simulations were also considered in the validation.

First, it was verified that the outputs generated by the network for a particular set of input conditions made physical sense. Then, a comparison of the averaged profiles simulated by the neural network and the ones obtained by the CFD code was performed. Figures 5.9 and 5.10 show two examples of the validation process for the averaged profiles. Typical temperature profiles are characterized by a sharp increase in temperature during the first instants until a peak

temperature is reached, since most of the combustion takes place near the burners. Subsequently, as the particles move away from the flame, the temperature decreases until a relative constant value is reached. In the same way, typical oxygen partial pressure profiles show the opposite behaviour. During the first instants, oxygen is highly consumed in the combustion process, and so the profiles decreases until near zero oxygen values. Then, the oxygen concentration increases until a relative constant value is reached. From these figures, the fitness of the averaged profiles given by the neural network system compared to the same averaged profiles given by the CFD code demonstrate a remarkable correlation. In the same way, similar results were obtained for the rest of cases considered in the validation, thus leading us to the conclusion that the neural networks system adequately reproduces the profiles obtained by any CFD simulation in the operational conditions range of the study plant.

The goal of generating these profiles is to use them as inputs in an advanced combustion model to determine the combustion efficiency within the furnace. Therefore, before closing this chapter, it is worthwhile to look at the time scales of Figures 5.8 and 5.9 to appreciate in detail the quality standard of the profiles and their influence on the later combustion calculations. It is only during the first 500 ms, when most of the combustion process takes place, when the neural network system is used to generate data every 5 ms; that is, 100 discrete points are obtained. From 0.5 seconds residence time onwards the time step has been progressively increased to save on computing time, as long as the coal conversion has been completed and the temperature and oxygen gradients are reduced. Note if computing processing power is not an issue it is possible to keep the time step increment of 5 ms due to the large amount of data used in the training stage from the CFD simulations i.e. around 100 million data points. Together, the high resolution detail standard used in the profiles (5 ms in the near burner region) and the high accuracy of the fitness of the profiles make the combined CFD codes and neural network algorithms a powerful tool for describing and solving the thermal and fluid dynamics behaviour much more accurately than a zonal approach.

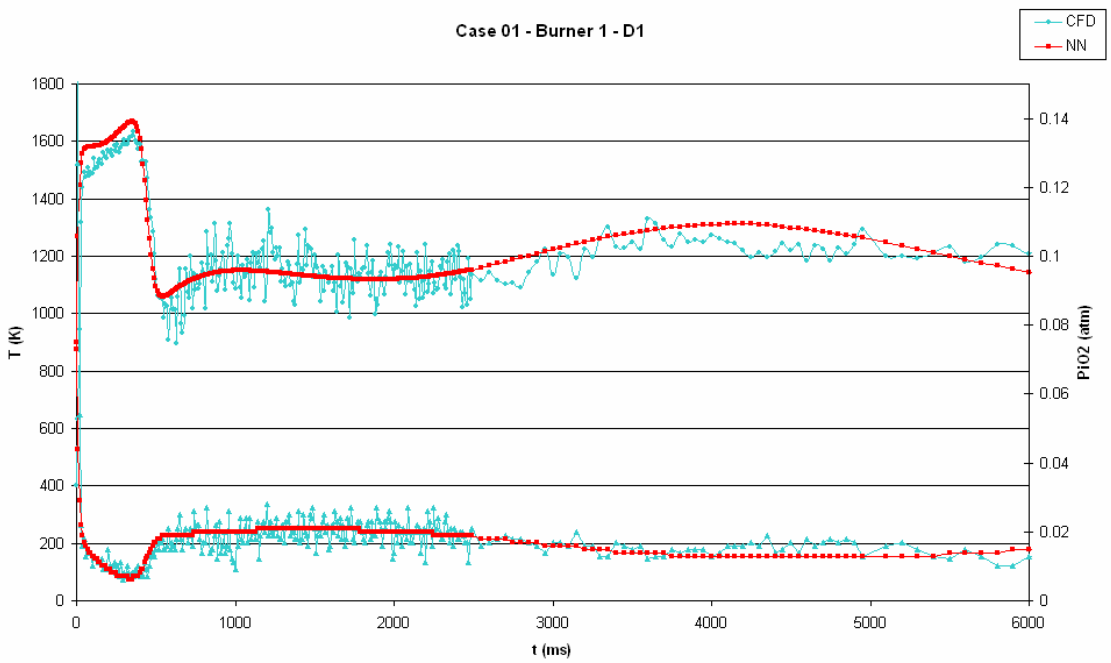

Fig. 5.9 Real (CFD) and Neural Networks (NN) T^a and P_iO_2 averaged profiles: Case 1, Burner 1, Particle size D1 (< 30 μm)

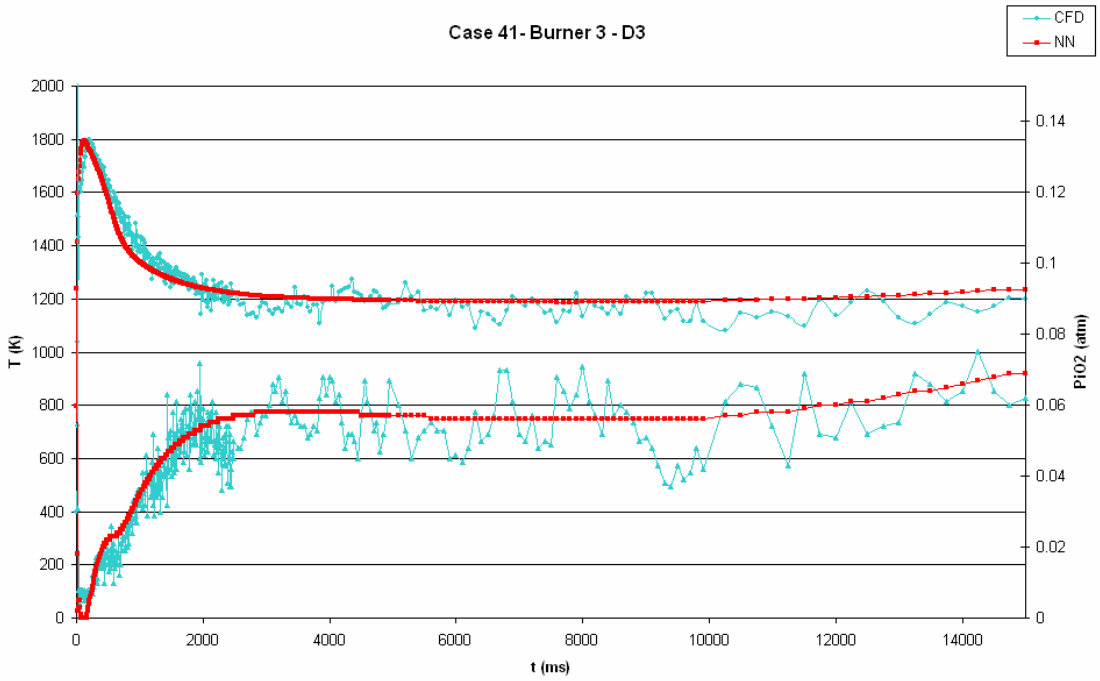

Fig. 5.10 Real (CFD) and Neural Networks (NN) T^a and P_iO_2 averaged profiles: Case 41, Burner 3, Particle size D3 (60 – 90 μm)

5.5 Conclusions

One of the marked disadvantages in the use of a CFD code in a predictive system is its high computational cost. Consequently, with this kind of tool it is not possible to develop a system that works on-line. Furthermore, it is not convenient to ignore the accuracy of CFD codes, especially in combustion prediction problems, where a detailed characterization of main temperature and oxygen gradients during the first instants of the process is required for an accurate description and prediction of the full system. In the last two decades neural networks have been used in many research and technological areas, resolving very different problems based on pattern recognition from a previous experimental knowledge of the problem. Moreover, neural networks offer multiple advantages as compared to other techniques, since they are robust, fault-tolerant, fast, simple and cheap.

Taking advantage of these qualities in this work by developing a neural network system to learn, reproduce and interpolate the results (by means of temperature and oxygen partial pressure profiles, and particles' residence times) obtained from a CFD code for any particular boiler operating conditions. To achieve this, we have performed a number of CFD simulations, covering the operational range of the study plant, to develop, train and validate a neural network system. As a result of the study, it is concluded that that the neural network system, called the local combustion conditions model, accurately reproduces the profiles obtained by the CFD simulations. Moreover, due to the generalization capability of the neural networks, it is possible to obtain solutions for any operating conditions as long as they belong to the range used during the training stage. In addition the accuracy of the thermal and fluid description obtained is much better than the ones obtained by any zonal approach, and all with negligible computing cost. We can therefore conclude that the combination of CFD codes and neural networks algorithms is the more suitable tool for the development of the combustion predictive system of this thesis work.

Nomenclature

a	activation function
b	bias
d_p	particle diameter (m)
d_{pm}	Rosin Rammler distribution mean particle diameter (m)
e	error vector of the neural network
n	transfer function
n_{rr}	Rosin Rammler dispersion factor distribution
p	input of the neural network
P_iO_2	oxygen partial pressure (N/m^2)
Q_a	primary air mass flow (kg/s)
Q_c	coal mass flow (kg/s)
t	time (s)
t_{res}	residence time (s)
T_g	bulk gas temperature (K)
w	parameters vector (weights and bias) of the neural network
x	levels of the factorial analysis
α_i	exponents of the factorial design
μ	convergence coefficient

Acronyms

CFD	computational fluid dynamics
MIMO	multi input multi output
MISO	multi input single output
NN	neural network

6 COMBUSTION MODEL

Solving combustion problems for the determination of unburned carbon losses requires dealing in detail with the fluid dynamic and thermal behaviour of the problem, as well as with the combustion process itself. It is worthless to precisely calculate the fluid and thermal behaviour of the problem by means of CFD codes, if finally, simple combustion models are used. This is in fact the biggest problem within commercial CFD codes where coal combustion models are very simple. In order to obtain a first approach to the solution, to determine general trends, or in problems where results are not strongly affected by combustion kinetics, simple models are adequate and regularly used (Stopford, 2002). However, in more specific problems which demand a detailed treatment of the combustion process, i.e. an unburned carbon predictive system, these models are insufficient. Thus, it is necessary to have recourse to advanced combustion models, as the ones described in Chapter 2 (FLASCHAIN, FG-DVC or CPD for devolatilization; CBK or CBK8 for char oxidation).

As was described in Chapter 1, within the computational methods, two main approaches are used to solve pulverized coal combustion problems:

- CFD codes: They give a detailed description of the transport phenomena, but use simple coal combustion models.

- Advanced combustion kinetics models: They precisely describe the combustion process. However, the fluid dynamics and thermal behaviour of the problem are generally obtained from a zonal approach (Pallarés et al., 2007).

In this work, we have developed a new methodology that takes advantage of both of the following approximations: the detailed fluid and thermal description of CFD codes and the precise combustion calculations of advanced kinetics models. To achieve this aim, we have considered two possibilities:

1. To fully couple the advanced combustion kinetics model into a CFD code.

2. To use the temperature and oxygen partial pressure profiles for a representative number of particles from a CFD code and then introduce them as inputs into an advanced combustion kinetics model.

The first possibility was discarded since it was impossible to introduce all the combustion equations into a commercial code with licence and copyright. Following this line, we carried out few modifications in the combustion model of the commercial code CFX-4, introducing rank dependant correlation for char reactivity, through the activation energy and the pre-exponential factor (Hurt and Mitchell, 1992) and a sub-model describing ash inhibition effects (Hurt and Sun, 1998) (see Chapters 2, 3 and 4). As a result, we considerably improved unburned carbon predictions as compared with the results obtained with the one film model implemented in CFX (Figure 6.1) (Pallarés et al., 2005).

However, since these modifications do not take into account the variations in char porous structure and reactivity as combustion proceeds, they are only able to predict general trends and fail in the prediction of quantitative values (Pallarés et al., 2005, 2007). Another advantage of considering the second alternative is that, this way, it is possible to un-couple the fluid and thermal calculations from the combustion model. Consequently, we would be able to separate the variables that exclusively govern the combustion process, i.e. the coal properties and therefore, small changes in these variables would not require a recalculation from the CFD simulation for the new conditions resulting in a subsequent saving in CPU time.

This de-coupling assumption is accomplished in case that the combustion model used by the CFD code to obtain the temperature and oxygen partial pressure profiles, is the same as the one used in the post-process. Otherwise, the variations in the reaction kinetics and in the heat

released during the post-process, with respect to the ones calculated by the CFD code to obtain the profiles, would modify the temperature and oxygen partial pressure map in the boiler, introducing an error in the prediction. In spite of the fact that in this work both models, CFD combustion model (Chapter 3) and advanced combustion model (Chapter 6), are different, this error can be considered negligible for several reasons. Firstly, the differences between models are relevant in the local description of the intrinsic and morphological phenomena taking place on the particle level, but not enough to significantly alter the temperature and oxygen distribution in the furnace. Furthermore, this error is minimized by exporting from the CFD, the profiles corresponding to the Eulerian description of the gas phase (cell values), instead of the variables values at the surface of the particles. As it will be seen in this chapter, it is during the post-process when an energy balance in the particle is carried out to determine the temperature and oxygen partial pressure at the outer surface of the particle from the bulk gas phase values. And finally, the validation carried out in Section 6.3 puts in relevance the goodness of the approach that clearly improves the results obtained exclusively with the CFD code.

Finally, and also as a consequence of this de-coupling, it is easier and more intuitive to develop a neural network system, as the one described in Chapter 5, that substitutes the CFD calculations, generating oxygen partial pressure and temperature profiles.

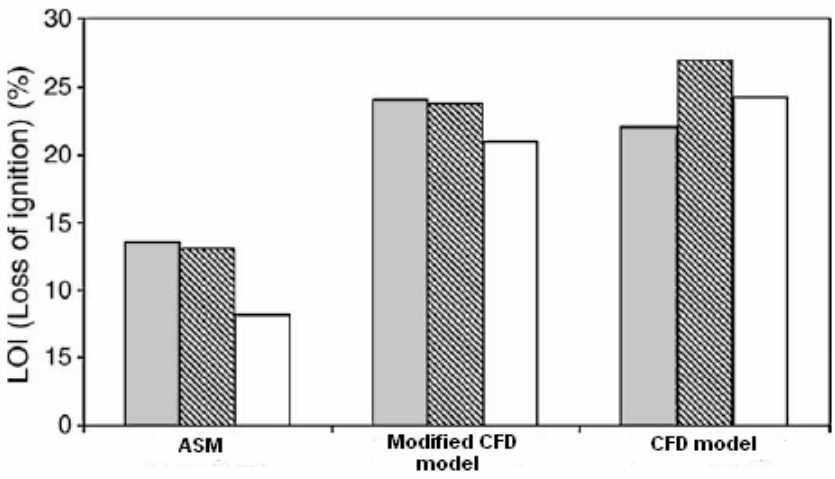

Fig. 6.1 Comparison of results for LOI (%) gathered at the ASM Brescia power station, against the calculated values from the CFD code (simple model) and from the CFD code (modified model) (Pallarés et al., 2005)

This chapter analyzes the definition of the combustion model. The description and development of the model is focused on the reactions that take place on the particle surface, that is, devolatilization and char oxidation. Firstly, we determine the coal pyrolysis and once this stage

is finished, char oxidation is considered. This assumption is commonly used in coal combustion modelling, although there exist some exceptions which take into account a possible overlapping of both stages when oxygen succeeds in diffusing into the particle surface area under maximum reaction rate conditions (Gurgel et al., 1999). In this work, devolatilization was modelled using a macromolecular network pyrolysis model (FG-DVC), whilst for char oxidation an intrinsic formulae based on the carbon burnout kinetic model (CBK8) (Sun and Hurt, 2000) was developed and programmed in Fortran. This model allows the transition to Zone I and includes the variation in char porous structure and reactivity as combustion proceeds, mineral matter effects and the influence of coal macerals on char reactivity.

Finally, we have carried out the validation of the combustion model. To achieve this, we have considered nine operation scenarios of the study plant (Lamarmora ASM Brescia), and we have compared predictions from the burnout model against plant values.

6.1 Devolatilization model

In Chapter 2 a review of the more widespread devolatilization models in combustion research works was presented. This time, the first goal is to decide which model is more suitable for our system. On one hand, we have the weight loss models (SFOR, DAEM, 2CSM), regularly used in combustion problems. These models, advantageous due to their simplicity, turn out to be inadequate when a more rigorous treatment is required, i.e. to determine quantitatively unburned carbon losses. It is well know that the devolatilization rate and yield increases with temperature and heating rate and ultimately determines the porous structure and the number of active sites of the char residue and thus its reactivity. Porosity is particularly important because it controls the rates of diffusion of chemical species into and out of the char particle during combustion when that takes place under internal diffusion controlled conditions. Furthermore, under pulverized fuel conditions the peak temperature to which the coal is heated reaches 1500 – 2200 K and the volatiles' yield is significantly higher than the volatile matter content determined by the standard ASTM test. This causes a decrease in the char produced whose oxidation provides the rate controlling step in coal combustion burnout. As a result, the devolatilization step is crucial in the overall burnout determination. For this reason, we should fall back on more complex models, i.e. network pyrolysis models. There are a number of such commercial computer codes, FG-DVC (Solomon et al., 1988), FLASHCHAIN (Niksa, 1991) and CPD (Fletcher et al., 1992) that predict the rate of the volatile release and the composition of key species linked to the resulting macroporous and microporous structure of the char. To elucidate with an example

of the importance on the choice of the devolatilization model in the unburned carbon determination, we are going to suppose that we determine the devolatilization process using both, a weight loss model and a network pyrolysis model, obtaining a difference in the volatile matter release of only 5 % between models. This difference would not affect the final solution in a heat transfer or deposition study calculation. However, in a carbon-in-ash study, considering for example a coal with a mean ash content of 6 %, this difference would result in a variation in the prediction of around 2 %. This margin may be a critical result, especially taking into account that power stations work close to the carbon-in-ash limit that allow them to sell the ash to cement factories.

Within the network pyrolysis models, we should decide which one is the most suitable for our problem. With regard to the computing capabilities and the accuracy on modelling the processes taking place during the devolatilization stage, the three models are very similar. There are a few differences as set out below (Backreedy, 2002):

- All the models give the volatile yield and weight distributions of the gas, tar and char. However, only the FG-DVC model gives the functional groups' compositions of tar and char.

- Both FG-DVC and FLASHCHAIN predict weight loss rates for tar, gas and other volatile species, while CPD does not.

These characteristics do not clarify which model is more suitable for our problem. Consequently, we should study which model determines the most realistic devolatilization process, for a wide range of coals, under typical reactor conditions. Two parameters easily measured to characterize devolatilization, are the final volatile yield and the kinetic parameters of the process (E_v, A_v). Within Backreedy's (2002) work, different devolatilization tests with DTF and HWM facilities, using typical heating rates in pulverized coal boilers (10^5 K/s), are described, comparing experimental results against predicted values from the three macromoleclar network pyrolysis models (FG-DVC, FLASHCHAIN and CPD).

The most remarkable results of Backreedy's work are summarized below:

1. In general, the three models adequately predict the volatiles yield. Only in the case where char nitrogen yield needs to be determined (in calculating NO_x predictions), did the CPD

model provide better results, since in this model, the nitrogen yield calculation is directly linked to the evolution of the coal chemical structure during pyrolysis.

2. With regard to the kinetic parameters (E_v, A_v), FG-DVC and CPD models agree better with results obtained with a DTF, while FLASHCHAIN agrees better with the ones from a HWM. This result is explained from the construction of the models itself, since the data used for the development of the FG-DVC, CPD and FLASHCHAIN models were determined from experiments on a TGA, a FFB and a HWM respectively.

The pyrolysis model gives us the final high temperature volatile yield and composition, and as a consequence, the resultant char residue in which the char oxidation model is applied. From the discussion in the first point, any of the models may be suitable for our work. However, from the results in the second point, it seems logical to choose the pyrolysis model that better reproduces the real process under typical pulverized fuel combustion conditions. To this purpose, the FG-DVC model is suitable in combustion studies developed in DTF and utility boilers (Jones et al., 1999). Therefore, because of its applicability to a wide range of coals (subbituminous, bituminous and lignites) and heating rates (0.05 to 10^5 K/s), and its ability to predict the variations in species yield with reactor conditions, FG-DVC was used in this work.

6.2 Char oxidation model

Just like with the devolatilization models, Chapter 2 presented a review of the more wide spread char oxidation models in combustion research works. Char oxidation is the slowest step in the combustion process, and therefore, it finally determines burnout. For this reason, in this stage it is especially important to carry out a description of the process in as much detail as possible. This is the weak point of CFD codes which only account for simple global or intrinsic models i.e. Field's (1967) model, Baum and Street's (1970) model or Smith's model (1978, 1982). These models ignore reactivity and porous structure variations as combustion proceeds. Consequently, they adequately predict general trends, but fail when it is necessary to obtain quantitative results.

A correct description of char porous structure variations during combustion significantly influences the results attained. For this reason it is preferable to use intrinsic models instead of global models when attempting rigorous combustion calculations. In the same way, these intrinsic models are divided into macroscopic or microscopic porous models, depending on the

level of detail used for the description of the diffusion process through the porous structure. The former models use an effective diffusion coefficient for a characteristic particle mean pore size while the latter use statistical distributions to characterize the different pore sizes in the particle and the diffusion process through them. Since the contribution of the smallest pores (micropores and mesopores) is negligible when compared with the paths provided by the larger pores (Sun and Hurt, 2000), a macroscopic characterization of the porous structure provided more than adequate accuracy for this work.

Another determining factor governing coal combustion, and especially for the unburned carbon determination in utility boilers, is the change in char reactivity during the combustion process. This behaviour is more relevant in the late stages of combustion, when char reactivity decreases, promoting a transition from Zone II to Zone I (Abd El-Samed, 1990; Hurt et al., 1993, 1999; Essenhigh, 1999). This behaviour is known as thermal annealing or deactivation of the char. Not including this effect in coal combustion calculations explains why many combustion models correctly determine burnout in DTF or burner facilities where char conversion hardly exceeds 70 %, and why they fail to predict burnout in utility boilers where char conversion easily exceeds 90 % (Hurt et al., 1998).

Another relevant factor in the char oxidation process, and therefore indicating a need to be included in the model, is the influence of the mineral matter content (Hampartsoumian et al., 1989; Unsworth et al., 1991). At low oxidation temperatures (< 600 ºC), mineral matter may have a catalytic effect on char reactivity. However, at higher temperatures (> 600 ºC) there is no evidence of this catalytic effect, and on the contrary, the presence of an ash film layer covering the particle surface area obstructs the diffusion of the oxidant to the actives sites (Chan et al., 1999). Since catalytic effects take place at temperatures less typical of pulverized coal combustion in utility boilers (> 900 ºC) and the mechanisms that cause this are not clear (Backreedy, 2002), in this work we have only considered the ash inhibition effect which is especially relevant by the end of combustion when the ash film layer usually covers the whole surface area of the particle.

Finally, another important factor governing char reactivity is the presence of various coal maceral types (Unsworth et al., 1991). Generally, reactivity is expressed as a function of coal elemental analysis. However, different studies (Hampartsoumian et al., 1989; Unsworth et al., 1991; Cloke et al., 2003) have shown that by developing expressions for reactivity as a function of coal petrographic characteristics, considerable improvements to burnout predictions due to the influence of macerals on char reactivity are realised.

Taking into account all these factors, in this work we have developed and programmed (Fortran) an intrinsic combustion model which, based on the CBK8 model (Sun and Hurt, 2000), uses several subroutines to include all the effects described in the previous paragraphs:

- Thermal annealing
- Particle porous structure evolution
- Ash inhibition effects on oxidant diffusion
- Coal macerals effects on char reactivity

The model calculates, for every time step considered, the carbon mass that has reacted. Eq. 6.1 shows how the carbon content of a particle at a defined time is calculated from the carbon content of the particle in the previous instant, minus the carbon mass that has reacted according to a reaction rate q_c, during the time interval comprising both instants considered.

$$m_c(t+\delta t) = m_c(t) - q_c \cdot (\pi \cdot d_p^2) \cdot dt \qquad \text{(Eq. 6.1)}$$

As it will be seen through the model description, there exist large gradients of the variables involved in the combustion process, so that the time step *dt* should be chosen small enough to capture all these variations in order to correctly predict burnout and also to ensure the convergence of the model.

To start with the description of the model, the inputs of the program are set below:

- Coal properties: Proximate analysis, elemental analysis, petrographic analysis, initials carbon (ρ_c) and ash (ρ_{at}) densities, specific heats (Cp_c, Cp_a), ash thermal conductivity (λ_{at}), etc.

- Model constants: Swelling factor (*Swell*), critical ash film porosity (θ_{taf}), minimum ash film thickness (δ_m), pores tortuosity (τ), reaction order (n), activation energy (E_e), parameters of the activation energies distribution of the char deactivation process (E_d, A_d, σ_{lnEd}), parameters of the CO/CO_2 formation relation (E_c, A_c), etc.

- Particle profiles data (obtained from the CFD code): Initial particle mass (m_{p0}), residence time (t_{res}), and temperatures (T_g) and oxygen partial pressures (P_g) in the cells in which the particles go through.

- Result from the devolatization stage: High temperature volatiles yield (HTVM) and resultant char residue.

- Boiler operation conditions: Boiler pressure (P_{boiler}), burners arrangement, uneven mass flow distributions through the burners, particle size distribution (d_{pm}, n_{rr}), furnace wall temperatures (T_w), etc.

The overall reaction rate q_c is determined by the oxygen transport to the particle surface and the reactivity of the char, which depends on the temperature and composition of the gaseous environment and the size, porosity and temperature of the particle. As it was described in Chapter 2, q_c is expressed as a function of the carbon mass in the particle m_c, an effectiveness factor η, an intrinsic char reactivity R_i, the temperature of the particle T_p, the oxygen partial pressure at the surface of the particle P_s and the reaction order n (Eq. 6.2). Additionally, a maceral correction factor f_{mac}, has been included to account for the influence of coal macerals on char reactivity.

$$q_c = m_c \cdot \eta \cdot R_i \cdot \left(\frac{P_s}{R \cdot T_p} \right)^n \cdot f_{mac} \qquad \text{(Eq. 6.2)}$$

To calculate the reaction rate q_c along the residence time of a particle we should determine, in every time step dt considered, all the terms on the right side of Eq. 6.2.

The char intrinsic reactivity R_i, is expressed as an Arrhenius type expression of kinetic parameters A_i and E_e (Eq. 6.3).

$$R_i = A_i \cdot \exp(-E_e / R \cdot T_p) \qquad \text{(Eq. 6.3)}$$

In the literature different values for the activation energy E_e in the range 105 – 200 kJ/mol, are reported (Smith, 1982; Mitchell and McLean, 1982; Charpenay et al., 1982; Sun and Hurt, 2000; Backreedy et al., 1999, 2002, 2006; etc.). Each author determines a value or a range of values (for different coals) of E_e, so that according to the coal combustion model used in the calculations, the combustion process is correctly described. However, as will be explained later, the combustion model developed in this work allows us to use different thermal annealing subroutines, so that it is not possible to use a single value of E_e for all of them. For this reason, depending on the sub-model used in the calculations and also on coal properties, a range of

values for E_e is specifically defined. We will take up this discussion again, once the thermal annealing sub-models have been described.

Returning to Eq. 6.3, it is obvious that if kinetic parameters (E_e, A_i) are defined with constant values, the reactivity over the whole process will remain invariable. This way, the decrease in the char reactivity is neglected and as a result burnout may be over-predicted. For this reason, we have introduced in the model, through the pre-exponential factor, a deactivation function to account for char reactivity loss. Moreover, in this work we have programmed three different char deactivation sub-models (Hurt et al., 1998; Van der Lans et al., 1998; and Backreedy et al., 2006), making it possible to choose the appropriate model depending on the type of problem, thus providing a more flexible use of the combustion code. For example, the Hurt et al. (1998) thermal deactivation sub-model adequately reproduces char reactivity loss in DTF combustion tests, as it is shown in Figure 2.8 (Chapter 2). However, since there may exist a significant difference in the heating rate and furnace environmental conditions in a full scale boiler, this sub-model tends to overvalue the reactivity loss. For this reason, we have also included two additional models that mitigate this effect and can accurately reproduce power plant data. We will take up this discussion again during the validation of the model. Next, the formulation of the three thermal annealing sub-models is described.

The thermal annealing sub-model described by Hurt et al. (1998) is developed from Suuberg's (1991) work. In this model a deactivation function $f_E(E_d(t))$ is used to account for the decreasing of active sites (local emplacements where oxidation reactions may take place) in the char matrix.

$$A_i = k \cdot S = k_0 \cdot S_0 \cdot \int_0^{\infty} f_E(E_d(t))dE_d \qquad \text{(Eq. 6.4)}$$

Where, the product kS represents a specific char intrinsic reactivity, and k_0S_0 the initial specific char intrinsic reactivity, defined as a function of the coal rank according to Eq. 6.5 (Sun et al., 2000).

$$Log_{10}(k_0 \cdot S_0) = 14{,}97 - 0.0764 \cdot \%C \qquad \text{(Eq. 6.5)}$$

The time variation of the distribution function $f_E(E_d(t))$ is assumed to obey a first-order thermal process according to Eq. 6.6.

$$\frac{\delta f_E(E_d(t))}{\delta t} = -f_E(E_d(t)) \cdot A_d \exp(-\frac{E_d(t)}{R \cdot T_p}) \quad \text{(Eq. 6.6)}$$

Introducing Eq. 6.6 into Eq. 6.4, and then, discretizating the integral in E_d, for a number (30) of equivalent intervals (Hurt et al., 1998), the general expression of the thermal annealing process is expressed according to Eq. 6.7. Then, this equation is introduced in the main model through Eq. 6.3.

$$A_{i\,(t+\Delta t)} = k \cdot S = k_0 \cdot S_0 \cdot \sum_{i=1}^{30} \left[f_{Ei\,(t)} \cdot \left(\exp\left(-\Delta t \cdot A_d \cdot \exp\left(\frac{-E_{di}}{R \cdot T_p} \right) \right) \right) \right] \quad \text{(Eq. 6.7)}$$

Where, $f_{Ei\,(t)}$ is the value of the distribution function for an activation energy E_{di} at the initial instant t of the time interval considered. At time zero, the distribution function $f_{Ei\,(t=0)}$ is assumed to be a normalized lognormal distribution in E_{di} (Eq. 6.8) with parameters E_{dm} =16.44 kcal/mol, σ_{lnEd}=0.46 ln kcal/mol and A_d =8.863E+7 s^{-1} (Sun and Hurt, 2000) (Figure 6.2).

$$f_{Ei\,(t=0)}(E_d) = \frac{1}{\sigma_{\ln Ed} \cdot \sqrt{2 \cdot \pi}} \exp\left[\frac{-(E_d - E_{dm})^2}{2 \cdot \sigma_{\ln Ed}^{\,2}} \right] \quad \text{(Eq. 6.8)}$$

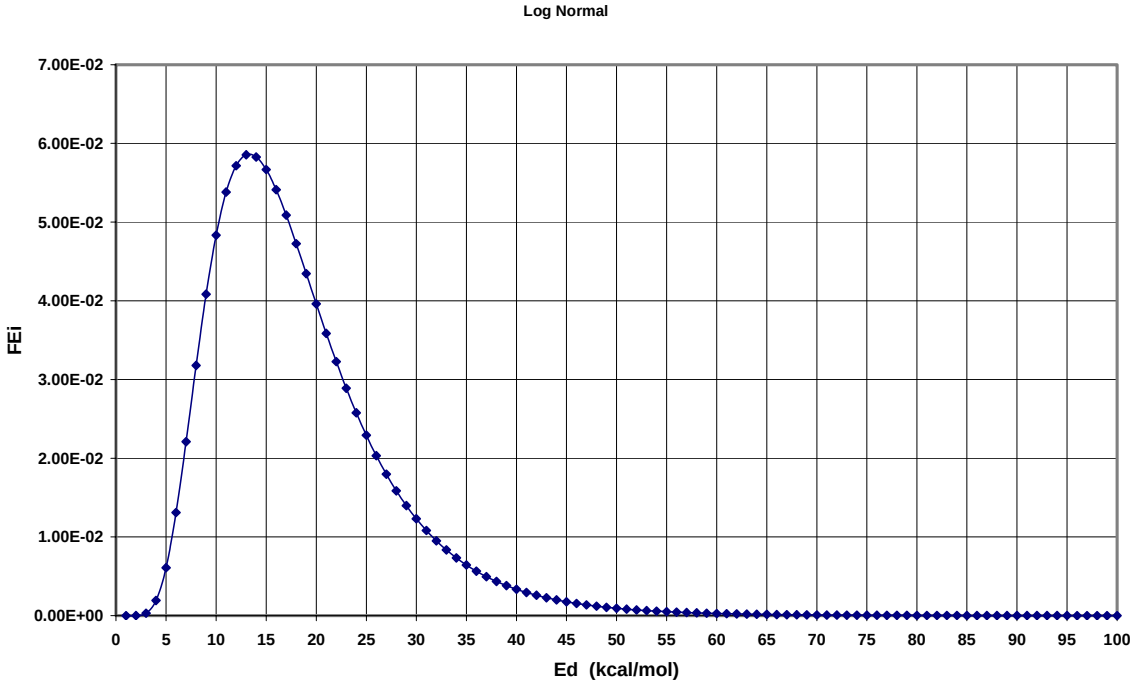

Fig. 6.2 Normalized lognormal distribution function in E_d of the thermal deactivation process at time zero

To discretize the distribution function in thirty intervals, the initial values for the activation energies E_{di} have been chosen in order that the probability of finding active sites was greater than 0.0001 with activation energies E_{di} at time zero, (Table 6.1).

E_{d1}=5	f_{E1}=0.01	E_{d16}=34	f_{E16}=0.01502
E_{d2}=6	f_{E2}=0.02144	E_{d17}=36	f_{E17}=0.0113
E_{d3}=8	f_{E3}=0.0636	E_{d18}=38	f_{E18}=0.00915
E_{d4}=10	f_{E4}=0.0971	E_{d19}=40	f_{E19}=0.00675
E_{d5}=12	f_{E5}=0.1128	E_{d20}=42	f_{E20}=0.005
E_{d6}=14	f_{E6}=0.1197	E_{d21}=44	f_{E21}=0.004
E_{d7}=16	f_{E7}=0.10256	E_{d22}=46	f_{E22}=0.003
E_{d8}=18	f_{E8}=0.0938	E_{d23}=48	f_{E23}=0.003
E_{d9}=20	f_{E9}=0.0802	E_{d24}=50	f_{E24}=0.002
E_{d10}=22	f_{E10}=0.0654	E_{d25}=52	f_{E25}=0.002
E_{d11}=24	f_{E11}=0.0513	E_{d26}=54	f_{E26}=0.001
E_{d12}=26	f_{E12}=0.0413	E_{d27}=56	f_{E27}=0.001
E_{d13}=28	f_{E13}=0.0308	E_{d28}=58	f_{E28}=0.001
E_{d14}=30	f_{E14}=0.02551	E_{d29}=60	f_{E29}=0.001
E_{d15}=32	f_{E15}=0.01827	E_{d30}=61	f_{E30}=0.001

Table 6.1 Discretization in thirty intervals, of the activation energies E_{di} for the thermal annealing process and the corresponding values of the distribution function $f_{Ei}(E_d)$ at time zero

At any other instant, the distribution function is calculated from the values obtained in the precedent instant according to Eq. 6.9.

$$f_{Ei\,(t+\delta t)} = f_{Ei\,(t)} \cdot \left(\exp\left(-dt \cdot A_d \cdot \exp\left(\frac{-E_{di}}{R \cdot T_p} \right) \right) \right) \qquad \text{(Eq. 6.9)}$$

Other authors have preferred to develop alternative expressions for the char reactivity deactivation, i.e. Van der Lans et al. (1998) or Backreedy et al. (2006) who expressed the reactivity loss by thermal annealing as a function of char conversion m_c/m_{c0} (Eqs. 6.10 and 6.11-6.13 respectively).

$$A_i = k \cdot S = k_0 \cdot S_0 \cdot \left(1 - \left(\frac{m_c}{m_{c0}} \right) \right)^{0.5} \qquad \text{(Eq. 6.10)}$$

$$A_i = f_{ann} \cdot \alpha_D \cdot A_0 \qquad \text{(Eq. 6.11)}$$

$$\alpha_D = 0.3 \cdot \left(-28.44 \cdot \left(\frac{m_c}{m_{c0}} \right)^4 + 85.33 \cdot \left(\frac{m_c}{m_{c0}} \right)^3 - 85.33 \cdot \left(\frac{m_c}{m_{c0}} \right)^2 + 28.44 \cdot \left(\frac{m_c}{m_{c0}} \right) + 1 \right) \qquad \text{(Eq. 6.12)}$$

$f_{ann} = 0.9$ if 70 % < %C < 90%, 20 μm < d_p < 100 μm, T_p > 1400 ºC (Eq. 6.13)

Taking up again the discussion posed in Eq. 6.3 about the choice of the activation energy E_e; from the validation of the model, and using the three thermal deactivation sub-models, the values for the coals used in this study are presented:

- E_e = 162 ± 10 kJ/mol in case of using Van der Lans et al. (1998) or Backreedy et al. (2006) thermal annealing sub-model.

- E_e = 140 ± 10 kJ/mol in case of using Hurt et al. (1998) thermal annealing sub-model.

The efficiency of the diffusion process through the porous structure of the char is expressed by means of an effectiveness factor η. This factor is obtained from the integration of the mass balance of the reactive for a porous spherical particle under catalytic reaction, assuming a first order reaction (Eq. 6.14).

$$\eta = \frac{3}{\phi}\left[\frac{1}{\tanh(\phi)} - \frac{1}{(\phi)}\right] \quad \text{(Eq. 6.14)}$$

Where, ϕ is the Thiele modulus that combines the reaction and diffusion phenomena as is shown in Eq. 6.15.

$$\phi = \frac{d_p}{6} \cdot \left[\frac{(n+1)\cdot \rho \cdot R_i \cdot (P_s / R \cdot T_p)^{n-1}}{2 \cdot D_{eff}}\right]^{0.5} \quad \text{(Eq. 6.15)}$$

This way, an effectiveness factor close to unity indicates that the reaction is within Zone I where the observed reaction rate is approximately equal to the intrinsic reaction rate. Effectiveness factors much less than unity indicate that the reaction is within Zone II where the observed reaction rate is much less than the intrinsic reaction rate, due to a decrease in the diffusion rate (Sun and Hurt, 2000).

To account for the porous nature of the char, and the fact that the oxidant penetrates this structure and reacts on the internal surface area, the effective diffusivity D_{eff} to the interior of the particle is modelled as a function of the particle porosity θ and a geometric pore factor τ/f = 6, according to a macroscopic pore model given by Eq. 6.16.

$$D_{eff} = D_{O2} \cdot \frac{\theta \cdot f}{\tau} \quad \text{(Eq. 6.16)}$$

Where, the effective diffusivity is expressed as a function of the bulk diffusivity (Eq. 6.17) assuming that the larger pores mainly provide the paths to the diffusion of the oxidant, while micropores and mesopores (< 1 μm), in which a Knudssen diffusion type is expected, hardly contribute to the oxygen transport (Gale et al., 1996; Sun and Hurt, 2000).

$$D_{O2} = 1.543 \cdot \frac{T_m^{1.67}}{P_{boiler}} \quad \text{(Eq. 6.17)}$$

The transition from Zone II to Zone I in the late stages of combustion, is the result of the extinction phenomena. To explain this behaviour, a different mechanism has been considered that includes reactivity loss by thermal annealing and ash inhibition effects. The thermal annealing process has already been explained in the previous paragraphs, so next, the ash film layer effect term within the model is discussed. To aid the explanation, we will consider an alternative expression to Eq. 6.2, in which the reaction rate q_c is expressed as a function of a diffusion kinetic constant k_d according to Eq. 6.18.

$$q_c = k_d (P_g - P_s) \quad \text{(Eq. 6.18)}$$

If only the diffusion of the oxidant through the boundary layer that surrounds the char particle is considered, then the diffusion kinetic constant k_d can be expressed, for example, according to Field's (1967) or Baum and Street's (1970) expressions (Eqs. 6.19 and 6.20 respectively)

$$k_d = \frac{24 \cdot \varphi \cdot D_{O2}}{d_p \cdot R \cdot T_m} \quad \text{(Eq. 6.19)}$$

$$k_d = \frac{2.53E-7 \cdot \varphi}{d_p} \cdot \left(\frac{T_p + T_g}{2} \right)^{0.75} \cdot \left(\frac{1}{10} \right) \quad \text{(Eq. 6.20)}$$

However, if it is desirable to include the effect of the ash, this diffusion kinetic constant k_d should account for an additional resistance due to the ash film layer covering the particle surface (Hurt et al., 1998) (Eq. 6.21).

$$k_d = \frac{Sh \cdot D_{O2} \cdot d_p \cdot {\theta_{af}}^{2,5}}{R \cdot T_m \cdot (Sh \cdot \delta \cdot d_c + {\theta_{af}}^{2,5} \cdot {d_c}^{2,5})} \quad \text{(Eq. 6.21)}$$

Where, *Sh* is the Sherwood dimensionless number (for characteristic pulverized coal sizes, *Sh* = 2), θ_{af} is the ash film porosity, δ is the ash film thickness and d_c is the char particle diameter excluding the ash film layer (Eq. 6.22).

$$d_p = d_c + 2 \cdot \delta \quad \text{(Eq. 6.22)}$$

In the same way as other determining factors considered in the model, the description of the ash film layer (d_p, d_c, δ, θ_{af}, ρ_c, ρ_a) does not remain invariable during the combustion process. In the beginning, when carbon conversion is small, the ash film layer is dispersed in the form of grains over the particle surface, filling a minimum thickness δ_m. As the conversion progresses, more grains are added, decreasing the porosity of the film. After a certain time, the grains start to agglomerate, increasing the ash film thickness to within a constant porosity value called the critical ash film porosity. Consequently, we may assume two different states: first, a state in which a minimum ash film thickness remains constant, while the ash film porosity decreases so long as more grains are added to the ash layer; and second, a state in which a critical porosity is reached remaining constant onwards, while the ash film thickness increases. To define the transition through these states, Hurt et al. (1998) propose to calculate, at every time step considered, the ash film thickness corresponding to the critical porosity ($\theta_{af} = \theta_{taf}$ = 0.16 - 0.25) from Eqs. 6.22 and 6.23.

$$d_c = d_p \cdot \left(\frac{(X_a \cdot \rho - \rho_{at} \cdot (1 - \theta_{taf}))}{(X_{a0} \cdot \rho_c - \rho_{at} \cdot (1 - \theta_{taf}))} \right)^{1/3} \quad \text{(Eq. 6.23)}$$

$$\theta_{af} = 1 - \left(\frac{X_a \cdot \rho - X_{a0} \cdot \rho_0 \cdot (1 - \frac{2 \cdot \delta_m}{d_p})^3}{\rho_{at} - \rho_{at} \cdot (1 - \frac{2 \cdot \delta_m}{d_p})^3} \right) \quad \text{(Eq. 6.24)}$$

If the calculated ash film thickness is lower than the minimum ash film thickness considered (5 μm), which corresponds with the mean grain size, then it is assumed that $\delta = \delta_m$, and both the ash film porosity θ_{af} and the particle diameter d_p, are recalculated according to Eqs. 6.22 and 6.24. On the other hand, if the calculated ash film thickness is larger than the minimum ash film

thickness, then the initial assumption that considers the critical ash film porosity has been reached, $\theta_{af} = \theta_{taf}$ is maintained and it is not necessary to recalculate d_p, d_c and δ.

Again, to allow a greater flexibility to the model, the user can choose to include this ash inhibition effect through Eq. 6.21, or on the contrary, to obviate it using the default expression given in Eq. 6.20.

For the moment, most of the expressions presented depend in some way on char properties (d_p, d_c, δ, θ, ρ_c, ρ_a, X_a.). Since combustion is a dynamic process, it is also necessary to calculate the density and particle diameter variations at every time step along the whole combustion process. Assuming a decrease in density and particle diameter with burnout, Hurt et al. (1998) postulate a decrease in the particle core density according to Eq. 6.25.

$$\frac{\rho_c}{\rho_{c0}} = \left(\frac{m_c}{m_{c0}} \right)^{0.2} \qquad \text{(Eq. 6.25)}$$

$$\rho_a = \rho_{at} \cdot (1 - \theta_{af}) \qquad \text{(Eq. 6.26)}$$

From the carbon core density ρ_c (corresponding to a core diameter d_c) and the ash film density (calculated according to Eq. 6.26 as a function of the ash density ρ_{at} = 2.65 g/cm^3 and the ash film porosity θ_{af}), the overall particle density is obtained (Eq. 6.27).

$$\frac{1}{\rho} = \frac{(1 - X_a)}{\rho_c} + \frac{X_a}{\rho_a} \qquad \text{(Eq. 6.27)}$$

Finally, the char particle diameter is calculated from geometric considerations according to Eq. 6.28.

$$\frac{d_p}{d_{p0}} = \left(\frac{m_p}{m_{p0}} \cdot \frac{\rho_0}{\rho} \right)^{1/3} \qquad \text{(Eq. 6.28)}$$

Additionally, swelling of the particle during devolatilization is accounted for by including a swelling factor that modifies the initial diameter and then the density of the char particle. This swelling factor is an input of the model and should be determined experimentally for each coal.

Returning to Eq. 6.2, there is still the missing definition of the maceral factor f_{mac}, in which the influence of coal macerals on char reactivity is introduced. According to Hampartsoumian et al. (1989), the introduction of this term is especially important with coals coming from the southern hemisphere, since generally these coals have an inertinite content higher than those in the northern hemisphere and inertinite macerals take more time to complete combustion than vitrinite macerals (Unsworth et al., 1991). This factor is computed in the model from the work of Hampartsoumian et al. (1989), in which f_{mac} is described as a function of the vitrinite, pseudovitrinite, inertinite and fussinite content of the parent coal (Eq. 6.29).

$$f_{mac} = \left[1.4 \cdot \left(Vit_M + 0.83 \cdot Vit_{PS}\right)\right] - \left[0.6 \cdot \left(In_R + 1.6 \cdot In_{LR}\right)\right] \quad \text{(Eq. 6.29)}$$

Since, power stations do not generally perform this petrographic analysis, it may be useful to include in the model an abbreviated expression for Eq. 6.29 where the maceral factor f_{mac} is expressed exclusively as a function of the vitrinite and inertinite content (Eq. 6.30) (Backreedy et al., 2006).

$$f_{mac} = 1.68 \cdot Vit - 0.6 \cdot In \quad \text{(Eq. 6.30)}$$

One important consideration that has not yet been discussed, and represents possibly the most controversial discussion in the scientific community as was exposed in Chapter 2, is the magnitude of reaction order with respect to O_2. In this work, since the model is based on the CBK8 model (Sun and Hurt, 2000), we have adopted the same reaction order $n = 0.5$.

Once the main characteristics of the model have been defined, the resolution method is explained. Eq. 6.2 is defined as a function of the oxygen partial pressure P_s at the particle surface and the particle temperature T_p (assuming a constant temperature in the whole particle). However, the oxygen partial pressure and temperature profiles obtained from the solutions of the CFD code are defined at every cell in which a particle passes through (T_g , P_g), that is in the nearby field of the particle but not at its surface (T_p ,P_s). To solve this situation we have made use of the iterative method scheme in Figure 6.3. From Eqs. 6.2 and 6.18, and by guessing a value for the oxygen partial pressure at the particle surface P_{S0}, a Newton-Raphson method to determine the oxygen partial pressure at the particle surface P_S, is applied in an inner iteration loop, comparing the reaction rates q_c until the error is driven to zero (Error P_s < 0.001 atm). In the same way, from Eq. 6.2 considering the energy balance in the particle (Eq. 6.31) and guessing a value for the particle temperature T_{p0}, a Newton-Raphson method to determine the

particle temperature T_p, is applied in an outer iteration loop, which includes the previous inner loop, comparing the reaction rates q_c until the error is driven to zero (Error T_p < 0.1 K).

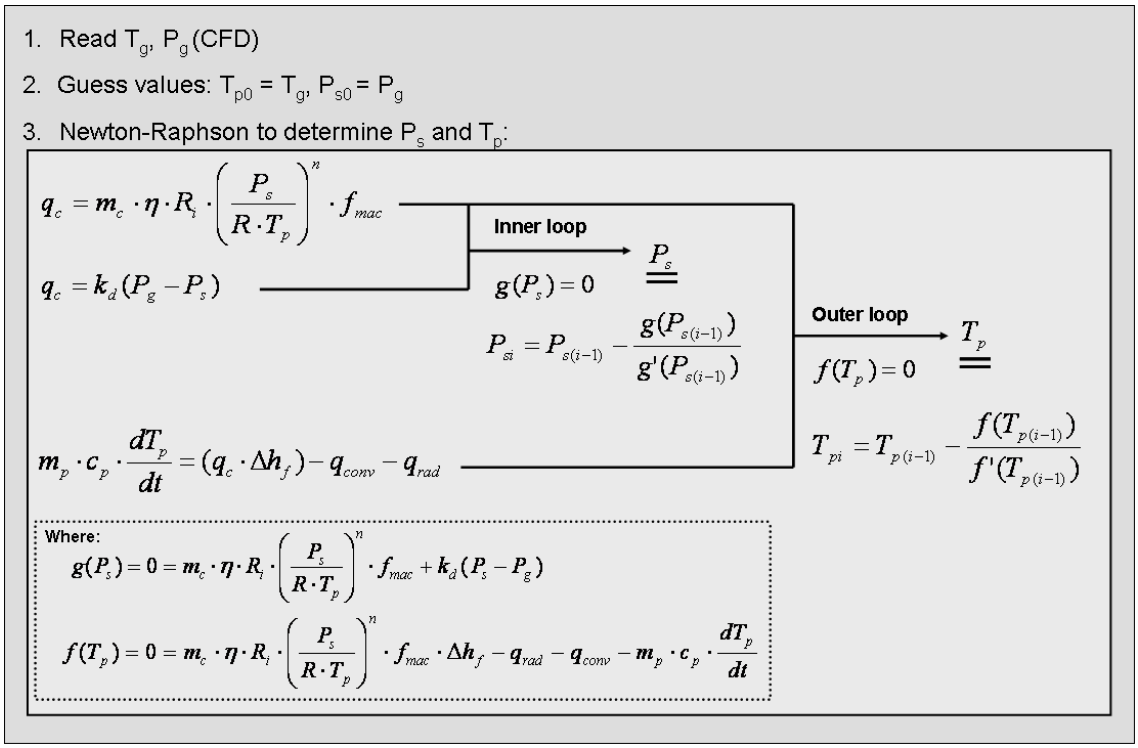

Fig. 6.3 Numerical resolution method scheme for T_p and P_s determination

In general, the convergence of the method is quickly achieved using as estimates for T_{p0} and P_{s0}, the corresponding gas stream values (T_g and P_g) and evaluating all the properties in the middle of the time interval ($t + \delta t/2$). However, during the first milliseconds of the combustion process, there exist large temperature and oxygen partial pressure gradients. Consequently, to ensure the convergence of the particle heat balance (Eq. 6.31), a grid refinement in the CFD model was carried out in the near burner area to obtain data for key variables approximately every 5 ms. Additionally, in cases where the temperature change was greater than 100 K, the char combustion routine subdivides the calculations into smaller time intervals by linear interpolation of the bulk variables. Figure 6.4 shows an example of the difference in the evaluation of the reaction rate q_c within a time interval in which there exists a large temperature gradient (400 to 2000 K). Considering just one time interval, since the reaction rate is computed from the values of the bulk variables in the middle of the time interval, q_c is given by the dashed-line of the checked area in Figure 6.4. In contrast, subdividing the calculation into smaller time intervals, the computed q_c is given by the dotted-line of the plain area in Figure 6.4 and shows a more realistic description of the reaction rate.

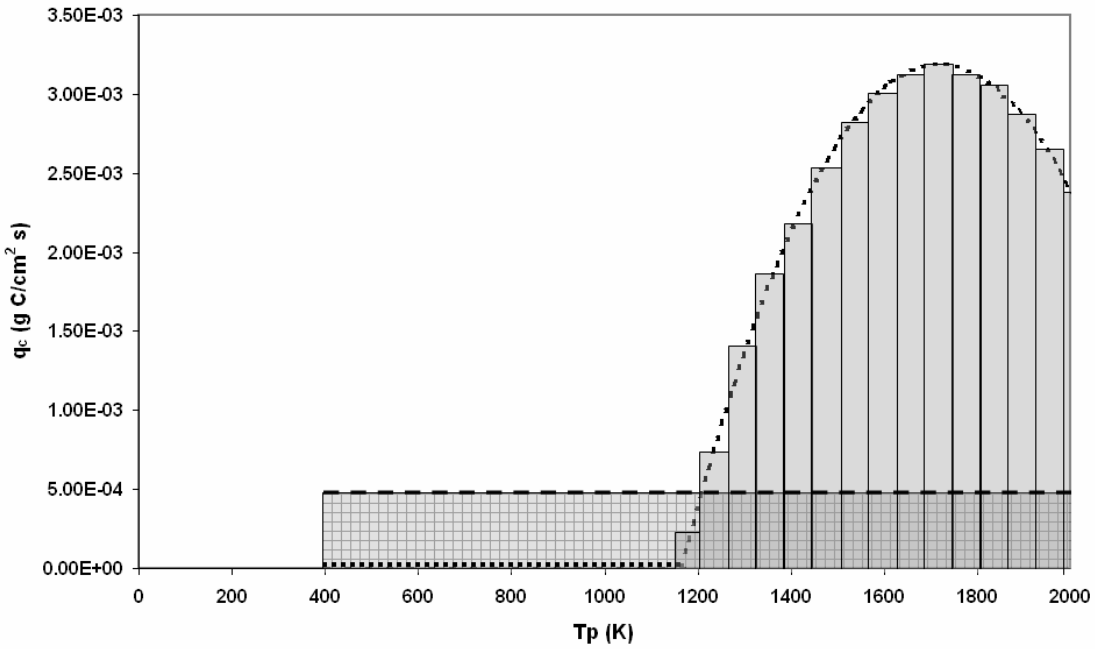

Fig. 6.4 Comparison of the reaction rate q_c within a time interval in which there exists a large temperature gradient: Considering one time interval (dashed-line in the checked area) and subdividing the calculation into smaller time intervals (dotted-line in the plain area)

In the iterative resolution of the particle temperature and oxygen partial pressure, an energy balance in the particle is carried out according to Eq. 6.31.

$$m_p \cdot c_p \cdot \frac{dT_p}{dt} = (q_c \cdot \Delta h_f) - q_{conv} - q_{rad} \qquad \text{(Eq. 6.31)}$$

The temperature variation in the particle is due to the contribution of three sources: reaction, convection and radiation. Below, all these terms are briefly explained.

Firstly, since we are considering small enough time steps Δt, we can linearize the variation of temperature with time in the interval (Eq. 6.32).

$$\frac{dT_p}{dt} \approx \frac{T_p - T_{pant}}{\Delta t} \qquad \text{(Eq. 6.32)}$$

The convective term is calculated through a global heat transfer coefficient U defined as a function of the dimensions of the particle, the ash film layer and two convective heat transfer coefficients (Eqs. 6.33 – 6.37) (Sun and Hurt, 2000).

$$q_{conv} = U \cdot (T_p - T_g) \quad \text{(Eq. 6.33)}$$

$$U = \frac{\left(\frac{d_p}{d_c}\right)^2}{\left(\frac{1}{h_{ext}} + \frac{1}{h_{\text{int}}}\right)} \quad \text{(Eq. 6.34)}$$

$$h_{ext} = \frac{\lambda_g \cdot Nu}{d_p} \quad \text{(Eq. 6.35)}$$

$$h_{\text{int}} = \frac{2 \cdot \lambda_a}{\delta} \cdot \frac{d_c}{d_p} \quad \text{(Eq. 6.36)}$$

$$\lambda_a = \theta_{af} \cdot \lambda_g + (1 - \theta_{af}) \cdot \lambda_{at} \quad \text{(Eq. 6.37)}$$

The radiative term is calculated according to Eq. 6.38, in which T_w is the furnace wall temperature.

$$q_{rad} = \sigma_B \cdot \varepsilon \cdot (T_p^{\,4} - T_w^{\,4}) \quad \text{(Eq. 6.38)}$$

Finally, the term Δh_f represents the combustion enthalpy of the oxidation reaction to CO/CO_2 (Eq. 6.39). The heat released in the reaction to CO_2 is three and half times higher than in the reaction to CO, so that the particle temperature strongly depends on the formation relation of CO/CO_2 (Longwell et al., 1993).

$$\Delta h_f = \Delta h_{CO2} \cdot f_{CO2} + \Delta h_{CO} \cdot (1 - f_{CO2}) \quad \text{(Eq. 6.39)}$$

Where, f_{CO} is the carbon fraction that reacts to give CO_2, calculated as a function of the particle temperature according to Eqs. 6.40 and 6.41.

$$f_{CO2} = \frac{1}{1 + CO/CO2} \quad \text{(Eq. 6.40)}$$

$$CO/CO2 = A_c \cdot \exp(-E_c / R \cdot T_p) \qquad \text{(Eq. 6.41)}$$

To close this section, Figure 6.5 summarizes the resolution scheme of the char oxidation sub-model, in order to determine the unburned carbon losses.

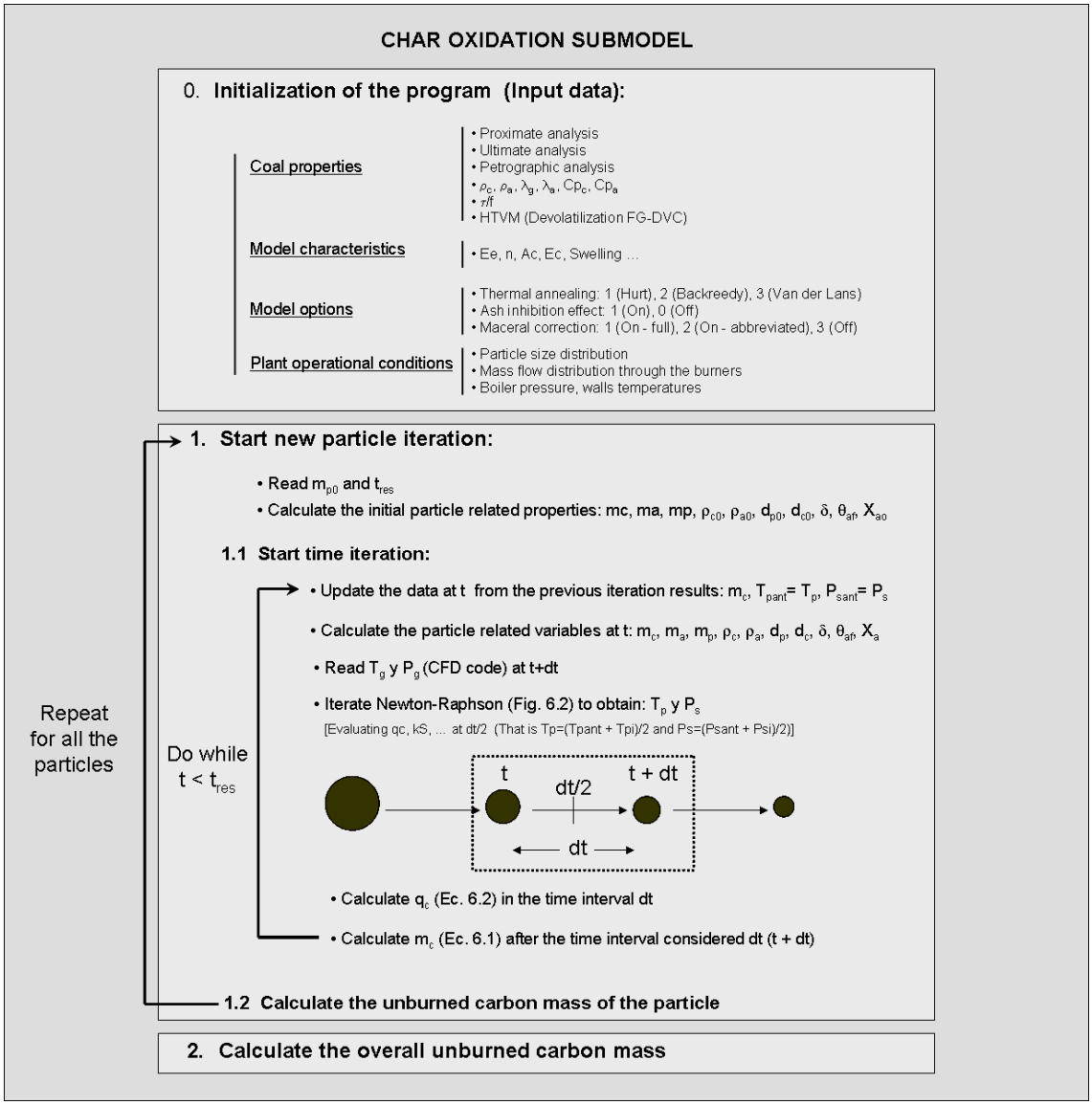

Fig. 6.5 Resolution method scheme of the char oxidation sub-model

6.3 Validation of the advanced combustion model

To investigate the burnout prediction capability of the model a total of nine scenarios, presented in Table 2 were tested with standard plant instrumentation measurements gathered at the Lamarmora (ASM Brescia) power station in the year 2005. Study cases were selected covering

the regular range of variation in mean oxygen (vol. %) and flue gases (2.5 – 4 %) under full load operating conditions. Differences among scenarios are the result of the normal operation of the plant where small variations in operating conditions and mass flow imbalances between mills are encountered. The mills' classifiers were adjusted to give a particle size distribution of mean diameter of 55 μm. Table 6.3 summarizes the operation conditions during the tests.

In the study, two coals from Central America commonly used in the plant over the last five years ('Guasare' from Venezuela and 'Carboandes' from Colombia) and a coal from Russia, recently used to evaluate its influence on the combustion efficiency, were burned separately. Table 6.2 shows the proximate, ultimate and petrographic (when available) analysis for these three coals. Since no petrographic analysis was available, inertinite and vitrinite values for Guasare coal were taken from Barranco et al. (2003).

Proximate analysis (as received)	**Guasare**	**Carboandes**	**Russian**
Moisture (%)	6.91	9.6	9.56
Ash (%)	5.75	6.44	7.14
Volatile (%)	35	34.17	36.09
Fixed carbon (%)	52.34	49.79	47.21
Ultimate analysis (as received)			
Carbon (%)	72.75	69.21	65.62
Hidrogen (%)	4.93	4.38	4.66
Oxigen (%)	7.75	8.38	10.74
Nitrogen (%)	1.27	1.36	1.9
Sulfur (%)	0.64	0.64	0.38
Petrographic analysis			
Inertinite (%)	0.24	N/A	N/A
Vitrinite (%)	0.76	N/A	N/A
Heating value			
HHV (kcal/kg)	7220	6715	6725

Table 6.2 Proximate, ultimate and petrographic analysis for the three study coals (fixed carbon calculated by difference)

Scenarios	Case 1	Case 2	Case 3	Case 4	Case 5	Case 6	Case 7	Case 8	Case 9
Coal type	Guasare	Guasare	Guasare	Carboandes	Carboandes	Carboandes	Russian	Russian	Russian
Mill 1 load (t/h)	12.4	12.53	10.43	13.28	13.06	12.93	13.4	13.44	13.41
Mill 2 load (t/h)	12.44	12.6	10.46	13.3	13.01	13.04	13.27	13.42	13.48
Total air flow rate (kNm3/h)	208.03	218.45	181.41	218.29	215.11	209.39	219.11	218.68	216.73
Primary air flow rate Mill 1 (kNm3/h)	25.28	25.39	23.60	26.03	25.85	25.73	26.14	26.17	26.14
Primary air flow rate Mill 2 (kNm3/h)	25.32	25.45	23.63	26.05	25.80	25.83	26.02	26.15	26.21
Primary air T^a (°C)	80	80	80	80	80	80	80	80	80
Secondary air flow rate (kNm3/h)	157.43	167.61	134.19	166.21	163.46	157.83	166.95	166.36	164.38
T^a secondary air (°C)	249.9	257	254.39	256.48	254.99	257.29	254.21	254.9	254.18
Mean particle size (μm) *	55	55	55	55	55	55	55	55	55
% O2 (exit boiler)	3.18	3.91	3.52	3.81	3.48	3.45	3.31	3.06	2.97

Table 6.3 Nominal-load operating scenarios from the case study power plant

* Rosin Rammler distribution (d_{pm} = 55 μm, n_{rr} = 1.02)

The CFD model was applied to these nine cases. Solutions in the form of the gas temperature and the oxygen partial pressure profiles that every representative coal particle is subject to was obtained, and subsequently used as an input in the coal combustion kinetic model. Fig. 6.6 shows an example of the variation in these temperature and oxygen partial pressure profiles among particles as a result of the complex fluid dynamics involved in the problem. This example gives an idea of the importance of carrying out a detailed description of the thermal and fluid dynamic behaviour. This approach (CFD + advanced combustion model) permits the model to be sensitive to the changes that arise from slight changes in operating conditions and uneven flow variations which strongly affects the overall burnout prediction. This fact represents an advantage over other zonal-based predictive models which commonly consider a reduced number of zones and particle trajectories.

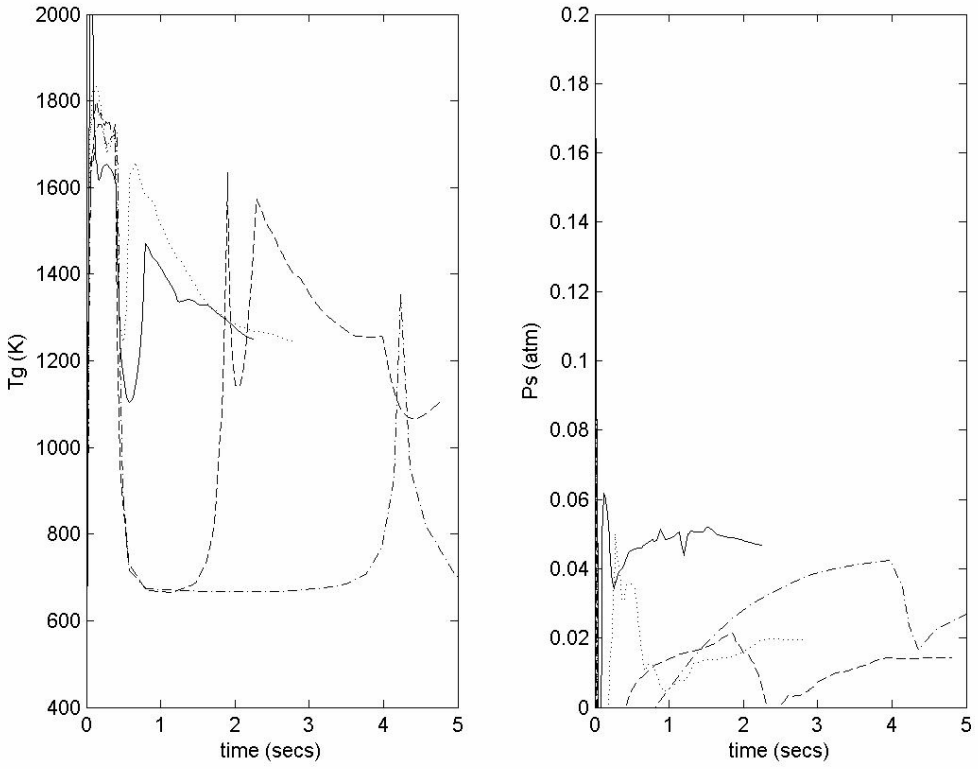

Fig. 6.6 Oxygen partial pressure and temperature CFD profiles for a number of representative particles of the same size (103 μm) fed from different locations in the same burner (Burner 1) under full load conditions (Case 1)

Once the simulations have been run and the accuracy of the numerical resolution has been verified according to the methodology described in Chapters 3 and 4 so as to validate the CFD model, predictions on the oxygen content in flue gases were compared with available plant measurements for the scenarios tested, which showed good agreement as shown in Table 6.4.

This table, along with the predictions of burnout hereinafter discussed, permit to conclude that the simulation of coal combustion was reasonable for the variety of coal feedstock tested.

Scenarios	Case 1	Case 2	Case 3	Case 4	Case 5	Case 6	Case 7	Case 8	Case 9
Meean % O_2 plant value	2.63	3.57	3.1	3.63	3.21	3.37	3.31	3.02	2.89
Meean % O_2 CFD prediction	3.18	3.91	3.52	3.81	3.48	3.45	3.31	3.06	2.97

Table 6.4 Experimental values compared with numerical predictions for mean oxygen content (vol. %) in the flue gases for the nine simulated scenarios

Then, to determine char and volatile yields, FG-DVC calculations were performed under conditions relevant to pulverised coal combustion, namely a heating rate of 10^5 K/s and final temperature of 1750 K for 150 ms have been considered to be appropriate conditions. Tables 6.5 and 6.6 show the predicted yield and composition for char, tar, gas and paraffins and olefins during the pyrolysis.

Coal	char (%)	tar (%)	gas (%)	P-O (%)
Guasare	49	34.8	13.4	2.8
Carboandes	45.7	38	13.4	2.9
Russian	51.9	26.4	18.1	3.7

Table 6.5 Predicted char, tar, gas and (paraffins and olefins) yields (%) by FG-DVC for the study coals (10^5 K/s – 1750 K – 150 ms)

Guasare	%	c	h	o	n	s
char	49	96.5	1.34	0	1.68	0.49
tar	34.8	83.96	5.48	8.4	1.47	0.69
gas	13.4	41.74	19.12	36.81	0.71	1.62
o + p	2.8	84.53	15.47	0	0	0

Carbonandes	%	c	h	o	n	s
char	45.7	97.22	0.39	0	1.88	0.51
tar	38	83.25	5.01	9.39	1.64	0.72
gas	13.4	39.05	19.21	39.4	0.78	1.57
o + p	2.9	84.56	15.44	0	0	0

Russian	%	c	h	o	n	s
char	51.9	95.94	1.02	0	2.71	0.32
tar	26.4	80.23	5.37	11.64	2.35	0.41
gas	18.1	36.17	16.73	45.08	1.18	0.85
o + p	3.7	84.64	15.36	0	0	0

Table 6.6 Predicted char, tar, gas and (paraffins and olefins) elemental composition (%) by FG-DVC for the study coals (10^5 K/s – 1750 K – 150 ms)

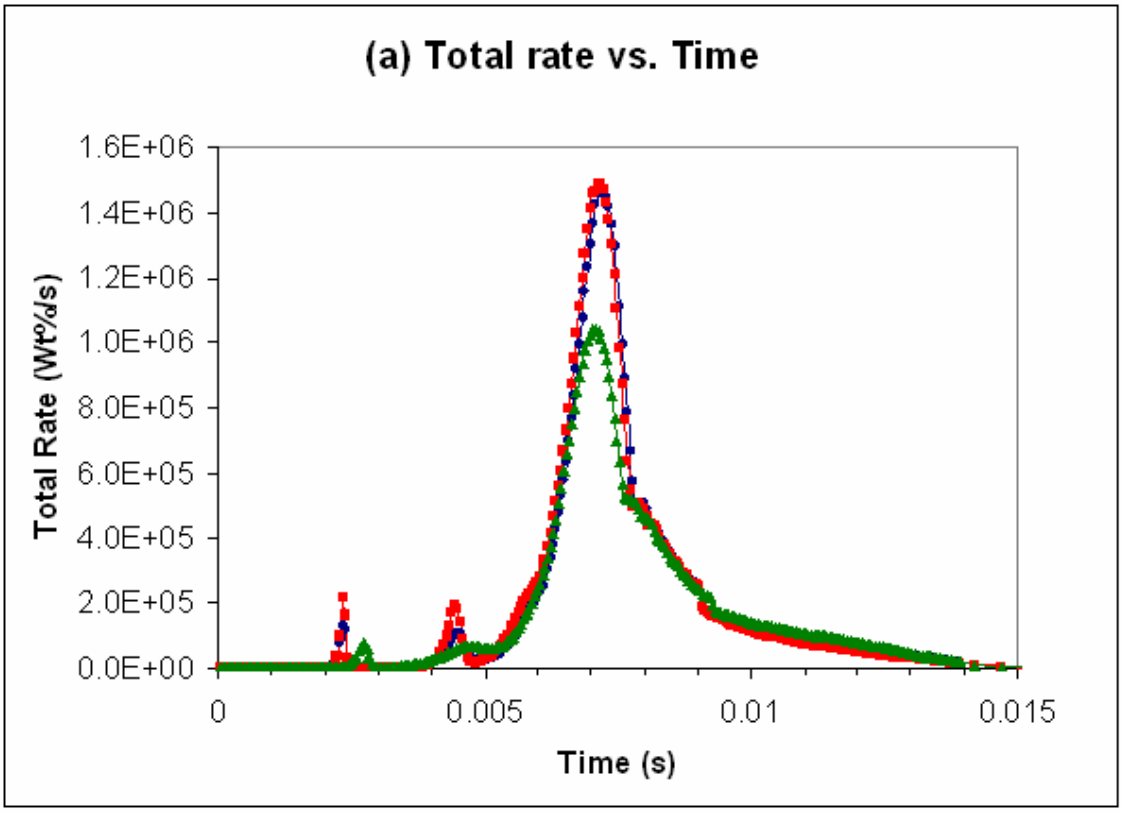

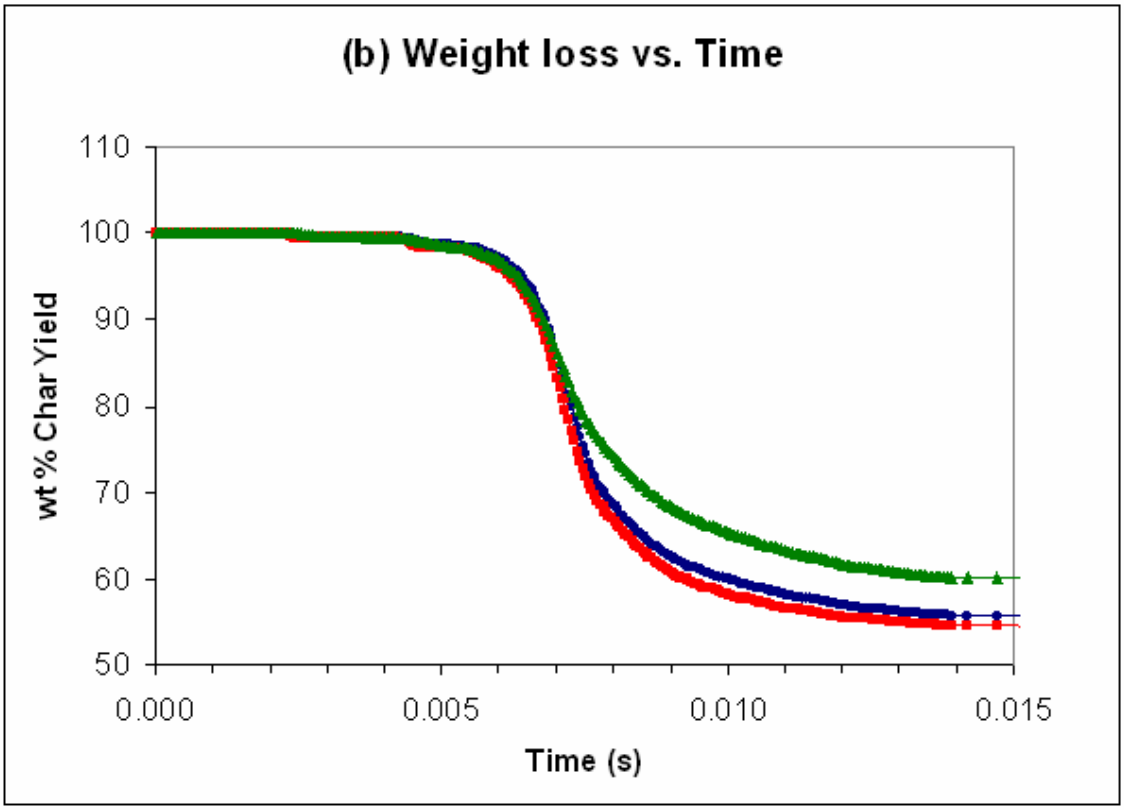

Fig. 6.7 FG-DVC (10^5 K/s – 1750 K – 150 ms). (a) Total rate vs. Time (b) Weight loss vs. Time, for ● Guasare, ■ Carboandes and ▲ Russian coals

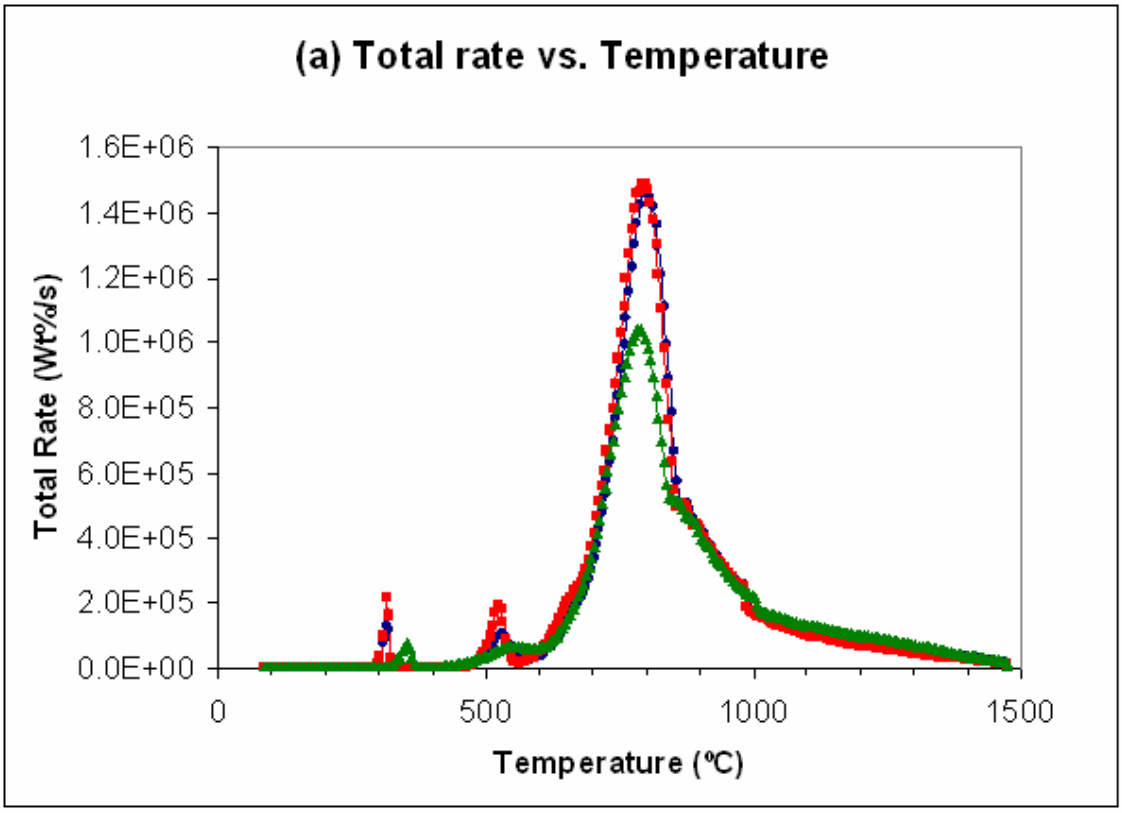

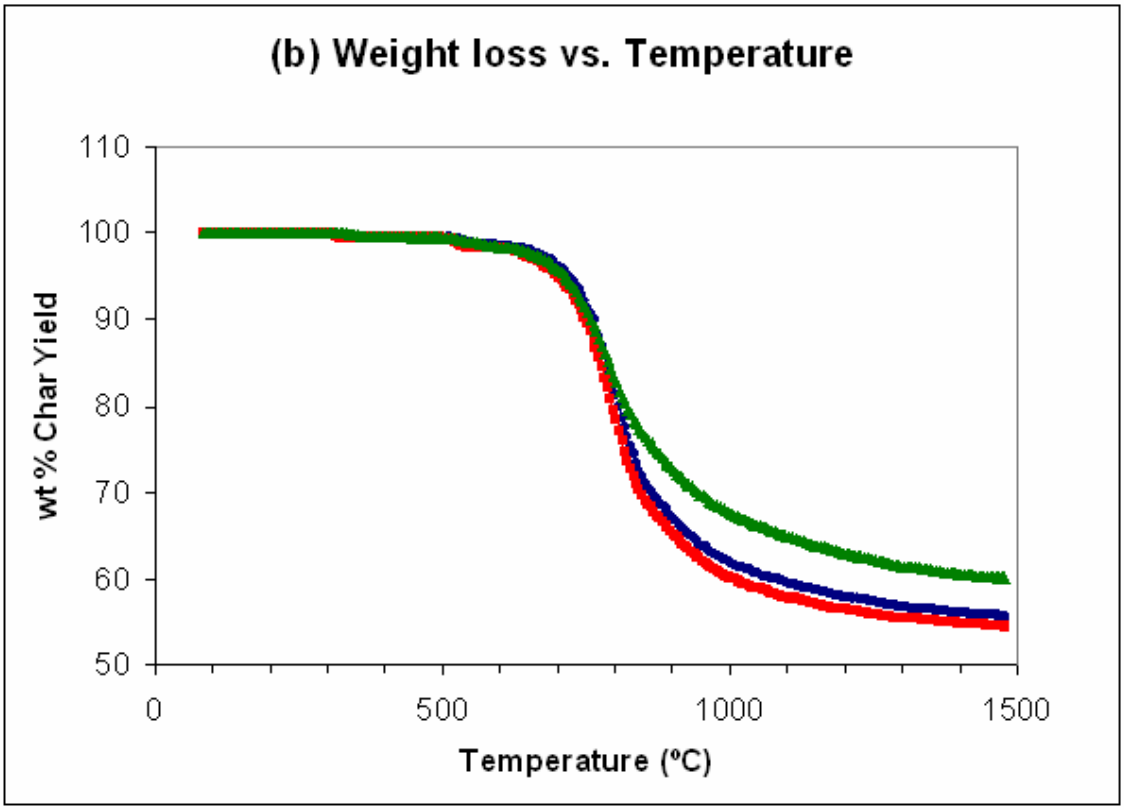

Fig. 6.8 FG-DVC (10^5 K/s – 1750 K – 150 ms). (a) Total rate vs. Temperature (b) Weight loss vs. Temperature, for ● Guasare, ■ Carboandes and ▲ Russian coals

Results presented in Figures 6.7 and 6.8 show a different behaviour of the Russian coal, which gives the lowest volatile rate and yield at high temperature. This behaviour can be explained in terms of the cross-linking and bridge breaking balance competition on the depolymerization of the macromolecular network. In general for lower rank coals cross-linking rates occurs in advance of the bridge breaking, increasing the coordination number of the macromolecular network and thus reducing the yield.

Finally, the char burnout sub-model presented in Section 6.2 was run for each scenario, using as inputs:

- Particle size distribution (Table 6.3): d_{pm} = 55, n_{rr} = 1.02 (Rosin Ramler)
- Coal properties (Table 6.2)
- Volatile and char yield (Table 6.6)
- Oxygen partial pressure and temperature profiles (CFD simulations)
- Model parameters (Section 6.2):
    - E_e = 162 ± 10 kJ/mol, n = 0.5
    - E_c = 9 kcal/mol, A_c = 200
    - δ_m = 5 μm, θ_{taf} = 0.21
    - *Swell* = 1.14
- Sub-models (Section 6.2):
    - Thermal annealing: Van der Lans et al. (1998)
    - Ash inhibition: On
    - Maceral correction: Abbreviated (Guasare), Backreedy et al. (2006)

Results on the overall burnout for the model are compared against the initial CFD predictions and plant data measurement in Fig. 6.9. CFD predictions clearly under-predict the overall burnout as a result of using a simple combustion model that does not account for reactivity loss. On the contrary, the results from the model show that general trends and quantitative values on burnout are accurately predicted. Small discrepancies can be found for Carboandes coal, in cases 5 and 6, where the model slightly differs from the overall burnout value obtained in the plant. This result can be partially explained by the fact that no petrographic information was available for this coal, and thus no maceral correction was applied in the model, besides the intrinsic uncertainty on the choice of the kinetic model parameters, since no DTF studies were carried out. However, deliberate changes in the operating conditions of the plant or mass flow imbalance situations between burners (see Table 6.3) that noticeably distort the particles' trajectories and thus their combustion behaviours are sufficiently resolved for all the coals.

We can therefore conclude that the combination of CFD codes and advanced combustion models notably improve the results exclusively obtained by a CFD code. Moreover, this methodology allows us to detect the changes that arise from slight operational condition changes and uneven flow variations which strongly affect the overall burnout prediction.

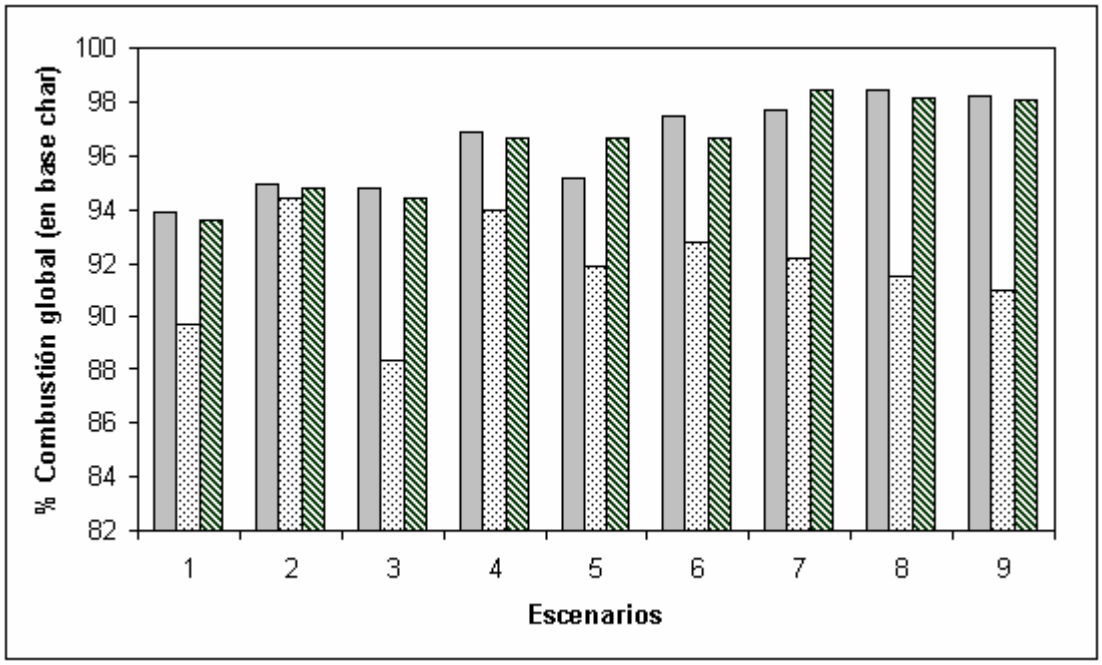

Fig. 6.9 Result for burnout (% char basis) for: ASM CFD predictions Model predictions

6.4 Conclusions

A new methodology that combines the advantages of CFD codes (detailed thermal and fluid dynamic description) and advanced combustion models (detailed combustion kinetics), to improve combustion related predictions in power plants has been presented. This methodology uses the temperature and oxygen partial pressure profiles for a representative number of particles from CFD simulations, and then introduces them, together with coal properties, into an advanced combustion kinetics model.

This chapter focused on the description, development and validation of the combustion model. Devolatilization was modelled using a macromolecular network pyrolysis model (FG-DVC), because of its applicability to a wide range of coals (subbituminous, bituminous and lignites) and heating rates (0.05 to 10^5 K/s), and its ability to predict the variations in species yield with reactor conditions. Char oxidation was modelled and programmed in Fortran using a developed intrinsic formulae based on the carbon burnout kinetic model (CBK8) (Sun and Hurt, 2000),

that allows the transition to Zone I and includes the variation in the porous structure and reactivity of the char as combustion proceeds, mineral matter effects, and the influence of coal's maceral content.

To investigate the burnout prediction capability of the model a total of nine scenarios were tested with standard plant instrumentation measurements gathered at the Lamarmora (ASM Brescia) power station in the year 2005. Results from the study show a good agreement in trends and quantitative values, even where a notable sensibility of the model is expected when slight operational variations were applied. Results also confirm an acceptable approach to the methodology, formulation and assumptions have been proposed in this work. We can therefore conclude that the combination of CFD codes and advanced combustion models permits the predictive system to be sensitive to the changes that arise from slight variations in operating conditions and uneven flow variations which strongly affect the overall burnout prediction.

Nomenclature

A_c pre-exponential factor of the formation relation CO/CO_2

A_d pre-exponential factor of the thermal annealing process (s^{-1})

A_i pre-exponential factor of the kinetic reaction rate (g C/cm^2 s atm^n)

d_c char particle core diameter (cm)

C_p specific heat of char (J/g K)

C_{pa} specific heat of ash (J/g K)

C_{pc} specific heat of carbon (J/g K)

D diffusion coefficient (m^2 /s)

D_{eff} effective diffusion coefficient (cm^2 /s)

D_{O2} molecular diffusion coefficient for O_2 into N_2 (cm^2 /s)

d_p char particle diameter (cm)

d_{p0} char particle initial diameter (cm)

d_{pm} mean diameter Rosin Rammler distribution (μm)

E_e activation energy (kJ/mol)

E_c activation energy of the formation relation CO/CO_2 (kcal/mol)

E_d activation energy of the thermal annealing process (kJ/mol)

E_{dm} mean activation energy of the thermal annealing process (kJ/mol)

f_{ann} thermal annealing factor

$f_E(E_d)$ statistical distribution function in E_d of the thermal annealing process

f_{mac} maceral correction factor

f_{CO2} carbon mass fraction that reacts to CO_2

h_{ext} convective coefficient (W/cm^2 K)

h_{int} convective coefficient (W/cm^2 K)

h_c convective coefficient (W/m^2 K)

HTVM % wt. high temperature volatile yield

In inertinite

In_{LR} fusinite

In_R semi-fusinite

k_d diffusional kinetic constant (g C/cm^2 s atm)

k_m mass transfer coefficient (m/s)

kS specific intrinsic reactivity (1/s atm^n)

k_0S_0 initial specific intrinsic reactivity (1/s atm^n)

L_c characteristic length (m)

m_c carbon mass of the char (g C)

m_{c0} initial carbon mass of the char (g C)

m_p mass of the char particle (g)

m_{p0} initial mass of the char (g)

n apparent reaction order

n_{rr} dispersion factor Rosin Rammler distribution

Nu Nusselt dimensionless number $\left(Nu = h_c \ L_c / \lambda\right)$

P_{boiler} furnace pressure (Pa)

P_g bulk oxidant partial pressure (atm)

P_s oxidant partial pressure at the particle surface (atm)

q_c combustion rate (g C/cm^2 s)

q_{conv} convective heat transfer (W/cm^2)

q_{rad} radiative heat transfer (W/cm^2)

R universal ideal gas constant (8.3145 J/mol K)

R_i intrinsic reactivity (g C/cm^2 s atm^n)

Sh Sherwood dimensionless number $\left(Sh = k_m \ L_c / D\right)$

Swell swelling factor

t time (s)

t_{res} residence time (s)

T_g bulk gas temperature (K)

T_m average temperature (K)

T_p particle temperature (K)

T_{pant} particle temperature in the previous instant (K)

T_w furnace walls temperature (K)

U overall heat transfer coefficient (W/cm^2 K)

Vit vitrinite and pseudo-vitrinite

Vit_M vitrinite

Vit_{PS} pseudo-vitrinite

X_a ash mass fraction

X_{a0} initial ash mass fraction

%C % wt. carbon content (d.a.f.)

Δh_f combustion enthalpy in the oxidation reaction to CO/ CO_2 (J/g)

Δh_{CO2} combustion enthalpy in the oxidation reaction to CO_2 (J/g)

Δh_{CO} combustion enthalpy in the oxidation reaction to CO (J/g)

α_D deactivation factor

δ ash film thickness (cm)

δ_m minimum ash film thickness (cm)

ε	char emissivity
φ	stoichiometric factor
ϕ	Thiele modulus
λ	thermal conductivity (W/m K)
λ_{at}	ash thermal conductivity (W/cm K)
λ_g	bulk gas thermal conductivity (W/cm K)
η	effectiveness factor
θ_{af}	ash film porosity
θ_{taf}	critical ash film porosity
θ	particle porosity
ρ	char density (g/cm^3)
ρ_{at}	ash density (g/cm^3)
ρ_a	ash density in the char (g/cm^3)
ρ_c	carbon density (g/cm^3)
ρ_{c0}	initial carbon density (g/cm^3)
ρ_0	initial char density (g/cm^3)
τ	tortuosity
$\sigma_{\ln Ed}$	standard deviation of the thermal annealing process (kJ/mol)
σ_B	Stephan Boltzman constant (5.67 E-12 W/cm^2 K^4)

Acronyms

CBK	carbon burnout kinetics
CFD	computational fluid dynamics
DAEM	distributed activation energy models
DTF	drop tube furnace
HHV	high heating value
HTVM	high temperature volatile matter
HWM	heated wire mesh
FFB	flat flame burner
LOI	lost of ignition
SFOR	single first order reaction
TGA	thermo-gravimetric analyzer
2CSM	two-competing step model

7 UNBURNED CARBON PREDICTION SYSTEM

The construction of the unburned carbon prediction system (UPS) from the elements introduced in previous chapters, mean the culmination of the main goal of this thesis. In this chapter we will present the development of a predictive system that provides an on-line estimation of the unburned carbon in ash for a given operating condition in a utility boiler.

The combination of predictive techniques, that are generally used isolated, allows us to unify the following advantages within the same system: fluid dynamics and heat transfer from CFD codes, detailed chemical kinetics from advanced combustion models and reduced computing cost and interpolation capabilities from neural networks.

Throughout this chapter, the coupling of the local combustion conditions model (Chapter 5) and the advanced combustion model (Chapter 6) is described. Finally, the system is validated using standard plant instrumentation measurements gathered during three months at Lamarmora plant (ASM Brescia) under different operation conditions. From these results, an evaluation of the system is assessed, hinting at the most significant conclusions, and comparing its features and accuracy with other unburned carbon predictive systems.

7.1 Unburned carbon prediction system description

The unburned carbon prediction system described in this final chapter is the result of the contributions of the models developed in previous chapters. However, before the selection and development of the sub-models that constitute the final system, the basic design conditions were established, meeting the requirements and suggestions given by technical personnel of several power plants. This reflection tries to discard an interpretation of the system as a simple addition of models. In general, the chronology of the design process can be summarized in four phases:

1. Definition of the unburned carbon loss problem
2. Definition of the design conditions for the predictive system
3. Sub-model selection
4. Construction of the predictive system from the sub-models

It is noticeable that the design process does not follow a successive evolution along these phases. On the contrary, there are permanent interactions between phases 3 and 4 that involve many modifications in the sub-models until the final design is achieved. Significant examples of these modifications are the changes in the burner's geometry and the grid refinement of the CFD model, the time step adaptation to ensure the convergence in the coal combustion model, or the continuous changes on the neural networks structure and the input parameters to capture the thermal and fluid dynamics behaviour of the problem.

Focusing on the selection of the sub-models it is important to remember the two main design features of the system: accuracy and reduced computing cost. With regard to accuracy, in any problem that involves turbulent combustion, two aspects namely, fluid dynamics and chemical kinetics, determine the precision reached. As a result, the better the accuracy in the characterization of both these aspects, the better the overall predictions achieved with the model. Traditionally, CFD codes give a detailed description of the transport phenomena (Chapter 4), but on the other hand, they use simple combustion models. To balance this deficiency, we have developed an advanced combustion model (Chapter 6), which is used as a post-process on the temperature and oxygen partial pressure profiles obtained from a CFD simulation. With regard to the computing time, a system that includes a CFD code in its structure can be seriously restrictive. To overcome this limitation, without leaving aside the detailed fluid and thermal description of the CFD codes, we have developed a neural network system trained with data from the CFD simulations that is able to reproduce the temperature and

oxygen profiles found by the particles in their trajectories through the boiler and their residence times provided with the CFD code (Chapter 5).

The final system is formed by the union of the neural network system, called the local combustion conditions model, with the advanced combustion model. Figure 7.1 shows the final structure of the predictive system.

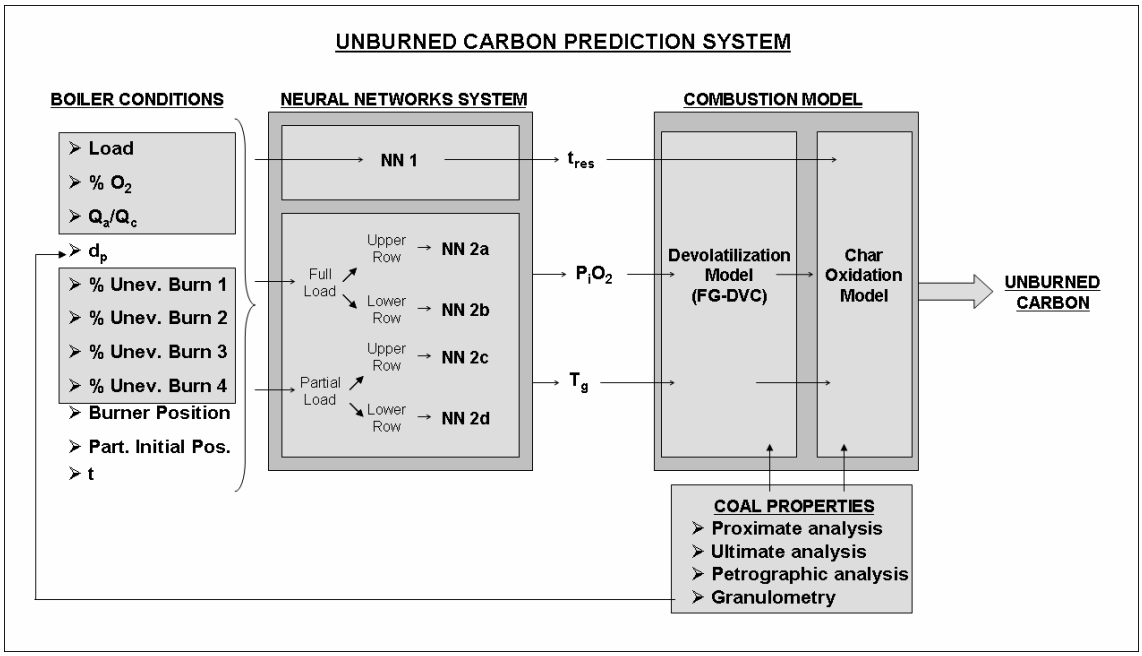

Fig. 7.1 Unburned coal prediction system block diagram

The order sequence for running the system is simple: For a given boiler condition, the system starts the local combustion conditions model (neural network system) and generates an output file containing the temperature and oxygen partial pressure information for the particles in the furnace as well as their residence times. Immediately after this output file has been generated the coal properties are also introduced as an input in the coal combustion model to determine the unburned carbon in ash.

The combustion model is divided into two subroutines corresponding to the devolatilization and char oxidation stages. The former determines the amount of volatiles yielded together with the resultant char residue in which the intrinsic char oxidation model is applied.

One of the main advantages of this predictive system is the reduced number of inputs (boiler conditions and coal properties) required to run the model and their availability at any power station:

- Load: Coal consumption is a common control/operation signal in power stations.
- % Excess oxygen at the exit of the boiler: Excess oxygen is a common control/operation signal in power stations.
- Primary air to coal mass flow ratio: It is easily determined from the operation curve and the load capacity of each mill.
- Uneven mass flow distributions in the boiler: This factor is probably the only one that is not directly measured at the plant, especially for individual burners. However, the mass flow passing through each mill is usually controlled so that it is possible to calculate the mass flow differences through burners fed from different mills. In this work, it is possible to adapt this input to the information available in the plant.
- Proximate and ultimate coal analysis: Proximate and ultimate analysis are commonly performed in power stations.
- Petrographic analysis: Usually, power stations do not determine this analysis. As a consequence, this input will only be considered in the model when this information is available and so this input will be avoided.
- Pulverized coal size distribution: It is commonly determined in power stations.

In this list of inputs, the kinetic parameters of the combustion model have been omitted. As it was discussed in Chapter 6, in order to describe the combustion process correctly, these parameters can be either determined empirically by DTF experiments or be approached through correlations or databases. These parameters form part of a third group of inputs which are directly introduced in the combustion model (Chapter 6).

7.2 Validation of the unburned carbon prediction system

The validation of the unburned carbon prediction system is carried out using standard plant instrumentation measurements gathered at Lamarmora ASM Brescia power station (see description of the plant in Chapter 4) during the year 2005 (January – March 2005). Study cases were obtained covering the regular range of variation under full and partial load conditions.

In the study, two coals from Central America commonly used in the plant over the last 5 years (‘Guasare’ from Venezuela and ‘Carbonandes’ from Colombia) and a coal from Russia, recently used to evaluate its influence on the combustion efficiency, were burned separately. Proximate, ultimate and petrographic (when available) analysis for these three coals are presented in Table

6.2 (Chapter 6). Generally, petrographic analysis is not performed in power plants. In such case, we can make use of databases (for example Penn State Coal Data Bank), where coals from all over the world are catalogued. In this work, since no petrographic analysis was available, inertinite and vitrinite values for Gausare coal were taken from Barranco et al. (2003).

Tables 7.1 to 7.6 show the plant conditions data gathered in the study unit during the test period (January – March 2005):

- Table 7.1: Guasare (full load)
- Table 7.2: Guasare (partial load)
- Table 7.3: Carboandes (full load)
- Table 7.4: Carboandes (partial load)
- Table 7.5: Russian (full load)
- Table 7.6: Russian (partial load)

Case Number	*Acquisition Date*	*CIA (550 °C)*	*Total Coal Load to Mills*	*Primary Air Deviation Mill 1*	*Primary Air Deviation Mill 2*	*O2 (exit boiler)*	*Total Air Mass Flow*	*Coal Load to Mill 1*	*Coal Load to Mill 2*
		%	*t/h*	*km^3N/h*	*km^3N/h*	*%*	*km^3N/h*	*t/h*	*t/h*
1	10-feb-05	17.9	24.84	0	0	3.08	214.09	12.33	12.36
2	11-feb-05	31.2	24.83	0	0	2.63	208.03	12.4	12.44
3	12-feb-05	27	24.88	0.2	0.35	3.03	214.05	12.43	12.45
4	13-feb-05	23.8	25.03	0.4	0.2	3.19	218.47	12.5	12.55
5	14-feb-05	26.6	24.95	5	5	2.98	215.14	12.45	12.51
6	15-feb-05	33.5	23.91	0	0	2.97	214.93	11.89	11.98
7	16-feb-05	17.7	24.58	0	0	3.09	214.97	12.26	12.32
8	17-feb-05	24.4	24.68	0	0	3.01	212.21	12.31	12.4
9	18-feb-05	23.1	24.94	0	0	2.93	212.87	12.44	12.51
10	19-feb-05	25.7	24.95	0	0	2.95	213.09	12.45	12.51
11	20-feb-05	26	25.07	0	0	2.63	213.03	12.47	12.58
12	21-feb-05	18	25.52	0	0	2.66	214.07	12.74	12.81
13	22-feb-05	25.5	24.9	0.2	0.7	2.83	218.06	12.45	12.44
14	24-feb-05	22.5	25.8	0	0	3	217.28	12.84	12.92
15	26-feb-05	28.5	25.3	1	0	3.12	214.75	12.65	12.72
16	27-feb-05	21.8	25.4	0.5	0	3.25	213.89	12.63	12.72
17	28-feb-05	21.2	25.5	0.5	0	3.44	214.66	12.77	12.74
18	01-mar-05	24.6	25.17	0	0	3.31	214.76	12.58	12.64
19	02-mar-05	29.4	25.4	0	0	3.21	215.94	12.67	12.71
20	03-mar-05	27.4	25.16	0	0	3.57	218.45	12.53	12.6
21	04-mar-05	23.8	25.86	1	0	3.37	217.04	12.9	12.95
22	05-mar-05	24.7	25.22	1	0	3.56	217.24	12.57	12.63
23	06-mar-05	24.5	25.69	1	0	3.34	218.19	12.54	13
24	07-mar-05	24.6	25.52	0.2	0	3.29	215.83	12.71	12.82
25	08-mar-05	27.2	25.85	0	0	3.1	215.92	12.91	12.94
26	09-mar-05	26	25.39	0	0	3.17	212.1	12.64	12.76
27	10-mar-05	25.1	24.69	0	0	3.19	212.61	12.37	12.32
28	14-mar-05	27.9	20.91	1.5	0	3.1	181.41	10.43	10.46
	AVERAGED	**25**	**25**	**0.4**	**0.2**	**3.1**	**213.7**	**12.5**	**12.5**
	UBC – COLLECTED FROM THE FIRST FIELD OF ELECTROSTATIC PRECIPITATOR								

Table 7.1 Test data: Guasare – full load (Lamarmora ASM Brescia 2005)

Case Number	*Acquisition Date*	*CIA (550 °C)*	*Total Coal Load to Mills*	*Primary Air Deviation Mill 1*	*Primary Air Deviation Mill 2*	*O2 (exit boiler)*	*Total Air Mass Flow*	*Coal Load to Mill 1*	*Coal Load to Mill 2*
		%	*t/h*	*km^3N/h*	*km^3N/h*	*%*	*km^3N/h*	*t/h*	*t/h*
29	10-feb-05	14	16.66	1	0	5.27	167	8.33	8.34
30	11-feb-05	14.7	16.58	0	0	5.36	160.88	8.26	8.31
31	12-feb-05	12.6	15.27	0.04	0.1	6.1	158.17	7.54	7.57
32	13-feb-05	12.1	15.34	0.32	0.04	6.36	162.17	7.61	7.63
33	14-feb-05	18.4	15.72	0	0	5.58	155.42	7.72	7.73
34	15-feb-05	15.1	15.15	0	0	5	150.91	7.61	7.64
35	16-feb-05	8.7	15.97	0.5	0	5.18	159.15	8.07	7.9
36	17-feb-05	19.7	15.55	0.5	0	5.17	153.57	7.86	7.87
37	18-feb-05	13.9	16.95	0.5	0	4.72	161.63	8.47	8.48
38	19-feb-05	16.4	15.33	0.3	0	5.17	147.93	7.65	7.69
39	20-feb-05	14.6	14.9	1.1	0	5.93	155.16	7.43	7.47
40	21-feb-05	11.8	16.25	1	0	5.29	160.26	8.25	8.14
41	22-feb-05	16.5	16.2	1	0	5.04	155.95	8.12	8.06
42	23-feb-05	15.5	15.9	0.5	0	4.9	152.56	7.99	8.01
43	24-feb-05	8.8	16.5	1.1	0	5.78	165.63	8.27	8.28
44	25-feb-05	9.6	16.2	1.2	0	5.52	164.46	8.07	8.09
45	26-feb-05	14.8	17	0	0	5.52	166.51	8.48	8.48
46	27-feb-05	16.4	17.4	1.1	0	5.56	169.92	8.68	8.68
47	28-feb-05	12.5	16.6	1.01	0.07	5.64	163.43	8.39	8.4
48	01-mar-05	16.9	16.47	0.9	0.4	5.6	168.33	8.88	8
49	04-mar-05	14.7	17.56	1.5	0.3	5.26	167.8	8.79	8.77
50	06-mar-05	18.4	17.15	1.6	0	4.96	164.61	9.07	8.08
51	07-mar-05	15.3	16.28	2	0.4	5.23	156.86	8.2	8.25
52	08-mar-05	17.6	17.79	1.5	0	4.69	166.59	9.08	9.02
53	09-mar-05	15.8	17.08	1	0.5	4.93	161.03	8.74	8.33
54	10-mar-05	18.2	16.33	1.7	0	4.8	152.92	8.16	8.15
55	13-mar-05	21.7	14.71	2.15	0.5	6.04	150.16	7.47	7.32
56	14-mar-05	16.4	16.3	1	0.1	4.52	150.88	8.21	8.22
57	15-mar-05	21.8	14.61	1	0	5.3	145.97	7.28	7.32
58	16-mar-05	16.9	14.52	1.23	0	5.87	150.32	7.26	7.27
59	17-mar-05	15.7	14.32	0.63	0	5.48	141.24	7.19	7.19
	AVERAGED	**15.3**	**16.1**	**0.9**	**0.1**	**5.3**	**158.3**	**8.1**	**8**
	UBC – COLLECTED FROM THE FIRST FIELD OF ELECTROSTATIC PRECIPITATOR								

Table 7.2 Test data: Guasare – partial load (Lamarmora ASM Brescia 2005)

Case Number	Acquisition Date	CIA (550 °C)	Total Coal Load to Mills	Primary Air Deviation Mill 1	Primary Air Deviation Mill 2	O2 (exit boiler)	Total Air Mass Flow	Coal Load to Mill 1	Coal Load to Mill 2
		%	t/h	km^3N/h	km^3N/h	%	km^3N/h	t/h	t/h
60	23-jan-05	10.5	26.41	2.01	0.7	2.93	210.51	13.18	13.23
61	24-jan-05	15.1	26.4	1.7	1.3	2.79	210.17	13.19	13.23
62	25-jan-05	15.9	26.66	2	1.3	3.25	210.59	13.3	13.35
63	25-jan-05	13.9	26.51	2	1.5	2.98	209.03	13.22	13.29
64	26-jan-05	15.7	26.33	2	2	3.63	218.29	13.28	13.3
65	27-jan-05	22.3	26.05	2.21	1.32	3.21	215.11	13.06	13.01
66	28-jan-05	18.6	26.03	1.36	0.51	3.24	215.84	12.99	13.02
67	29-jan-05	15.8	26.37	2.2	1.7	3.19	217.22	13.14	13.22
68	30-jan-05	12.4	26.59	2.2	1	3.28	216.91	13.29	13.32
69	31-jan-05	13.2	26.01	1.5	1	3.37	209.39	12.93	13.04
70	31-jan-05	15	26.57	1.7	0.7	2.98	214.59		
	AVERAGED	**15.3**	**26.4**	**1.9**	**1.2**	**3.2**	**213.4**	**13.2**	**13.2**
	UBC – COLLECTED FROM THE FIRST FIELD OF ELECTROSTATIC PRECIPITATOR								

Table 7.3 Test data: Carboandes – full load (Lamarmora ASM Brescia 2005)

Case Number	Acquisition Date	CIA (550 °C)	Total Coal Load to Mills	Primary Air Deviation Mill 1	Primary Air Deviation Mill 2	O2 (exit boiler)	Total Air Mass Flow	Coal Load to Mill 1	Coal Load to Mill 2
		%	t/h	km^3N/h	km^3N/h	%	km^3N/h	t/h	t/h
71	24-jan-05	6.8	17.78	2	0.7	4.85	154.99	8.9	8.91
72	25-jan-05	11.4	17.36	2	1.5	5.02	161.76	9.29	9.3
73	26-jan-05	16.5	18.56	1	0.4	4.67	162.84	9.26	9.3
74	27-jan-05	15.6	18.14	2	0.5	4.98	159.89	9.12	9.24
75	28-jan-05	16.9	18.33	1.2	0.3	4.48	162.99	9.18	9.14
76	29-jan-05	11	17.89	1.6	0	5.19	165.04	8.97	8.97
77	30-jan-05	8.2	19	2	1.3	4.78	168.45	9.68	9.67
78	31-jan-05	7.7	18.46	1	1	5.2	164.57	9.28	9.29
	AVERAGED	**11.8**	**18.2**	**1.6**	**0.7**	**4.9**	**162.6**	**9.2**	**9.2**
	UBC – COLLECTED FROM THE FIRST FIELD OF ELECTROSTATIC PRECIPITATOR								

Table 7.4 Test data: Carboandes – partial load (Lamarmora ASM Brescia 2005)

Case Number	Acquisition Date	CIA (550 °C)	Total Coal Load to Mills	Primary Air Deviation Mill 1	Primary Air Deviation Mill 2	O2 (exit boiler)	Total Air Mass Flow	Coal Load to Mill 1	Coal Load to Mill 2
		%	t/h	km^3N/h	km^3N/h	%	km^3N/h	t/h	t/h
79	24-mar-05	12.2	26.58	1	0.1	3.31	219.11	13.4	13.27
80	25-mar-05	8.3	27.06	1.5	0	3.12	221.04	13.58	13.58
81	29-mar-05	8.6	26.85	1.1	1.5	3.02	218.68	13.44	13.42
82	30-mar-05	9.7	26.88	1.5	2	2.89	216.73	13.41	13.48
83	31-mar-05	7.5	26.93	1.3	0.9	2.99	218.01	13.41	13.5
	AVERAGED	**9.2**	**26.9**	**1.3**	**0.9**	**3.1**	**218.7**	**13.4**	**13.5**
	UBC – COLLECTED FROM THE FIRST FIELD OF ELECTROSTATIC PRECIPITATOR								

Table 7.5 Test data: Russian – full load (Lamarmora ASM Brescia 2005)

Case Number	*Acquisition Date*	*CIA (550 °C)*	*Total Coal Load to Mills*	*Primary Air Deviation Mill 1*	*Primary Air Deviation Mill 2*	*O2 (exit boiler)*	*Total Air Mass Flow*	*Coal Load to Mill 1*	*Coal Load to Mill 2*
		%	t/h	km^3N/h	km^3N/h	%	km^3N/h	t/h	t/h
84	24-mar-05	7.80	16.79	1.50	0.50	5.32	157.14	8.31	8.68
85	25-mar-05	4.90	17.63	1.50	0.00	4.64	157.53	8.55	9.10
86	26-mar-05	7.60	16.43	1.20	1.80	5.63	158.30	6.87	9.67
87	26-mar-05	6.80	16.74	1.50	0.00	5.48	155.48	7.57	9.14
88	28-mar-05	6.20	16.35	1.35	2.00	4.89	147.58	7.68	8.67
89	29-mar-05	4.00	17.15	1.40	2.00	4.56	153.67	8.25	9.17
90	30-mar-05	4.70	17.24	1.50	2.00	4.50	152.35	7.60	9.67
91	31-mar-05	5.30	18.31	1.50	2.50	4.48	161.21	8.13	10.15
	AVERAGED	**5.9**	**17.1**	**1.4**	**1.4**	**4.9**	**155.4**	**7.9**	**9.3**
	UBC – COLLECTED FROM THE FIRST FIELD OF ELECTROSTATIC PRECIPITATOR								

Table 7.6 Test data: Russian – partial load (Lamarmora ASM Brescia 2005)

With regard to the milling system, Figure 7.2 shows the performance characteristic curve of both mills, that, together with the primary air deviation, allows us to calculate the air to coal mass flow ratio for each mill. Furthermore, during the tests, both mills' classifiers were adjusted to give a particle size distribution of mean diameter of 55 μm (Rosin-Rammler distribution: d_{pm} = 55 μm, n_{rr} = 1.02).

Finally, the group of inputs exclusively related to the combustion model has been selected with regard to the discussion presented in Chapter 6:

- Model parameters (Section 6.2):
  - E_e = 162 ± 10 kJ/mol, n = 0.5
  - E_c = 9 kcal/mol, A_c = 200
  - δ_m = 5 μm, θ_{taf} = 0.21
  - *Swell* = 1.14

- Sub-models (Section 6.2):
  - Thermal annealing: Van der Lans et al. (1998)
  - Ash inhibition: On
  - Maceral correction: Abbreviated (Guasare), Backreedy et al. (2006)

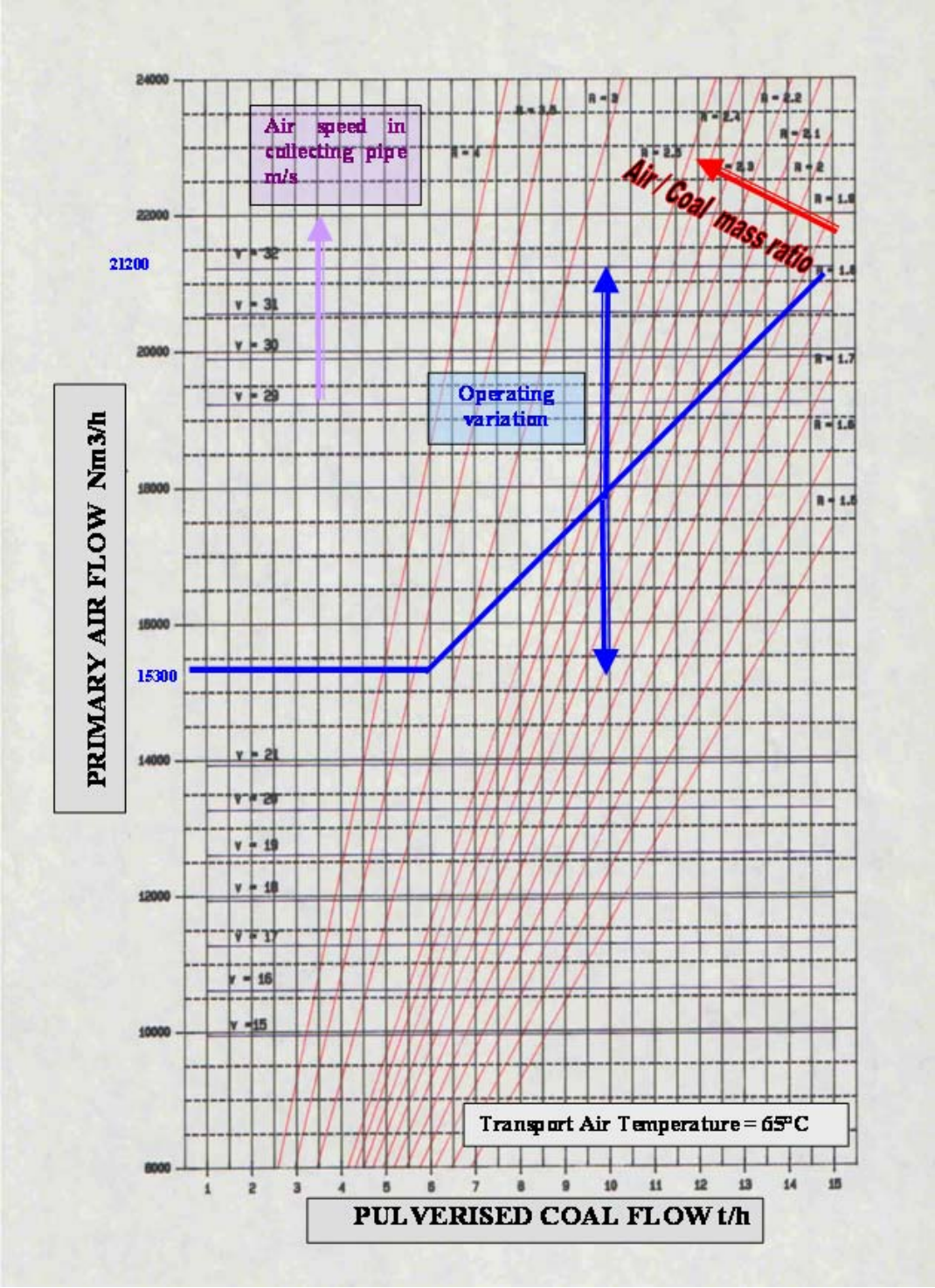

Fig. 7.2 Operation curve of the mills (Lamarmora ASM Brescia 2005)

Once the inputs for all the cases (Tables 7.1 to 7.6) were defined, we ran the unburned carbon prediction system, obtaining the corresponding carbon-in-ash results. Note that Case 70 has been excluded from the study, since some of the data were incorrectly gathered during the test (see Table 7.3).

The average computational time for each case calculation, using an Intel Core 2 DUO 6300 (1.86 GHz, 0.86 GB of RAM) machine, is less than one minute. Table 7.7 shows the carbon-in-ash values gathered at the power station and those calculated by the unburned carbon prediction system for all the cases.

CASE	CIA ASM (%)	CIA UPS (%)
1	17.9	25.66
2	31.2	26.99
3	27	25.99
4	23.8	24.62
5	26.6	25.66
6	33.5	26.59
7	17.7	25.45
8	24.4	25.62
9	23.1	25.78
10	25.7	25.70
11	26	26.79
12	18	26.39
13	25.5	26.27
14	22.5	25.45
15	28.5	24.62
16	21.8	23.89
17	21.2	22.93
18	24.6	23.76
19	29.4	24.19
20	27.4	21.90
21	23.8	22.80
22	24.7	22.04
23	24.5	22.44
24	24.6	23.37
25	27.2	24.57
26	26	24.28
27	25.1	24.95
28	27.9	26.35
29	14	15.31
30	14.7	15.31
31	12.6	12.72
32	12.1	12.10
33	18.4	14.50
34	15.1	13.79
35	8.7	15.04
36	19.7	14.39
37	13.9	12.67
38	16.4	13.90
39	14.6	12.61
40	11.8	15.42
41	16.5	14.66
42	15.5	14.12
43	8.8	16.52
44	9.6	16.05
45	14.8	16.05

CASE	CIA ASM (%)	CIA UPS (%)
46	16.4	16.52
47	12.5	17.08
48	16.9	16.88
49	14.7	16.00
50	18.4	17.39
51	15.3	14.99
52	17.6	13.34
53	15.8	15.57
54	18.2	13.95
55	21.7	12.55
56	16.4	11.63
57	21.8	12.50
58	16.9	12.10
59	15.7	12.55
60	10.5	15.60
61	15.1	16.15
62	15.9	14.44
63	13.9	15.13
64	15.7	11.27
65	22.3	15.30
66	18.6	15.04
67	15.8	15.00
68	12.4	14.31
69	13.2	14.35
71	6.8	8.91
72	11.4	11.41
73	16.5	9.35
74	15.6	9.25
75	16.9	9.25
76	11	10.80
77	8.2	10.46
78	7.7	10.56
79	12.2	6.96
80	8.3	7.43
81	8.6	8.20
82	9.7	8.15
83	7.5	8.15
84	7.80	7.53
85	4.90	5.15
86	7.60	7.59
87	6.80	8.50
88	6.20	6.23
89	4.00	5.32
90	4.70	5.48
91	5.30	5.21

Table 7.7 Carbon-in-ash values gathered at Lamarmora plant and calculated with the UPS (Unburned carbon Prediction System)

To analyze the results in Table 7.7, Figures 7.3 and 7.4 show the dispersion diagrams for the carbon-in-ash values gathered at the plant during the test period against the calculated values from the predictive system, under full and partial load conditions.

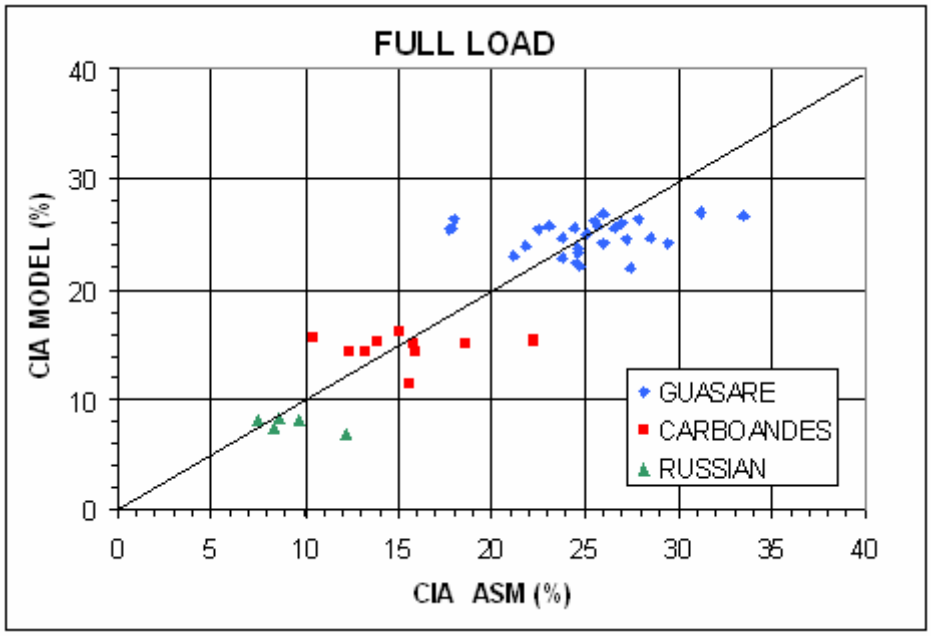

Fig. 7.3 Carbon-in-ash values under full load conditions for the three study coals: ASM vs. UPS (Unburned carbon Prediction System)

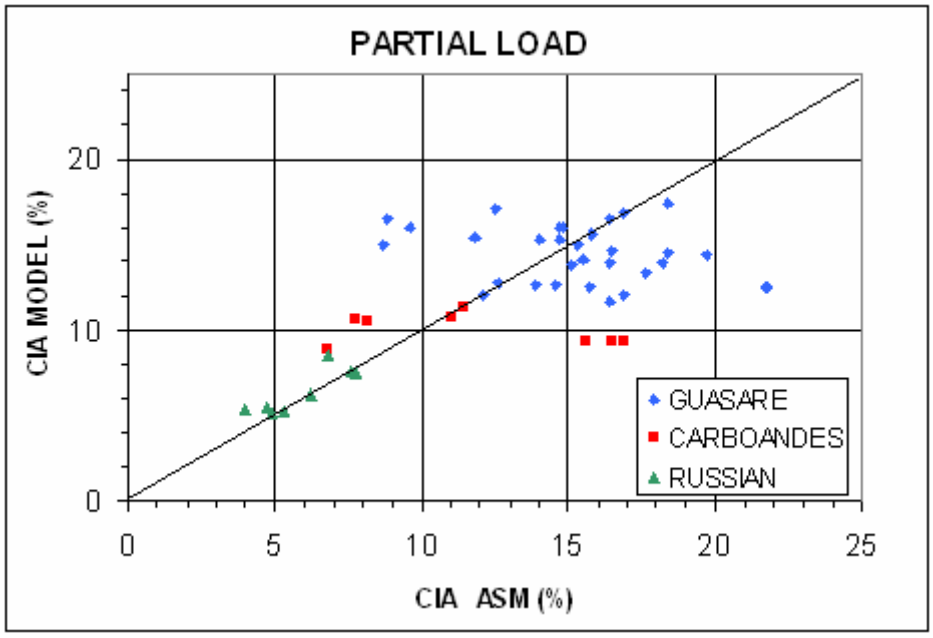

Fig. 7.4 Carbon-in-ash values under partial load conditions for the three study coals: ASM vs. UPS (Unburned carbon Prediction System)

Figures 7.3 and 7.4 indicate an adequate correspondence with plant data and calculated values from the predictive system, since the cloud of points are close to the bisector of the first quadrant for both diagrams. Next, it is necessary to analyze, separately, the results obtained under full load conditions where the variation in the operating conditions is slight and the results obtained under partial load conditions where this operational range is larger. As a result, the fitness of the model under full load conditions (Figure 7.3) shows a good agreement for the three study coals. Focusing now on the more distant points from the bisector, it is not possible to identify the reason for this inaccuracy since the operating conditions in those cases were very similar to the ones in other cases where the carbon-in-ash values were apparently "normal". Consequently, these "fault points" may have been due to the data gathering process or due to other factors not included in the instrumented controls of the plant and therefore not considered in the model development. Fortunately, these "fault points" represent a negligible percentage and do not affect the general conclusions of the model. With regards to the results under partial load conditions (Figure 7.4), there exists a larger dispersion between plant data and the calculated values from the predictive system. The reason for this discrepancy can be explained from a fluid dynamics point of view. Of course, under partial load conditions the stratification of the conditions within the boiler is more relevant than in the case of full load conditions where there is a greater uniformity in the temperature and oxygen partial pressure profiles. Starting from this assumption and taking into account that neural networks average and interpolate those values in the furnace, the results found are not strange. In fact, this behaviour illustrates one of the biggest challenges of the problem and thus, where we have placed an increased emphasis in the neural networks system development (Chapter 5). Designing a neural network with a higher number of neurons would improve the fluid and thermal description within the furnace. However, an excessive number of neurons should be avoided since it would result in an overtraining situation leading to a decrease in the generalization capability of the network. Consequently, in order to find a balanced situation, we opted for complicating the neural networks system design by considering different networks for the upper and lower row of burners and including the starting feeding position of the particles within the burner. Finally, we carried out an iterative process to select the most suitable number of neurons for the problem. The details of the neural networks structure and its development were presented in Chapter 5. Again, regarding the more distant points from the bisector, it was possible to use the same analysis as the one presented for the full load conditions cases.

It is also noticeable that Figures 7.3 and 7.4 show a clear distinction between the three coals in the results. Obviously, carbon-in-ash values depend on the mineral matter content of the coal. Therefore, in order to obtain a rigorous estimation of the accuracy of the unburned carbon

prediction system, it is necessary to view the results in the same base line i.e. the overall burnout. Therefore, Table 7.8 presents the burnout results (%, coal basis) for the data gathered at the power station and those calculated by the predictive system together with the prediction error for every case considered in the study.

CASE	Burnout ASM (%)	Burnout UPS (%)	ERROR (%)
1	98.56	97.73	-0.84
2	97.01	97.56	0.55
3	97.56	97.69	0.12
4	97.94	97.85	-0.09
5	97.61	97.73	0.11
6	96.68	97.61	0.93
7	98.58	97.75	-0.83
8	97.87	97.73	-0.14
9	98.02	97.71	-0.31
10	97.72	97.72	0.00
11	97.69	97.59	-0.10
12	98.55	97.64	-0.92
13	97.75	97.65	-0.09
14	98.09	97.75	-0.34
15	97.37	97.85	0.47
16	98.16	97.93	-0.23
17	98.23	98.04	-0.19
18	97.85	97.95	0.10
19	97.26	97.90	0.64
20	97.51	98.15	0.64
21	97.94	98.05	0.11
22	97.84	98.14	0.30
23	97.86	98.09	0.23
24	97.85	97.99	0.14
25	97.54	97.85	0.31
26	97.69	97.89	0.20
27	97.79	97.81	0.02
28	97.45	97.64	0.19
29	98.93	98.81	-0.12
30	98.86	98.81	-0.06
31	99.05	99.04	-0.01
32	99.09	99.09	0.00
33	98.51	98.88	0.37
34	98.83	98.95	0.12
35	99.37	98.83	-0.54
36	98.38	98.89	0.51
37	98.94	99.04	0.11
38	98.71	98.94	0.23
39	98.87	99.05	0.18
40	99.12	98.80	-0.32
41	98.70	98.87	0.17
42	98.79	98.92	0.13
43	99.36	98.70	-0.67
44	99.30	98.74	-0.56
45	98.86	98.74	-0.12

CASE	Burnout ASM (%)	Burnout UPS (%)	ERROR (%)
46	98.71	98.70	-0.01
47	99.06	98.64	-0.42
48	98.66	98.66	0.00
49	98.86	98.75	-0.12
50	98.51	98.61	0.10
51	98.81	98.84	0.03
52	98.59	98.99	0.39
53	98.76	98.78	0.02
54	98.53	98.93	0.40
55	98.17	99.05	0.88
56	98.71	99.13	0.42
57	98.16	99.06	0.90
58	98.66	99.09	0.43
59	98.77	99.05	0.28
60	99.10	98.58	-0.52
61	98.64	98.52	-0.11
62	98.55	98.71	0.16
63	98.76	98.63	-0.13
64	98.57	99.03	0.45
65	97.80	98.62	0.82
66	98.25	98.64	0.39
67	98.56	98.65	0.09
68	98.91	98.72	-0.19
69	98.83	98.72	-0.12
71	99.44	99.25	-0.19
72	99.01	99.01	0.00
73	98.49	99.21	0.72
74	98.58	99.22	0.64
75	98.44	99.22	0.78
76	99.05	99.07	0.02
77	99.32	99.10	-0.21
78	99.36	99.10	-0.27
79	98.81	99.36	0.55
80	99.22	99.31	0.09
81	99.19	99.23	0.04
82	99.08	99.24	0.16
83	99.30	99.24	-0.07
84	99.27	99.30	0.03
85	99.56	99.53	-0.02
86	99.29	99.30	0.00
87	99.37	99.20	-0.17
88	99.43	99.43	0.00
89	99.64	99.52	-0.12
90	99.58	99.50	-0.07
91	99.52	99.53	0.01

Table 7.8 Burnout (%, coal basis) gathered at Lamarmora plant and calculated with the UPS (Unburned carbon Prediction System) and prediction error

Before determining the accuracy of the predictive system, we have performed a statistical study to analyze in detail the correspondence existing between plant data and the values calculated by the predictive system. For this, we have compared the statistical distributions of both data sets (plant data and system predicted values). Since the distributions' type is unknown, the

Anderson-Darling normality test for both sets has been carried out. Figures 7.5 (All data), 7.6 (Full load) and 7.7 (Partial load), show the probability diagrams obtained from the Anderson-Darling test, overlaid for both data sets and including the limits corresponding to a confidence level of 95 %.

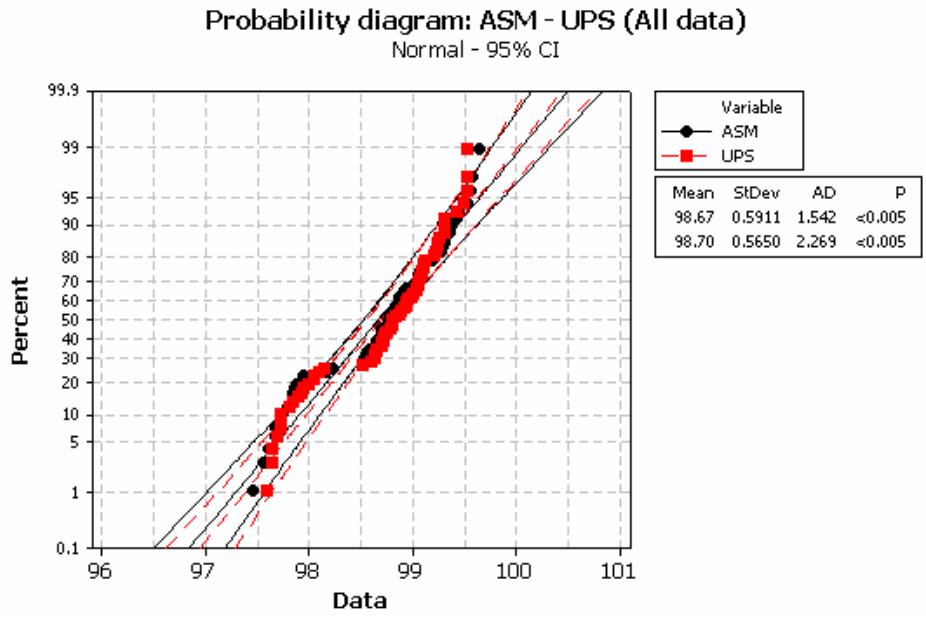

Fig. 7.5 Burnout (% - coal basis) probability diagrams: ASM and UPS (Unburned carbon Prediction System)

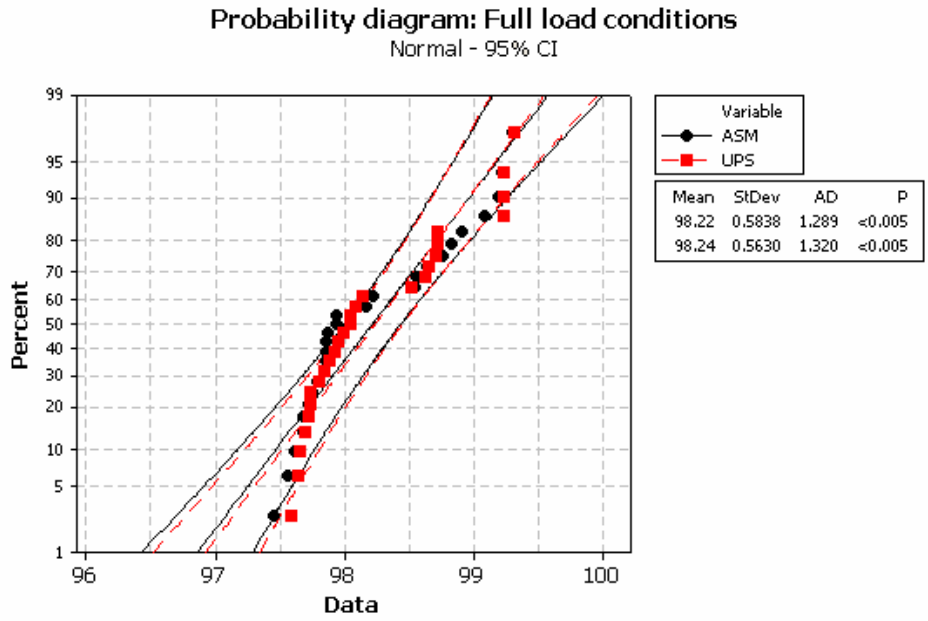

Fig. 7.6 Burnout (% - coal basis) probability diagrams under full load conditions: ASM and UPS (Unburned carbon Prediction System)

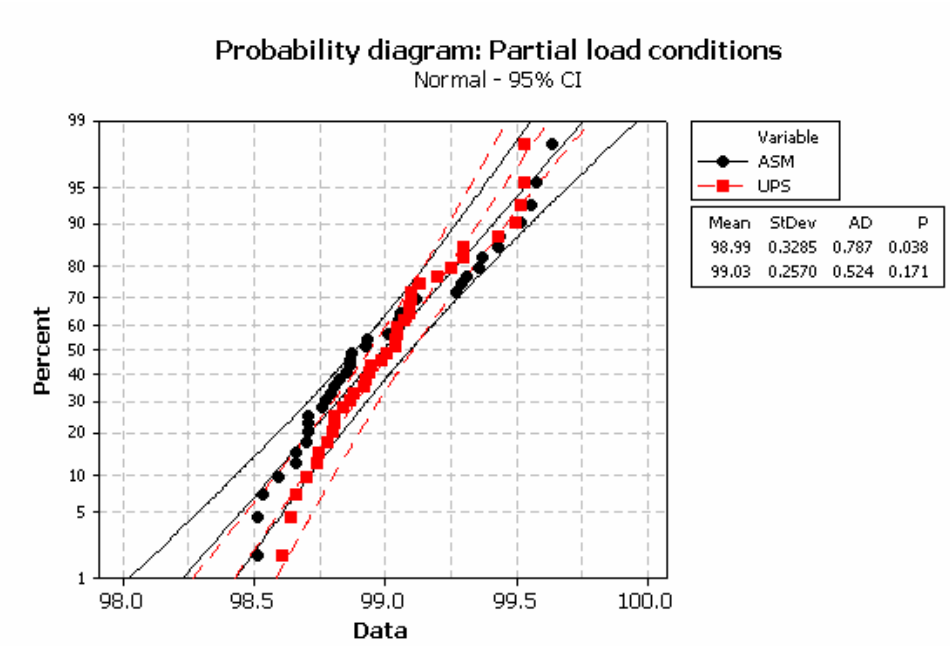

Fig. 7.7 Burnout (% - coal basis) probability diagrams under partial load conditions: ASM and UPS (Unburned carbon Prediction System)

The interpretation of Figures 7.5, 7.6 and 7.7 suggests that both data sets are not normal (p-value < 0.005). Therefore, in order to compare both distributions, we should make use of the mean, standard deviation, and the probability diagram itself. Figure 7.5, which includes all data, shows a good agreement between samples, both in the probability diagram representation along the whole range of variation and in the mean and standard deviation. Next, we have considered separately the probability diagrams for full and partial load conditions. First, under full load conditions the comparison of the probability diagrams together with mean and standard deviation for both sets shows a good agreement. On the other hand, under partial load conditions the correspondence with the mean is in agreement, but there exists a discrepancy in the standard deviation. These results confirm the discussion presented for Figures 7.3 and 7.4. In spite of this fact, from Figure 7.5 we can conclude that the system predicts reasonably well over the whole range of operating conditions of the study plant.

The last step in the development of the system lies in determining and expressing the global accuracy of the model. To achieve this, we have analyzed the statistical distribution of the "Error" column in Table 7.8. Again, the Anderson-Darling normality test has been applied, this time giving a positive result for the test (p-value = 0.012), as can be seen in Figure 7.8.

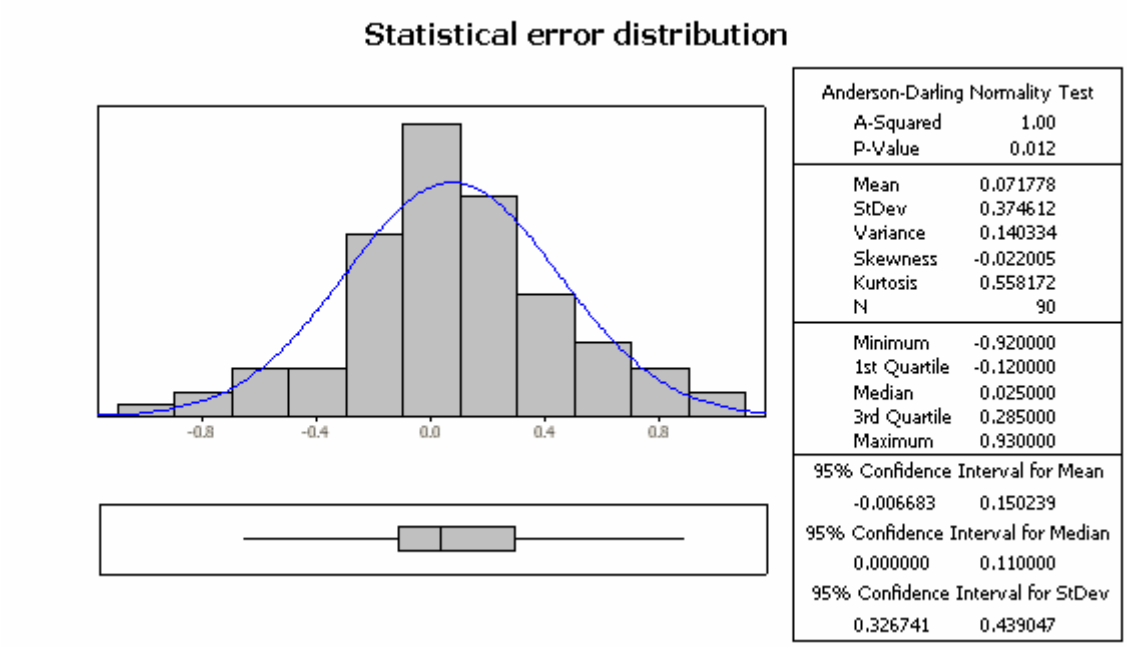

Fig. 7.8 Statistical distribution of the UPS burnout (%, coal basis) prediction error

It is outstanding that, in spite of the fact that the p-value is small, we have obtained a leptokurtic distribution (kurtosis = 0.558172), showing a smaller concentration of points in the extremes with a greater concentration around the mean value. This gives an extra confidence in the results obtained when analyzing the normal distribution. Another important result is that the mean is moved a little from zero which means that the model slightly over-predicts burnout. This result is not worrying since it is very small (0.071778) but it should be considered in the construction of the confidence intervals.

Taking the values of the 95.5 % confidence interval for the mean and standard deviation from Figure 7.8, it is possible to define an interval for the prediction error of a punctual estimation, with a 95.5 % confidence level, according to Eq. 7.1.

$$P(\mu - 2\cdot\sigma \le X \le \mu + 2\cdot\sigma) = 0.955 \qquad \text{(Eq. 7.1)}$$

That is, 95.5 % of the probability mass of the prediction error is inside the interval [μ - 2σ, μ + 2σ]. Consequently, assuming that ($\mu = \bar{x}$, $\sigma = \hat{\sigma}$), the error for a punctual estimation can be expressed according to Eq. 7.2.

$$E_{Bnt} = \mu \pm 2\cdot\sigma \approx \pm 0.82\ \% \qquad \text{(Eq. 7.2)}$$

Now, since the mean of the distribution is moved from zero, the lower extreme of the interval of Eq. 7.2 is in fact – 0.75 %. However, to simplify the interpretation, the error has been expressed using a symmetric interval from the higher value (0.82 %) according to Eq. 7.2, so that the confidence level is in fact higher than 95.5 %.

Therefore, the model accuracy within a confidence level of 95.5 % can be expressed in terms of burnout (%, coal basis) according to Eq. 7.3.

$$Bnt_{ASM} = Bnt_{UPS} \pm E_{Bnt} = Bnt_{UPS} \pm 0.82\ \% \qquad \text{(Eq. 7.3)}$$

In addition to the determination of the prediction error for a punctual estimation of the model, it is advisable to give the averaged prediction error for a set of random estimations. This practice is especially suitable in the case where using an on-line data acquisition system that collects data in short periods of time and, due to the fluctuations, target control variables are usually expressed as an average. Following this analysis, the average error for a number of random estimations ($n_o > 30$) is within the interval defined in Eq. 7.4.

$$\left[\overline{x}_n - \frac{\hat{\sigma}}{\sqrt{n_o}} \cdot z_{1-\alpha/2},\ \overline{x}_n + \frac{\hat{\sigma}}{\sqrt{n_o}} \cdot z_{1-\alpha/2} \right] \qquad \text{(Eq.7.4)}$$

Where, for a 95 % confidence level ($\alpha = 0.05$), the average prediction error estimation for a set of random estimations is expressed according to Eq. 7.5.

$$\overline{E}_{Bnt} = \overline{x}_n \pm \frac{\hat{\sigma}}{\sqrt{n_o}} \cdot z_{1-\alpha/2} \approx \pm\ 0.15\ \% \qquad \text{(Eq. 7.5)}$$

Again, a symmetric interval has been given, notwithstanding that the mean of the distribution has moved from zero, and so, the lower extreme of the interval of Eq. 7.5 is in fact – 0.07 %.

Therefore, for a set of random estimations, the model accuracy within a 95 % confidence level can be expressed in terms of burnout (%, coal basis) according to Eq. 7.6.

$$Bnt_{ASM} = Bnt_{UPS} \pm \overline{E}_{Bnt} = Bnt_{UPS} \pm 0.15\ \% \qquad \text{(Eq. 7.6)}$$

In order to obtain an indicator of the model accuracy in terms of the unburned carbon in ash (%), we can make use of the Kurose et al.'s (2001) expression (Chapter 1, Section 1.4, Eq. 1.1). This leads to the following Eqs. 7.7 to 7.10, that depend on the mineral matter content of the coal and the burnout.

$$CIA_{ASM} = CIA_{UPS} \pm E_{CIA} \quad \text{(Eq. 7.7)}$$

$$E_{CIA} = abs(CIA_{Bnt} - CIA_{Bnt+e}) \quad \text{(Eq. 7.8)}$$

$$CIA_{Bnt} = 100 \cdot \frac{100 - Bnt_{UPS}}{\left(\frac{Z}{1-Z}\right) + (100 - Bnt_{UPS})} \quad \text{(Eq. 7.9)}$$

$$CIA_{Bnt+e} = 100 \cdot \frac{100 - Bnt_{UPS} \pm E_{Bnt}}{\left(\frac{Z}{1-Z}\right) + (100 - Bnt_{UPS} \pm E_{Bnt})} \quad \text{(Eq. 7.10)}$$

Where, Z is the ash content (%), CIA_{Bnt} is the carbon-in-ash value corresponding to a burnout level Bnt_{UPS}, and CIA_{Bnt+e} is the carbon-in-ash value corresponding to a burnout level Bnt_{UPS} and considering a prediction error E_{Bnt} in the burnout determination.

Depending on the type of error that is used in Eq. 7.10, punctual or averaged for a number of random estimations, we will obtain both expressions for the accuracy of the model, respectively.

Considering the most disadvantageous situation and using Eqs. 7.7 to 7.10, Table 7.9 summarizes the maximum error achieved for the three study coals, both for a punctual estimation and for the average of a set of random estimations.

CIA maximum errors (%)

	Punctual estimation	Averaged estimation
Guasare	9.48	1.52
Carbonandes	8.44	1.38
Russian	7.73	1.27

Table 7.9 Maximum errors in the prediction of carbon-in-ash values within a confidence level of 95 % for the three study coals.

The evaluation of the results and the comparison with other unburned carbon prediction models are carried out in the next section. However, at this point it is interesting to mention two comments regarding the results in Table 7.9. Firstly, it should be noted that the calculated values in this table, are maximum errors. That is, these points would be located at the extremes of the distribution function (close to a signification level $\alpha/2$ or 1-$\alpha/2$). Furthermore, it should be remembered that the more sharpened the shape of the probability distribution function (positive kurtosis), the more points are located around the mean value, and consequently, this shows that the values presented in Table 7.9 are very exceptional. Finally, it should be considered that none of the prediction errors obtained in Table 7.8 have been discarded from the analysis. Generally, in statistical studies, the values located furthest away from the mean are discarded from the analysis if there is not a logical interpretation for them according to the data available in the problem. In the analysis of Figures 7.3 and 7.4, it was mentioned that the more distant points from the bisector did not indicate any apparent reason to infer an error in the model. In spite of this, we have decided to keep these fault points in the error analysis, in order to give a more conservative estimation of the prediction error and so taking into consideration the errors derived from the acquisition data process.

7.3 Unburned carbon prediction system analysis and valuation

To compare the prediction capability of the UPS (Unburned carbon Prediction System) performed in this work, we have undertaken an intensive search of the specialized literature. However, it is difficult to find references related to the unburned carbon determination, since most of the studies done in the last two decades have been focused on NO_x reduction problems. The reason for this is that power plants needed to reduce SO_2, NO_x and CO_2 particle emissions in order to meet the strict limits imposed by Community environmental policies. Once this kind of technology matured, power plant generators then started to worry about the unburned carbon problem which influences the global efficiency of the plant and adds an increment onto the generation cost.

It is common to find in most of the NO_x reduction related publications that the application of this kind of technique notably increases unburned carbon levels. Unfortunately, there is no quantification for the amount increased. In the same way, other papers related to CFD simulation of utility boilers conclude that a quantitative unburned carbon determination is difficult with the combustion models commonly used (see Chapters 1 and 6), and then, only general trends can be assessed (Stopford et al., 2002; Pallarés et al., 2005; Severin et al., 2005).

Recall that the unburned carbon prediction systems mentioned in Chapter 1 can be classified into three groups (Table 7.10).

Prediction System	Advantages	Disadvantages
1. Facility test experiments	Permit to carry out a detailed study of the coal combustion process under different conditions	High investment costs It is difficult to scale up the result to real boilers
2. Combustion kinetics models	Detailed combustion calculations	Simplified fluid dynamics and thermal behaviour
3. CFD codes	Detailed fluid dynamics and thermal behaviour	Simplified combustion calculations

Table 7.10 Unburned carbon prediction systems

Excluding the experimental methods, since they cannot be used in an on-line predictive system; the following discussion is focused on the other two types of systems: combustion kinetics models and CFD codes.

We consider the detailed coal combustion kinetics models, generally developed from the study of the real combustion process in experimental facilities, which has the advantage to simulate the coal combustion process in a very realistic way. However, these models need the fluid and thermal behaviour in the boiler, which is usually obtained from simplified zonal approaches. The other group of models, namely CFD codes, present the opposite features. That is, they give a detailed description of the thermal and fluid dynamics behaviour in the boiler but they use simple combustion models that cannot be used for a quantitative burnout determination. Moreover, the computing cost can be high and cannot be implemented in an on-line predictive system.

The predictive system developed in this work has the same structure as the so-called combustion kinetics models. However, it obtains the fluid and thermal description through CFD simulations. To solve the handicap of the high computational cost needed to run a CFD simulation, a neural network system is used to reproduce the solutions given by the CFD code.

In principle, it seems reasonable that by using this methodology the unburned carbon predictions will be improved compared with other combustion kinetics models based on zonal approaches. Coming back to the literature, again, only a few publications discuss the unburned

carbon phenomena. In fact, we have only found one publication, Severin et al. (2005), which presents quantitative results on carbon-in-ash predictions in a utility boiler. In this paper, Severin et al. (2005), uses a combustion kinetics model which includes variations in the char reactivity, the char superficial area and includes ash inhibition effects. The thermal and fluid dynamics behaviour is introduced through a zonal approach which divides the flow domain into a number of cells, enough to characterize main flow interactions in the boiler. This predictive system is run for the 300 MWe Sines power station (Portugal), under three different operating conditions, obtaining a deviation of the unburned carbon in ash prediction of over 3.5 %. Table 7.11 shows the proximate and ultimate analysis of the coal blends feed during the tests. Table 7.12 shows the carbon-in-ash values measured at the plant against the predictions of the model.

	Case 1	Case 2	Case 3	
Proximate analysis (% wt, dry basis)	**Rows 1-5**	**Rows 1-5**	**Row 1**	**Rows 2-5**
Z	13.36	13.36	9.88	10.56
VM	28.85	28.85	34.78	32.4
FC	51.02	51.02	55.34	57.04
Ultimate analysis (% wt, dry basis)				
C	67.68	67.68	72.85	71.95
H	4.4	4.4	4.75	4.32
O	5.31	5.31	10.33	11.02
N	1.54	1.54	1.4	1.48
S	0.94	0.94	0.79	0.67

Table 7.11 Proximate and ultimate analysis of the coal blends Severin et al. (2005)

	CIA Sinnes (%)	CIA Model (%)	Error (%)
Case 1	3.2	6.7	3.5
Case 2	2.5	6.2	3.7
Case 3	4	7.7	3.7

Table 7.12 Carbon-in-ash results at Sinnes power station and Severin et al. (2005) model prediction

As it was mentioned before, to compare the accuracy of both models, it is not possible to contrast directly the error obtained in the carbon-in-ash prediction since this itself depends on the ash content of the coal. From the analysis in Table 7.11 and Eqs. 7.7 to 7.10, we have obtained the error in terms of burnout for the three scenarios in Severin et al. (2005) (Table 7.13)

	E_{brnt} (%)
Case 1	-0.6
Case 2	-0.62
Case 3	-0.49

Table 7.13 Prediction error (% burnout) Severin et al. (2005)

Even with the results in Table 7.13 it is not possible to rigorously compare the prediction capabilities of both models since in the referred publication there is no mention as to how they have obtained these values. It is not clear if they represent punctual or averaged estimations and in addition the number of scenarios is too small. Therefore, we will only discuss two brief considerations. First, the predictive system described by Severin et al. (2005), over-predicts burnout in all three scenarios (Table 7.13). On the contrary, the UPS (Unburned carbon Prediction System) in this work has shown an error distribution whose mean is close to zero (Figure 7.8). Second, if the prediction errors in Table 7.13 are introduced into the error distribution in Figure 7.8, those values would be out of the 95 % confidence interval for the mean [-0.006683, 0.150239]. That is, although these values would be in the error range of the UPS model, they would be located in a very low probability area. This is one of the advantages of giving the prediction error of the system through a statistical study, since this way, it is easy to perform a comparative study. Another reason is that by only giving a single value of the accuracy of the system the result could be misleading. For example, if we had given a single result for the accuracy of the model by averaging the results over the total number of cases, we would have obtained a burnout prediction error of 0.07 % and in terms of carbon-in-ash values of 1.07 %, 0.92 % and 0.82 % for the coals Guasare, Carboandes and Russian, respectively.

Finally, to close this comparative study, Severin et al. (2005) stated in their conclusions that the prediction error achieved was due to the simplifications that were made in the description of the particles trajectories and in the temperature and oxygen partial pressure description in the boiler, in order to reduce the computational cost. To this effect, the unburned carbon prediction system developed in this work has led to a more realistic description of the temperature and oxygen partial pressure profiles found by the particles in their trajectories across the boiler, without compromising the computational time. This fact, allowed us to conclude that we have obtained an acceptable prediction accuracy of the system, improving the results obtained with any zonal approach.

To close this chapter, we will discuss the most controversial aspect of the UPS proposed in this work. Firstly, it should be mentioned that in spite of the advantages previously presented, and although the global prediction of the system is adequate, there are still some uncertainties in the validation of the model under partial load conditions. In the previous section we discussed the importance of the neural network system development and its influence on the later combustion calculations. However, this design should be balanced to achieve a good generalization and to avoid overtraining situations.

Nevertheless, as a final conclusion, the results presented in this work allow us to affirm that the predictive system complies with the requirements proposed in this thesis.

7.4 Conclusions

In this final chapter, we have developed the unburned carbon prediction system that provides an on-line estimation of the unburned carbon in ash for a given operating condition in a utility boiler.

The final system is formed by the local combustion conditions model (Chapter 5) and an advanced combustion model (Chapter 6). The former provides the system with the evolution of the temperature and oxygen partial pressure profiles found by the particles in their trajectories across the boiler. This sub-model, based on a neural network system, for the range of operation conditions in the study plant, reproduces the values calculated for these profiles by means of CFD simulations. The advantage of this system is that it allows us to obtained profiles under any other condition not specifically used during the training stage of the networks. Moreover, the computational cost is negligible (less than a minute) when compared with CFD simulations. The other sub-model is the combustion model itself which is divided into two subroutines. One corresponding to the devolatilization of the coal particle (FG-DVC) and the other the char oxidation intrinsic model which includes: thermal annealing, variations in the porous structure as combustion proceeds, ash inhibition effects and the influence of macerals in the reactivity of the char.

The validation of the unburned carbon prediction system has been carried out using standard plant instrumentation measurements gathered at Lamarmora ASM Brescia power station during the year 2005 (January – March 2005), where three coals of different provenance were burned separately covering the regular range of variation in the plant operating conditions. Results from the predictive system have been compared against those gathered at the plant, after carrying out a statistical study for validating and determining the prediction capability of the system. The comparison of both sets of data (gathered at the plant and predicted by the system) has shown an excellent correspondence in the probability distribution, mean and standard deviation along the whole range of situations studied. The maximum error achieved for the burnout prediction is 0.82 % for a punctual estimation and 0.15 % for the average of a number of random estimations. Finally, the predictive system developed in this work has been compared with another predictive system based on a zonal approach. The analysis of both

models have shown a considerably improvement in the accuracy of the system with the methodology used in this work.

As a final conclusion, it should be noted that the system complies with the design requirements established at the beginning of this work (accuracy and reduced time response).

Finally, the main advantages of the unburned carbon prediction system can be presented in a schematic way:

- The system includes a detailed description of the transport phenomena involved in the problem by implementing the neural network system which was trained with CFD simulations covering the operational range of the plant.
- The neural network system itself allows us to interpolate for other conditions not specifically used during the training stage.
- The combustion model describes in detail both devolatization and char oxidation.
- The number of inputs of the predictive system is small and they are available at any power station.
- The computational time, less than a minute, allows us to use it in an on-line monitoring system of a power station.
- The accuracy of the system is good enough in the whole range of operation of the plant and improves the results obtained with other predictive systems based on zonal approaches.

Nomenclature

A_c	pre-exponential factor of the formation relation CO/CO_2
Bnt_{ASM}	burnout measured at the plant
Bnt_{UPS}	burnout calculated by the UPS
CIA_{ASM}	carbon-in-ash measured at the plant
CIA_{Bnt}	carbon-in-ash corresponding to a burnout *Bnt*
CIA_{Bnt+e}	carbon-in-ash corresponding to a burnout Bnt_{UPS} and assuming an estimation error E_{Bnt}
CIA_{UPS}	carbon-in-ash calculated by the UPS
d_{pm}	mean particle diameter Rosin Rammler (m)
E_{Bnt}	UPS prediction error (% burnout)
E_c	activation energy of the formation relation CO/CO_2 (kcal/mol)
E_{CIA}	UPS prediction error (% carbon-in-ash)
E_e	activation energy (kJ/mol)
n	apparent order reaction
n_o	size of the data sample
n_{rr}	dispersion factor Rosin Rammler distribution
Swell	swelling factor
P_iO_2	oxygen partial pressure (N/m^2)
Q_a	primary air mass flow (kg/s)
Q_c	coal mass flow (kg/s)
t	time (s)
t_{res}	residence time (s)
Z	% ash content
α	signification level of the statistical distribution
δ_m	minimum ash film thickness (cm)
σ	standard deviation of the statistical distribution
θ_{taf}	critical ash film porosity
μ	mean of the statistical distribution

Acronyms

CFD	computational fluid dynamics

CIA	carbon-in-ash
DTF	drop tube furnace
UPS	unburned carbon prediction system

SYNTHESIS, CONTRIBUTIONS AND FUTURE DEVELOPMENTS

SYNTHESIS

In the last decades, pulverized coal-fired steam generators have been progressively affected by more restrictive requirements for particulate and gas emissions, in order to reduce atmospheric pollution, acid rain and the greenhouse effect. Thus, low NO_x techniques and efficient gas cleaning systems have been implemented to satisfy the environmental legislations. However, some drawbacks may arise when emission reduction techniques are applied. Unburned carbon levels increase when excess air decreases, limiting the reduction in NO_x formation which can be achieved by primary techniques through combustion modification.

Unburned char particles that leave the furnace represent a heat loss in the combustion process, reducing the thermal efficiency of the unit. Since the price of coal is the higher variable cost in the plant, a little save in its price may imply a significant reduction in the power plant expenditure. Moreover, unburned carbon increases heat exchangers erosion, may reduce the efficiency of dust separation/collection equipment and may impede the utilization of fly ash as a replacement for Portland cement or additives to concrete. In consequence power plant managers look for the most efficient combustion conditions, in order to maximize coal conversion while meeting the environmental legislations.

Increasing efficiency, controlling particulate and gas emissions, and minimizing unburned carbon losses, are partially attained by improving the combustion process. For this reason, predicting combustion efficiency in utility boilers, and particularly, determining unburned carbon levels, are essential to reach both objectives.

To achieve this, the main goal of this thesis work was to develop an unburned carbon prediction system, that provided an on-line estimation of carbon in ash losses for a given operating condition in a utility boiler. At the same time, a system with such characteristics may allow the plant personnel to identify the source of an increase in the carbon in ash level or to look for the most suitable conditions to minimize this loss. For the development and validation of this work, a unit from Lamarmora power plant (ASM Brescia, Italy) was chosen as the case-study boiler. This election was taken as a result of the close partnership established between ASM and CIRCE Foundation during the European research project 7220-PR-130-130-CARNO.

The starting point for the construction of an unburned carbon prediction system was to determine which factors are relevant in carbon burnout and to quantify their influence. Main factors affecting unburned carbon losses may be classified into three categories: coal and char related properties, coal preparation and grinding pre-treatments, and burners and boiler designs and operation conditions. Nevertheless, not all these factors may be modified during the daily operation of the plant, thus impacting the unburned carbon loss.

In this work, a sensitivity analysis of the main factors affecting unburned carbon losses was performed, which can be actuated by the technical personnel in the plant either directly or indirectly. The main parameters analyzed in this work have been:

- Primary air to coal mass flow ratio
- Excess air (stoichiometry)
- Particle size
- Secondary air swirl intensity
- Fuel/air mass flow imbalances through burners

To analyze and quantify their influence on unburned carbon formation, we carried out a double study of theses parameters, using a CFD commercial code (CFX-4, AEA Technology). Firstly, in the regular range of variation, we evaluated the contribution of each factor to the final unburned carbon level, keeping constant the rest of the parameters. Subsequently, we evaluated cross-related effects and interactions amongst these various factors. This study, in which we made used of multi-parameter factorial analysis techniques, gives a more realistic view of the

problem since the contribution of one factor may vary depending on the conditions of the other factors. Results suggested that the oxygen level is the most relevant factor in unburned carbon formation. However, other factors, that did not have a remarkable relevance in the individual parameter sensitivity study, may turnout to be relevant in coal burnout depending on the boiler conditions and on cross-related interactions amongst these factors.

Once the most relevant factors affecting unburned carbon losses were identified, we proceeded with the design of the structure of the unburned carbon prediction system. In general, the combustion behaviour of pulverized coal can be investigated by means of pilot-scale experiments, combustion kinetics models and CFD codes. Experimental approaches are very useful in design studies. However, for the daily monitoring of a real plant, the computational methods offer a flexibility as well as a saving of time and money, over current experimental facilities. Within the computational methods regularly used, detailed coal combustion kinetics models, generally developed from the study of the real combustion process in experimental facilities, have the advantage to simulate the coal combustion process in a very realistic way. However, these models need the fluid and thermal behaviour in the boiler, which is usually obtained from simplified zonal approaches. The other group of models, namely CFD codes, present the opposite features. That is, they give a detailed description of the thermal and fluid dynamics behaviour in the boiler, but they use simple combustion models that cannot be used for a quantitative burnout determination. Moreover, the computing cost can be high and cannot be implemented in an on-line predictive system.

In this work, we have developed a new methodology that takes advantage of both of the following approximations: the detailed fluid and thermal description of CFD codes and the precise combustion calculations of advanced kinetics models. To achieve this aim, we considered two possibilities:

1. To fully couple the advanced combustion kinetics model into a CFD code.

2. To use the temperature and oxygen partial pressure profiles for a representative number of particles from a CFD code and then introduce them as inputs into an advanced combustion kinetics model.

The first possibility was discarded since it was impossible to introduce all the combustion equations into a commercial code with licence and copyright. Following this line, we carried out few modifications in the combustion model of the commercial code CFX-4, introducing rank dependant correlation for char reactivity, through the activation energy and the pre-

exponential factor (Hurt and Mitchell, 1992), and a sub-model describing ash inhibition effects (Hurt and Sun, 1998). As a result, we considerably improved unburned carbon predictions as compared with the results obtained with the one film model implemented in CFX. However, these modifications, since they do not take into account the variations in char porous structure and reactivity as combustion proceeds, are only able to predict general trends and fail in the prediction of quantitative values.

For this reason, we decided to keep the use of the CFD code as a thermal and fluid-dynamic characterization tool, and then introducing this information (temperature and oxygen partial pressure histories of the simulated particles) as inputs into an advanced combustion kinetics model. To solve the problem of the high computational cost, we proposed the utilization of a neural network system that generates the oxygen partial pressure, and temperature profiles, and the residence time of particles for any operating condition. The advantage of introducing the neural network system in this way, is that it is possible to perform the calculations in a short period of time (less than a minute), and therefore, it can be used in the construction of an on-line predictive system. Another advantage is that, if the neural network system is appropriately trained, considering the variations and interactions of all parameters affecting unburned carbon formation, this system permits to interpolate in the range of variation used during the training stage. Thus, a predictive system covering the whole operational range of the plant can be obtained. Consequently, an unburned carbon prediction system with such characteristics allows us to unify the following advantages within the same system: fluid dynamics and heat transfer from CFD codes, detailed chemical kinetics from advanced combustion models, and reduced computing cost and interpolation capabilities from neural networks.

In order to obtain the data used to develop, train and validate the neural network system, we performed a set of 72 CFD simulations covering the operational range of the study plant. Thus, a new design of experiments based on factorial analysis was carried out, in such a way that three levels of the most relevant factors affecting carbon losses (excess oxygen, primary air to coal mass flow ratio, particle size, fuel/air mass flow imbalances through burners) were included, differentiating between full and partial load conditions.

For the development of the model, the commercial code Matlab Neural Network Toolbox 4.0 was used. The neural network system learn, reproduce and interpolate the results (by means of temperature and oxygen partial pressure profiles, and particles' residence times) obtained from the CFD code for any particular boiler operating conditions. As a result of the study, it was concluded that that the neural network system, called the local combustion conditions model, accurately reproduced the profiles obtained by the CFD simulations. Moreover, due to the

generalization capability of the neural networks, it was possible to obtain solutions for any operating conditions as long as they belong to the range used during the training stage.

With regard to the combustion model, a revision of each stage in the combustion process (devolatilization, homogeneous combustion of volatile products, and char oxidation), describing the mechanisms and the more characteristics models available in the specialized literature, was performed. From this revision, an advanced combustion model was developed, focusing on the reactions that take place on the particle surface, that is, devolatilization and char oxidation. Devolatilization was modelled using a macromolecular network pyrolysis model (FG-DVC). Char oxidation was modelled and programmed in Fortran using a developed intrinsic formulae based on the carbon burnout kinetic model (CBK8) (Sun and Hurt, 2000), that allows the transition to Zone I and includes the variation in the porous structure and reactivity of the char as combustion proceeds, mineral matter effects, and the influence of coal's maceral content. To investigate the burnout prediction capability of the model a total of nine scenarios of the case-study boiler were studied, showing a good agreement in trends and quantitative values with standard plant instrumentation measurements.

Finally, the construction of the unburned carbon prediction system (UPS) from the previous elements (CFD + Neural networks and advanced combustion model), meant the culmination of the main goal of this thesis, that is, the development of a predictive system that provides an on-line estimation of the unburned carbon in ash for a given operating condition in a utility boiler.

The validation of the unburned carbon prediction system has been carried out using standard plant instrumentation measurements gathered at Lamarmora ASM Brescia power station during the year 2005 (January – March 2005), where three coals of different provenance were burned separately covering the regular range of variation in the plant operating conditions. Results from the predictive system have been compared against those gathered at the plant, after carrying out a statistical study for validating and determining the prediction capability of the system. The comparison of both sets of data (gathered at the plant and predicted by the system) has shown an excellent correspondence in the probability distribution, mean and standard deviation along the whole range of situations studied. The maximum error achieved for the burnout prediction is 0.82 % for a punctual estimation and 0.15 % for the average of a number of random estimations. Finally, the predictive system developed in this work has been compared with another predictive system based on a zonal approach. The analysis of both models have shown a considerably improvement in the accuracy of the system with the methodology used in this work.

CONTRIBUTIONS

Chapter 2

A revision of each stage in the combustion process (devolatilization, homogeneous combustion of volatile products, and char oxidation), describing the mechanisms and the more characteristics models available in the specialized literature, is performed. Of course, it is not possible to perform a complete compilation of all the published models used for modelling coal combustion. However, we have attempted to present the most classical models, together with advanced models that go deeply into more particular aspects of pulverized coal combustion. The selection criteria for the models described in this work responds to three premises:

- The general applicability under typical pulverized coal combustion conditions.
- The acceptance level in the scientific community.
- That serves as reference and starting point for the coal combustion model development carried out in this work in Chapter 6.

Chapter 3

In this chapter, general characteristics of CFD codes are described, specifying the numerical resolution method and the physical and chemical models involved in the modelling of coal combustion in utility boilers, for the commercial code used in this work (CFX-4, AEA Technology). Finally, the validation process followed in this work is presented. To achieve this, the chapter is divided in the following sections:

- Finite volume method: discretization of the domain and the transport equations governing the problem.
- Description of the mathematical models involved in the problem (turbulence, multi-phase flow, homogeneous combustion, heterogeneous combustion, and radiation).
- Description of the boundary conditions for the problem.
- Validation of the numerical resolution method, describing all the uncertainties associated with the numerical discretization of the equations, and the uncertainties associated with the modelling of the real process, suggesting how to estimate their contribution.

Chapter 4

In this chapter, we performed a review of combustion related publications, in which reaction stoichiometry and coal grain-size distributions were reported as the most influence factors on combustion efficiency. In spite of this fact, most of these studies were carried out in scale burner-test facilities, in which some determining factors such as primary and secondary air

mixing, swirling intensity, burner to burner flow interactions, reversed-flow regions or mass flow imbalances, were not possible to study. For this reason, in this work, since CFD tools are not limited with respect to these aspects, we included all the factors that may have an effect on combustion and studied their influence on unburned carbon losses. To achieve this, we performed a sensitivity study of main factor affecting carbon burnout: excess oxygen, primary air to coal mass flow ratio, particle size distribution, secondary air swirling intensity, and mass flow imbalances through the burners. The study was divided in two phases. First, we performed a preliminary sensitivity study to analyze individual contributions of each factor, maintaining constant the rest. Results suggested that the oxygen level is the most relevant factor in unburned carbon formation, specially for excess oxygen values under 4 %. However, the rest of factors, such as mass flow imbalances, particles size and primary air to coal mass flow ratio, may be turned relevant for excess oxygen values over 4 %. Next, a second sensitivity study was performed analyzing the effects of interactions, since these factors in real utility boilers do not take place individually, and their interaction may have important influence on the total unburned carbon. When several sources of variation are acting simultaneously on a set of observations, it is particularly useful to fall back on variance analysis techniques. In order to reduce the number of simulations needed to complete the full experiment, a fractional factional analysis was applied, performing a variance analysis of the simulated values. Result for this multi-parameter sensitivity study confirmed the results from the preliminary study, showing that, other factors such as primary air to coal mass flow ratio or mass flow imbalances through the burners, or their interactions may have a remarkable relevance in coal burnout depending on the boiler conditions.

From the results obtained in the sensitivity study, it is possible to establish actions lines that allows the plant personnel to identify the source of an increase in the carbon in ash level or to look for the most suitable conditions to minimize this loss.

Chapter 5

In this chapter, a neural network system that learn, reproduce and interpolate the results (by means of temperature and oxygen partial pressure profiles, and particles' residence times) obtained from the CFD code for any particular boiler operating conditions, have been developed. The constitution of the neural network model is divided into three stages (design of the structure, training of the neural network, and validation), establishing an iterative revision process that concludes once the neural network obeys the design criteria. To achieve this, we have performed a number of CFD simulations, covering the operational range of the study plant. In order to obtain the data used to develop, train and validate the neural network system, a new design of experiments based on factorial analysis was carried out. As a result of the study, it is

concluded that that the neural network system, accurately reproduces the profiles obtained by the CFD simulations. Moreover, due to the generalization capability of the neural networks, it is possible to obtain solutions for any operating conditions as long as they belong to the range used during the training stage.

Chapter 6

In this chapter, a new methodology that combines the advantages of CFD codes (detailed thermal and fluid dynamic description) and advanced combustion models (detailed combustion kinetics), to improve combustion related predictions in power plants has been presented. This methodology uses the temperature and oxygen partial pressure profiles for a representative number of particles from CFD simulations, and then introduces them, together with coal properties, into an advanced combustion kinetics model.

This chapter focused on the description, development and validation of the combustion model. Devolatilization was modelled using a macromolecular network pyrolysis model (FG-DVC), because of its applicability to a wide range of coals and heating rates, and its ability to predict the variations in species yield with reactor conditions. Char oxidation was modelled and programmed in Fortran using a developed intrinsic formulae based on the carbon burnout kinetic model (CBK8) (Sun and Hurt 2000), that allows the transition to Zone I and includes the variation in the porous structure and reactivity of the char as combustion proceeds, mineral matter effects, and the influence of coal's maceral content.

To investigate the burnout prediction capability of the model a total of nine scenarios were tested with standard plant instrumentation measurements gathered at the Lamarmora (ASM Brescia) power station. Results from the study show a good agreement in trends and quantitative values, even where a notable sensibility of the model is expected when slight operational variations were applied. Results also confirm an acceptable approach to the methodology, formulation and assumptions have been proposed in this work. We can therefore conclude that the combination of CFD codes and advanced combustion models permits the predictive system to be sensitive to the changes that arise from slight variations in operating conditions and uneven flow variations which strongly affect the overall burnout prediction.

Chapter 7

In this final chapter, we have developed the unburned carbon prediction system that provides an on-line estimation of the unburned carbon in ash for a given operating condition in a utility boiler.

The final system is formed by the local combustion conditions model (Chapter 5) and an advanced combustion model (Chapter 6). The former provides the system with the evolution of the temperature and oxygen partial pressure profiles found by the particles in their trajectories across the boiler. This sub-model, based on a neural network system, for the range of operation conditions in the study plant, reproduces the values calculated for these profiles by means of CFD simulations. The advantage of this system is that it allows us to obtained profiles under any other condition not specifically used during the training stage of the networks. Moreover, the computational cost is negligible (less than a minute) when compared with CFD simulations. The other sub-model is the combustion model itself which is divided into two subroutines. One corresponding to the devolatilization of the coal particle (FG-DVC), and the other the char oxidation intrinsic model which includes thermal annealing, variations in the porous structure as combustion proceeds, ash inhibition effects, and the influence of macerals in the reactivity of the char.

The validation of the unburned carbon prediction system has been carried out using standard plant instrumentation measurements gathered at Lamarmora ASM Brescia power station during the year 2005 (January – March 2005), where three coals of different provenance were burned separately covering the regular range of variation in the plant operating conditions. Results from the predictive system have been compared against those gathered at the plant, after carrying out a statistical study for validating and determining the prediction capability of the system. The comparison of both sets of data (gathered at the plant and predicted by the system) has shown an excellent correspondence in the probability distribution, mean and standard deviation along the whole range of situations studied. The maximum error achieved for the burnout prediction is 0.82 % for a punctual estimation, and 0.15 % for the average of a number of random estimations. Finally, the predictive system developed in this work has been compared with another predictive system based on a zonal approach. The analysis of both models have shown a considerably improvement in the accuracy of the system with the methodology used in this work.

Finally, the main advantages of the unburned carbon prediction system can be presented in a schematic way:

- The system includes a detailed description of the transport phenomena involved in the problem by implementing the neural network system which was trained with CFD simulations covering the operation range of the plant.
- The neural network system itself allows us to interpolate for other conditions not specifically used during the training stage.

- The combustion model describes in detail both devolatization and char oxidation.
- The number of inputs of the predictive system is small and they are available at any power station.
- The computational time, less than a minute, allows us to use it in an on-line monitoring system of a power station.
- The accuracy of the system is good enough in the whole range of operation of the plant and improves the results obtained with other predictive systems based on zonal approaches.

FUTURE DEVELOPMENTS

Future work after finishing this thesis are classified into two categories: system developments and developments in the user interface of the system

A. System developments

In this first group, all the developments that may be taken into account in a future system are considered in order to improve burnout predictions. Sometimes, further developments in the models will result in a greater complexity of the system, and thus, a penalty in the computational time. For this reason, depending on the specific application of the system and the accuracy required in the solutions, the designer will have to weigh up both precision and computational time.

By analogy with the outline of this work and with the structure of the system itself, future developments are presented grouped into the different blocks of the system.

1. CFD model developments

In order to improve the accuracy in the simulations, a number of suggestions are pointed out. At this point, special attention should be paid to the computational time.

- Geometry: The inclusion of radiant superheaters will improve the thermal and flow behaviour description in the boiler.

- Mesh: By refining the mesh grid, more precise values for the flow variables will be obtained, especially in the near burner region where major temperature, velocity and species concentration gradients take place. Nevertheless, the mesh size structure used in this work established a convergence criteria for the control variable (% burnout, coal basis) variation of 0.1 %, and proves to be adequate for our problem (Chapter 4, Section 4.2.4).

- Particle transport model: In order to obtain a more detailed description of the particles trajectories, turbulent dispersion effects may be included. To achieve this, it will be necessary to model a larger number of particles (at least one order of magnitude higher than in the case of not considering turbulent dispersion effects), resulting in a huge increase of the computational time. Furthermore, some authors suggest that including this effect, it is more difficult to achieve the convergence of the problem (Chen and Shuen, 1993).

- Radiation model: Since the absorption and emission of participative gases depend on the gas temperature and partial pressure, a multi-grey gas model description will better describe real gas mixture behaviour.

2. Neural network system developments

Neural network system developments can be evaluated from two points of view: improved precision and improved generalization. Both aims are in opposition, so improving the accuracy to reproduce the training data for the same dataset decreases the network capability to generalize and vice versa. In fact, as it was described in Chapters 5 and 7, the balance of this competition entails one of the biggest challenges of the problem and thus, the area where we have placed an increased emphasis in the neural networks system development. This problem is more pronounced under partial load conditions since the stratification of the conditions within the boiler is more relevant than in the case of full load conditions where there is a greater uniformity in the temperature and oxygen partial pressure profiles.

Consequently, one solution proposed to improve both aspects (precision and generalization) would lie in increasing the number of CFD simulations in order to obtain more training data. In this way, it would be possible to enlarge the neural network structure, improving the accuracy and avoiding overtraining situations.

An alternative solution would lie in developing a more complex design of the neural network system. This solution was adopted in this work, by considering different networks for the upper and lower row of burners and including the starting feeding position of the particles within the burner. In the same way, it would be possible to improve the model by increasing the number of inputs or complicating further the structure of the neural network system.

3. Advanced combustion model developments

In the following discussion, in order to point out future developments in the combustion model we will distinguish between improvements in the model application, and improvements in the model development.

The first group, improvements in the model application, is related with the available kinetic and structural information of the coal in the models. Devolatilization kinetic rate parameters for the case-study coals have been extrapolated from a database included in the FG-DVC code. Similarly, the char oxidation kinetic parameters, the structural characteristics of the coals (mean pore size, porosity, ash properties, etc.), the petrographic information and the combustion behaviour of the study coals (swelling, fragmentation, etc.) were obtained from previous studies, discussions and suggestions from other authors and databases.

Therefore, an improvement in the accuracy of the burnout predictions would be obtained by fitting from experiments the kinetic and coal structural parameters of the model: characterization of the devolatilization process (volatile yield and rate), determination of the initial char reactivity and porosity, conducting ash composition and properties analysis, determination of coal petrographic composition, etc.

With regard to the second group of improvements, the combustion model developed in this work is probably one of the most complete models in the literature. Nevertheless, one of the most promising investigations in coal combustion modelling focuses on the development of intrinsic models based on complex reaction mechanism. An example of this kind of mechanisms is the three-step semi-global kinetics proposed by Hurt and Calo (2001) (see Chapter 2, Section 2.3.1).

B. Developments in the user interface of the system

In this second group, the improvements in the user interface of the system are considered. At the moment, the core of the unburned carbon prediction system is divided into two blocks programmed in Fortran. The first block contains the neural network system description and is responsible for generating a solution file with the temperature and oxygen partial pressure profiles, and particles' residence times. The second block contains the combustion model in which the previous solution file is applied. In general, the structure and interface of the system is very intuitive. In order to help the user to run the system, the data acquisition process is guided by the program displaying specific windows that ask for the input parameters. However, if the system is going to be incorporated into the control system of a power plant, it would be advisable to modify the user interface in order to show a more familiar windows environment.

Annexe PUBLICATIONS

P.1

“Numerical prediction of unburned carbon levels in large pulverized coal boilers”

Fuel 84 (2005) 2364-2371

J. Pallarés, I. Arauzo, L.I. Díez

Available online at www.sciencedirect.com
SCIENCE DIRECT®
Fuel 84 (2005) 2364–2371
FUEL
www.fuelfirst.com

Numerical prediction of unburned carbon levels in large pulverized coal utility boilers

Javier Pallarés*, Inmaculada Arauzo[1], Luis Ignacio Díez[2]

Centre of Research for Energy Resources and Consumptions (CIRCE), Thermal Division, University of Zaragoza, María de Luna 3, 50018 Zaragoza, Spain

Received 6 April 2004; received in revised form 18 March 2005; accepted 10 May 2005
Available online 13 June 2005

Abstract

Advanced combustion kinetics models are of widespread use to predict carbon losses from coal combustion. However, those models cannot completely capture the complexity of the real phenomena affecting the fluid flow in a full-scale utility boiler, such as burner-to-burner interactions and bottom hopper vortexes or reversed-flows, and usually underpredict carbon in ash values. The use of CFD codes offers a more detailed treatment of the fluid dynamics involved in the boiler. However, most of them do not incorporate advanced kinetics submodels for char oxidation. In this paper, rank-dependent correlations and ash inhibition submodel have been coupled to a commercial CFD code, significantly improving carbon in ash predictions. Results from the simulation of the ASM Brescia power plant (Italy) for three different South-American coals are compared against plant laboratory values, using either the popular single film combustion model or the modified combustion model discussed in this paper.

Keywords: Unburned coal; Coal combustion; CFD

1. Introduction

In the last decades, pulverized coal-fired steam generators have been progressively affected by more restrictive requirements for particulate and gas emissions. Thus, low NO_x techniques and efficient gas cleaning systems have been implemented to meet the environmental legislations. However, some drawbacks may arise when emission reduction techniques are applied. Unburned carbon levels increase when air excess decreases, limiting the reduction in NO_x formation that can be achieved by primary techniques, i.e. by combustion modifications. Unburned char particles that leave the furnace represent a heat loss in the combustion process, reducing the thermal efficiency of the unit. Moreover, they increase heat exchangers erosion, may reduce the efficiency of dust separation/collection equipment and may impede the utilization of fly ash as a replacement for Portland cement or additive to concrete [1]. Under this perspective, power plant managers are interested in strictly controlling the levels of unburned carbon in ash.

The main factors that influence unburned carbon loss may be classified into three categories: coal inherent characteristics, coal milling and drying process and, finally, combustion conditions themselves. The first category includes pulverized coal and char properties such as heating value, char yield on pyrolysis, char internal structure, char reactivity, ash content and composition. The second category accounts for coal preparation and grinding manoeuvres, affecting particle size distribution and moisture remaining in the pulverized coal entering the furnace. Finally, the third category comprises all the operating strategies affecting the boiler performance, as for the selection of the rows of burners in service, air excess, air flow distributions and position of burner vanes. The selection and combination of these factors determine fuel and air mixing, combustion temperatures and residence times, which ultimately condition the combustion process of the coal particle [1].

The combustion behaviour of pulverized coal can be investigated by means of pilot-scale experiments,

* Corresponding author. Tel.: +34 976 762 562; fax: +34 976 732 078.
E-mail address: jpallare@unizar.es (J. Pallarés).
[1] Tel.: +34 976 761 863; fax: +34 976 732 078.
[2] Tel.: +34 976 762 564; fax: +34 976 732 078.

0016-2361/$ - see front matter © 2005 Elsevier Ltd. All rights reserved.
doi:10.1016/j.fuel.2005.05.011

Nomenclature

A_a	pre-exponential factor for oxidation (kg C/m^2 s Pa$^{1/2}$)
C	ultimate analysis carbon content in coal as received (%)
d_c	diameter of carbon-rich core (μm)
d_p	diameter of the coal particle (μm)
D_o	molecular diffusivity of O_2 in N_2 (m/s^2)
E_a	activation energy for oxidation (J/mol)
k_c	chemical reaction rate coefficient (kg/m^2 Pa s)
$k_{c,1750}$	chemical reaction rate coefficient at a particle temperature of 1750 K (kg/m^2 Pa s)
k_d	diffusion rate coefficient (kg/m^2 Pa s)
M	moisture content in coal as received (%)
P_g	oxygen partial pressure at particle surface (Pa)
P	furnace pressure (Pa)
q	burning rate (kg C/m^2 s)
R	gas universal constant (J/mol K)
Sh	Sherwood number for mass transfer to a spherical particle
T_m	average temperature of particle surface and gas free stream (K)
Z	ash content in coal as received (%)
δ	thickness of the ash film (μm)
θ_{af}	ash film porosity

mathematical combustion models and CFD codes. Pilot-scale testing suffers from two basic shortcomings. Firstly, the physical processes involved in utility boilers are not completely scalable and, in consequence, small-scale experiments can be only considered as approximations. On the other hand, an experimental rig involves very high investment and maintenance costs.

An alternative method relies on using a detailed mathematical combustion model. The basis of this approach is to separate the influence of fuel properties and combustion conditions on coal burnout behaviour. The fuel-related empirical parameters in the model have to be fitted from laboratory experiments. These data are then used to predict burnout behaviour under full-scale furnace conditions [2]. Coal combustion models are made up of a devolatilization submodel and a char oxidation submodel. Traditional devolatilization submodels like single reaction model [3] or two competing reactions models [4,5] are being progressively substituted by commercial codes that predict major species yield and local concentrations [6–8]. Single film char oxidation models [9,10] have led to other advanced kinetics models, which account for variations in reactivity during combustion and internal pore structure [8,11–14]. In general, the benefit of using detailed mathematical combustion models is that results can be obtained in a quick and non-expensive way for boilers of very different arrangements and operating conditions.

However, those models cannot completely capture the complexity of the physical and chemical phenomena that occur in an industrial furnace significantly disturbing the fluid flow and the turbulent mixing, resulting in a severe underprediction of the carbon in ash levels. Dealing with these aspects, the use of computational fluid dynamics (CFD) models constitutes a powerful tool to study and characterize some complex processes that take place in the boiler, providing a great amount of precise numerical values for velocity, temperature and concentration fields, irradiation profiles, heat transfer distribution and pollutants formation. In spite of the fact, most of the commercial CFD codes still use single film char oxidation submodels, and none of the advanced combustion kinetics models outlined above have been still fully coupled to a commercial CFD code.

The aim of this paper is to evaluate the capability of prediction of carbon in ash levels by coupling elements of the Hurt's CBK model [11] to a commercial CFD code. Comparisons between conventional single film model and a modified combustion model predictions are discussed in the paper, for a specific case-study unit (Brescia ASM power plant, Italy) under different conditions for coal supply and boiler operation.

2. Experimental data

ASM Brescia power plant generates a total output of 139 MWe and consists of three front-fired units, with natural circulation and single reheat. The case-study unit is 63 MWe gross load, equipped with four burners arranged in two rows of two burners each. A vertical rod mill feeds the two burners of the same row.

Operation data gathering was carried out at the plant during the year 2003, when three coals from different provenance were burned separately (Guasare, Unicoal and Saif coals). For the current work, one representative operating scenario for each coal type has been inferred from plant data to perform the CFD simulations. The three scenarios, summarised in Table 1, correspond to nominal load conditions, when higher carbon in ash levels are typically encountered. Albeit slight differences arise concerning fuel flow rates, mean particles size and excess air, discrepant figures are obtained for unburned carbon in ash levels, as discussed later. Proximate and ultimate analysis and gross calorific values for the involved coals are shown in Table 2, as provided by the plant laboratory. The three coals fall within the category of high volatile bituminous coals, according to the ASTM classification standards.

Table 1
Nominal-load operating scenarios from the case-study power plant

Operating conditions	Guasare	Unicoal	Saif
Load (%)	100	100	100
Primary air flow rate (Nm^3/h)	20,000	20,000	20,000
Temperature of primary air (°C)	80	80	80
Secondary air flow rate (Nm^3/h)	220,000	220,000	220,000
Secondary air temperature (°C)	243	243	243
Milling load (t/h)	25.10	27.06	25.78
Mean particle diameter (μm)	42.63	49.77	47.82
Main steam temperature (°C)	510	510	510
Gas temperature at boiler exit (°C)	310	310	310
Mean O_2 at boiler exit (%)	2.82	3.49	3.53

Table 2
Composition and heating value for the case-study coals

	Guasare	Unicoal	Saif
Proximate analysis (as received)			
Moisture (%)	8.45	11.03	7.69
Ash (%)	6.96	4.32	6.19
Volatile (%)	34.16	36.85	35.30
Fixed carbon (%)	50.43	47.80	50.82
Ultimate analysis (as received)			
Carbon (%)	70.24	66.94	70.53
Hydrogen (%)	4.68	4.77	4.64
Nitrogen (%)	1.32	1.34	1.41
Oxygen (%)	7.68	11.10	8.84
Sulphur (%)	0.66	0.50	0.70
Heating value (as received)			
Gross calorific value (kcal/kg)	7166	6638	6881

3. CFD modelling of the case-study boiler

A commercial CFD application, CFX 4.4 developed by AEA Technology, has been chosen to perform the simulations [15].

3.1. Geometry description

Full boiler geometry has been modelled up to the plenum to make easy the definition of an appropriate boundary condition at the outlet section and allowing the inclusion of the radiant superheater geometry in a further development.

The selected mesh is structured and made up of 130,000 square elements. Its size is refined in the nearby of the burners belt to better characterize the major gradients, and it is progressively increased in size up to the top of the furnace. A detail of the burners grid structure is displayed in Fig. 1, where the square elements in the middle are considered as solid walls, simulating the zone where the ignitors and flame detectors are located; the three internal circular rings simulate the inlet section for coal and primary air, and the other three external circular rings simulate the inlet section for secondary and tertiary air.

3.2. Mathematical models

The numerical resolution of the governing equations implies the modelling of all processes that take place in the furnace: turbulent flow, coal combustion and mass transfer, solid particle transport and radiative and convective heat transfer.

The gas flow is modelled, under the Eulerian assumption, solving the steady-state Reynolds average Navier Stokes equations (RANS) along the computational domain. Since the flow is turbulent, the widely used standard k–ε model of Launder and Spalding [16] is coupled to close the turbulence problem. The flow is assumed to behave similarly to incompressible flow, making the density only dependent on temperature through a reference pressure $\rho = \rho(T,P_{ref})$, a reasonable assumption for problems with Mach number under 0.3.

Coal combustion modelling comprises volatiles yield and homogeneous combustion, and char heterogeneous oxidation. Devolatilization rate is modelled using the single

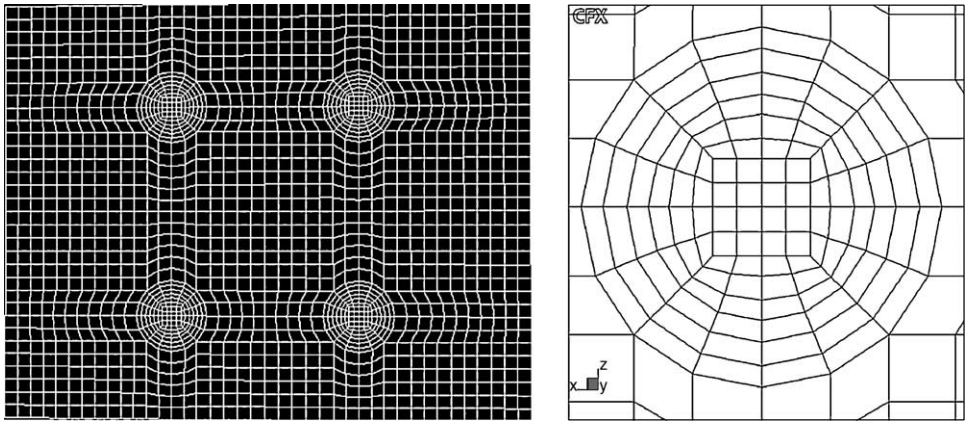

Fig. 1. Detail of mesh structure at the burner belt region.

step model of Badzioch and Hawsksley [3], which states that the rate of production of volatile gases is given by a first-order reaction and the rate constant is expressed in an Arrhenius form. The homogeneous combustion of volatiles released from the particle are modelled using the mixed-is-burnt model, see for instance [17], which assumes infinitely fast chemistry. The instantaneous mass fractions are given in terms of the instantaneous mixture fraction. The mean mass fraction of fuel, oxidant and products are obtained from the mean and variance of the mixture fraction assuming the beta probability density function, β-PDF.

The process of char oxidation is modelled using the popular single film char oxidation model developed by Field et al. [9] coupling both rank-dependent empirical correlations [18] and a specific submodel describing ash inhibition at the late stages of combustion [11]. As a matter of fact, the inclusion in this enlarged combustion model of rank dependant correlations for the global pre-exponential factor, A_a, and for the global activation energy, E_a, establishes a direct dependence between char reactivity and coal properties. These empirical correlations are suitable for the prediction of coal burning under pulverized coal conditions in utility boilers: gas temperatures over 1500 K, particle diameters in the range from 75 to 200 μm and oxygen partial pressures over 0.03 bar [18]. Furthermore, the ash inhibition submodel introduces an additional diffusion resistance to account for the inhibitory effect of ash on char oxidation, introducing two new parameters: the critical ash porosity and the minimum ash film thickness [11]. All the expressions used in the char oxidation model are summarized in Table 3: coal consumption rate q (first row of the table), oxygen diffusion rate k_d (second and third row) and chemical reaction rate k_c (two last rows).

The coal combustion model has to be necessarily combined with a particle transport calculation. A Lagrangian approach has been chosen, considering the influence of a diluted particle phase on the fluid flow, two-way coupling [19]. Interactions between particles have been neglected. The total mass flow of particles has been modelled by tracking a number of 2000 trajectories, assuming that each simulated particle represents a sample of the real number of particles.

Table 3
Summary of models used for coal modelling

Global reaction [9]	$q = \frac{P_g^{0.5}}{\frac{1}{k_d}+\frac{1}{k_c}}$
Diffusion rate constant [11]	$k_d = \frac{Sh D_o d_p \theta_{af}^{2.5}}{RT_m(Sh\delta d_c + \theta_{af}^{2.5} d_c^2)}$
Diffusion coefficient, Jensen and Mitchell (1993) [20]	$D_o = 1543 \times 10^{-4} \frac{T_m^{1.67}}{P}$
Reaction rate constant	$k_c = A_a\, e^{(-E_a/RT_p)}$
Empirical kinetics [18]	$E_a = 4186.9\left(-5.94 + 35.5\frac{C}{1-Z-M}\right)$
	$A_a = \exp\left(\ln(k_{c,1750\ K}) + \frac{E_a}{1750R}\right)$
	$\frac{10}{101325^{1/2}}$
	$\ln(k_{c,1750}) = 2.8 - 7.58\frac{C}{1-Z-M}$

Table 4
Summary of models used for CFD simulation of furnace performance

Phenomenon	Model	Reference
Turbulence	Standard k–ε	Launder and Spalding [16]
Devolatilization	Single-step devolatilization	Badzioch and Hawsksley [3]
Volatiles combustion	Mixed is burnt	Wartnatz et al. [17]
Char oxidation	Conventional single film +	Field et al. [9]
	Rank-dependant correlations +	Hurt and Mitchel [18]
	Ash inhibition (CBK)	Hurt et al. [11]
Radiation	Discrete transfer	Lockwood and Shah [20]
Particles tracking	Lagrangian approach (two-way coupling)	

The thermal radiation in the furnace is the dominant heat transfer mechanism due to the presence of a mixture of participative gases and particles at high temperature. The radiative heat transfer has been modelled using the Discrete Transfer method [21], which solves a transport equation for the radiation intensity along paths between two boundary walls. For simplicity, a grey gas model is considered to evaluate the properties of the gas phase, considering a constant value for the absorption coefficient over the whole wavelength spectrum. The influence of the particles, also participating in the radiative heat transfer, is accounted by including a specific heat source in the energy conservation equation. Summing up, Table 4 shows the combination of models used for performing the CFD simulation of the case-study boiler.

3.3. Validation of furnace modelling

Besides the main validation of the target prediction of this paper (unburned carbon in ash level), which is discussed in Section 4, additional verifications of furnace simulation correctness are highly desirable. Unfortunately, available instrumentation in the case-study boiler does not allow a detailed validation, just limiting it to the prediction of the oxygen content in flue gases. In fact, this is a usual situation in large-scale utility boilers, which are conventionally instrumented for control and safe operation purposes, but not for undertaking accurate thermal calculations. Moreover, the aggressive environment of high temperatures and ash particles in the furnace make unfeasible the insertion of

Table 5
Experimental value against numerical prediction for mean oxygen content in flue gases for the three simulated scenarios

	Guasare	Saif	Unicoal
Mean $\%O_2$ plant value	2.82	3.53	3.49
Mean $\%O_2$ CFD prediction	3.05	3.35	3.25

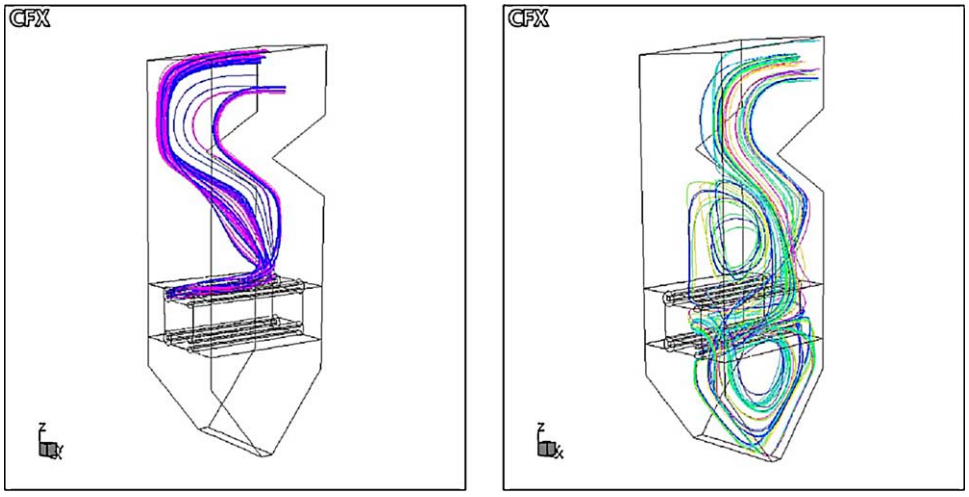

Fig. 2. Predicted particle trajectories tracked from different inlets.

long-term durable measurement probes in most cases, restricting the on-line available information to very few gas temperature and oxygen samples at the cold exit of the boiler convective section [22,23].

Numerical predictions for the mean values of oxygen content in flue gases show good agreement with available plant measurements, for the three tested full-load scenarios, as shown in Table 5. These figures, along with the predictions of unburned carbon hereinafter discussed, permit to conclude that the simulation of coal combustion is reasonable for the variety of coal feedstock tested.

4. Results and discussion

Six simulations have been carried out concerning the unburned carbon prediction, two for each coal type: one using the conventional single film char oxidation model and the other one introducing the modifications to the char oxidation model already explained in Section 3. A complete simulation, including fluid flow, coal combustion, heat transfer and particle tracking, has been performed for each case.

Three large recirculation loops can be typically distinguished in large front-fired furnaces, which largely affect the particles trajectories and modify the coal burnout behaviour. This effect is stronger in the lower burner level (as shown in Fig. 2 for the case-study boiler), where most of the particles are captured by the reversed-flow zone in the bottom hopper region. In addition, interactions between the inlet flows from neighbour burners and interactions with the confining walls are significant enough to noticeably distort the coal particles trajectories.

The near burner region, see flame prediction in Fig. 3, is highly relevant because volatile matter combustion is completed in this zone and the recirculating combustion products provide the heat release needed to ensure flame stability. Downstream of this core zone, char particles and combustion gases follow an intricate path through the furnace to reach the exit. In general, such flow interactions, vortexes and reversed-flows delay oxygen and fuel mixing, resulting in larger combustion times, and therefore, affecting carbon in ash levels.

Once each simulation is completed, particle track files are generated. Therefore, the amount of unburned carbon in ash for every specific condition is calculated in a post-processing task. As it is often reported in the literature, see for instance [24], char burnout is quite difficult to pinpoint as an absolute value, but at least generic trends are usually indicated in a correct way by CFD codes when variations in parameters like excess air and size of entering particles are imposed. However, it is more difficult to accurately predict variations in carbon in ash levels when only fuel properties are varied. This fact is currently becoming of great relevance, since coal blends of different origin are usually burnt together to reduce fuel supply costs.

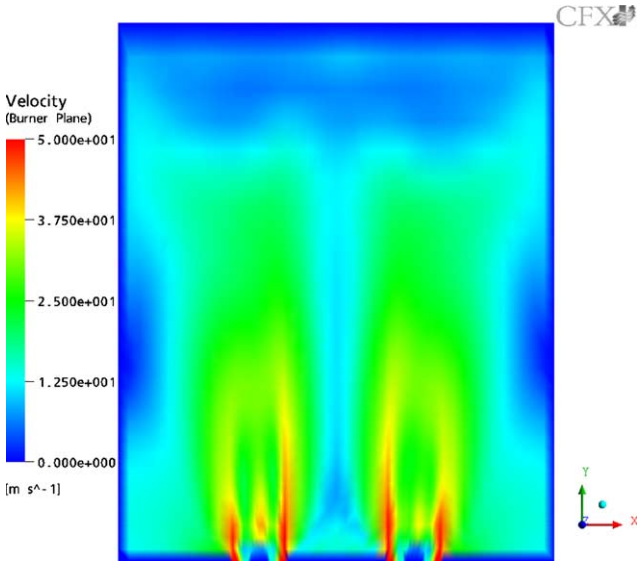

Fig. 3. Velocity flow distribution in the near burner region.

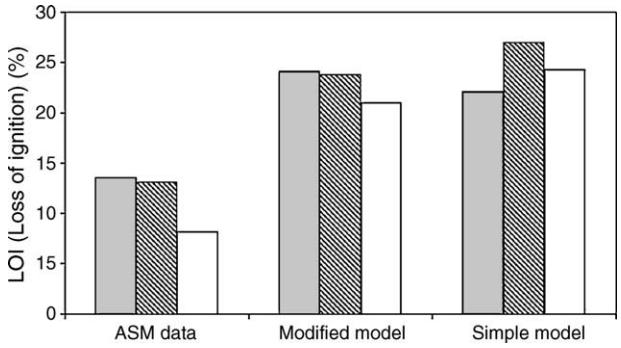

Fig. 4. Results for Loss of Ignition (LOI). ▒ Guasare, ▨ Saif and □ Unicoal.

In Fig. 4, the results obtained for unburned carbon in ash levels are compared against the information provided by the plant laboratory. Independent of the combustion model used for the calculation, results from CFD simulations are higher than the averaged data from the plant. This result can be partially explained considering the ash sampling procedure followed in the plant. Ash samples provided to the Loss of Ignition (LOI) test, which measures the heat released from the ash under standardized conditions for the determination of the unburned material, are compiled from the hopper of the first electrostatic precipitator field because of its easy accessibility. However, before entering the electrostatic precipitators, combustion gases flows through the economizer section and through the air pre-heaters, where about 10–20% of the fly ash deposits in both their respective hoppers and stagnation zones. This percentage depends to a great amount of non-controlled factors, mainly: gas flow pattern, ash size distribution and geometrical arrangement of the circuit (ducts, dampers, elbows, etc.). Considering that larger unburned coal particles, which reasonably correspond in most cases to the higher initial diameter particles, are preferentially deposited in the economizer and air pre-heaters hoppers, its contribution is in fact being ignored to account for the overall unburned carbon loss in the LOI test. To illustrate their relevant influence on the results, Table 6 summarizes the initial percentage of particles classified into three sieves fractions and their final contribution to the total unburned carbon losses as predicted by the CFD model.

If the contribution of those larger particles that presumably do not reach the electrostatic precipitator is discounted from the final predictions, by means of an additional CFD post-processing task, the predicted values for unburned carbon in ash remarkably improve, as shown in Fig. 5. The figure displays a best approach to the plant laboratory values, since a decrease is observed once larger particles contribution is removed. Of course, there are no sound criteria to select a value for the percentage of ashes retained in the hoppers of the gas circuit and tentative values have to be compulsorily considered, moreover, when in situ verification is technically and economically unfeasible.

Table 6
Starting particle distribution mass percentages divided into three sieve fractions and their final contribution to the predicted total unburned carbon losses

		$d_p < 50$ μm	$50 < d_p <$ 125 μm	125 μm $> d_p$
Guasare	%Initial particles	66.34	27.41	6.25
	%Unburned carbon	52.70	28.90	18.40
Saif	%Initial particles	64.90	28.82	6.82
	%Unburned carbon	50.84	30.37	18.79
Unicoal	%Initial particles	63.40	29.90	6.70
	%Unburned carbon	36.34	34.22	29.44

Looking back to Fig. 4, predictions from the modified combustion model follow the same trend for the three different coals and reproduce the same quantitative increment as the observed for the plant values, while results from the conventional single film model clearly differ. The explanation relies on the inclusion of both rank dependant correlations that establish a direct dependence between char reactivity and coal composition and an additional diffusion resistance that accounts for the inhibitory effect of ash on oxygen diffusion through the particle. Fig. 6 shows the comparison of predictions for the averaged oxygen mass fraction and the gas temperature in the nearby of the particle as the combustion proceeds for the three case-study coals. Oxygen mass fraction decreases to a very low value during devolatilization, which usually takes a time between 0.1 and 0.2 s and where peak flame temperature is reached. Afterwards, oxygen fraction rises during one second. Since more than 80% of the conversion takes place in the first two seconds, only the first 2.5 s have been plotted. From the laboratory data in Fig. 4, Unicoal presents the lowest carbon in ash content, while the other coals (Guasare and Saif)

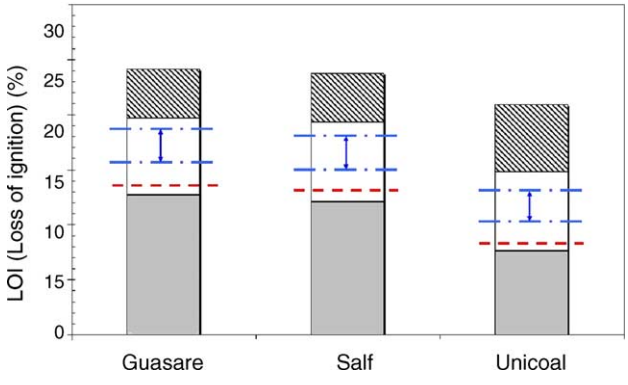

Fig. 5. Carbon in ash distribution depending on the initial particle diameter (d_p) sieve fractions. ▒ $d_p < 50$ μm, □ 50 μm $< d_p <$ 125 μm and ▨ $d_p >$ 125 μm. Dashed line (- - -) represents plant laboratory LOI values and alternating dash and dotted lines (-·-·-) represent LOI values from numerical modelling within the correction range.

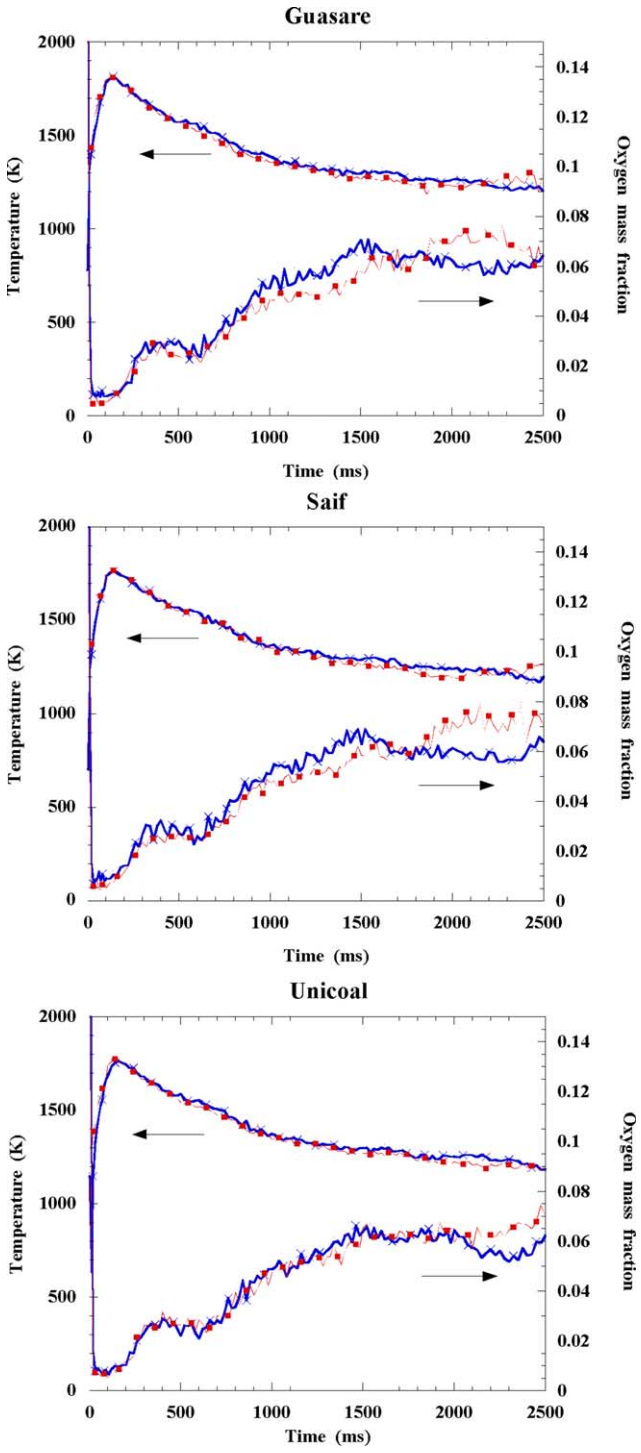

Fig. 6. Oxygen mass fraction and temperature against residence time in the furnace for the three case-study coals using the conventional single film combustion model (■) and the modified combustion model (X).

produce approximately the same level. In consequence, appreciable differences should arise in the oxygen consumption along the path track by the particles. Results from Fig. 6 agree with this assumption, showing a very similar behaviour for the Guasare and the Saif coals, and a very different one for the Unicoal. To better understand how both

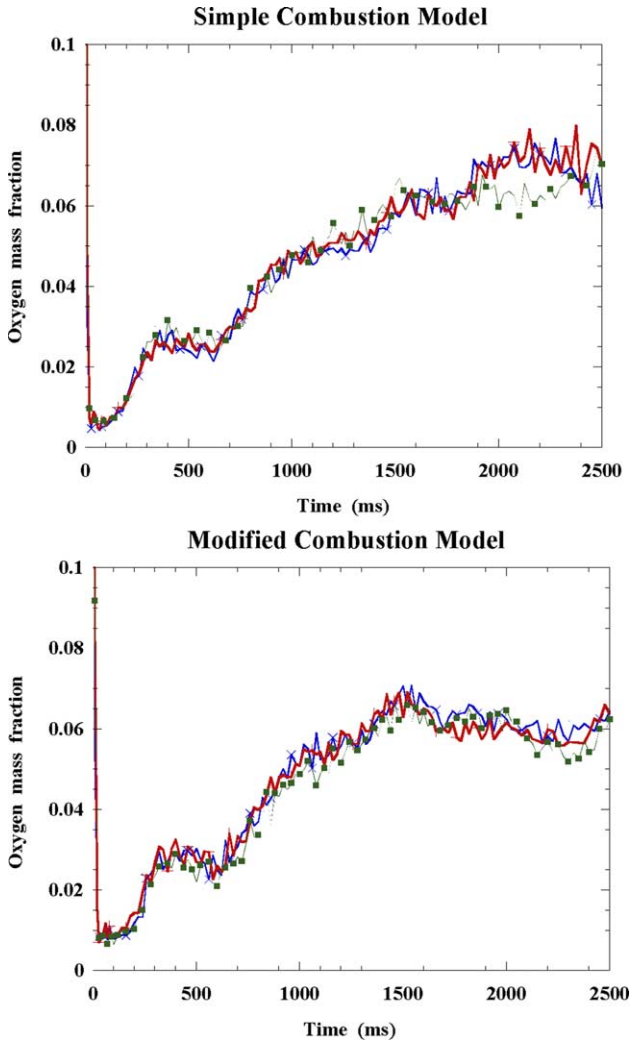

Fig. 7. Detail of oxygen mass fraction against residence time in the furnace using the conventional single film combustion model (a) and the modified combustion model (b) for the three involved coals: Guasare (X), Saif (+) and Unicoal (■).

combustion models behave (conventional against modified one), Fig. 7 plots oxygen concentration profiles for the three coals together. Using the conventional single film combustion model, Fig. 7a, it is not possible to identify which coal behaves in a different way. Maximum and minimum oxygen profiles values alternate from one coal to another at different time positions. However, using the modified combustion model, Fig. 7b, Unicoal shows lower oxygen mass fraction values than the other two coals. Therefore, more oxygen consumption and higher coal conversion have occurred, what agrees with the available experimental data.

5. Conclusions

Commercial CFD codes, mostly using simplified models for coal combustion, clearly fail in the accurate prediction of unburned carbon losses. To better predict the carbon

burnout in a large utility boiler, relatively simple modifications of the combustion models can significantly improve the predictions. To this purpose, both rank-dependent correlations and ash inhibition submodel have been coupled to a commercial CFD combustion model.

CFD simulations have been performed for a case-study utility boiler, for three different nominal load-operating scenarios and coal supplies, either coupling a conventional single film oxidation model or the modified model discussed in the paper. Results from the study show the disagreement between plant laboratory experimental data and conventional model predictions. On the contrary, when the above-mentioned modifications are implemented, trends in unburned carbon values are in good agreement with the collected data. In order to further progress in the development of unburned coal predictive systems, future mid-term works should go in the direction to fully couple advanced kinetics models within CFD codes, maintaining reasonable computing times.

Acknowledgements

The work presented in this paper has been partially supported by the research project 7220-PR-130-CARNO 'Development of a carbon-in-ash notification system' funded by the European Commission under the ECSC research program. The authors gratefully acknowledge ASM Brescia plant personnel for their support and collaboration. Chair-Professor Cristóbal Cortés (University of Zaragoza) is specially acknowledged for many useful comments and suggestions.

References

[1] Walsh PM, Xie J. Effect of coal quality on unburned carbon loss. Third international conference on the effects of coal quality on power plants, San Diego; 1992.
[2] Unsworth JF, Barrat DJ, Roberts PT. Coal quality and combustion performance, an international perspective. Coal Sci Technol 1991;19: 339–408.
[3] Badzioch S, Hawsksley PGW. Kinetics of thermal decomposition of pulverized coal particles. Ind Eng Chem Process Des Develop 1970;9: 521–30.
[4] Ubhayakar SK, Stickler DB, Rosenberg CWV, Gannon RE. Rapid devolatilziation coal in hot combustion gases. Energy Prod Coal 1976;427–36.
[5] Kobayashi H, Howard JB, Sarofim AF. Coal devolatilization at high temperatures. 16th symposium (international) on combustion. Pittsburgh , PA: The Combustion Institute; 1976 p. 411–25.
[6] Backreedy RI, Habib R, Jones JM, Pourkashanian M, Williams A. An extended coal combustion model. Fuel 1999;78:1745–54.
[7] Williams A, Backreedy R, Habib R, Jones JM, Pourkashanian M. Modelling coal combustion: the current position. Fuel 2002;81: 605–18.
[8] Backreedy RI, Jones JM, Pourkashanian M, Williams A. Burn-out of pulverized coal and biomass chars. Fuel 2003;82:2097–105.
[9] Field MA, Gill DW, Morgan BB, Hawksley PGW. Combustion of pulverized coal.: BCURA; 1967.
[10] Baum MM, Street PJ. Predicting the combustion behaviour of coal particles. Combust Sci Technol 1971;3:231–43.
[11] Hurt R, Sun J-K, Lunden M. A kinetic model of carbon burnout in pulverized coal combustion. Combust Flame 1998;113:181–97.
[12] Hurt R, Sun J-K. Mechanism of extinction and near-extinction in pulverized solid fuel combustion. Proc Combust Inst 2000;28: 2205–13.
[13] Hurt R, Calo JM. Semi-global intrinsic kinetics for char combustion modeling. Combust Flame 2001;125:1138–49.
[14] Cloke M, Wu T, Barranco R, Lester E. Char characterization and its application in a coal burnout model. Fuel 2003;82:1989–2000.
[15] AEA Technology plc. CFX 4.4 user manuals; 1998.
[16] Launder BE, Spalding DB. The numerical computation of turbulent flows. Comput Meth Appl Mech Eng 1974;3:269–89.
[17] Warnatz J, Mass U, Dibble RW. Combustion. Berlin: Springer; 1996.
[18] Hurt RH, Mitchel RE. Unified high-temperature char combustion kinetics for a suite of coals of various rank. 24th symposium (international) on Combustion. Pittsburgh, PA: The Combustion Institute; 1992 p. 1243–50.
[19] Sommerfeld M. Theoretical and experimental modelling of particulate flow. Lectures series.: von Karman Institute for Fluid Dynamics; 2000.
[20] Jensen PT, Mitchell RE. High temperature char reactivity measurements in the sandia laminar Flow Reactor. Energy Research Project No. 1323/87-16, Ministry of the Environment, Geological Survey of Denmark; 1993.
[21] Lockwood FC, Shah NG. A new radiation solution method for incorporation in general combustion procedure. 18th symposium on combution. Pittsburgh, PA: The Combustion Institute; 1981 p. 1405–14.
[22] Chojnowski B, Soloukhin RI, Afgan NH. Research and operational measurements on modern power station boilers: a selective survey. 15th ICHMT symposium on heat and mass transfer measurement techniques; 1985. p. 465–89.
[23] Díez LI, Cortés C, Arauzo I, Valero A. Combustion and heat transfer monitoring in large utility boilers. Int J Therm Sci 2001;40: 489–96.
[24] Stopford PJ. Recent applications of CFD modeling in the power generation and combustion industries. Appl Math Modell 2002;26: 351–74.

P.2

“Integration of CFD codes and advanced combustion models for quantitative burnout determination”

Fuel 86 (2007) 2283-2290

J. Pallarés, I. Arauzo, A. Williams

Available online at www.sciencedirect.com
ScienceDirect
Fuel 86 (2007) 2283–2290
FUEL
www.fuelfirst.com

Integration of CFD codes and advanced combustion models for quantitative burnout determination

Javier Pallarés [a,*], Inmaculada Arauzo [a,1], Alan Williams [b,2]

[a] Centre of Research for Energy Resources and Consumptions (CIRCE), University of Zaragoza, María de Luna, 3. 50 018 Zaragoza, Spain
[b] Energy and Resources Research Institute, Leeds University, Houldsworth Building, Leeds LS2 9JT, UK

Received 20 November 2006; received in revised form 22 January 2007; accepted 25 January 2007
Available online 2 March 2007

Abstract

CFD codes and advanced kinetics combustion models are extensively used to predict coal burnout in large utility boilers. Modelling approaches based on CFD codes can accurately solve the fluid dynamics equations involved in the problem but this is usually achieved by including simple combustion models. On the other hand, advanced kinetics combustion models can give a detailed description of the coal combustion behaviour by using a simplified description of the flow field, this usually being obtained from a zone-method approach. Both approximations describe correctly general trends on coal burnout, but fail to predict quantitative values.

In this paper a new methodology which takes advantage of both approximations is described. In the first instance CFD solutions were obtained of the combustion conditions in the furnace in the Lamarmora power plant (ASM Brescia, Italy) for a number of different conditions and for three coals. Then, these furnace conditions were used as inputs for a more detailed chemical combustion model to predict coal burnout. In this, devolatilization was modelled using a commercial macromolecular network pyrolysis model (FG-DVC). For char oxidation an intrinsic reactivity approach including thermal annealing, ash inhibition and maceral effects, was used. Results from the simulations were compared against plant experimental values, showing a reasonable agreement in trends and quantitative values.

Keywords: CFD; Coal combustion; Modelling

1. Introduction

Power companies and power equipment makers' projections suggest a significant switch from gas to coal as the preferred fuel in the coming decade. This re-emergence of coal as a primary fuel for power generation is the result of technological changes that have reduced the amount of pollutants and particulate emissions to the atmosphere, and recent international worries about security of gas supply.

The introduction of emissions control techniques and the increasing competition in the electric generation sector have raised two main issues which require special attention. Firstly, the use of low NO_x burners and furnaces can increase unburned carbon levels thus reducing the thermal efficiency of the plant, increasing heat exchangers erosion, reducing the performance of electrostatic precipitators and the wholesale value of the fly ash [1,2]. Secondly, whilst traditionally utility boilers were designed for a particular single coal, blending of coals is today a common practice to reduce fuel cost, or to overcome a problem with a particular coal. Blending properties for ignition and burnout are not additive properties that can be derived from the components, so this complicates coal burnout predictions [3]. The requirement that power plant managers must meet both the environmental regulations and specifications for an economically profitable coal supply, have resulted in a new interest in predictive techniques.

In the last two decades, the use of computational fluid dynamics (CFD) codes, both as a predictive and design

* Corresponding author. Tel.: +34 976762562; fax: +34 976732078.
E-mail address: jpallare@unizar.es (J. Pallarés).
[1] Tel.: +34 976761863; fax: +34 976732078.
[2] Tel.: +44 113 3432507; fax: +44 113 2467310.

0016-2361/$ - see front matter © 2007 Elsevier Ltd. All rights reserved.
doi:10.1016/j.fuel.2007.01.036

Nomenclature

A_i	mass-specific intrinsic reactivity, 1/s $(mol/m^3)^n$	q_{cmb}	char burning rate (g/cm^2s)
A_o	initial mass-specific intrinsic reactivity, 1/s $(mol/m^3)^n$	R	gas universal constant, 8.3145 J/mol K
		R_i	intrinsic reactivity of the char $(1/s\ atm)^n$
C_{daf}	dry ash free carbon content in coal (%)	T_p	temperature of particle surface (K)
C_p	specific heat of the char particle (J/g K)	T_g	temperature of the bulk gas (K)
d_c	diameter of carbon-rich core (cm)	T_w	temperature of the environment (K)
d_p	diameter of the char particle (cm)	Vit	vitrinite content in coal (%)
D_M	molecular diffusivity of O_2 in N_2 (cm^2/s)	X	overall burnout
D_{eff}	effective molecular diffusivity (cm^2/s)	Δh_f	combustion enthalpy of carbon (J/g)
E	activation energy for oxidation (J/mol)	α	mode of burning parameter
f	fraction of the total porosity in feeder pores	θ	overall particle porosity
f_{mac}	abbreviated maceral correction factor	ρ_p	density of the char particle (g/cm^3)
In	inertinite content in coal (%)	ρ_c	density of the carbon $(g\ C/cm^3)$
m_c	mass of carbon in the char particle (g C)	τ	tortuosity
m_p	mass of the char particle (g)	Φ	Thiele modulus for spheres
n	reaction order	ψ_1	convective heat transfer coefficient $(W/cm^2\ K)$
P_s	oxygen partial pressure at particle surface (atm)	ψ_2	radiative heat transfer coefficient $(W/cm^2\ K^4)$
P	furnace pressure (Pa)	η	effectiveness factor

technique for the improvement of energy systems efficiency, has complemented other experimental techniques based on expensive pilot scale tests. In spite of the relative precision that a CFD code can give to describe the complex fluid dynamics that take place in the boiler of a power plant, it becomes of doubtful accuracy when detailed coal combustion performance is investigated, particularly carbon burnout because of the complexity of the process. The reason is that commercial CFD codes still use simple devolatilization and char oxidation sub-models. Although previous work has shown that introducing simple modifications on the combustion model can significantly improve CFD burnout predictions [4], they still fail to predict precise quantitative values of burnout [4,5] because these changes do not accurately account for variations in reactivity and internal pore structure during the combustion process.

In order to obtain more accurate predictions on coal burnout a different approach was developed which combines CFD tools to account for detailed fluid dynamics, and a more detailed combustion kinetic model to account for carbon burnout. CFD calculations for a 63 MWe front wall fired unit under different conditions for coal supply and boiler operation were solved to obtain oxygen partial pressure and temperature profiles for a number of representative particles. Then these profiles were used as input for the detailed combustion model to obtain carbon burnout. Devolatilization was modelled using a macromolecular network pyrolysis model (FG-DVC) [6], whilst for char oxidation an intrinsic formulae based on the carbon burnout kinetic model (CBK8) that allows the transition to Zone I was used [7]. It also includes a correction factor to account for the effect of coal maceral content on char properties and reactivity [8,10,11]. Predictions from the burnout model were compared against plant data.

2. Computer model methodology

It was important to develop a methodology that combines a detailed treatment of the fluid dynamics, furnace environment and the kinetics of combustion. Devolatilization of the coal and char combustion are both influenced not only by the properties of the parent coal, but also by the temperature–time history which the coal particle experiences during combustion. The CFD solution contains such information for hundreds of particles with different sizes. Every single particle trajectory across the flow domain is unique and depends on the coal milling operation and boiler conditions, such as particle size, inlet position, excess air, primary to secondary air mass flow ratio, burner tilt, swirl number, burner to burner interactions, uneven mass flow distributions in the boiler, air in-leakages and particle–wall interactions. Therefore the first step lies in solving the CFD code to obtain the overall furnace conditions. At the same time, a first approximation of the carbon burnout solution was obtained. Then the variations in gas temperature and oxygen partial pressure for every particle tracked in the CFD simulation were introduced in the detailed combustion model together with the size distribution and the fuel-related properties obtained experimentally in the plant laboratory. This combustion model includes a network pyrolysis sub-model for devolatilization and an intrinsic sub-model for char oxidation.

2.1. CFD sub-model

A commercial CFD program, CFX 4.4, was used to perform the calculations [12]. Furnace simulations were undertaken on a mesh of approximately 150,000 cells shown in Fig. 1 and 2000 representative coal particles were

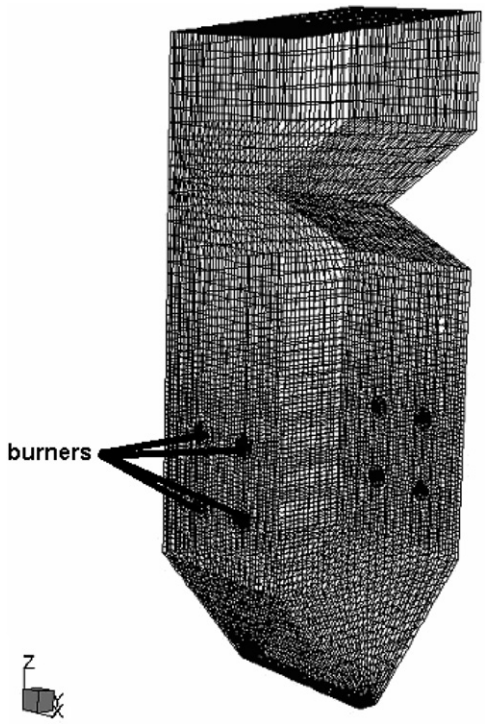

Fig. 1. Boiler computer grid structure.

simulated. Gas flow was modelled solving the steady-state Reynolds averaged Navier–Stokes equations (RANS) along the computational domain, using the standard $k-\varepsilon$ model [13] to close the turbulence problem. Coal devolatilization was modelled using the simple single step model of Badzioch and Hawsksley [14]. A mixed-is-burnt model assuming infinite fast chemistry and a beta probability density function, β-PDF was used for the combustion of volatiles. Char oxidation was modelled using the Baum and Street approximation [15] coupled with both rank-dependent empirical correlations [16] and a specific sub-model describing ash inhibition at the late stages of combustion [17]. Radiative heat transfer was modelled using the Discrete Transfer method [18] assuming a grey gas model to evaluate the properties of the gas phase.

In order to validate the CFD model, predictions on the oxygen content in flue gases were compared with available plant measurements for the scenarios tested, showing good agreement as shown in Table 1. This table, along with the predictions of burnout hereinafter discussed, permit to conclude that the simulation of coal combustion was reasonable for the variety of coal feedstock tested.

2.2. Devolatilization sub-model

It is well know that the devolatilization rate and yield increases with temperature and heating rate, and ultimately determines the porous structure and the number of active sites of the char residue, thus its reactivity. Porosity is particularly important because it controls the rates of diffusion of chemical species into and out of the char particle during combustion when that takes place under internal diffusion controlled conditions [19]. Furthermore, under pulverized fuel conditions the peak temperature to which the coal is heated reaches 1500–2200 K and the volatiles yield is significantly higher than the volatile matter content determined by the standard ASTM test. This causes a decrease of the char produced whose oxidation provides the rate controlling step in coal combustion burn-out [20]. As a result, the devolatilization step is crucial in the overall burnout determination.

Mathematical modelling of coal devolatilization is difficult due to its complexity. Simple models, single rate or two competing rates are used when the level of detail required is not very stringent. Nevertheless to predict variations in yield with reaction conditions (temperature, heating rate, pressure, particle size and coal type) more detailed models which predict the evolution of tar, gas and char, major species yield and local concentrations must be used. There are a number of such commercial computer codes, FG-DVC, FLASHCHAIN and CPD that predict the rate of the volatile release and the composition of key species linked to the resulting macroporous and microporous structure of the char [6]. Because of its applicability to a wide range of coals (subbituminous, bituminous and lignites) and heating rates ($0.05–10^5$ K/s), and its ability to predict the variations in species yield with reactor conditions [6], FG-DVC was used in this work.

2.3. Char oxidation sub-model

The overall burning rate of a char particle is determined by the oxygen transport to the particle surface and the reactivity of the char, which depend on the temperature and composition of the gaseous environment and the size, porosity and temperature of the particle (see Eq. (1)) [21]

$$q_{\mathrm{cmb}} = f(T_{\mathrm{p}}, P_{\mathrm{s}}, \eta, R_{\mathrm{i}}, n, d_{\mathrm{p}}, \rho_{\mathrm{p}}, \theta) \tag{1}$$

The intrinsic reactivity of the char, R_{i}, was expressed in the form:

$$R_{\mathrm{i}} = A_{\mathrm{i}} \cdot \exp(-E/R \cdot T_{\mathrm{p}}) \tag{2}$$

Table 1
Experimental values compared with numerical predictions for mean oxygen content (vol.%) in flue gases for the nine simulated scenarios

	Case 1	Case 2	Case 3	Case 4	Case 5	Case 6	Case 7	Case 8	Case 9
Mean % O_2 plant value	2.63	3.57	3.1	3.63	3.21	3.37	3.31	3.02	2.89
Mean % O_2 CFD prediction	3.18	3.91	3.52	3.81	3.48	3.45	3.31	3.06	2.97

There is a wide spread of activation energy values E in the literature [7,9,11,21,22]. A value for E of 167 ± 5 kJ/mol was used based on the validation of the model for the type of coals used in this work (172 kJ/mol for Guasare, 167 kJ/mol for Carboandes, and 162 kJ/mol for Russian). However, Arrhenius expressions with constant kinetic parameters cannot account for the changing reactivity occurring during burnout. A deactivation function, proposed by Lans et al. [23], was introduced in the model in order to express reactivity loss by thermal annealing as a function of char conversion (see Eq. (3))

$$A_i = A_0 \cdot (1 - X)^{0.5} \tag{3}$$

where X represents the overall burnout of the char particle and A_0 the initial mass-specific intrinsic reactivity based on the dry, ash-free carbon content of the parent coal, correlated for a wide range of coals by Hurt et al. [17] (see Eq. (4))

$$\log(A_0) = 14.97 - 0.0764 \cdot (\%C_{daf}) \tag{4}$$

The effectiveness factor, η, was obtained from the integration of the mass balance of the reactive for a porous spherical particle under catalytic reaction, assuming a first order reaction (see Eq. (5)) [7]

$$\eta = \frac{1}{\Phi}\left(\coth(3 \cdot \Phi) - \frac{1}{3 \cdot \Phi}\right) \tag{5}$$

where Φ is the Thiele modulus that combines the reaction and diffusion phenomena as is shown in Eq. (6) [7]

$$\Phi = \frac{d_c}{6}\left(\frac{(n+1) \cdot \rho_p \cdot R_i \cdot \left(P_s/R \cdot T_p\right)^{n-1}}{2 \cdot D_{eff}}\right)^{0.5} \tag{6}$$

To account for the porous nature of the char and the fact that the oxygen penetrates the porous structure and reacts on the internal surface area, the effective diffusivity to the interior of the particle was modelled according to Eq. (7) [7]

$$D_{eff} = D_M \cdot \left(\frac{\theta \cdot f}{\tau}\right) \tag{7}$$

where θ is the total porosity of the particle, τ/f is a carbon pore structure parameter which was set to 6 [7], and D_M is the bulk diffusion coefficient given by Eq. (8) [24]

$$D_M = 1.543 \cdot \left(T_p\right)^{1.67}/P \tag{8}$$

The transition from Zone II to Zone I reaction mode is the result of the extinction phenomena in the late stages of combustion. To explain this behaviour, different mechanism, including reactivity loss by thermal annealing and ash inhibition effects, have been considered [7]. The former was already introduced in the model through Eq. (3). The latter was accounted for the inclusion of an additional diffusion resistance in the mass transfer coefficient used for the determination of the oxygen partial pressure at the outer core of the char particle. This diffusion resistance was expressed in terms of the ash film porosity, ash film thickness and particle core diameter. These variables are computed from the char particle size and density evolution of the particle during combustion, which were modelled relating the char particle density decrease to the carbon conversion and considering a burning mode α of 0.2 (see Eq. (9)). Swelling of the particle during devolatilization is accounted by including a swelling factor that modifies the initial diameter and then the density of the char particle. This swelling factor was estimated to be 1.10 for the three coals. Then, the char particle diameter is obtained by geometric considerations [17].

$$\rho_c = \rho_{c,0} \cdot \left(\frac{m_c}{m_{c,0}}\right)^{\alpha} \tag{9}$$

Other important parameter governing char reactivity is the presence of various coal maceral types. This fact acquires a greater relevance in coal blends combustion. Typically northern hemisphere coals are rich in vitrinite, whilst coals formed in the southern hemisphere have a high inertinite content [8]. To account for this behaviour, an abbreviated maceral correction factor, f_{mac}, was introduced when coals of the southern hemisphere are considered (see Eq. (10)) [11]

$$f_{mac} = 1.68 \cdot \mathrm{Vit} - 0.6 \cdot In \tag{10}$$

Introducing the above considerations into Eq. (1), the overall burning rate of a char particle was expressed as shown in the following equation:

$$q_{cmb} = m_c \cdot \eta \cdot f_{mac} \cdot R_i \cdot (P_s)^n \tag{11}$$

Although in the scientific community there is no general agreement on the magnitude of the reaction order with respect to O_2, Hurt et al. showed that global power-law kinetics are capable of correctly describe combustion rates as a consequence of the heterogeneity of real carbon surfaces [25,26]. A value of 0.5 was used in this work.

From an energy balance in the particle, the program calculates, in every time-step iteration, the particle temperature T_p and the burning rate q_{cmb} by estimating the particle temperature and comparing the combustion rates in an iterative process until the error is driven to zero (Error $T_p < 0.1$ K). The oxygen partial pressure in the outer surface is determined in an internal iteration with the guessed particle temperature value (Error $P_s < 0.001$ atm)

$$m_p \cdot C_p \cdot \frac{dT_p}{dt} = (q_{cmb} \cdot \Delta h_f) - \psi_1 \cdot (T_p - T_g) - \psi_2 \cdot (T_p^4 - T_w^4) \tag{12}$$

where Δh_f is the combustion enthalpy of the oxidation reaction to CO/CO_2 [17], and ψ_1 and ψ_2 are the convective and radiation heat transfer coefficients, respectively.

3. Results and discussion

To investigate the burnout prediction capability of the model a total of nine scenarios, presented in Table 2 were

Table 2
Nominal-load operating scenarios from the case-study power plant

	Case 1	Case 2	Case 3	Case 4	Case 5	Case 6	Case 7	Case 8	Case 9
Coal	Guasare	Guasare	Guasare	Carboandes	Carboandes	Carboandes	Russian	Russian	Russian
Mill 1 load (t/h)	12.4	12.53	10.43	13.28	13.06	12.93	13.4	13.44	13.41
Mill 2 load (t/h)	12.44	12.6	10.46	13.3	13.01	13.04	13.27	13.42	13.48
Total air flow rate (kNm^3/h)	208.03	218.45	181.41	218.29	215.11	209.39	219.11	218.68	216.73
Primary air flow rate Mill 1 (kNm^3/h)	25.28	25.39	23.60	26.03	25.85	25.73	26.14	26.17	26.14
Primary air flow rate Mill 2 (kNm^3/h)	25.32	25.45	23.63	26.05	25.80	25.83	26.02	26.15	26.21
Primary air T^a (°C)	80	80	80	80	80	80	80	80	80
Secondary air flow rate (kNm^3/h)	157.43	167.61	134.19	166.21	163.46	157.83	166.95	166.36	164.38
Secondary air T^a (°C)	249.9	257	254.39	256.48	254.99	257.29	254.21	254.9	254.18
Mean particle diameter (μm)[a]	55	55	55	55	55	55	55	55	55

[a] Rossin Rammler distribution ($d_{pm} = 55$ μm, $n_{rr} = 1.02$).

tested with standard plant instrumentation measurements gathered at the Lamarmora (ASM Brescia) power station in the year 2005. Study cases were selected covering the regular range of variation of mean oxygen (vol.%) in flue gases (2.5–4%) under full load operating conditions. Differences among scenarios are the result of the normal operation of the plant where small variations in conditions and mass flow imbalances between mills are encountered. The mills classifiers were adjusted to give a particle size distribution of mean diameter of 55 μm. The unit studied was a 63 MWe front wall-fired boiler with four burners arranged in two rows, natural circulation, single reheat and two vertical rod mills feeding each row of burners. In the study, two coals from Central America commonly used in the plant over the last 5 years (Guasare from Venezuela and Carboandes from Colombia) and a coal from Russia, recently used to evaluate its influence on the combustion efficiency, were burned separately. Since no petrographic analysis were available, inertinite and vitrinite values for Guasare coal were taken from Barranco et al. [27]. Table 3 gives the standard ASTM proximate and ultimate analysis, and maceral analysis when available.

Table 3
Proximate, ultimate and petrographic analysis for the coals used in the study

Proximate analysis (as received)	Guasare	Carboandes	Russian
Moisture (%)	6.91	9.60	9.56
Ash (%)	5.75	6.44	7.14
Volatile (%)	35.00	34.17	36.09
Fixed Carbon (%)[a]	52.34	49.79	47.21
Ultimate analysis (as received)			
Carbon (%)	72.75	69.21	65.62
Hydrogen (%)	4.93	4.38	4.66
Oxygen (%)[a]	7.75	8.38	10.74
Nitrogen (%)	1.27	1.36	1.90
Sulphur (%)	0.64	0.64	0.38
Petrographic analysis			
Inertinite (%)	0.24	N/A	N/A
Vitrinite (%)	0.76	N/A	N/A

[a] Calculated by difference.

The CFD model was applied to the nine cases. Solutions in the form of the gas temperature and the oxygen partial pressure profiles that every representative coal particle is subject to was obtained, and subsequently used as an input in the coal combustion kinetic model. Fig. 2 shows an example of the variation in these temperature and oxygen partial pressure profiles among particles as a result of the complex fluid dynamics involved in the problem. This approach permits the model to be sensitive to the changes that arise from slight operational condition changes and uneven flow variations which strongly affects the overall burnout prediction. This fact represents an advantage over other zonal-based predictive models which commonly consider a reduced number of zones and particle trajectories.

Then, to determine char and volatile yields, FG-DVC calculations were performed under conditions relevant to pulverised coal combustion, namely a heating rate of 10^5 K/s and final temperature of 1750 K for 150 ms which have been considered to be appropriate conditions [9,11]. Results presented in Table 4 and Fig. 3 shows a different behaviour of the Russian coal, which gives the lowest volatile rate and yield at high temperature. This behaviour can be explained in terms of the cross-linking and bridge breaking balance competition on the depolymerization of the macromolecular network. In general for lower rank coals crosslinking rates occurs in advanced of the bridge breaking, increasing the coordination number of the macromolecular network and thus reducing the yield [28].

Finally, the char burnout sub-model was run for each scenario, using as inputs the particle size distribution (Table 2) and coal properties (Table 3), the char and volatiles yield from the FG-DVC calculations (Table 4), the oxygen partial pressure and temperature profiles from the CFD simulation (Fig. 2) and the model parameters as described in Section 2.2. To ensure the convergence of the particle heat balance (Eq. (12)), a grid refinement in the CFD model was carried out in the near burner area to obtain data of key variables approximately every 5 ms. Additionally, in case the temperature change was greater than 100 K, the char combustion routine subdivides the calculations into smaller time intervals by linear interpolation of the bulk variables.

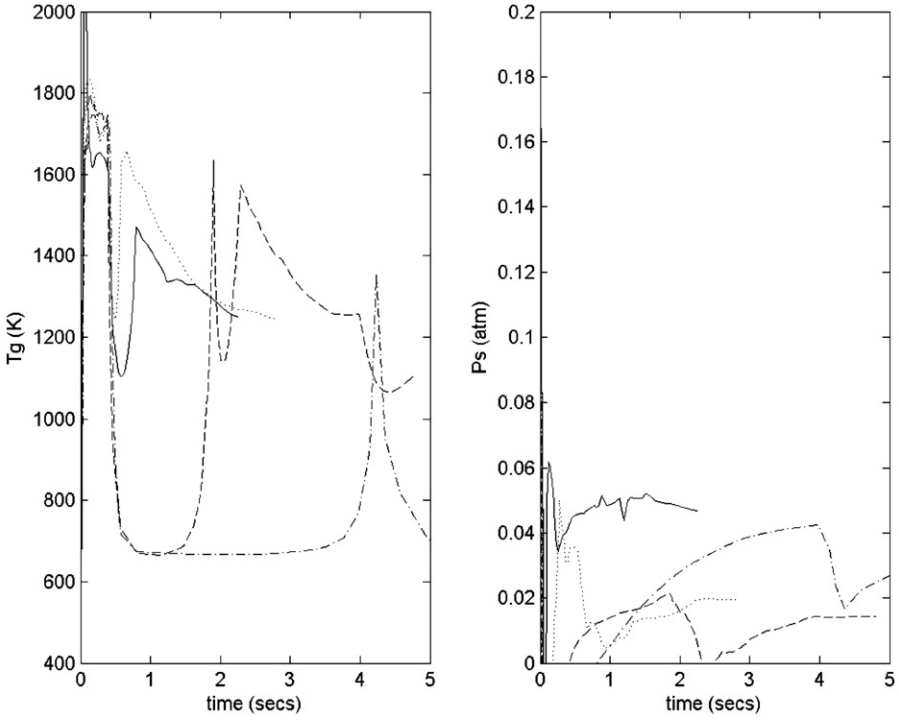

Fig. 2. Oxygen partial pressure and temperature profiles computed by CFD for a number of representative particles of the same diameter (103 μm) fed at different locations in the same upper burner (Case 1 conditions).

Table 4
Predicted char, tar, gas and (paraffins + olefins) yields (% by FG-DVC for the y coals studied (10^5 K/s to 1750 K for 150 ms)

	Guasare	Carboandes	Russian
Char (%)	49.0	45.7	51.9
Tar (%)	34.8	38.0	26.4
Gas (%)	13.4	13.4	18.1
Paraffins + Olefins	2.8	2.9	3.7

Results on overall burnout for the model are compared against the initial CFD predictions and plant data measurement in Fig. 4. CFD predictions clearly under-predict the overall burnout as a result of using a simple combustion model that does not account for reactivity loss [4]. On the contrary, the results from the model show that general trends and quantitative values on burnout are accurately predicted. Small discrepancies can be found for Carboandes coal, in cases 5 and 6, where the model slightly differs from the overall burnout value obtained in the plant. This result can be partially explained by the fact that no petrographic information were available for this coal, and thus no maceral correction was applied in the model, besides the intrinsic uncertainty on the election of the kinetic model parameters, since no DTF studies were carried on. On the contrary, deliberately changes in the operation conditions of the plant or mass flow imbalance situations between burners (see Table 1) that noticeably distort the particles' trajectories and thus their combustion behaviours, are sufficiently resolved for all the coals.

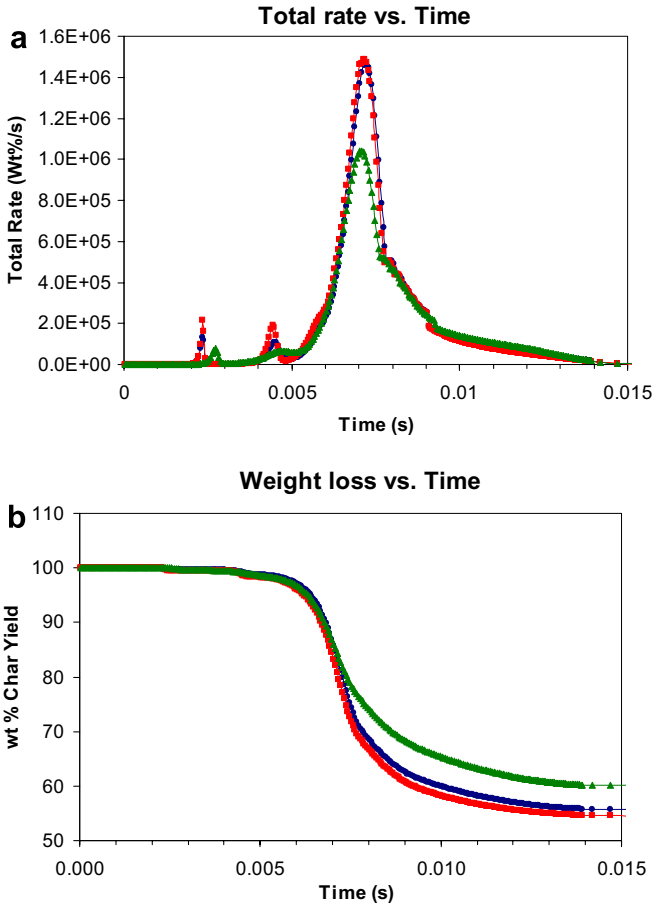

Fig. 3. Devolatilization at 10^5 K/s to 1750 K for 150 ms, (a) total rate against. time (b) weight against time, for: ● Guasare, ■ Carboandes and ▲ Russian coals.

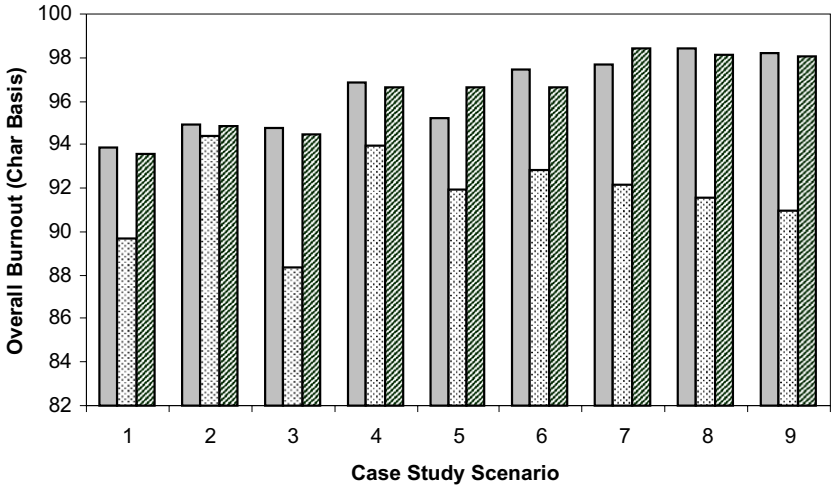

Fig. 4. Results for burnout (Char basis): ▒ ASM ▒ CFD predictions ▒ Model predictions.

4. Conclusions

A methodology that combines CFD codes and a detailed kinetics combustion models for the burnout determination in a large utility boiler has been developed. Nine scenarios of the ASM Brescia power plant under real operation conditions were used to test the model capability for burnout prediction. Results from the study show a good agreement in trends and quantitative values, showing a notable sensibility of the model to arise slight operational variations. Results also confirm to be acceptable the methodology, formulation and assumptions proposed in this paper. Nevertheless, whenever is possible it would be desirable to obtain an accurate description of the coal kinetic properties by means of analytical techniques such as TGA and DTF. Future development of this combustion efficiency predictive tool will be directed to reduce the response time which is limited by the CFD code calculations, but maintaining the model accuracy.

Acknowledgements

The work presented in this paper has been partially supported by the research project 7220-PR-130-CARNO 'Development of a carbon-in-ash notification system' funded by the European Commission under the ECSC research program. The authors gratefully acknowledge Lamarmora (ASM Brescia) plant personnel for their support and collaboration. We special acknowledge and thank helpful discussions held with Dr. Raymond I. Backeedy, Dr. Peter Stephenson and Dr. J.M. Jones for the coal combustion model development.

References

[1] Walsh PM, Xie J. Effect of coal quality on unburned carbon loss. In: Proceedings of third international, a conference on the effects of coal quality on power plants; San Diego; 1992.

[2] Hurt RH, Davis KA, Yang NYC, Headley TJ, Mitchell GD. Residual carbon from pulverized-coal-fired boilers: 2. Morphology and physicochemical properties. Fuel 1995;74:1297–306.

[3] Arenillas A, Backreedy RI, Jones JM, Pis JJ, Pourkashanian M, Rubiera F, et al. Modelling of NO formation in the combustion of coal blends. Fuel 2002;81:627–36.

[4] Pallarés J, Arauzo I, Díez LI. Numerical prediction of unburned carbon levels in large pulverized coal utility boilers. Fuel 2005;84:2364–71.

[5] Stopford PJ. Recent applications of CFD modeling in the power generation and combustion industries. Appl Math Model 2002;26:351–74.

[6] Solomon PR, Hamblen DG, Carangelo DG, Carangelo RM, Serio MA, Deshpande GV. General model of coal devolatilization. Energy Fuels 1988;2:405–22.

[7] Hurt R, Sun J-K. Mechanism of extinction and near-extinction in pulverized solid fuel combustion. Proc Combust Inst 2000;28:2205–13.

[8] Hampartsoumian E, Pourkashanian M, Williams A. Combustion rates of chars and carbonaceous residues. J Inst Energy 1989:48–56.

[9] Backreedy RI, Habib R, Jones JM, Pourkashanian M, Williams A. An extended coal combustion model. Fuel 1999;78:1745–54.

[10] Williams A, Backreedy RI, Habib R, Jones JM, Pourkashanian M. Modelling coal combustion: the current position. Fuel 2002;81:605–18.

[11] Backreedy RI, Fletcher LM, Ma L, Pourkashanian M, Williams A. Modelling pulverised coal combustion using a detailed coal combustion model. Sci Tech 2006;178:763–87.

[12] AEA Technology plc., CFX 4.4 User manuals; 1998.

[13] Launder BE, Spalding DB. The numerical computation of turbulent flows. Comput Methods Appl Mech Eng 1974;3:269–89.

[14] Badzioch S, Hawsksley PGW. Kinetics of thermal decomposition of pulverized coal particles. Ind Eng Chem Process Des Dev 1970;9:521–30.

[15] Baum MM, Street PJ. Predicting the combustion behaviour of coal particles. Combust Sci Technol 1971;3:231–43.

[16] Hurt RH, Mitchell RE. Unified high-temperature char combustion kinetics for a suite of coals of various rank. In: Prooceedings of 24th symposium (international) on combustion. The Combustion Institute; 1992. p. 1243–50.

[17] Hurt R, Sun J-K, Lunden M. A kinetic model of carbon burnout in pulverized coal combustion. Combust Flame 1998;113:181–97.

[18] Lockwood FC, Shah NG. A new radiation solution method for incorporation in general combustion procedure. In: Prooceedings of

18th symposium on combustion. The Combustión Institute; 1981. p. 1405–14.
[19] Chan ML, Jones JM, Pourkashanian M, Williams A. The oxidative reactivity of coal chars in relation to their structure. Fuel 1999;78:1539–52.
[20] Kobayashi H, Howard JB, Sarofim AF. Coal devolatilization at high temperatures. In: Prooceedings of 16th symposium (international) on combustion. The Combustion Institute; 1976. p. 411–25.
[21] Smith IW. The combustion rates of coal chars: a review. In: Prooceedings of 19th symposium (international) on combustion. The Combustion Institute; 1982. p. 1045–65.
[22] Charpenay S, Serio MA, Solomon PR. The prediction of coal char reactivity under combustion conditions. In: Prooceedings of 24th symposium (international) on combustion. The Combustion Institute; 1992. p. 1189–97.
[23] Lans RP, Glarborg P, Dam-Johansen K, Knudsen P, Hesselmann G, Hepburn P. Influence of coal quality on combustion performance. Fuel 1998;77:1317–28.
[24] Jensen PT, Mitchell RE. High temperature char reactivity measurements in the Sandia laminar flow reactor. Energy Research Project No. 1323/87-16, Ministry of the Environment, Geological Survey of Denmark; 1993.
[25] Hurt RH, Haynes BS. On the origin of power-law kinetics in carbon oxidation. Proc Combust Inst 2004;30:2161–8.
[26] Hurt R, Calo JM. Semi-global intrinsic kinetics for char combustion modelling. Combust Flame 2001;125:1138–49.
[27] Barranco R, Cloke M, Lester E. Prediction of the burnout performance of some South American coals using a drop-tube furnace. Fuel 2003;82:1893–9.
[28] Users guide for FG-DVC model. Advanced Fuel Research Inc.; 1992.

P.3

“Design of an engineering system for unburned carbon prediction”

Submitted to Fuel (Sept. 2007)

J. Pallarés, I. Arauzo, E. Teruel

Development of an engineering system for unburned carbon prediction

Author: Javier Pallarés
Affiliation: Centre of Research for Energy Resources and Consumptions (CIRCE), University of Zaragoza (Spain).
Postal address: María de Luna, 3. 50 018 Zaragoza (Spain)
Telephone number: +34 976762562
Fax number: +34 976732078
Email: jpallare@unizar.es

Co-Author: Inmaculada Arauzo
Affiliation: Centre of Research for Energy Resources and Consumptions (CIRCE), University of Zaragoza (Spain).
Postal address: María de Luna, 3. 50 018 Zaragoza (Spain)
Telephone number: +34 976761863
Fax number: +34 976732571
Email: iarauzo@unizar.es

Co-Author: Enrique Teruel
Affiliation: Centre of Research for Energy Resources and Consumptions (CIRCE), University of Zaragoza (Spain).
Postal address: María de Luna, 3. 50 018 Zaragoza (Spain)
Telephone number: +34 976762352
Fax number: +34 976732078
Email: eteruel@unizar.es

Abstract

Within the computational methods used for the prediction of unburned carbon, coal combustion kinetics models, generally developed from the study of the real combustion process in experimental facilities, has the advantage to simulate the coal combustion process in a very realistic way. However, these models need the fluid and thermal behaviour in the boiler, which is usually obtained from simplified zonal approaches. The other group of models, namely CFD codes, present the opposite features. That is, they give a detailed description of the thermal and fluid dynamics behaviour in the boiler, but they use simple combustion models that cannot be used for a quantitative burnout determination. Moreover, the computing cost can be high and cannot be implemented in an on-line predictive system.

The predictive system developed in this work has the same structure as the so-called combustion kinetics models, however, it obtains the fluid and thermal description through CFD simulations. To solve the handicap of the high computational cost needed to run a CFD simulation, a neural network system is used to reproduce the solutions given by the CFD code. Moreover, a neural network system permits to interpolate in the range of variation used during the training stage, and thus, a predictive system covering the whole operational range of the plant can be obtained.

Results from the predictive system have been compared against those gathered at Lamarmora power plant (ASM Brescia, Italy), after carrying out a statistical study for validating and determining the prediction capability of the system. The comparison of both sets of data permits to conclude that the system predicts reasonably well over the whole range of operating conditions of the study plant.

Keywords: Unburned carbon; Coal combustion; CFD; Neural Networks

Introduction

There exist many approaches, experimental and computational, to develop an unburned carbon predictive system. Experimental approaches are very useful in design studies. However, for the daily monitoring of a real plant, the computational methods offer a flexibility as well as a saving of time and money, over current experimental facilities. Within the computational methods regularly used, CFD codes can precisely characterize the processes that take place inside the furnace. Despite this, for the study of unburned coal in utility boilers, these codes have two important drawbacks. Firstly, for the heterogeneous char particle combustion modelling, these codes rely on simple models, that prove to be inadequate for obtaining quantitative values of the combustion process. To solve this difficulty a methodology based on obtaining temperature and oxygen partial pressure profiles for a representative number of particles, that are entered in an advanced combustion model using a CFD code is used [1]. The second disadvantage of CFD codes is their typically high computational cost as creating and solving new simulations may take several days, which makes the use of this kind of tool in taking in situ real plant decisions impossible. Thus, in the development of predictive systems for combustion, some authors prefer to sacrifice part of the problem information using zonal approaches to solve the fluid-dynamics [2, 3]. However, these zonal models also present serious limitations such as the impossibility to correctly characterize many relevant factors that affect the combustion process i.e. primary and secondary air mixing, swirling intensity, burner to burner flow interactions, reversed-flow regions or mass flow imbalances. For that reason, in this work, the use of the CFD code as a thermal and fluid-dynamic characterization tool was kept. To solve the problem of the high computational cost, the utilization of a neural network system that generates the oxygen partial pressure, and temperature profiles, and the residence time of particles for any operating condition is proposed. In this way, a number of CFD simulations, that are representative of the factors influencing unburned carbon losses within the plant operating condition ranges, are carried out. These simulations are then used to train a neural network system, so that this system is able to reproduce the solutions given by the CFD code. As in the case of the CFD code, the solutions from the neural network system are given in the form of oxygen partial pressure and temperature profiles, and particles residence times, to run

immediately after an advanced combustion model. The advantage of introducing the neural network system in this way, is that it is possible to perform the calculations in a short period of time (less than a minute), and therefore, it can be used in the construction of an on-line predictive system. Another advantage is that, if the neural network system is appropriately trained, considering the variations and interactions of all parameters affecting unburned carbon formation, this system permits to interpolate in the range of variation used during the training stage. Thus, a predictive system covering the whole operational range of the plant can be obtained.

Throughout the paper, the development of the neural networks model is described: design of the neural network system structure, training of the system from a number of CFD simulations of the plant, and finally, its validation. Then, the construction of the unburned carbon prediction system (UPS) from the coupling of the neural network model and the advanced combustion model is described. Finally, the system is validated using standard plant instrumentation measurements gathered during three months at Lamarmora plant (ASM Brescia) under different operation conditions. From these results, an evaluation of the system is assessed, hinting at the most significant conclusions.

2. Neural network model

Neural networks form a set of programming and controlling techniques within the subject of Artificial Intelligence, which allows a system to learn; that is, recognize patterns and predict the behaviour from a number of training data [4]. The use of neural networks present many advantages over more traditional techniques. Firstly, they use simple mathematical calculations, reducing the computational cost, which allows them to be used in an on-line application. Moreover, these systems are very robust and fault-tolerant.

The construction of the network system is carried out through an iterative process through the design, training and validation stages. The choice of the neural network architecture is one of the most important stages in designing the system. The first step consists of selecting the most suitable type of neural network for the problem. At this point, a Feedforward network type was chosen, since, as opposed to other designs, it has a great generalization capability and generates reasonable outputs even when the inputs have not been explicitly defined during the training stage. The hidden layer is made up of sigmoid type neurons since they allow the simulation of both linear and non linear systems. The output layer is formed by linear type neurons to allow the network to simulate any function without discontinuities.

The outputs of the system are the oxygen partial pressure, the temperature and the residence time of each particle. The system can be constituted with different architectures using multi input-multi output networks (MIMO) or multi input-single output networks (MISO). The former architecture may save efforts in the design process, since a single network that produces several outputs is used. However, since the weights of the network are the same, the convergence of one output will determine the convergence of the others therefore complicating the process. In this way, it is advisable to use MIMO networks when the simulated outputs bear a similar relation to the inputs and depend on similar parameters. In this work, two independent neural network systems were chosen: a MISO network to generate the particles' residence time, and two-outputs MIMO networks to obtain the oxygen partial pressure and temperature profiles. The initial design of the oxygen partial pressure and temperature neural network was built using a single MIMO network for the whole operational range of the plant. However, large differences in the behaviour of the simulated profiles between full and partial load conditions were found. Therefore, separate networks for both load conditions were used. Similarly, since the case-study unit is equipped with four burners arranged in two rows of two burners each, in order to improve the convergence and accuracy of the results, separate networks for the upper and lower row of burners were considered. As a consequence of these modifications, the final design of the oxygen and temperature profiles network was formed by four MIMO networks. As far as the residence time network was concerned, a high fitness allowed only one MISO network to be adopted for the whole operational range.

The choice of the inputs must contribute to achieve the simplest possible model. For this reason, a carefully selection of the inputs must be done, improving the convergence of the problem. From a factorial analysis, which established the most relevant parameters affecting carbon losses, the inputs for both neural networks were selected (*a* – residence time network; *b* – oxygen and temperature profiles network):

- Load (full or partial load): 1 input [a,b]
- Excess O_2: 1 input [a,b]
- Air to coal mass flow ratio: 1 input [a,b]
- Particle diameter: 1 input [a,b]
- Uneven mass flow distributions among burners and mills: 4 inputs [a,b]
- Burner position (upper or lower row): 1 input [a]
- Starting feeding position of the particle in the burner: 1 inputs [b]
- Time: 1 input [b]

The hidden layer gives the network the capability of reproducing non linear effects. Since, in Feedforward neurons the hidden layer is made up of sigmoid functions which by themselves have the capability of simulating these non linear effects, it is enough to include one single hidden layer and thus reduce the complexity of the network. Next, the number of neurons that will constitute the hidden layer is determined. Increasing the number of neurons is equivalent to increasing the degrees of freedom of the system, which means that the network will be able to reproduce more accurately the training data. However, an excessive number of neurons should be avoided, since it will result in an overtraining situation. On the contrary, reducing the number of neurons, increases the network capability to generalize, at the expense of a decrease in the accuracy. It is necessary to balance both situations. Usually, the number of neurons is determined according to previous experiences, and then, from the results, an iterative process for the proper selection of the number of neurons is carried out. In general, it is preferable to start with a reduced number of neurons, and then increase this number by one unit at a time until the addition of a new neuron does not improve anymore the convergence of the problem. The hidden layer of the residence time network is formed by 20 neurons, whilst the oxygen and temperature profiles networks are made up of 15 neurons each.

Before starting the training of the neural network, a pre-treatment of the input data in order to expedite the learning process was carried out, removing from the training set any error in the inputs. Besides, the input and output data were normalized in the range -1 to 1. In this way, the range of values for all the inputs is the same, and as a consequence, the training is faster, and accuracy problems in the variables with lower values are avoided.

In order to obtain the data used to train the neural network, a design of experiments based on factorial analysis was carried out, in such a way that three levels of the most relevant factors affecting carbon losses (Excess oxygen, primary air to coal mass flow ratio, particle size, fuel/air mass flow imbalances through burners) were included, differentiating between full and partial load conditions. In order to completely characterize this design, 72 CFD simulations were carried out using a commercial application, CFX 4.4 (AEA Technology plc.) running on a Windows machine, Pentium IV X-dual processor 2.8 GHz, 2 GB RAM each. Once the accuracy of the numerical resolution was verified, we proceeded with the validation. For that purpose, the oxygen values at the exit of the boiler obtained in the simulations were compared against the predetermined values for each case. Figures 1.a and 1.b show the results obtained, and allows us to accept the correctness of the simulation.

For training the networks, the Levenberg-Marquardt algorithm with Bayesian regularization implemented in MatLab (trinbr), was used. This algorithm uses an approximation technique

based in Newton's method. In this way, the network learns by modifying the weights vector of the neurons. The Levenberg-Marquardt algorithm as compared with other training methods, gives the fastest response with a minimum convergence error. In addition, the Bayesian regularization provides the training algorithm with a superior generalization capability. This technique modifies the optimization function, including the quadratic sum of the network parameters (weights and bias) into the sum of the quadratic errors. This way, at the same time as the error is reduced, the network parameters are reduced too, so that the network generates softer responses that contribute to avoid overtraining situations [5]. The stop criterion for the training was reached when the quadratic errors and the weights remained relatively constant.

The validation process lies in verifying the correlation and generalization capabilities of the network. The validating methods widely used in the research community are based on graphical techniques. These kinds of methods vary also depending on the type of output that needs to be validated. As a result, in this work, two different graphical techniques to validate the residence time network and the oxygen and temperature profiles network were applied. For the former, a correlation graph that shows the comparison of the simulated and real data was used. In this way, it is possible to verify the fitness and the range of values where the best fit is attained. Figure 2 shows a good fitness for the residence times generated by the neural network over a wide range of values (4 s – 25 s), which covers the most probable variation of this parameter. With regard to the oxygen and temperature profiles networks validation, the most suitable graphical method to validate these is to represent together the real and simulated values as a function of time. Since the final use of the network lie in generating oxygen partial pressure and temperature profiles as a function of time for a particular operating condition; it is appropriate to verify if the simulated data adequately reproduces the oxygen and temperature profiles obtained by the CFD code for a wide range of conditions. Since there is a large number of profiles for each output (72 simulations x 1920 particles = 138240 profiles), the validation is a tedious and difficult task. So in order to interpret and compare the results, average temperature and oxygen profiles in five sieve fractions (< 30 μm, 30 – 60 μm, 60 – 90 μm, 90 - 120 μm, > 120μm) were represented for each burner and simulation case considered. In addition to the seventy two CFD simulations used for the model development, twenty additional simulations were also considered in the validation. Figures 3.a and 3.b show two examples of the validation process for the averaged profiles. In the same way, similar results were obtained for the rest of cases considered in the validation, thus leading us to the conclusion that the neural networks system adequately reproduces the profiles obtained by any CFD simulation in the operational conditions range of the study plant.

The goal of generating these profiles is to use them as inputs in an advanced combustion model to determine the combustion efficiency within the furnace. Therefore, it is worthwhile to look at the time scales of Figure 3 to appreciate in detail the quality standard of the profiles and their influence on the later combustion calculations. It is only during the first 500 ms, when most of the combustion process takes place, when the neural network system is used to generate data every 5 ms; that is, 100 discrete points are obtained. From 0.5 seconds residence time onwards the time step has been progressively increased to save on computing time, as long as the coal conversion has been completed and the temperature and oxygen gradients are reduced. Furthermore, if computing processing power is not an issue it is possible to keep the time step increment of 5 ms due to the large amount of data used in the training stage from the CFD simulations i.e. around 100 million data points.

2. Combustion model

The development of the combustion model is focused on the reactions that take place on the particle surface, that is, devolatilization and char oxidation. Devolatilization was modelled using a commercial macromolecular network pyrolysis model (FG-DVC) [6]. Char oxidation was modelled and programmed in Fortran using a developed intrinsic formulae based on the carbon burnout kinetic model (CBK8) [7], that allows the transition to Zone I and includes the variation in the porous structure and reactivity of the char as combustion proceeds, mineral matter effects, and the influence of coal's maceral content [1].

3. Unburned carbon prediction system

The unburned carbon prediction system is formed by the union of the neural network system with the advanced combustion model. The combination of predictive techniques, that are generally used isolated, allows us to unify the following advantages within the same system: fluid dynamics and heat transfer from CFD codes, detailed chemical kinetics from advanced combustion models, and reduced computing cost and interpolation capabilities from neural networks. Figure 4 shows the final structure of the predictive system.

The order sequence for running the system is simple: For a given boiler condition, the system starts the neural network system and generates an output file containing the temperature and oxygen partial pressure information for the particles in the furnace, as well as their residence times. Immediately after this output file has been generated, the coal properties are also introduced as an input in the coal combustion model to determine the unburned carbon in ash. The combustion model is divided into two subroutines corresponding to the devolatilization and

char oxidation stages. The former determines the amount of volatiles yielded together with the resultant char residue in which the intrinsic char oxidation model is applied.

One of the main advantages of this predictive system is the reduced number of inputs (boiler conditions and coal properties) required to run the model and their availability at any power station: coal load, excess oxygen at the exit of the boiler, primary air to coal mass flow ratio, uneven mass flow distributions in the boiler (this input is adapted to the information available in the plant), proximate and ultimate coal analysis, petrographic coal analysis (if available), and pulverized coal size distribution. The kinetic parameters of the combustion processes form part of a third group of inputs which are directly introduced in the combustion model. These parameters can be either determined empirically by DTF experiments or be approached through correlations or databases [1].

3.1 Validation and discussion

The validation of the unburned carbon prediction system is carried out using standard plant instrumentation measurements gathered at Lamarmora ASM Brescia power station during the year 2005 (January – March 2005). Study cases were obtained covering the regular range of variation under full and partial load conditions. In the study, two coals from Central America commonly used in the plant over the last 5 years (Guasare from Venezuela and Carbonandes from Colombia) and a coal from Russia, recently used to evaluate its influence on the combustion efficiency, were burned separately. Proximate, ultimate and petrographic (when available) analysis for these three coals are presented in Table 1. Generally, petrographic analysis is not performed in power plants. In such case, we can make use of databases, where coals from all over the world are catalogued. In this work, since no petrographic analysis was available, inertinite and vitrinite values for Gausare coal were taken from [8].

The average computational time for each case calculation, using an Intel Core 2 DUO 6300 (1.86 GHz, 0.86 GB de RAM) machine, was less than one minute. Figures 5.a and 5.b show the dispersion diagrams for the carbon-in-ash values gathered at the plant during the test period against the calculated values from the predictive system, under full and partial load conditions.

Figures 5.a and 5.b indicate an adequate correspondence with plant data and calculated values from the predictive system, since the cloud of points are close to the bisector of the first quadrant for both diagrams. Next, it was necessary to analyze, separately, the results obtained under full load conditions where the variation in the operating conditions is slight and the results obtained under partial load conditions where this operational range is larger. As a result, the fitness of the model under full load conditions (Figure 5.a) shows a good agreement for the

three study coals. Focusing now on the more distant points from the bisector, it is not possible to identify the reason for this inaccuracy, since the operating conditions in those cases were very similar to the ones in other cases where the carbon-in-ash values were apparently "normal". Consequently, these "fault points" may have been due to the data gathering process or due to other factors not included in the instrumented controls of the plant and therefore not considered in the model development. Fortunately, these "fault points" represent a negligible percentage and do not affect the general conclusions of the model. With regards to the results under partial load conditions (Figure 5.b), there exists a larger dispersion between plant data and the calculated values from the predictive system. The reason for this discrepancy can be explained from a fluid dynamics point of view. Of course, under partial load conditions the stratification of the conditions within the boiler is more relevant than in the case of full load conditions where there is a greater uniformity in the temperature and oxygen partial pressure profiles. Starting from this assumption and taking into account that neural networks average and interpolate those values in the furnace, the results found are not strange. In fact, this behaviour illustrates one of the biggest challenges of the problem and thus, where an increased emphasis in the neural networks system development have been placed. Designing a neural network with a higher number of neurons would improve the fluid and thermal description within the furnace. However, an excessive number of neurons should be avoided since it would result in an overtraining situation leading to a decrease in the generalization capability of the network. Consequently, in order to find a balanced situation, we opted for complicating the neural networks system design by considering different networks for the upper and lower row of burners and including the starting feeding position of the particles within the burner. Finally, an iterative process to select the most suitable number of neurons for the problem was carried out.

Additionally to the correlation diagrams in Figures 5.a and 5.b, a statistical study to analyze in detail the correspondence existing between plant data and the values calculated by the predictive system was performed. For this, the statistical distributions of both data sets (plant data and system predicted values) were compared. Since the distributions type was unknown, the Anderson-Darling normality test for both sets was carried out. Figures 6.a (Full load) and 6.b (Partial load), show the probability diagrams obtained from the Anderson-Darling test, overlaid for both data sets and including the limits corresponding to a confidence level of 95 %. The interpretation of Figures 6.a and 6.b suggests that both sets are not normal (p-value < 0.005). Therefore, in order to compare both distributions, we should make use of the mean, standard deviation, and the probability diagram itself. Under full load conditions, the comparison of the probability diagrams together with mean and standard deviation for both sets shows a good agreement. On the other hand, under partial load conditions the correspondence with the mean

is in agreement, but there exists a discrepancy in the standard deviation. These results confirm the discussion presented for Figures 5.a and 5.b.

It is also noticeable that Figures 5.a and 5.b show a clear distinction between the three coals in the results. Obviously, carbon-in-ash values depend on the mineral matter content of the coal. Therefore, in order to obtain a rigorous estimation of the accuracy of the unburned carbon prediction system, it is necessary to view the results in the same base line i.e. the overall burnout.

The last step in the development of the system lies in determining and expressing the global accuracy of the model. To achieve this, the statistical distribution of the overall burnout prediction error, calculated by difference of the plant data and the values predicted by the system, was analyzed. Again, the Anderson-Darling normality test was applied, this time giving a positive result for the test (p-value = 0.012), as can be seen in Figure 7. It is outstanding that, in spite of the fact that the p-value is small, a leptokurtic distribution (kurtosis = 0.558172) was obtained, showing a smaller concentration of points in the extremes with a greater concentration around the mean value. This gives an extra confidence in the results obtained when analyzing the normal distribution. Another important result is that the mean is moved a little from zero, which means that the model slightly overpredicts burnout. This result is not worrying, since it is very small (0.071778), but it should be considered in the construction of the confidence intervals.

Taking the values of the 95.5 % confidence interval for the mean and standard deviation from Figure 7, it is possible to define an interval for the prediction error of a punctual estimation, with a 95.5 % confidence level. That is, 95.5 % of the probability mass of the prediction error is inside the interval $[\mu - 2\sigma , \mu + 2\sigma]$. Consequently, the error for a punctual estimation (E_{Bnt}) can be expressed according to Eq. (1).

$$E_{Bnt} = \mu \pm 2 \cdot \sigma \approx \pm 0.82\ \% \qquad (1)$$

Since the mean of the distribution is moved from zero, the lower extreme of the interval of Eq. (1) is in fact – 0.75 %. However, to simplify the interpretation, the error has been expressed using a symmetric interval from the higher value (0.82 %) according to Eq. (1), so that the confidence level is in fact higher than 95.5 %.

In addition to the determination of the prediction error for a punctual estimation of the model, it is advisable to give the averaged prediction error for a set of random estimations. This practice is especially suitable in the case where using an on-line data acquisition system that collects

data in short periods of time and, due to the fluctuations, target control variables are usually expressed as an average. Following this analysis, the average error for a number of random estimations ($n_o > 30$) for a 95 % confidence level ($\alpha = 0.05$) is within the interval defined in Eq. (2).

$$\overline{E}_{Bnt} = \overline{x}_n \pm \frac{\hat{\sigma}}{\sqrt{n_o}} \cdot z_{1-\alpha/2} \approx \pm 0.15\ \% \qquad (2)$$

Again, a symmetric interval has been given, notwithstanding that the mean of the distribution has moved from zero, and so, the lower extreme of the interval of Eq. (2) is in fact – 0.07 %.

In order to obtain an indicator of the model accuracy in terms of the unburned carbon in ash (%), we can make use of the Kurose's et al. [9] expression (Eq. (3)). This leads to expressions, that depend on the material matter content of the coal and the burnout.

$$CIA_{Bnt} = 100 \cdot \frac{100 - Bnt_{UPS}}{\left(\frac{Z}{1-Z}\right) + (100 - Bnt_{UPS})} \qquad (3)$$

Where Z is the ash content (%), and CIA_{Bnt} is the carbon-in-ash value corresponding to a burnout level (%, coal basis) Bnt_{UPS}.

Depending on the type of error that is used in Eq. (3), punctual or averaged for a number of random estimations, we will obtain respectively both expressions for the accuracy of the model. Considering the most disadvantageous situation, Table 2 summarizes the maximum error achieved for the three study coals, both for a punctual estimation and for the average of a set of random estimations. It should be noted that the calculated values in this table, are maximum errors. That is, these points would be located at the extremes of the distribution function (close to a signification level $\alpha/2$ or $1-\alpha/2$). Furthermore, it should be remembered that the more sharpened the shape of the probability distribution function (positive kurtosis), the more points are located around the mean value, and consequently, this shows that the values presented in Table 2 are very exceptional. Finally, it should be considered that none of the prediction errors obtained in the study have been discarded from the analysis. Generally, in statistical studies, the values located furthest away from the mean are discarded from the analysis if there is not a logical interpretation for them according to the data available in the problem. In the analysis of Figures 5.a and 5.b, it was mentioned that that the more distant points from the bisector did not correspond to any apparent reason to infer an error in the model. In spite of this, we have decided to keep these fault points in the error analysis, in order to give a more conservative estimation of the prediction error and so taking into consideration the errors derived from the acquisition data process.

4. Conclusions

In this work, an unburned carbon prediction system that provides an on-line estimation of the unburned carbon in ash for a given operating condition in a utility boiler has been developed.

The final system is formed by a neural network model and an advanced combustion model. The former provides the system with the evolution of the temperature and oxygen partial pressure profiles found by the particles in their trajectories across the boiler for the range of operation conditions in the study plant. The other sub-model is the combustion model itself which is divided into two subroutines. One corresponding to the devolatilization of the coal particle (FG-DVC), and the other the char oxidation intrinsic model which includes thermal annealing, variations in the porous structure as combustion proceeds, ash inhibition effects, and the influence of macerals in the reactivity of the char.

Results from the predictive system have been compared against those gathered at the plant, after carrying out a statistical study for validating and determining the prediction capability of the system. The comparison of both sets of data (gathered at the plant and predicted by the system) has shown an excellent correspondence in the probability distribution, mean and standard deviation along the whole range of situations studied. The maximum error achieved for the burnout prediction is 0.82 % for a punctual estimation, and 0.15 % for the average of a number of random estimations.

Finally, the main advantages of the unburned carbon prediction system are presented in a schematic way:

- The system includes a detailed description of the transport phenomena involved in the problem by implementing the neural network system which was trained with CFD simulations covering the operation range of the plant.
- The neural network system itself allows us to interpolate for other conditions not specifically used during the training stage.
- The combustion model describes in detail both devolatization and char oxidation.
- The number of inputs of the predictive system is small and they are available at any power station.
- The computational time, less than a minute, allows us to use it in an on-line monitoring system of a power station.
- The accuracy of the system is good enough in the whole range of operation of the plant, and improves the results obtained with other predictive systems based on zonal approaches.

Acknowledgments

The work presented in this paper has been partially supported by the research project 7220-PR-130-CARNO 'Development of a carbon-in-ash notification system' funded by the European Commission under the ECSC research program. The authors gratefully acknowledge Lamarmora (ASM Brescia) plant personnel for their support and collaboration. We also thank helpful discussions held with Dr. Pedro Jodrá for the statistical study of the results.

References

1. Pallarés J, Arauzo I, Williams A. Integration of CFD codes and advanced combustion models for quantitative burnout determination. Fuel, 2007 (In press).
2. Fiveland WA, Jamaluddin AS. An efficient method for predicting unburned carbon in boilers. Combustion Science and Technology, 1992, 81: 147-167.
3. Severin T, Wirtz S, Scherer V, Roth K. Simulation of pulverised coal fired boilers with a simplified cellnet model. Chemie-Ingenieur-Technik, 2005; 77: 1042.
4. Bishop CM. Neural networks for pattern recognition. Oxford University Press, 1995.
5. Demuth H, Beale M. Mat Lab Neural Network Toolbox 4.0. 2002.
6. Solomon PR, Hamblen DG, Carangelo DG, Carangelo RM, Serio MA, Deshpande GV. General model of coal devolatilization. Energy & Fuels, 1988; 2:405-422.
7. Hurt R, Sun J-K, Lunden M. A kinetic model of carbon burnout in pulverized coal combustion. Combustion and Flame, 1998; 113:181-197.
8. Barranco R, Cloke M, Lester E. Prediction of the burnout performance of some South American coals using a drop-tube furnace. Fuel, 2003; 82:1893-1899.
9. Kurose R, Ikeda M, Makino H. Combustion characteristics of high ash coal in a pulverized coal combustion. Fuel, 2001; 80: 1447-1455.

Table 1

Proximate analysis (as received)	**Guasare**	**Carboandes**	**Russian**
Moisture (%)	6.91	9.60	9.56
Ash (%)	5.75	6.44	7.14
Volatile (%)	35.00	34.17	36.09
Fixed Carbon (%)[cd]	52.34	49.79	47.21
Ultimate analysis (as received)			
Carbon (%)	72.75	69.21	65.62
Hydrogen (%)	4.93	4.38	4.66
Oxygen (%)[cd]	7.75	8.38	10.74
Nitrogen (%)	1.27	1.36	1.90
Sulphur (%)	0.64	0.64	0.38
Petrographic analysis			
Inertinite (%)	0.24	N/A	N/A
Vitrinite (%)	0.76	N/A	N/A

Table 1. Proximate, ultimate and petrographic analysis for the coals used in the study.

[cd] Calculated by difference

Table 2

CIA maximum errors (%)

	Punctual estimation	Averaged estimation
Guasare	9.48	1.52
Carbonandes	8.44	1.38
Russian	7.73	1.27

Table 2. Maximum errors in the prediction of carbon-in-ash values within a confidence level of 95 % for the three study coals.

Captions to illustrations

- Fig. 1. Experimental values compared with numerical predictions for mean oxygen content (vol. %) in flue gases for the simulated scenarios: (a) Full load, (b) Partial load.
- Fig. 2. Correlation graph of CFD simulated and neural network prediction residence time.
- Fig. 3. Graphical comparison of temperature and oxygen partial pressure averaged profiles simulated by the neural network and the ones obtained by the CFD code: (a) Particle size (< 30 μm), (b) Particle size (60 - 90 μm).
- Fig. 4. Unburned coal prediction system block diagram.
- Fig. 5. Correlation graph of simulated (UPS) and real (plant) carbon-in-ash values (%): (a) Full load, (b) Partial load.
- Fig. 6. Probability diagrams of simulated (UPS) and real (plant) carbon-in-ash values (%): (a) Full load, (b) Partial load.
- Fig. 7. Statistical distribution of the UPS burnout (%, coal basis) prediction error.

Figure 1

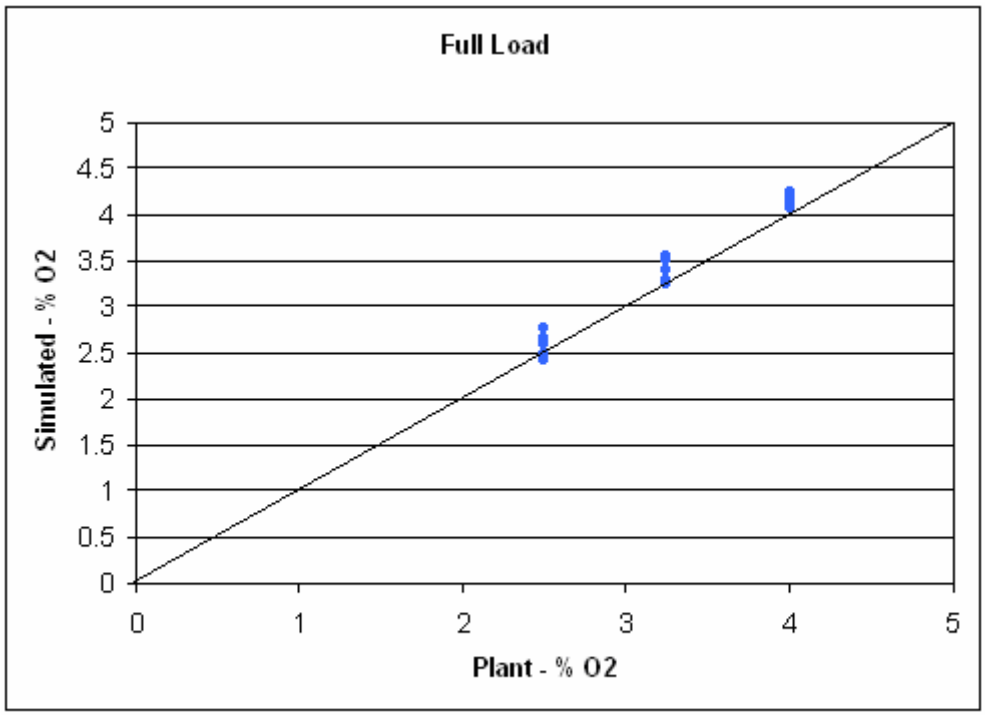
Full Load
Simulated - % O2
Plant - % O2
0
0.5
1
1.5
2
2.5
3
3.5
4
4.5
5
0
1
2
3
4
5

(a)

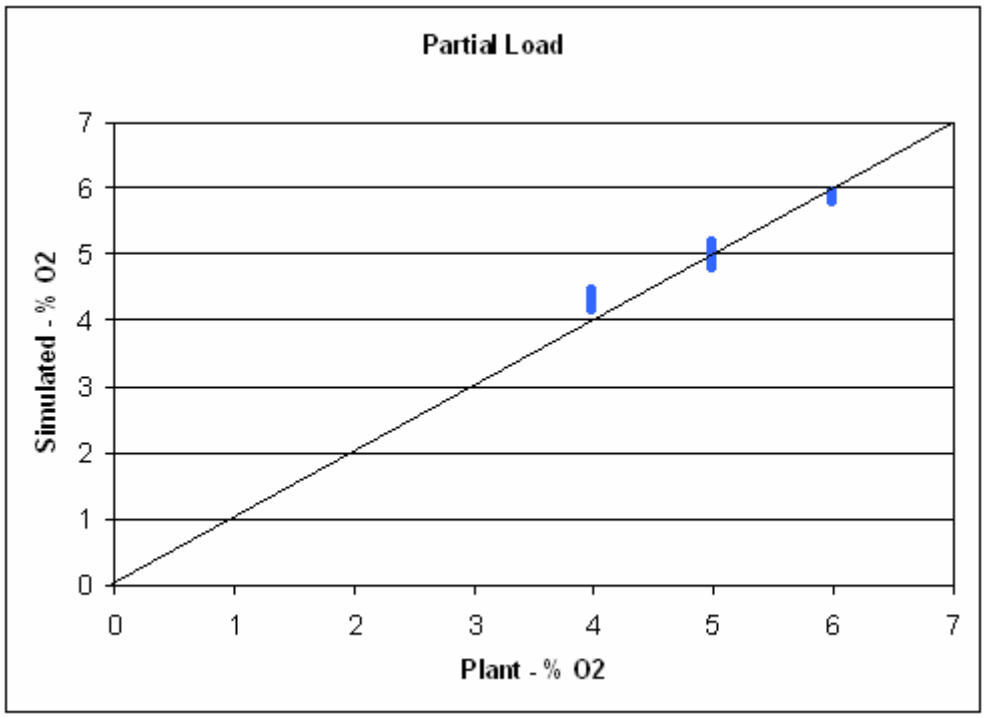
Partial Load
Simulated - % O2
Plant - % O2
0
1
2
3
4
5
6
7
0
1
2
3
4
5
6
7

(b)

Figure 2

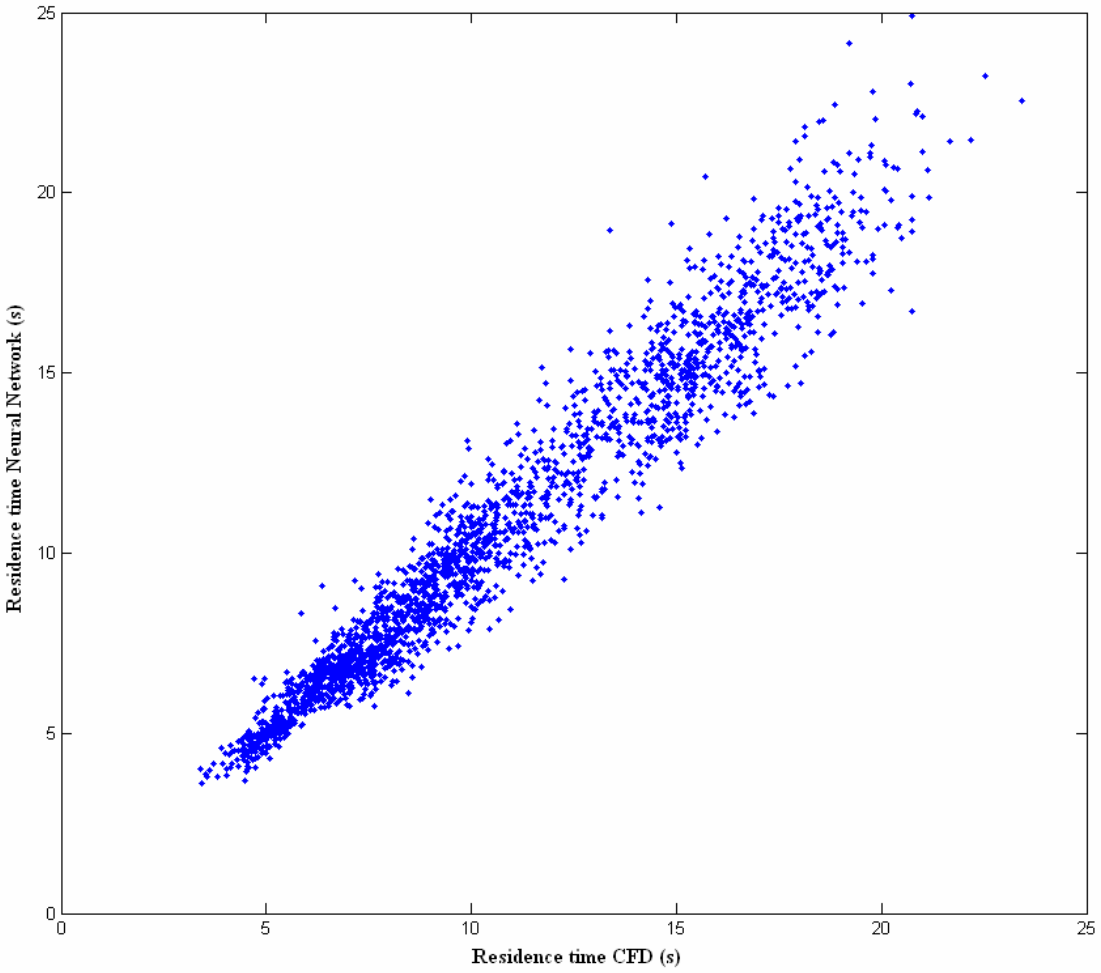
Residence time Neural Network (s)
Residence time CFD (s)
0
5
10
15
20
25

Figure 3

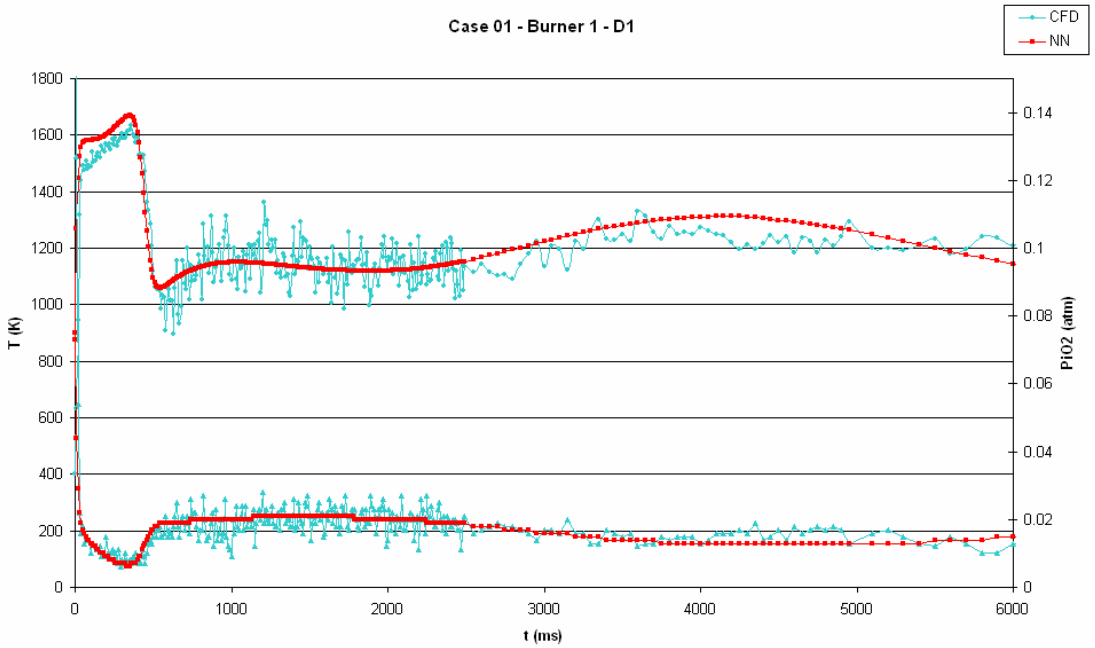
Case 01 - Burner 1 - D1
CFD
NN
T (K)
PiO2 (atm)
t (ms)
0
200
400
600
800
1000
1200
1400
1600
1800
0.02
0.04
0.06
0.08
0.1
0.12
0.14
1000
2000
3000
4000
5000
6000

(a)

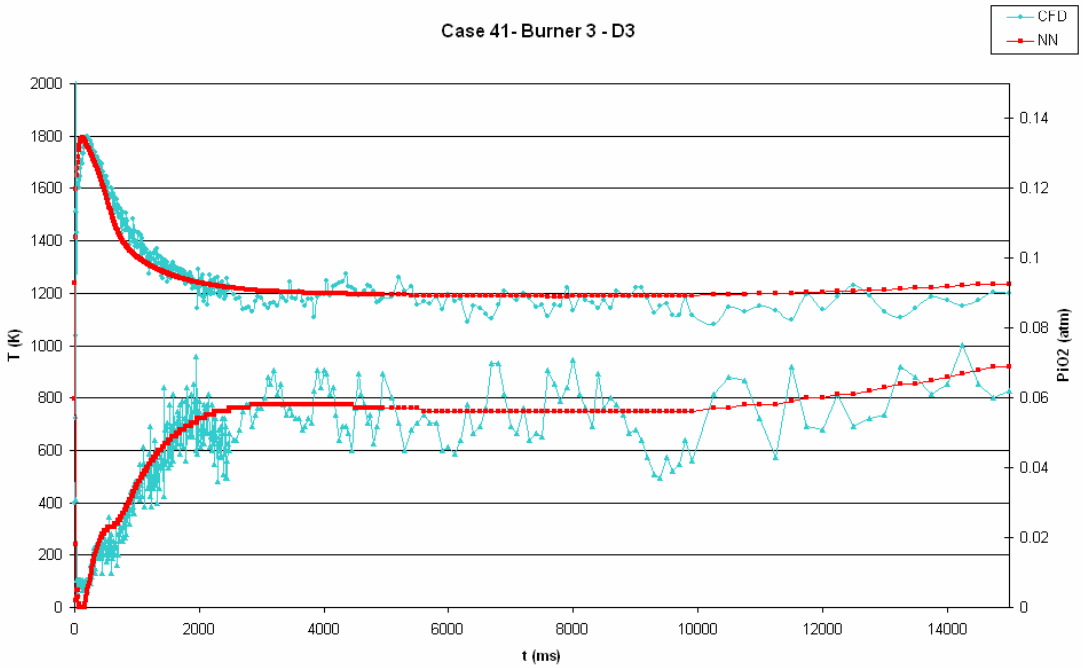
Case 41- Burner 3 - D3
CFD
NN
T (K)
PiO2 (atm)
t (ms)
0
200
400
600
800
1000
1200
1400
1600
1800
2000
0.02
0.04
0.06
0.08
0.1
0.12
0.14
2000
4000
6000
8000
10000
12000
14000

(b)

Figure 4

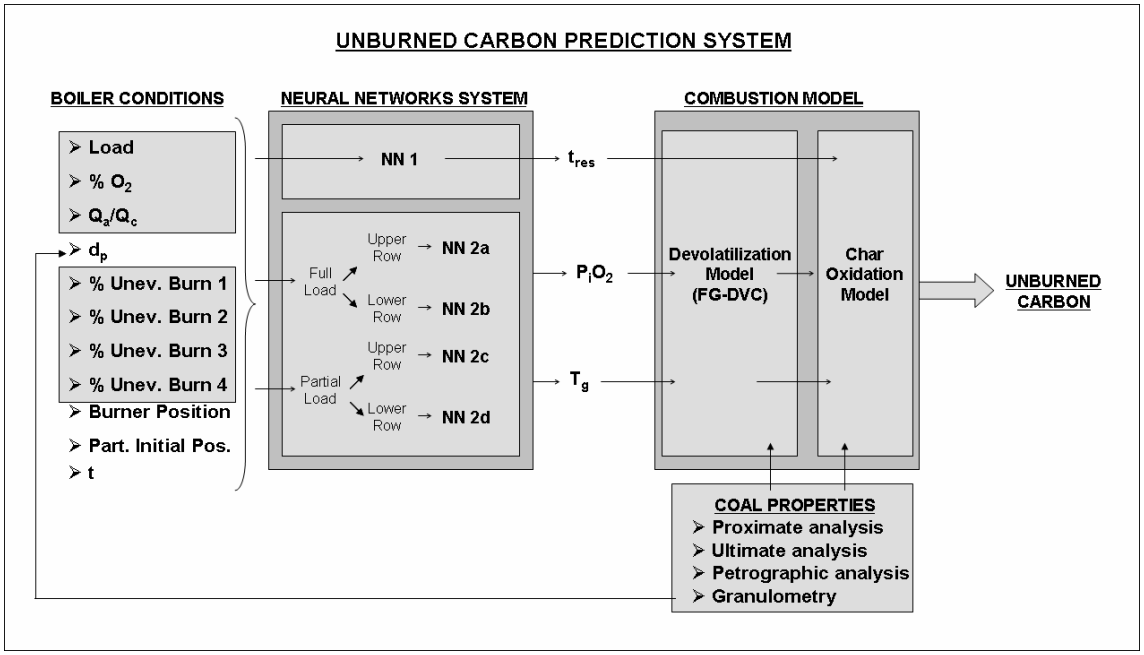
UNBURNED CARBON PREDICTION SYSTEM
BOILER CONDITIONS
NEURAL NETWORKS SYSTEM
COMBUSTION MODEL
Load
% O2
Qa/Qc
dp
% Unev. Burn 1
% Unev. Burn 2
% Unev. Burn 3
% Unev. Burn 4
Burner Position
Part. Initial Pos.
t
NN 1
tres
Full Load
Partial Load
Upper Row
Lower Row
NN 2a
NN 2b
NN 2c
NN 2d
PiO2
Tg
Devolatilization Model (FG-DVC)
Char Oxidation Model
UNBURNED CARBON
COAL PROPERTIES
Proximate analysis
Ultimate analysis
Petrographic analysis
Granulometry

Figure 5

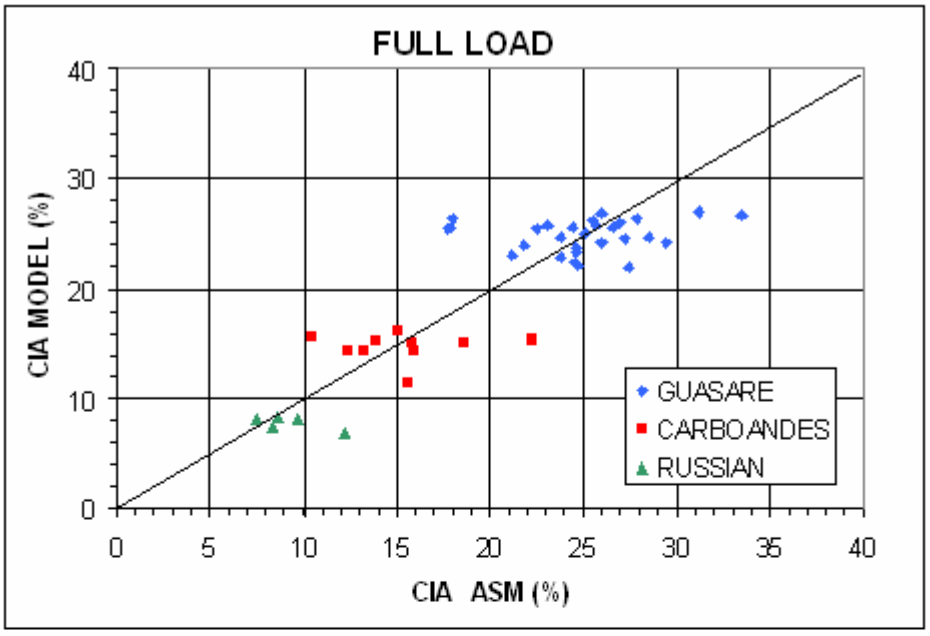
FULL LOAD
CIA MODEL (%)
CIA ASM (%)
0
10
20
30
40
0
5
10
15
20
25
30
35
40
GUASARE
CARBOANDES
RUSSIAN

(a)

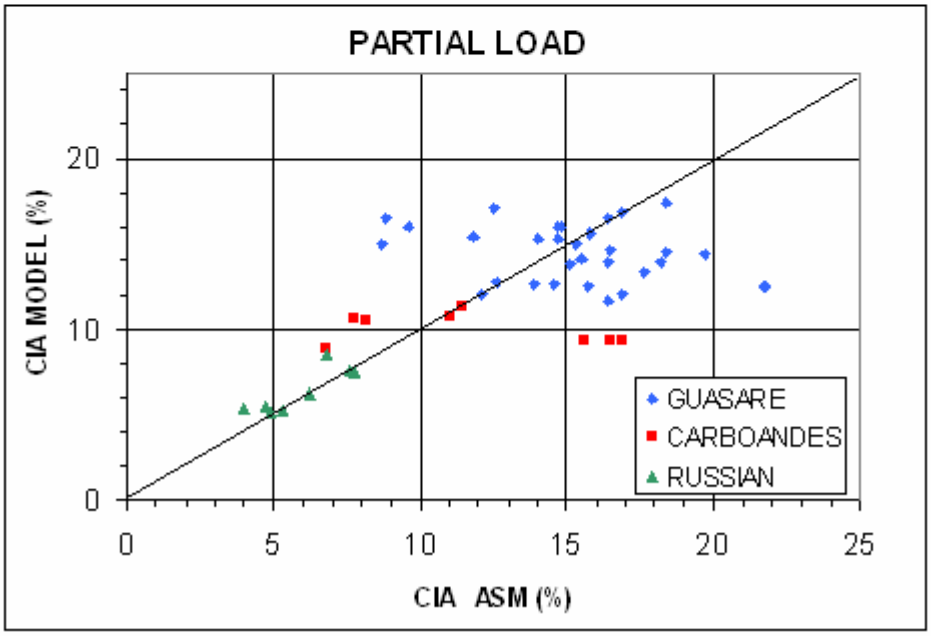
PARTIAL LOAD
CIA MODEL (%)
CIA ASM (%)
0
10
20
0
5
10
15
20
25
GUASARE
CARBOANDES
RUSSIAN

(b)

Figure 6

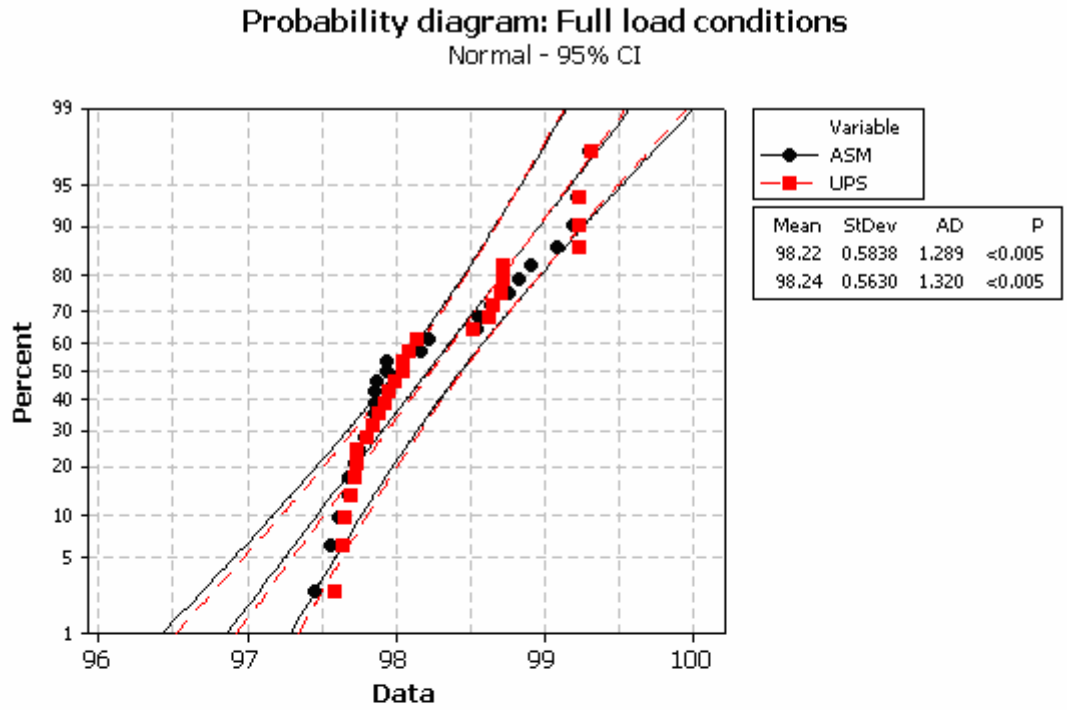
Probability diagram: Full load conditions
Normal - 95% CI
Percent
Data
Variable
ASM
UPS
Mean StDev AD P
98.22 0.5838 1.289 <0.005
98.24 0.5630 1.320 <0.005

(a)

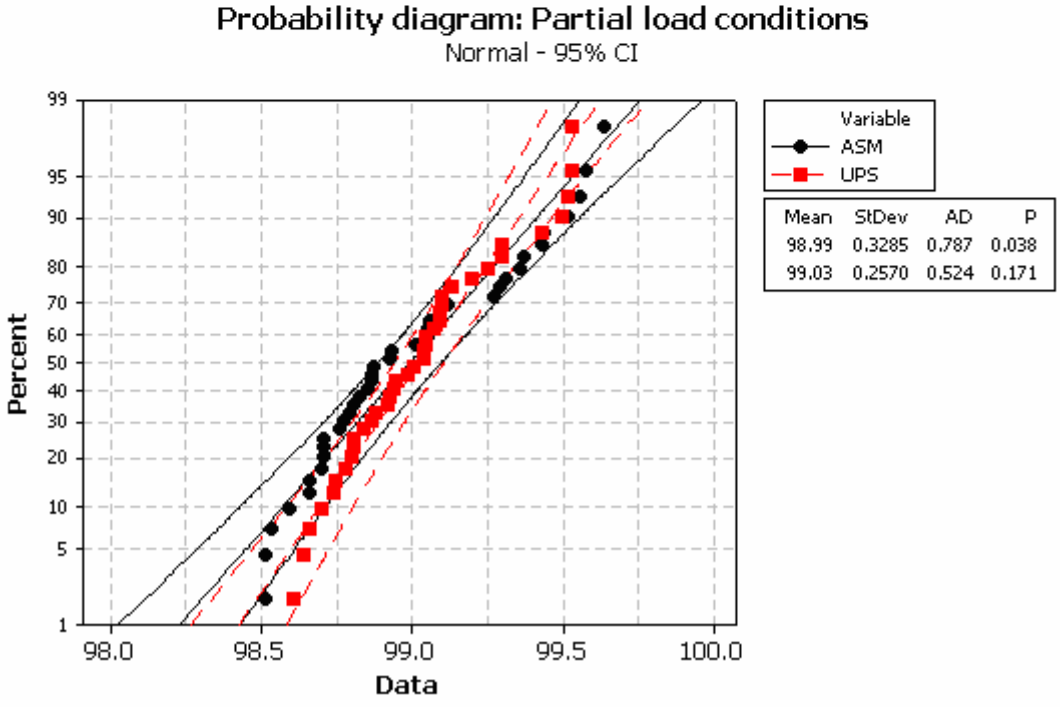
Probability diagram: Partial load conditions
Normal - 95% CI
Percent
Data
Variable
ASM
UPS
Mean StDev AD P
98.99 0.3285 0.787 0.038
99.03 0.2570 0.524 0.171

(b)

Figure 7

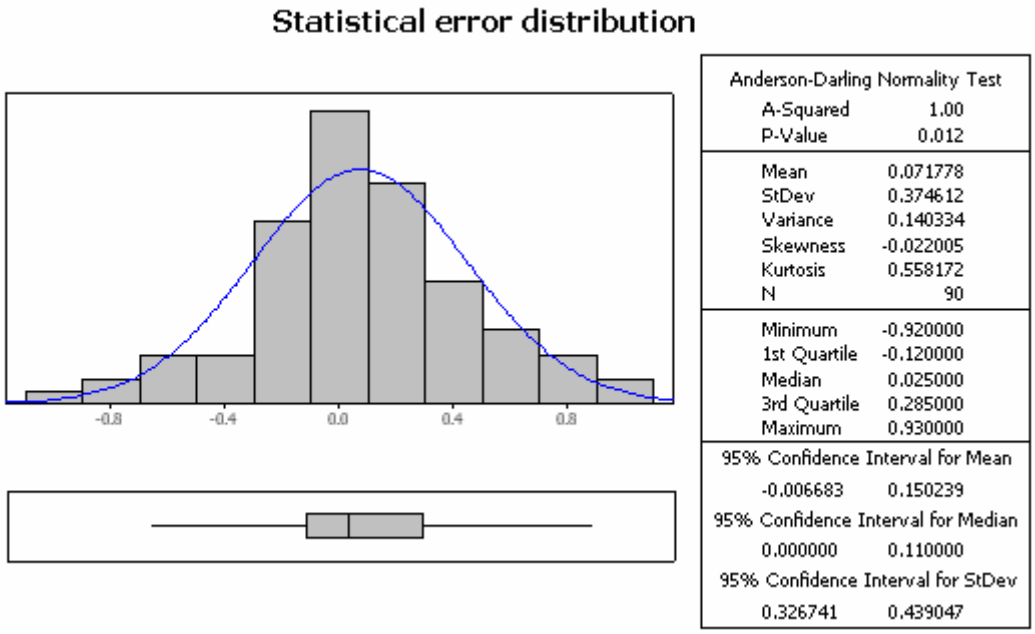
Statistical error distribution
-0.8
-0.4
0.0
0.4
0.8
Anderson-Darling Normality Test
A-Squared 1.00
P-Value 0.012
Mean 0.071778
StDev 0.374612
Variance 0.140334
Skewness -0.022005
Kurtosis 0.558172
N 90
Minimum -0.920000
1st Quartile -0.120000
Median 0.025000
3rd Quartile 0.285000
Maximum 0.930000
95% Confidence Interval for Mean
-0.006683 0.150239
95% Confidence Interval for Median
0.000000 0.110000
95% Confidence Interval for StDev
0.326741 0.439047

BIBLIOGRAPHY

- Aarna I, Suuberg EM. Changes in reactive surface area and porosity during char oxidation. 27th (Intenational) on Combustion. The Combustion Institute, 1998: 2933-2939.
- Abd El-Samed AK, Hampartsoumian E, Farag TM, Williams A. Variations of char reactivity during simultaneous devolatilization and combustion of coals in a drop-tube reactor. Fuel, 1990; 69: 1029-1036.
- Anderson JD. Introduction to computational fluid dynamics. Lecture Series von Karman Institute for Fluid Dynamics, 2000.
- Anthony DB, Howard JB, Hottel HC, Meissner HP. Rapid devolatilization and hydrogasification of bituminous coals. Fuel, 1976; 55: 121-128.
- Badzioch S, Hawksley PGW. Kinetics of thermal decomposition of pulverized coal particles. Industrial engineering chemical processes design development, 1970; 9: 521-530.
- Backreedy RI, Habib R, Jones JM, Pourkashanian M, Williams A. An extended coal combustion model. Fuel, 1999; 78: 1745-1754.
- Backreedy RI. Modelling the combustion of pulverized coal. Tesis Doctoral. Department of Fuel and Energy, University of Leeds, 2002.
- Backreedy RI, Jones JM, Pourkashanian M, Williams A. Burn-out of pulverised coal and biomass chars. Fuel, 2003; 82: 2097-2105.
- Backreedy RI, Jones JM, Ma L, Pourkashanian M, Williams A, Arenillas A, Arias B, Pis JJ, Rubiera F. Prediction of unburned carbon and NOx in a tangentially fired power station using single coals and blends. Fuel, 2005; 2196-2203.
- Backreedy RI, Fletcher LM, Ma L, Pourkashanian M, Williams A. Modelling pulverized coal combustion using a detailed coal combustion model. Combustion Science and Technology, 2006; 178: 763-787.
- Barranco R, Cloke M, Lester E. Prediction of the burnout performance of some South American coals using a drop-tube furnace. Fuel, 2003; 82: 1893-1899.
- Bartok W, Sarofim AF. Fossil Fuel Combustion. John Wiley & Sons, Inc. 1991.
- Basu P, Cefa K, Jestin L. Boilers & Burners: Design and Theory. Springer, 2000.
- Baum MM, Street PJ. Predicting the combustion behaviour of coal particles. Combustion Science and Technology, 1971; 3: 231-243.
- Beely TJ, Crelling JC, Gibbins JR, Hurt R, Man CK, Williamson J. Coal Science, 1995: 615-618.
- Belosevic S, Sijercic M, Oka S, Tucakovic D. Three-dimensional modelling of utility boiler pulverized coal tangentially fired furnace. International Journal of Heat and Mass Transfer, 2006; 49: 3371-3378.

- Bews IM, Hayhurst AN, Richardson SM, Taylor SG. The order, Arrhenius parameters and mechanism of the reaction between gaseous oxygen and solid carbon. Combustion and Flame, 2001; 124: 231-245.
- Bhatia SK, Perlmutter DD. A random pore model for fluid-solid reactions: II Diffusion and transport effects. AiChE, 1981; 27: 247-254.
- Bishop CM. Neural networks for pattern recognition. Oxford University Press, 1995.
- Carpenter AM. Coal classification. IEA Coal Research, 1988; 12.
- Carpenter AM, Skorupska NM. Coal combustion – analysis and testing. IEA Coal Research, 1993; 64.
- Carsky M, Kuwornoo DK. Neural network modelling of coal pyrolysis. Fuel, 2001; 80: 1021-1027.
- CFX-4.4 manuals. AEA Technology plc, 1997.
- Chan ML, Jones JM, Pourkashanian M., Williams A. The oxidative reactivity of coal chars in relation to their structure. Fuel, 1999; 78: 1539-1552.
- Charpenay S, Serio MA, Solomon PR. The prediction of coal char reactivity under combustion conditions. 24th Symposium (International) on Combustion. The Combustion Institute, 1992; 1189-1197.
- Chen KH, Shuen JS. A coupled multi-block solution procedure for spray combustion in complex geometries. AIAA press, 1993.
- Cloke M, Lester E, Belghazi A. Characterisation of the properties of size fractions from ten world coals and their chars produced in a drop-tube furnace. Fuel, 2002; 81: 699-708.
- Cloke M, Lester E, Thompson AW. Combustion characteristics of coals using a drop-tube furnace. Fuel, 2002; 81: 727-735.
- Cloke M, Wu T, Barranco R, Lester E. Char characterisation and its application in a coal burnout model. Fuel, 2003; 82: 1989-2000.
- Coelho LMR, He XG, Costa M, Azevedo JLT. Full boiler performance modelling. Joule III Programme. Clean Coal Technology R&D, 2000.
- Coimbra CFM, Azevedo JLT, Cavalho MG. 3-D numerical model for predicting NO_x emissions from an industrial pulverized coal combustor. Fuel, 1994; 73: 1128-1134.
- Cortés C, Gil A. Modeling the gas and particle flow inside cyclone separators. Progress in Energy and Combustion Science, 2007; 33: 409-452.
- Cremer MA, Wang DH, Chiodo AP. CFD based evaluation of the sensitivity of furnace conditions to burner air and fuel imbalances. EPRI-EPA-DOE-A&WMA Power Plant Air Pollutant Control Mega Symposium, Washington DC (USA), 2004.
- Crowe CT, Sharma MP, Stock DE. The particle-source-in cell (PSI-cell) model for gas droplets flows. Journal of Fluids Engineering, 1977; 99:325-32.

- Davis KA, Eddings EG, Heap MP. Computational investigation of carbon-in-ash levels for a wall-fired boiler after low-NOx combustion modifications. Pittsburgh Coal Conference, 1998.
- Dick E. Introduction to finite volume methods in computational fluid dynamics. Lecture Series von Karman Institute for Fluid Dynamics, 2000.
- Demuth H, Beale M. Mat Lab Neural Network Toolbox 4.0. 2002.
- Díez LI. Monitorización y simulación en tiempo real de calderas de potencia de carbón pulverizado. Tesis Doctoral, Universidad de Zaragoza, 2002.
- Domino SP, Smith PJ. Loss on ignition in coal combustion simulations. Interim Report DE-FG22-949C9422, University of Utah, 1999.
- Driest ER. On turbulent flow near a wall. Journal of the Aeronautic Science, 1956; 1007-1011, 1036.
- Eaton AM, Smoot LD, Hill SC, Eatough CN. Components, formulations, solutions, evaluation, and application of comprehensive combustion models. Progress in Energy and Combustion Science, 1999; 25: 387-436.
- Eberhart RC, Dobbins RW. Neural network PC tools. Academic Press Inc., 1990.
- Essenhigh RH, Howard JB. Toward a unified combustion theory: The pyrolysis and combustion mechanism of carbonaceous solids. Industrial and Engineering Chemistry, 1966; 58: 14-23.
- Essenhigh RH, Klimesh HE, Förstch D. Combustion Characteristics of carbon: Dependence of the Zone I-Zone II transition temperature (Tc) on particle radius. Energy & Fuels, 1999; 13: 826-831.
- Essenhigh RH, Förtsch D, Klimesh HE. Combustion characteristics of carbon: Influence of the Zone I-Zone II transition on burn-out in pulverized coal flames. Energy & Fuels, 1999; 13: 955-960.
- Fan J, Quian L, Ma Y, Sun P, Cen K. Computacional modeling of pulverized coal combustion processes in tangentially fired furnaces. Chemical Engineering Journal, 2001; 81: 261-269.
- Farzan H, Essenhigh RH. High intensity combustion of coal. 19th Symposium (Intenational) on Combustion. The Combustion Institute, 1982: 1105-1111.
- Ferziger JH, Peric M. Computational methods for fluid dynamics. Springer, 2002.
- Field MA, Gill DW, Morgan BB, Hawksley PGW. Combustion of pulverized coal. BCURA, 1967.
- Fiveland WA, Jamaluddin AS. An efficient method for predicting unburned carbon in boilers. Combustion Science and Technology, 1992, 81: 147-167.

- Fletcher TH, Kerstein AR, Pugmire RJ, Grant DM. Chemical percolation model for devolatilization:II. Temperature and heating rate effects on products yield. Energy & Fuels, 1990; 4: 54.
- Fletcher TH; Kerstein RJ, Pugmire RJ, Solum MS, Grant DM. A chemical percolation model for devolatilization: 3. Chemical structure as a function of coal type. Energy and fuels, 1992; 6: 414.
- Fletcher TH, Kerstein A, Pugmire RJ, Solum M, Grant DM. A chemical percolation model for devolatilization: Summary. Brigham Young University, 1992.
- Fluent Inc. Manuals, 2001.
- Förtsch D, Essenhigh RH, Schnell U, Hein KRG. On the application of the Thiele/Zeldovich analysis to porous carbon combustion. Energy & Fuels, 2003; 17: 901-906.
- Gale TK, Bartholomew CH, Fletcher TH. Effects of pyrolysis heating rate on intrinsic reactivities of coal chars. Energy & Fuels, 1996; 10: 766-775.
- Gareta R. Sistema de supervision basado en modelos inteligentes para gestionar los ciclos de limpieza en una caldera de biomasa. Tesis Doctoral, Universidad de Zaragoza, 2004.
- Gavalas GR. Analysis of char combustion including the effect of pore enlargement. Combustion Science and Technology, 1981; 24: 197-210.
- Genetti DB. An advanced model of coal devolatilization based on chemical structure. Tesis doctoral. Department of chemical engineering, Brigham Young University, 1999.
- Gera D, Mathur M, Freeman M, O'Dowd W. Moisture and char reactivity modelling in pulverized coal combustors. Combustion Science & Technology, 2001; 172: 35-69.
- Glarborg P. Solid combustion course. Universidad de Zaragoza, 2001.
- Grant DM, Puigmire RJ, Fletcher TH, Kerstein AR. A chemical model of coal devolatilization using percolation lattice statistics. Energy & Fuels, 1989; 3: 175.
- Gouesbet G, Berlemont A. Eulerian and lagrangian approaches for predicting the behaviour of discrete particles in turbulent flows. Progress in Energy and Combustion Science, 1999; 25: 133-159.
- Graham DI, Moyeed RA. How many particles for my Lagrangian simulations? Powder Technology, 2002; 125: 179-186.
- Gurgel Veras CA, Saastamoinen J, Carvalho JR, Aho M. Overlapping of the devolatilization and char combustión stages in the burning of coal particles. Combustion and Flame, 1999; 116:567-579.
- Haas J, Tamura M, Weber R. Characterization of coal blends for pulverizad fuel combustión. Fuel, 2001; 80: 1317-1323.
- Hanjalic K. Turbulence closure Models. Lecture Series von Karman Institute for Fluid Dynamics, 2000.

- Hampartsoumian E, Pourkashanian M, Williams A. Combustion rates of chars and carbonaceous residues. Journal of the Institute of Energy, 1989; 48-56.
- Hampartsoumian E, Murdoch PL, Pourkashanian M, Trangmar DT, Williams A. The reactivity of coal chars gasified in a carbon dioxide environment. Combustion Science and Technology, 1993; 92: 105-121.
- Hampartsoumian E, Nimmo W, Rosenberg P, Thomsen E, Williams A. Evaluation of the chemical properties of coals and their maceral group constituents in relation to combustion reactivity using multi-variate analyses. Fuel, 1998; 77: 735-748.
- Hamor RJ, Smith IW, Tyler RJ. Kinetics of combustion of a pulverized brown coal char between 630 and 2200 K. Combustion and Flame, 1973; 21: 153-162.
- Hao Z, Kefa C, Jianbo M. Combining neural network and genetic algorithms to optimize low NOx pulverized coal combustion. Fuel, 2001; 80: 2163-2169.
- Haynes BS. A turnover model for carbon reactivity I. development. Combustion and Flame, 2001; 126: 1421-1432.
- Hesselmann G. Modelling of pulverised coal fired furnaces with advanced combustion systems by integrated performance programs. III Joule Programme. Clean Coal Technology R&D, 2000.
- Hong J, Hecker WC, Fletcher TH. Predicting effectiveness factor for m-th order and langmuir rate equations in spherical coordinates. ACS Division of Fuel Chemistry, 1999; 44: 1011-1015.
- Hong J. Modelling char oxidation as a function of pressure using an intrinsic Langmuir rate equation. Tesis Doctoral, Brigham Young University, 2000.
- Hottel HC, Sarofim AF. Radiative Transfer. McGraw Hill, 1967.
- Howard JB, Essenhigh RH. Pyrolysis of coal particles in pulverized fuel flames. I&EC Process Design and Development, 1967: 74-84.
- Hurt RH, Mitchell RE. Unified high-temperature char combustion kinetics for a suite of coals of various rank. 24th Symposium (Intenational) on Combustion. The Combustion Institute, 1992: 1243-1250.
- Hurt RH. Reactivity distributions and extinction phenomena in coal char combustion. Energy & Fuels, 1993; 7:721-733.
- Hurt RH, Gibbins JR. Residual carbon from pulverized coal fired boilers:1. Size distribution and combustion reactivity. Fuel, 1995; 74: 471-480.
- Hurt RH, Davis KA, Yang NYC, Headley TJ, Mitchell GD. Residual carbon from pulverized coal fired boilers: 2. Morphology and physicochemical properties. Fuel, 1995; 74: 1297-1306.
- Hurt RH. Statistical kinetics for char combustion and carbon burnout. Coal Science, 1995: 611:614.

- Hurt RH, Hadad C., Kerstein A. Fundamental models of coal char formation and combustion. Interim Report Federal Energy Technology Center DE-FG22-96PC96249, 1998.
- Hurt RH, Sun JK, Lunden M. A kinetic model of carbon burnout in pulverized coal combustion. Combustion and Flame, 1998; 113: 181-197.
- Hurt RH, Sun JK, Lang T. Extinction mechanisms in pulverized coal combustion. Prospects for Coal Science in the 21st Century, 1999: 379-382.
- Hurt RH, Calo JM. Semi-global intrinsic kinetics for char combustion modelling. Combustion and Flame, 2001; 125: 1138-1149.
- Hurt RH, Haynes BS. On the origin of power-law kinetics in carbon oxidation. Proceedings of the Combustion Institute, 2004; 125: 1138-1149.
- Iranzo I, Domingo E, Cortés C, Arauzo I. Combustion characterization of a pulverizad coal utility boiler based on CFD techniques. CIRCE press, 2001.
- Jamaluddin AS, Smith PJ. Predicting radiative transfer in rectangular enclosures using the discrete ordinates method. Combustion Science and Technology, 1988; 89: 321-340.
- Jensen A. Solid combustion course. Universidad de Zaragoza, 2001.
- Jensen PT, Mitchell RE. High temperature char reactivity measurements in the Sandia laminar flow reactor. Energy research project Nº 1323/87-16, Ministry of the Environment, Geological Survey of Denmark, 1993.
- Jones JM, Pourkashanian M, Rena CD, Williams A. Modelling the relationship of coal structure to char porosity. Fuel, 1999; 78: 1737-1744.
- Kobayashi H, Howard JB, Sarofim AF. Coal devolatilization at high temperatures. 16th Symposium (International) on Combustion. The Combustion Institute, 1976; 411-425.
- Külaots I, Gao YM, Hurt RH, Suuberg EM. Characterization of carbon in coal fly ash. Brown University press, 1999.
- Külaots Indrek, Hurt RH, Suuberg EM. Size distribution of unburned carbon in coal fly ash and its implications. Fuel, 2004; 83: 223-230.
- Kurose R, Ikeda M, Makino H. Combustion characteristics of high ash coal in a pulverized coal combustion. Fuel, 2001; 80: 1447-1455.
- Kurose R, Ikeda M, Makino H, Kimoto M, Miyazaki T. Pulverized coal combustion characteristics of high-fuel-ration coals. Fuel, 2004; 83: 1777-1785.
- Langmuir I. Chemical reaction on surfaces. Transactions of the Faraday Society, 1921; 606-621.
- Launder BE, Spalding DB. The numerical computation of turbulent flows. Computational Methods on Applied Mechanical Engineering, 1974; 3: 269-289.
- Levenspiel Octave. Ingeniería de las reacciones químicas. Ediciones Reverte, 2001.

- Lipson C, Sheth NJ. Statistical design and analysis of engineering experiments. McGraw Hill, 1973.
- Llera E. Modelo semiempírico de ensuciamiento de calderas alimentadas con mezclas de carbones. Tesis Doctoral, Universidad de Zaragoza, 2002.
- Lockwood FC, Shah NG. A new radiation solution method for incorporation in general combustion procedure. 18th (Intenational) on Combustion. The Combustion Institute, 1981: 1405-1414.
- Lockwood FC, Parodi SA. Performance prediction in advance coal fired boilers: burner-burner interaction. The Imperial College of Science press, 1998.
- Longwell JP, Sarofim AF, Lee CH. Effects of catalytic mineral mater on CO/CO2, temperature and burning time for char combustion. Massachusetts Institute of Technology, Progress Report DE-FG22-89PC89774, 1993; 14.
- Mann AP, Kent JH. A computational study of heterogeneous char reactions in a full-scale furnace. Combustion and Flame, 1994; 99: 147-156.
- Maroto-Valer MM, Taulbee DN, Hower JC. Characterization of differing forms of unburned carbon present in fly ash separated by density gradient centrifugation. Fuel, 2001; 80: 795-800.
- Martins N, Calisto H. Diagnostic system for boilers and furnaces using CFD tools and a neural network-based approach. Universidade de Aveiro (Portugal). 2006.
- Mehta BN, Aris R. Communications on the theory of diffusion and reaction – VII The isothermal pth order reaction. Chemical Engineering Science, 1971; 26: 1699-1712.
- Mitchell RE, McLean WJ. On the temperature and reaction rate of burning pulverized fuels. 19th Symposium (International) on Combustion. The Combustion Institute, 1982; 1113-1122.
- Modest MF. Radiative Heat Transfer. McGraw Hill, 1993.
- Montgomery DC. Diseño y análisis de experimentos. Grupo Editorial Iberoamérica, 1991.
- Niksa S, Kerstein AR. FLASHCHAIN theory for rapid coal devolatilization kinetics. 1. Formulation. Energy & Fuels, 1991; 5: 647-665.
- Niksa S. FLASHCHAIN theory for rapid coal devolatilization kinetics. 2. Impact of operating conditions. Energy & Fuels, 1991; 5: 665-673.
- Niksa S. FLASHCHAIN theory for rapid coal devolatilization kinetics. 3. Modeling the behavior of various coals. Energy & Fuels, 1991; 5: 673-683.
- Niksa S. FLASHCHAIN theory for rapid coal devolatilization kinetics. 4. Predicting ultimate yields from ultimate analyses alone. Energy & Fuels, 1994; 8: 659-670.
- Niksa S. FLASHCHAIN theory for rapid coal devolatilization kinetics. 5. Interpreting rates of devolatilization for various coal types and operating conditions. Energy & Fuels, 1994; 8: 671-679.

- Niksa S. Coal combustion Modelling. IEA Coal Research, 1996.
- Pallarés J, Arauzo I, Díez LI. Numerical prediction of unburned carbon levels in large pulverized coal utility boilers. Fuel, 2005; 84: 2364-2371.
- Pallarés J, Arauzo I, Williams A. Integration of CFD codes and advanced combustion models for quantitative burnout determination. Fuel, 2005; 86: 2283-2290.
- Pao YH. Adaptive pattern recognition and neural networks. Addison Wesley, 1989.
- Pope SB. Turbulent flows. Cambridge University Press, 2000.
- Rich E, Knight K. Inteligencia artificial. McGraw Hill, 1994.
- Roger Jang JS, Sun ChT, Mizutani E. Neuro-Fuzzy and soft computing. A computational approach to learning and machine intelligence. Prentice Hall, 1997.
- Romeo LM, Gareta R. Neural network for evaluating boiler behaviour. Applied Thermal Engineering, 2006; 26: 1530-1536.
- Rosendahl LA, Sorensen H. Anisotropic turbulent dispersion of non-spherical and spherical particles in swirling flow. Proceedings of ASME Fluid Engineering Summer Meeeting, 2000. Boston (USA).
- Sami M, Annamalai K, Wooldridge M. Co-firing of coal and biomass fuel blends. Progress in Energy and Combustion Science, 2001; 27: 171-214.
- Santamaría JM, Herguido J, Menéndez MA, Monzón A. Ingeniería de reactores. Editorial Síntesis, 1999.
- Sear LKA. UK practice- A review of fly ashes for use in concrete. Progress Workshop on Novel Products from Combustion Residues, 2001. Morella (Spain).
- Sear LKA. Fly ash standards, market strategy and UK practice. . Progress Workshop on Novel Products from Combustion Residues, 2001. Morella (Spain).
- Severin T, Wirtz S, Scherer V, Roth K. Simulation of pulverised coal fired boilers with a simplified cellnet model. Chemie-Ingenieur-Technik, 2005; 77: 1042.
- Sheng Ch, Moghtaderi B, Gupta R, Wall TF. A computational fluid dynamics bases study of the combustion characteristics of coal blends in pulverised coal-fired furnace. Fuel, 2004; 83: 1543-1552.
- Shim HS, Hurt RH. Thermal annealing of chars from diverse organic precursors under combustion-like conditions. Energy & Fuels, 2000; 14: 340-348.
- Simon GA. Coal pirolysis I. Pore evolution theory. Combustion and Flame, 1983; 53: 83-92.
- Smart JP, Nakamura T. NOx emissions and burnout from a swirl-stabilised burner firing pulverised coal: the effects of firing coal blends. Journal of the Institute of Energy, 1993; 66: 99-105.
- Smith IW. Kinetics of combustion of size-graded pulverized fuels in the temperature range 1200-2270 K. Combustion and Flame, 1971; 17: 303-314.

- Smith IW. The kinetics of combustion of pulverized semi-anthracite in the temperature range 1400-2200 K. Combustion and Flame, 1971; 17: 421-428.
- Smith IW, Tyler RJ. Internal burning of pulverized semi-anthracite: the relation between particle structure and reactivity. Fuel, 1972; 51: 312-321.
- Smith IW. The intrinsic reactivity of carbons to oxygen. Fuel, 1978; 57: 409-414.
- Smith IW. The combustion rates of coal chars: a review. 19th Symposium (Intenational) on Combustion. The Combustion Institute, 1982: 1045-1065.
- Smith JD, Smith PJ, Hill SC. Parametric sensitivity study of a CFD-based coal combustion model. AIChE Journal, 1993; 39: 1668-1679.
- Smith PJ, Fletcher TH, Smoot LD. Model for pulverized coal-fired reactors. 18th Symposium (Intenational) on Combustion. The Combustion Institute, 1981: 1285-1293.
- Smoot DL, Smith PJ. Coal combustion and gasification. The Plenum Chemical Engineering Series, 1985.
- Solomon PR, Colket MB. 17th Symposium (International) on Combustion. The Combustion Institute, 1979: 131-143.
- Solomon PR, Hamblen DG, Carangelo RM, Serio MA, Deshpande GV. General model of coal devolatilization. Energy & Fuels, 1988; 2: 405-422.
- Solomon PR, Hamblen DG, Yu ZZ, Serio MA. Network models of coal thermal decomposition. Fuel, 1990; 69: 754-763.
- Solomon PR, Serio MA, Carangelo RM, Bassilakis R, Yu ZZ, Charpenay S, Whelan J. Analysis of coal by thermogravimetry – Fourier transform infrared spectroscopy and pyrolysis modelling. Journal of Analitical and Appplied Pyrolysis, 1991; 1-14.
- Solomon PR, Hamblen DG, Serio MA, Yu ZZ, Charpenay S. A characterization method and model for predicting coal conversion behaviour. Fuel, 1993; 72: 469-488.
- Sommerfeld M. Theoretical and experimental modelling of particulate flow. Lecture Series von Karman Institute for Fluid Dynamics, 2000.
- Spalding DB. A single formula for the law of the wall. Journal of Applied Mechanics, 1961; 455-458.
- Stephenson PL. Mathematical modelling of semi-anthracite combustion in a single burner furnace. Fuel, 2003; 82: 2069-2073.
- Stopford PJ. Recent applications of CFD modeling in the power generation and combustion industries. Applied Mathematics Modelling, 2002; 26:351-374.
- Stubington JF, Linjewile TM. The effects of fragmentation on devolatilization of large coal particles. Fuel; 1989; 68: 155-160.
- Sun JK, Hurt RH. Mechanisms of extinction and near-extinction in pulverized solid fuel combustion. Proceedings of the Combustion Institute, 2000; 28: 2205-2213.

- Suuberg EM. Thermally induced changes in reactivity of carbons. Fundamental Issues in Control of Carbon Gasification Reactivity, 1991: 269-305.
- Suuberg E, Hurt RH, Külaots I, Gao YM. Fundamental mechanisms in high-carbon fly ash utilization. Brown University and Princeton University, 1999.
- Tan CK, Wilcox SJ, Ward J. Use of artificial intelligence techniques for optimisation of co-combustion of coal with biomass. Journal of the Energy Institute, 2006; 79: 19-25.
- Teruel E, Cortés C, Díez LI, Arauzo I. Monitoring and prediction of fouling in coal-fired utility boilers using neural networks. Universidad de Zaragoza, 2005.
- Timothy LD, Sarofim AF, Béer JM. Characteristics of single particle coal combustion. 19th Symposium (Intenational) on Combustion. The Combustion Institute, 1982; 1123-1130.
- Tomeczek J, Palugniok H. Kinetics of mineral matter transformation during coal combustion. Fuel, 2002; 81: 1251-1258.
- Turns SR. An introduction to combustion. McGraw Hill, 2000.
- Tyler RJ, Wouterlood HJ, Mulcahy MFR. Kinetics of the graphite-oxygen reaction near 1000 K. Carbon, 1976; 14: 271-278.
- Ubhayakar SK, Stickler DB, Rosenberg CW, Gannon RE. Rapid devolatilization of pulverized coal in hot combustion gases. Energy production from coal, 1976; 427-436.
- Ulloa C, Borrego AG, Gordon AL, García X. Char characterization and DTF assays as tools to predict burnout of coal blends in power plants. Fuel, 2005; 84: 247-257.
- Unsworth JF, Barratt DJ, Roberts PT. Coal quality and combustion performance. Coal Science and Technology, 1991; 19: 231-408.
- Users guide for FG-DVC model. Advanced Fuel Research Inc., 1992.
- Van der Lans RP, Glarborg P, Dam-Johansen K, Knudsen P, Hesselmann G, Hepburn P. Influence of coal quality on combustion performance. Fuel, 1998; 77: 1317-1328.
- Velilla J. Estudio del flujo en el interior del conducto de extracción de sólidos de un ciclón de una central térmica de lecho fluido a presión. Tesis Doctoral, Universidad de Zaragoza, 2004.
- Versteeg HK, Malalasekera W. An introduction to computational fluid dynamics – The finite volume method. Longman, 1995.
- Veynante D, Vervisch L. Turbulent combustion modelling. Lecture Series von Karman Institute for Fluid Dynamics, 2003.
- Wall TF. Principles of combustion engineering for boilers: The combustion of coal as pulverized fuel through swirl burners, 1987.
- Walsh P, Xie J, Douglas RE, Battista JJ, Zawadzki EA. Analysis of carbon loss from coal-fired utility boilers. EPRI Heat-Rate Improvement Conference, 1992. Birmingham (USA).
- Walsh P, Xie J, Douglas RE, Battista JJ, Zawadzki EA. Effect of coal quality on unburned carbon loss. EPRI Heat-Rate Improvement Conference, 1992. Birmingham (USA).

- Warnatz J, Mass U, Dibble RW. Combustion. Springer, 1996.
- White BR. Encyclopedia of fluid mechanics: Solids and gas-solids flows. Nicholas P. Cheremisinoff, 1996.
- Wilcox DC. Turbulence modelling for CFD. DCW industries, 1998.
- Williams A, Backreedy RI, Habib R, Jones JM, Pourkashanian M. Modelling coal combustion: the current position. Fuel, 2002; 81: 605-618.
- Wu Z. Prevention of particulate emission. IEA Coal Research report, 2000.
- Xu M, Azevedo JLT, Cavalho MG. Modelling of the combustion process and NO_x emissions in a utility boiler. Fuel, 2000; 79: 1611-1619.
- Xu M, Azevedo JLT, Cavalho MG. Modelling of a front fired utility boiler for different operating conditions. Computational Methods on Applied Mechanical Engineering, 2001; 190: 3581-3590.
- Young BC, Smith IW. The combustion of Loy Yang Brown coal char. Combustion and flame, 1989; 76: 29-35.
- Zhu Q, Jones JM, Williams A, Thomas KM. The predictions of coal/char combustion rate using an artificial neural network approach. Fuel, 1999; 78: 1755-1762.

Department of Mechanical Engineering
Centro Politécnico Superior
University of Zaragoza